From grains to rocks : the evolution of hydraulic and mechanical properties during diagesis

Lucille Carbillet

Institut Terre & Environnement de Strasbourg | ITES | UMR 7063 de l'Université de Strasbourg & CNRS & ENGEES

UNIVERSITÉ DE STRASBOURG

Ecole et Observatoire des Sciences de la Terre

ED 413 Sciences de la Terre et de l'Environnement

ÉCOLE DOCTORALE SCIENCES DE LA TERRE ET DE L'ENVIRONNEMENT

Institut Terre et Environnement de Strasbourg (UMR 7063)

THÈSE présentée par :

Lucille CARBILLET

soutenue le : **16 juin 2022**

pour obtenir le grade de : **Docteur de l'Université de Strasbourg**

Discipline/ Spécialité : Géophysique/Physique des roches

From grains to rocks: the evolution of hydraulic and mechanical properties during diagenesis.

THÈSE dirigée par :

M. HEAP Michael	Professeur, Université de Strasbourg
M. BAUD Patrick	Professeur, Université de Strasbourg

RAPPORTEURS :

M. MEREDITH Philip	Professeur, University College of London
M. FORTIN Jérôme	Directeur de recherche CNRS, ENS Paris

AUTRES MEMBRES DU JURY :

M. SULEM Jean	Professeur, Ecole des Ponts Paris-Tech Directeur de recherche, Laboratoire Navier
Mme DOAN Mai-linh	Maître de conférences, Université Grenoble-Alpes

For my sister Claire, the art-maker.

I leave Sisyphus at the foot of the mountain! One always finds one's burden again. But Sisyphus teaches the higher fidelity that negates the gods and raises rocks. He too concludes that all is well. This universe henceforth without a master seems to him neither sterile nor futile. Each atom of that stone, each mineral flake of that night filled mountain, in itself forms a world. The struggle itself toward the heights is enough to fill a man's heart. One must imagine Sisyphus happy.

Albert Camus, *The Myth of Sisyphus and Other Essays*, 1942

Acknowledgments

I acknowledge fundings from an Initiative d'Excellence (IDEX) "Contrats Doctoraux" grant provided by the French state. My laboratory equipment was funded in part by the Laboratoire d'Excellence (LABEX) grant ANR-11-LABX-0050_G-EAU-THERMIE-PROFONDE and so benefits from state funding managed by the Agence National de la Recherche (ANR) as part of the “Investissements d'avenir” program.

During my PhD, I had the privilege to be surrounded by dynamic and trustworthy people who rendered the past years challenging and exciting at once, but also truly fulfilling. I might not be able to cite all the people I think of, but I am sincerely grateful for their help.

First and foremost, I wish to thank Mike Heap and Patrick Baud for their sound guidance, their daily encouraging support, for always challenging me and for helping me grow more independent and confident. I am grateful to Fabian Wadsworth for his expert knowledge and creativity, without which I would never have learnt how to cook fake rocks properly. To them three, I am grateful for trusting me to be able to work on this project. I also wish to express my sincere gratitude to the members of my follow-up committee, Jérôme Fortin and Mai-linh Doan, joined by Jean Sulem and Philip Meredith as members of my jury thesis.

I express warm thanks to Thierry Reuschlé, whose extensive knowledge and solicitude have often saved me a great deal of time and fuelled ideas for solving technical difficulties. I would not have done much if it was not for Bertrand Renaudié, who cored and rectified hundreds of glass bead samples, for Christophe Nevado, who prepared most of the thin sections, and for Gilles Morvan, who spent hours looking at broken and unbroken sintered glass beads on the SEM with me.

I extend thanks to people who I had the opportunity to work with for different projects which are not presented here, including Hugh Tuffen, Holly Unwin, Steffi Burchardt, Tobias Schmiedel, Taylor Witcher, Emma Rhodes, Marina Rosas-Carbajal and Jean-Christophe Komorowski.

This work has greatly benefitted from discussions with Jérémie Vasseur and Dominique de Ligny, whose expertise on glass provided new perspectives and ideas on several occasions. I would also especially like to thank Alexandra Kushnir, for her enthusiasm and her wise words on many aspects of the work. In addition, fresh perspective was often brought by people from other fields of research, the curiosity and sincere interest of whom I am thankful for: Leo, Emmanuel, Pauline, Camille, Jeanne, Hugo, Frank, Cooper and Fred.

Music has certainly helped keep me sane throughout the PhD – and pandemic – and I cannot find the words to say how thankful I am to Prokop, for the music and for his unfailing support,

and to all the friends I have played gigs with and worked on albums and videoclips with. Finally, thanks to the ones who always have my back, my sister and my parents.

Résumé

Notre compréhension de la relation entre les attributs microstructuraux et les propriétés mécaniques des matériaux naturels découle des travaux expérimentaux en mécanique des roches. Des progrès considérables ont été réalisés mais l'hétérogénéité des roches naturelles, à la fois en termes de pétrologie que de microstructure, limite l'étude de la contribution de chaque paramètre microstructural de façon indépendante. Dans cette thèse, des roches synthétiques pour lesquelles ces paramètres peuvent être contrôlés sont utilisées pour déconvoluer et étudier la contribution d'attributs microstructuraux spécifiques sur les propriétés hydrauliques et mécaniques des roches. En combinant une caractérisation pétrophysique systématique et des expériences de déformation avec une étude de la microstructure, le contrôle de premier ordre de la porosité et de la taille des grains sur l'initialisation de la compaction inélastique est mis en évidence. Par ailleurs, il est montré que, en compression triaxiale, la distribution de la taille des grains exerce une influence significative sur la propension à la localisation de la compaction.

Porosité, taille des grains, distribution de la taille des grains, compaction inélastique, localisation de la compaction

Abstract

Experimental rock mechanics studies underpin our understanding of the relationship between microstructural attributes and bulk mechanical properties of natural materials. Considerable progress has been made but intrinsic variability from sample to sample and structural heterogeneity remain limitations to the study of the contribution of each microstructural parameter independently. In this work, synthetic rocks for which these parameters can be predetermined and designed are used to unravel the contribution of microstructural attributes on the hydraulic and mechanical properties of rocks. Combining systematic petrophysical characterisation and experimental rock deformation methods with analyses of the microstructure, the first-order control of porosity and grain size on the onset of inelastic compaction are exposed and grain size distribution is shown to have a significant influence on the propensity for compaction localisation under triaxial loading.

Porosity, grain size, grain size distribution, inelastic compaction, compaction localisation

Table of Contents

Acknowledgments 5
Résumé 6
Abstract 7
List of Figures and Tables 13

Chapter 1 Introduction

1.1 Fundamentals 18
1.1.1 Stress, strain and in-situ conditions for crustal rocks 18
1.1.2 Stress-strain behaviour of porous rocks 19
1.2 Diagenesis: original microstructure and macroscopic properties establishment 21
1.3 Phenomenology of mechanical compaction 23
1.3.1 Inelastic behaviour and failure mode 23
1.3.2 Microstructural observations 29
1.3.3 Micromechanics of failure under compressive loading 33
1.4 Influence of porosity on the hydromechanical behaviour of crustal rocks 35
1.4.1 The permeability-porosity relationship 35
1.4.2 Evolution of strength with porosity 36
1.4.3 Control of porosity on the brittle-ductile transition 37
1.4.4 Influence of porosity on the hydrostatic behaviour 38
1.5 Influence of grain size on the hydromechanical behaviour of crustal rocks 40
1.5.1 Microstructural description 40
1.5.2 Experimental observations 40
1.6 Modelling of the behaviour of porous rock using synthetic rock samples 42
1.6.1 Alternative use of synthetic rocks 42
1.6.2 Viscous sintering of glass beads 45
1.7 Structure of the thesis 45

Chapter 2 Preparation Procedure: The Cooking Recipe for Sintered Glass Bead Samples

2.1 Viscous sintering of glass beads under no external load: theoretical framework 49

2.1.1 State of forces acting on a liquid droplet 49

2.1.2 Coalescence and porosity decrease with time 50

2.1.3 Pore space and granular densification 52

2.1.4 Sintering glass beads: temperature-dependent viscosity and model parameters 54

2.2 Practical procedure for the preparation of synthetic rocks: ingredients and equipment 55

2.2.1 Ingredients 56

2.2.2 Equipment 58

2.3 Practical procedure for the preparation of synthetic rocks: instructions 58

2.3.1 Method 1: block preparation using a monodisperse distribution of beads 60

2.3.2 Method 2: block preparation using bidisperse or polydisperse distributions of beads 63

2.3.3 Method 3: single sample preparation 64

2.4 Overview of the synthetic samples: from the sample scale to the grain scale 65

2.5 Concluding remarks 68

Chapter 3 Methods and Sample Characterisation: Assessing the Suitability of Sintered Glass Beads as Analogues for Sandstones

3.1 Microstructural observations 71

3.2 Characterisation of the pore space 72

3.2.1 Porosity 72

3.2.2 Specific surface area 73

3.2.2.1 Experimental procedure 73

3.2.2.2 Results 74

3.3 Physical properties of sintered glass beads 75

3.3.1 Elastic wave velocity 75
3.3.1.1 Experimental procedure 75
3.3.1.2 Results: comparison to natural sandstones and model predictions 76
3.3.2 Thermal conductivity 78
3.3.2.1 Experimental procedure 78
3.3.2.2 Results: comparison to natural sandstones and model predictions 79
3.3.3 Electrical conductivity 80
3.3.3.1 Experimental procedure 80
3.3.3.2 Results: comparison to natural rocks and model predictions 81
3.3.4 Gas-permeability 82
3.3.4.1 Experimental procedure 82
3.3.4.2 Results: comparison to natural sandstones 85
3.3.4.3 Results: comparison to permeability models 87
3.4 Procedures for the deformation experiments 90
3.4.1 Experimental apparatus and sample preparation 90
3.4.2 Hydrostatic compression experiments 92
3.4.3 Triaxial compression experiments 92
3.5 Uniaxial compressive strength of the synthetic rock 93
3.5.1 Experimental procedure 93
3.5.2 Results: mechanical data and microstructure 93
3.5.3 Micromechanical interpretation 97
3.5.4 Comparison to natural rocks 99
3.6 Concluding remarks 100

Chapter 4 Mechanical Compaction of Monodisperse Porous Synthetic Rocks

4.1 Introduction 102
4.2 Preparation and characterisation of the synthetic samples 103
4.2.1 Viscous sintering of monodisperse populations of glass beads 103

4.2.2 Description of the sintered glass beads samples 104
4.3 Experimental procedures 105
4.4 Mechanical data 108
4.4.1 Results of the hydrostatic and triaxial tests 109
4.4.2 Critical stress states: effect of porosity and grain size 114
4.5 Microstructural observations 117
4.6 Discussion 120
4.6.1 Suitability of sintered glass beads as crustal analogues 120
4.6.2 Deconvolution of microstructural parameters 124
4.6.3 Influence of porosity and grain size on compactive yield 126
4.6.4 Compaction localisation 129
4.7 Crustal implications and concluding remarks 131

Chapter 5 Mechanical Compaction of Porous Synthetic Rocks: The Influence of Grain Size Distribution

5.1 Introduction 135
5.2 Materials and Methods 136
5.2.1 Experimental procedure for the preparation of the samples 136
5.2.2 Description of the samples 137
5.2.3 Deformation experiments 139
5.3 Results: hydrostatic compression 140
5.3.1 Mechanical data and microstructural observations 140
5.3.2 Influence of dispersivity 144
5.4 Results: triaxial compression 145
5.4.1 Mechanical data 145
5.4.2 Microstructural observations 147
5.5 Discussion 149
5.5.1 Comparison to monodisperse sintered glass beads samples 149
5.5.2 Comparison to natural porous rocks 152
5.5.3 Compaction localisation 155

5.6 Conclusions 160

Chapter 6 Conclusions and Perspectives

6.1 Conclusions 163

6.1.1 Suitability of sintered glass beads as analogues for porous crustal rocks 163

6.1.2 Porosity and grain size control on the mechanical behaviour of crustal rocks 164

6.1.3 The influence of grain size distribution on the mechanical behaviour of crustal rocks 166

6.2 Perspectives 167

References 171

Annex 1: Description of Spheriglass A glass and SiLiBeads Type S microspheres 188

Annex 2: Résumé de la thèse de doctorat (français) 188

List of Figures and Tables

Chapter 1

Figure 1.1 Typical stress-strain behaviour of porous sandstones 20

Figure 1.2 Schematic of the evolution of sediments during diagenesis, 22

Figure 1.3 Example of mechanical data for the hydrostatic loading of a porous rock 24

Figure 1.4 Example of mechanical data for selected triaxial experiments 25

Figure 1.5 Representative data for the mechanical behaviour of Bentheim sandstone 27

Figure 1.6 Microstructure and damage evolution under triaxial compression 30

Figure 1.7 Discrete compaction bands in Bentheim and Bleurswiller sandstones 32

Figure 1.8 Models for the micromechanics of compaction of porous rocks 34

Figure 1.9 Evolution of uniaxial compressive strength with porosity 36

Figure 1.10 Compilation of failure envelopes for porous sandstones 38

Figure 1.11 Mechanical data for sandstones deformed under hydrostatic compression 39

Figure 1.12 Compilation of uniaxial compressive strength data for porous sandstones as a function of mean grain size 41

Figure 1.13 Mechanical behaviour of synthetic rocks 44

Chapter 2

Figure 2.1 Coalescence of a many-droplet viscous system with time 51

Figure 2.2 Mean pore radius evolution during granular densification by viscous sintering 53

Figure 2.3 Temperature dependency of viscosity and porosity reduction during sintering 54

Figure 2.4 Types of grain size distributions used to prepare the synthetic samples 59

Figure 2.5 Experimental procedure for the preparation of sintered blocks 60

Figure 2.6 Grain radius distributions used to prepare synthetic samples 62
Figure 2.7 Experimental procedure for the preparation of individual samples 64
Figure 2.8 Overview of synthetic and natural sandstone samples 66
Figure 2.9 Microstructure of sintered glass bead samples 67
Table 2.1 Chemical composition of soda-lime-silica glass beads 56
Table 2.2 Thermal properties of soda-lime-silica glasses 57
Table 2.3 Mechanical properties of soda-lime-silica glasses 57
Table 2.4 Grain size distributions 61

Chapter 3

Figure 3.1 Specific surface area of synthetic samples 74
Figure 3.2 Experimental device for wave velocity measurements 76
Figure 3.3 Porosity dependency of P- and S-wave velocity 77
Figure 3.4 Experimental setup for thermal conductivity measurements 78
Figure 3.5 Dry thermal conductivity as a function of porosity 79
Figure 3.6 Electrical conductivity of the synthetic samples 82
Figure 3.7 Schematics of the benchtop steady state permeameter 83
Figure 3.8 Permeability evolution with porosity 86
Figure 3.9 Evolution of permeability as a function of the formation factor 88
Figure 3.10 Porosity dependency of the pore radius 89
Figure 3.11 Schematics of triaxial press 91
Figure 3.12 Evolution of the uniaxial compressive strength with porosity 94
Figure 3.13 Microstructural features in a deformed high-porosity sample 95
Figure 3.14 Microstructural features in a deformed low-porosity sample 96
Figure 3.15 Comparison of UCS data with the pore-emanated crack model predictions 97
Figure 3.16 Compilation of UCS data for synthetic samples and natural rocks 99

Chapter 4

Figure 4.1 Microstructural description of the monodisperse synthetic samples 104
Figure 4.2 Representative mechanical data and cumulative acoustic emission energy for hydrostatic tests on the monodisperse synthetic samples 109
Figure 4.3 Representative mechanical data and cumulative acoustic emission energy for triaxial tests in the brittle regime 111
Figure 4.4 Representative mechanical data and cumulative acoustic emission energy for triaxial tests in the regime of shear-enhanced compaction 112
Figure 4.5 Compilations of mechanical data from hydrostatic loading and triaxial tests 113
Figure 4.6 Compilations of failure envelopes for samples: the influence of porosity 115
Figure 4.7 Compilations of failure envelopes for synthetic samples: the influence of grain size 116
Figure 4.8. Microstructure of a monodisperse synthetic sample deformed under hydrostatic loading 118
Figure 4.9 Discrete compaction bands formed in a monodisperse sample 119
Figure 4.10 Data from tests performed on synthetic samples compared to data for sandstones 121
Figure 4.11 Compilation of porosity and grain diameter for laboratory sandstones 125
Figure 4.12 Influence of porosity on the compactive yield strength 127
Figure 4.13 Influence of grain diameter on the compactive yield strength 130
Table 4.1 Experimental conditions and mechanical data 106

Chapter 5

Figure 5.1 Grain size distributions of the bidisperse and polydisperse synthetic samples 137
Figure 5.2 Intact microstructure of samples with bidisperse and polydisperse grain size distribution 139
Figure 5.3 Mechanical data and acoustic emission energy for the hydrostatic 140

compression of polydisperse and bidisperse synthetic samples
Figure 5.4 Microstructure of synthetic samples deformed under hydrostatic loading 141
Figure 5.5 Influence of dispersivity on the onset of grain crushing 144
Figure 5.6 Mechanical data and cumulative acoustic emission energy for triaxial tests performed on polydisperse and bidisperse synthetic samples 145
Figure 5.7 Hydrostatic and triaxial mechanical data for polydisperse synthetic samples 146
Figure 5.8 Hydrostatic and triaxial mechanical data for bidisperse synthetic samples 147
Figure 5.9 Microstructure of polydisperse synthetic samples deformed under triaxial compression 148
Figure 5.10 Microstructure of bidisperse synthetic samples deformed under triaxial compression 149
Figure 5.11 Comparison of mechanical data for samples with bidisperse, polydisperse and monodisperse grain size distributions. 150
Figure 5.12 Comparison of mechanical data for synthetic samples and natural sandstones 153
Figure 5.13 Post-deformation microstructure of synthetic samples compared to Bleurswiller and Boise sandstones 157
Figure 5.14 Influence of dispersivity and porosity on compaction localisation 159
Table 5.1 Microstructural attributes and critical stress values 142

Chapter 6

Figure 6.1 The mechanical behaviour and failure mode of sintered glass bead samples: influence of porosity, grain size and dispersivity 164

Chapter 1

Introduction

1.1 Fundamentals

1.1.1 Stress, strain and in-situ conditions for crustal rocks

In classical mechanics, the motion of macroscopic bodies, often modelled as point particles, is described using two fundamental variables: the *position* of the body and the *force* that surrounding bodies exert on it. In rock mechanics, the objects which motion is studied are rock masses, i.e., deformable mineral aggregates whose different parts may have different motion, such that the point simplification is not valid, and the variables studied must be changed appropriately. For that purpose, the concepts of *stress* and *strain* are introduced (Jaeger et al., 2009). The forces applied to a rock mass are distributed over the entire volume, which is adequately capture by the notion of stress, mathematically defined as a force per unit area. When a solid rock is submitted to a certain state of stress, the position of the different particles of the rock change and the difference between the final and the initial position defines a displacement vector, which spatial derivative is the strain. In the case of in-situ compression, the stress state of rock masses is such that shear stress is zero. The stress tensor, which defines the stress state mathematically in the three directions of space, can therefore be written

$$\sigma = \begin{pmatrix} \sigma_1 & 0 & 0 \\ 0 & \sigma_2 & 0 \\ 0 & 0 & \sigma_3 \end{pmatrix} \tag{1.3}$$

where the diagonal components σ_1, σ_2 and σ_3 are the *maximum principal stress*, *intermediate principal stress* and mini*mum principal stress*, respectively. Conventionally,

compressive stresses and compactive strains (length and volume reductions) are taken to be positive.

The compressive stresses applied to the rocks in the Earth crust are mainly caused by gravitational forces, i.e., by the weight of the overburden that acts along the vertical direction. These lithostatic stresses can be derived from

$$\sigma = \rho g z \tag{1.4}$$

where ρ is the material density in [g.cm^3], g the gravitational acceleration in [m.s^{-2}] and z the coordinate in the vertical direction.

However, materials in the Earth crust are often saturated with groundwater or hydrocarbons. In the presence of a fluid in the pore space of a rock, the stress that the fluid exerts on the rock particles is superimposed to the lithostatic stress. Consequently, the stress applied to the rock mass is changed into

$$\sigma = \rho g z - P_p \tag{1.5}$$

where P_p is the pore fluid pressure in [kg.m^{-1}.s^{-2}].

1.1.2 Stress-strain behaviour of porous rocks

When porous fluid-saturated rocks are submitted to compression, the resultant deformation is assumed to be the sum of elastic and non-elastic terms. Elastic deformation occurs instantaneously and is reversed if the stress is released, i.e., elastic strain is neither time-dependent not associated to an energy dissipation (Bernabé et al., 1994). On the contrary, inelastic or plastic strain occurs after some time and is unrecoverable. The rapid release of energy in the rock associated to such deformation can generate a transient elastic wave, refer to as *acoustic emission* (AE) (Lockner, 1993). The rate of AE can be related to the inelastic strain rate (Lockner, 1993; Scholz, 1968) and while the location of the source of the radiated elastic wave informs on the spatial origin of the damage, the AE waveform carries information on the source micromechanism (Fortin et al., 2009). Under compression, the stress-strain behaviour of a porous rocks typically shows three stages, schematised in Figure

1.1: (1) non-linear elastic deformation due to the reversible closure or opening of microcracks, (2) linear elastic deformation and (3) inelastic deformation of the rock associated to a burst in AEs. Depending on the pressure and temperature conditions, the inelastic behaviour of a rock can vary from brittle to ductile (Figure 1.1). Macroscopically speaking, while the rock undergoes a substantial unrecoverable strain by the formation of a macroscopic fracture in the brittle regime, the rock is capable of undergoing such strain without macroscopic fracture in the ductile regime (Paterson & Wong, 2005). In that sense, the brittle-to-ductile transition is more accurately described as a faulting to flow transition, as proposed by Rutter (1986). Whether a rock behaves in a brittle or ductile manner is captured by differences in shape in the third phase of the stress-strain curve (Figure 1.1). As failure by brittle faulting occurs, the AE rate increases dramatically and the stress suddenly drops from its peak value to a residual level: such stress drop linked to macroscopic faulting is characteristic of the brittle field. Failure by plastic flow is marked by an increase in AEs and is manifested in the stress-strain behaviour by the absence of a stress drop and sometimes strain hardening. The phenomenology of the brittle-ductile transition in porous rocks will be discussed herein after (sections 1.3.1 and 1.4.3).

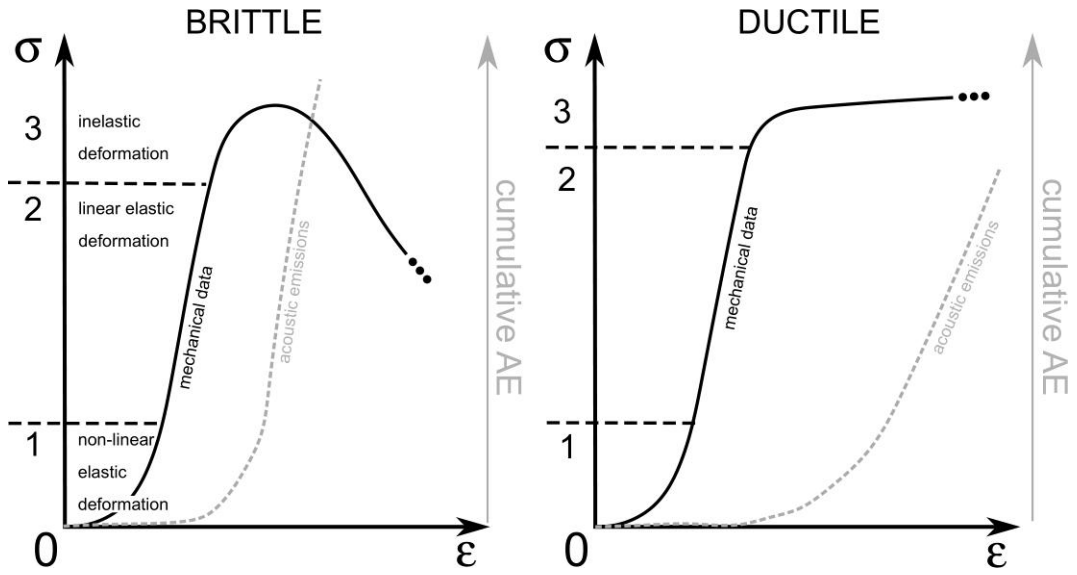

Figure 1.1 Schematic of the typical stress-strain behaviour of porous sandstones deformed at room temperature in the brittle (left) and ductile (right) regime. The mechanical data (solid black) are plotted as σ the differential stress against ε the axial strain and the corresponding acoustic emissions (AEs) are presented as the cumulative AEs against axial strain (dashed

grey). The characteristic evolution of the stress-strain curve and AEs during phase 1, 2 and 3 is described in the main text (derived from Guéguen & Palciauskas, 1994).

1.2 Diagenesis: original microstructure and macroscopic properties establishment

The Earth's crust is constituted of rocks materialised throughout different processes. These rocks are commonly divided into three generic types: igneous, metamorphic and sedimentary. The latter comprises rocks produced by diagenesis, defined in the Glossary of Geology as follows: "All the chemical, physical, and biologic changes undergone by a sediment after its initial deposition, and during and after its lithification, exclusive of surface alteration (weathering) and metamorphism." (Jackson & Bates, 1997). Diagenesis mobilises erosion products, which have been transported and deposited, and delivers variably cemented and consolidated sedimentary rocks. Besides cementation and compaction, a variety of processes such as authigenesis, neoformation, neomorphism or precipitation, can be involved in diagenesis and concur to build a sedimentary rock with an original mineralogy and microstructure. Figure 1.2 presents a schematic of the microstructural evolution throughout diagenesis for detritic sedimentary rocks. Deposited sediments stabilise at a certain initial porosity that depends on the depositional grain packing arrangement (0.4 for a random packing of uniform spheres, Beard & Weyl, 1973). With the progressive burial of the granular rock-forming materials by young sediments, the overburden load increases and, as it operates as an effective stress (Terzaghi, 1936), triggers the consolidation of the sediments and a decrease in bulk volume and porosity. Beyond the limit of elastic compaction, i.e., when deformation by means of grain rotation, sliding or fluid removal can no longer take place, subsequent bulk volume loss and porosity reduction due to further increase of effective stress is achieved through irreversible deformation of grains. During burial, grain-grain contact geometries evolve from discrete points through straight-elongated and concavo-convex to interpenetrative surfaces. Throughout diagenesis, as minerals grow or precipitate in pore spaces, form a cement, as other minerals are destroyed by interaction with fluids, as grain-grain contacts change, etc., the pore space is being shaped. To describe the original microstructure formed by the diagenetic processes, a variety of measurements such as porosity, pore size and shape distributions, pore throat size distribution or grain size and shape distributions can be used.

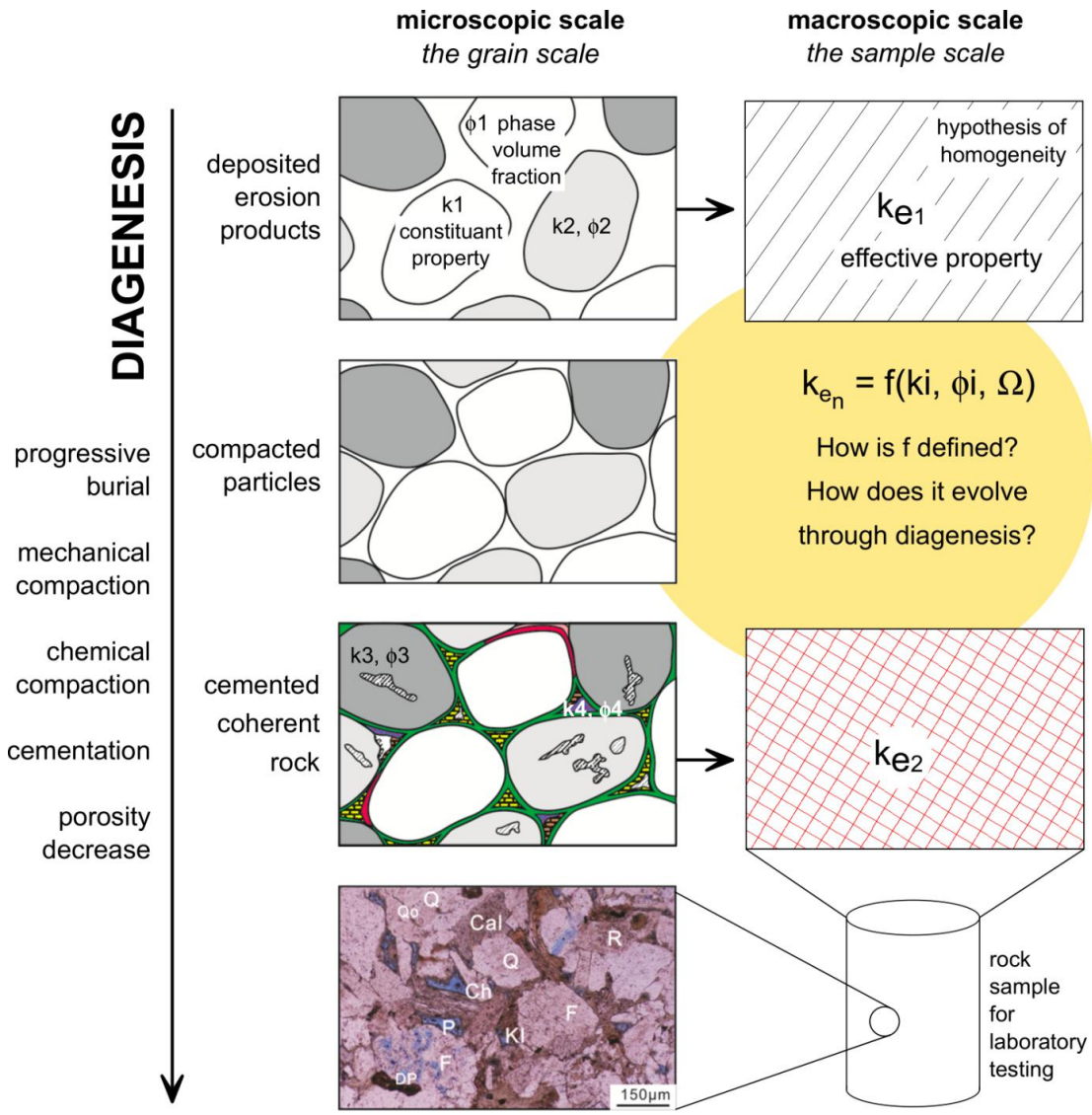

Figure 1.2 Schematic of the evolution of sediments during diagenesis, at the microscopic scale, in relation with the definition of effective properties. (From top to bottom) At a certain time, erosion products (e.g., sand grains) are deposited in a loose packing, and as they are progressively buried with an increasing amount of detritic grains deposited on top, the overburden load increases and the original loose packing of eroded particles evolves to close packing (compacted particles) and, by diagenetic processes such as chemical and mechanical compaction and cementation, to a cemented coherent sedimentary rock. Throughout diagenesis, porosity decreases, the pore space is shaped (microscopic scale) and bulk properties change accordingly (macroscopic scale). The coupling between changes at the grain scale and changes at the rock scale is complex: at all times, a given effective property (k_e) can be mathematically derived from the constituents' properties (k1 to k4) and phase

volume fractions (φ1 to φ4) and higher-order microstructural information (Ω) (equation from Torquato, 2002).

In collusion with the rock constituents' properties, these microstructural attributes, the geometrical information strictly speaking, control the bulk mechanical properties of the original sedimentary rock formed by diagenesis. Indeed, rocks can be described as natural random heterogeneous materials - in the sense that they are composed of domains of different phases (Torquato, 2002) - and assimilated to homogeneous materials with macroscopic or effective properties. Mathematically speaking, these effective properties are defined using the phases properties and phases volume fractions (Figure 1.2). However, effective properties are very rarely derived from simple mixture rules involving the phase properties and microstructural information and the detailed manner by which specific microstructural attributes control the mechanical behaviour or porous rocks is not fully understood.

1.3 Phenomenology of mechanical compaction

When the principal stresses σ_1, σ_2 and σ_3 are equal and positive, the rock sample on which they are applied is said to be under *hydrostatic* conditions. When the maximum principal stress σ_1 only is non-zero and positive, the rock sample is under *uniaxial* conditions and when the intermediate and minimal principal stresses σ_2 and σ_3 are non-zero, positive and equal, but inferior to σ_1, the rock sample is under *triaxial* conditions. These conditions mostly capture the different cases of in-situ compaction. Therefore, many experimental studies involving tests under either hydrostatic, uniaxial or triaxial conditions have been conducted and provided us with most of our current knowledge on the mechanical behaviour of natural rocks. A brief summary of the main conclusions that previous experimental work provided on the phenomenology of mechanical compaction is given here after.

In the following, we adopt the convention that the pressure of the fluid around the rock sample is the *confining pressure*, denoted P_c, and that of the fluid in the pore space is the *pore pressure*, denoted P_p. The difference between the confining pressure and the pore pressure is referred to as the *effective pressure* and denoted P_e. The *effective mean stress* is

given by the difference between the mean stress and the pore pressure: $P = (\sigma_1 + 2\sigma_3)/3 - P_p$ and the *differential stress* is given by the difference between the maximum and the minimum principal stresses $Q = \sigma_1 - \sigma_3$.

1.3.1 Inelastic behaviour and failure mode

Under hydrostatic loading, the rock undergoes progressive compaction through similar stages to the ones presented in section 1.1.3 (Figure 1.3): the pore volume fraction is successively reduced by non-linear elastic deformation (often considered the result of microcrack closure), linear elastic deformation and inelastic deformation. The transition to the inelastic domain of deformation starts at a critical effective pressure, the *onset of grain crushing*, denoted P^*, beyond which the porosity decreases dramatically as the pore space is reduced by *grain crushing* and *pore collapse* (Figure 1.3; Wong et al., 1997; Zhang et al., 1990).

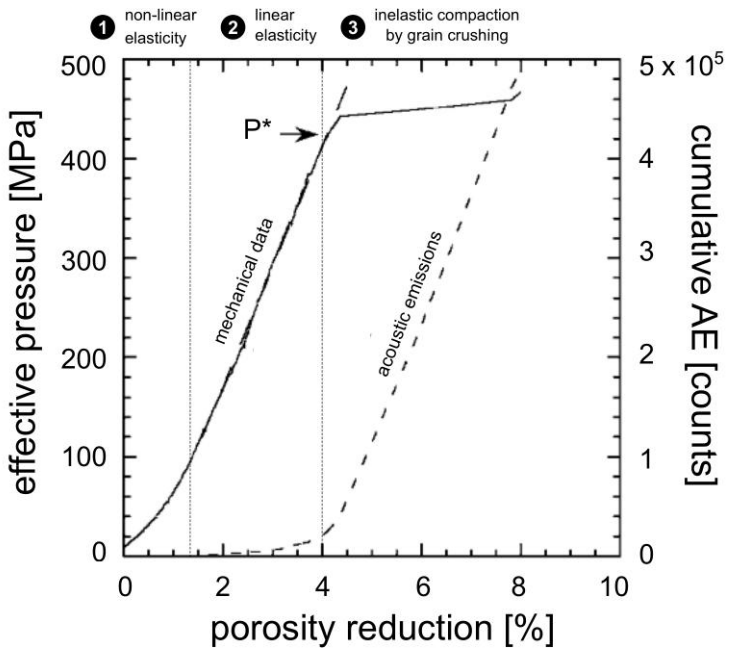

Figure 1.3 Example of mechanical data for the hydrostatic loading of a porous crustal rock. Data were obtained during a hydrostatic experiment on water-saturated Bentheim sandstone. The effective pressure is represented against the porosity reduction (solid line) and compiled with the corresponding recording of acoustic emissions, presented in cumulative (dashed line).

The onset of inelastic deformation by grain crushing is marked as P* (modified from Baud et al., 2006).

Sandstones tested in the laboratory under hydrostatic conditions undergo permanent compaction beyond critical stress values that span a wide range of effective pressures: P^* values from 75 to 420 MPa were reported by previous experimental studies (Wong & Baud, 2012; Zhang et al., 1990). The variability in the critical pressure P^* found for sandstones is primarily due to differences in porosity and grain size (Zhang et al., 1990). To a second order, P^* can be increased due to an increase in the cement content (Wong et al., 1997) or decreased in the presence of water in the pore space (Baud et al., 2000; Tembe et al., 2008). The influence of porosity and grain size on the hydrostatic behaviour is detailed here after (sections 1.4.4 and 1.5.2). The mechanical response of porous rocks to uniaxial compression and triaxial compression at low effective pressure is characteristic of the brittle regime, i.e., as brittle faulting occurs, stress suddenly drops (Figure 1.1). Figure 1.4 presents a compilation of mechanical data from triaxial compression tests conducted on samples of Adamswiller sandstone with a porosity of 0.23 under effective pressures ranging from 5 to 150 MPa (Wong et al., 1997).

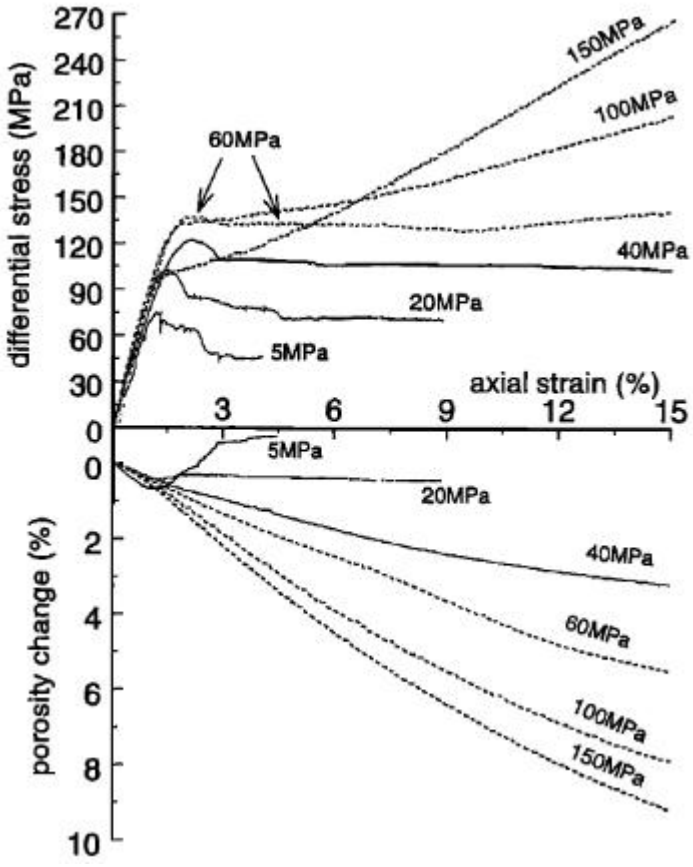

Figure 1.4 Example of mechanical data for selected triaxial experiments on Adamswiller sandstone with a porosity of 0.23. The effective pressure at which each triaxial test was conducted is indicated at the end of the corresponding curve. Negative and positive porosity changes respectively correspond to an increase and a reduction in porosity (dilatancy and compaction, respectively). Solid lines correspond to tests conducted in the brittle regime and dashed lines to tests conducted in the ductile regime (Wong et al., 1997).

While isotropic loading under hydrostatic conditions always causes compaction, a porous rock submitted to anisotropic loading, under either uniaxial or triaxial conditions, may dilate, i.e., the pore volume fraction increases, or compact, i.e., the pore volume fraction decreases (Wong & Baud, 1999, 2012).

The sample deformed at 5 MPa of effective pressure shows a typical brittle behaviour, which involves an initially compactant stage (porosity decreases up to approximately 1% of axial strain) which evolves to become dilatant (porosity increases progressively after 1.5% of axial

strain). In the brittle faulting regime, dilatancy takes place by opening and propagation of microcracks and ultimately, as the microcracks coalesce into a macroscopic fracture, brittle failure occurs as stress reaches its peak value (Paterson & Wong, 2005).

At higher effective pressure, the mechanical response of porous rocks transitions to a behaviour characteristic of the ductile regime, i.e., the stress-strain curve does not show a stress drop but sometimes strain hardening (Figure 1.1). The sample of Adamswiller sandstone deformed at 60 MPa of effective pressure shows a typical ductile behaviour, where both elastic and inelastic deformations are compactant (porosity decreases almost linearly, Figure 1.4). At 100 and 150 MPa of effective pressure, Adamswiller sandstone samples undergo strain hardening (Figure 1.4).

In the analysis of mechanical data obtained during deformation experiments, valuable insights are provided by the volumetric strain data, when available. Figure 1.5 presents a compilation of data from the literature for Bentheim sandstone (Klein et al., 2001). The evolution of mean stress as a function of volumetric strain for triaxial experiments conducted in the brittle faulting regime and in the ductile regime is presented in Figure 1.5(a) and (b), respectively. These nonhydrostatic data are compiled with the hydrostatic loading curve which helps to pinpoint the stress level for the onset of dilatant (brittle field, Figure 1.5(a)) or compactant (ductile field, Figure 1.5(b)) inelastic behaviour. Indeed, when deformation is poroelastic, volumetric strain is controlled by mean stress only (Wong & Baud, 2012). The triaxial data therefore deviate from the hydrostat when deformation enters the inelastic stage, i.e., the *onset of dilatancy* C' in the brittle faulting regime (Figure 1.5(a)) or the *onset of shear-enhanced compaction* C^* in the ductile regime (Figure 1.5(b)).

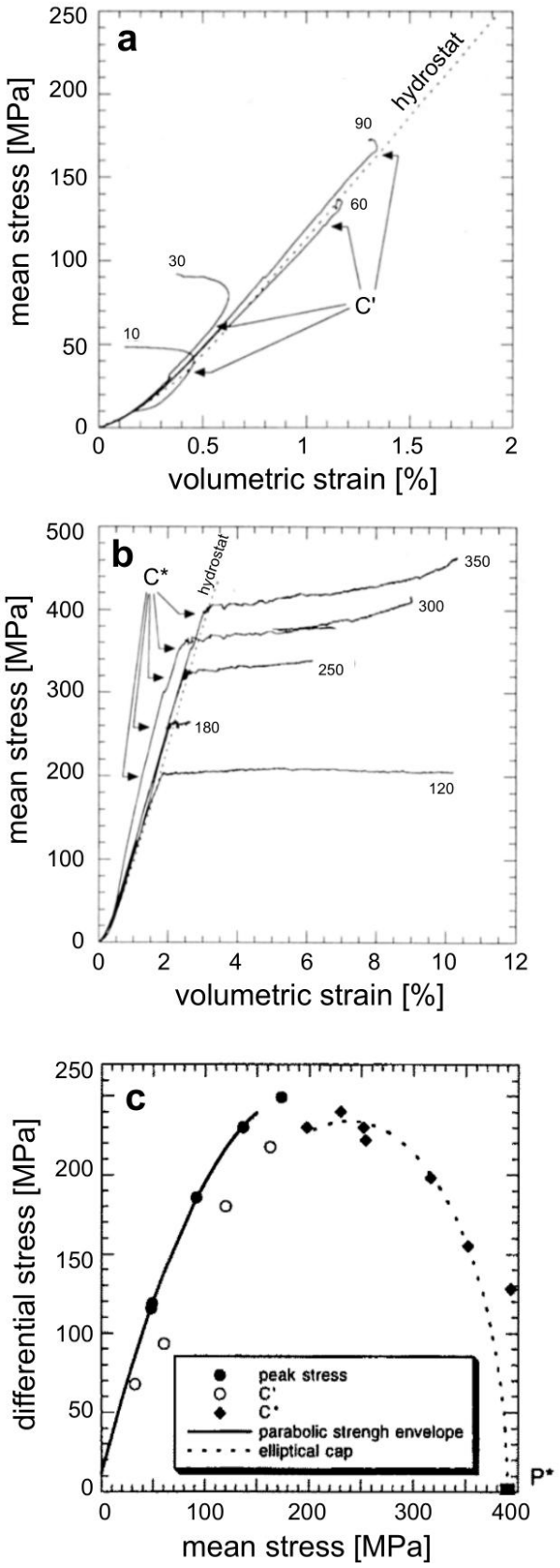

Figure 1.5 Representative mechanical data for the mechanical behaviour of Bentheim sandstone with a porosity of 0.23 (Klein et al., 2001). Mechanical data for the triaxial tests are presented as the mean stress against the volumetric strain. (a) Triaxial experiments at low effective pressure are representative for the brittle faulting regime, where dilatant inelastic strain starts at C', while (b) triaxial experiments at high effective pressure are representative for the shear-enhanced compaction regime, where compactive inelastic strain starts at C*. (c) Peak stresses values compiled in the stress space map out the brittle failure envelope and critical stresses for the onset of shear-enhanced compaction C* map out the compactive yield cap.

Thus, the analysis of mechanical data obtained from uniaxial and triaxial tests within the brittle regime allows for the identification of peak stresses σ_p (the peak stress value obtained from a uniaxial test is most often referred to as the uniaxial compressive strength or UCS) and critical stresses for the onset of dilatancy C' (Figure 1.5(a)), which map out the *brittle strength envelope* in the stress space (solid line in Figure 1.5(c)). Similarly, the analysis of data from triaxial tests within the ductile regime and hydrostatic tests allows for pinpointing the stress required to reach the onset of shear-enhanced compaction C^* (Figure 1.5(b)) and the onset of grain crushing P^* (Figure 1.3), respectively, which map out the *compactive yield cap* in the stress space (dashed line in Figure 1.5(c)). At stress states below the envelope, the rock is elastically compacted and as stresses are increased to a state above the envelope, the rock undergoes irreversible inelastic strain by dilatancy or compaction.

Several attributes of the brittle strength envelop and compactive yield cap of Bentheim sandstone mapped out by Klein et al. (2001), common to many of the sedimentary rocks tested in the laboratory (Wong & Baud, 2012), can be highlighted: (1) the brittle failure envelope and the compactive yield cap have inverse pressure dependency and (2) the brittle-ductile transition can be identified at the intersection of the compactive yield cap with the brittle envelope. Previous experimental work showed that the mean stress for the transition from brittle to ductile behaviour and the amplitude and shape of the compactive yield cap depend primarily on porosity and grain size but also on other microstructural attributes such cementation, clay content or the presence of porosity patches (Baud et al., 2015; Guéguen & Fortin, 2013; Menéndez et al., 1996; Wong et al., 1992, 1997). The influence of porosity on the brittle-ductile transition is detailed in section 1.4.3.

1.3.2 Microstructural observations

Using optical and electron microscopy, the microstructural changes preceding and accompanying the bulk deformation of rock samples submitted to isotropic and anisotropic stresses were extensively studied in the past decades. The development of brittle failure under stress has been thoroughly studied in the past decades and a comprehensive review on the brittle behaviour of rocks can be found in Paterson and Wong (2005).

Figure 1.6 presents a compilation of microscopy images illustrating the microstructural evolution of damage in porous sandstones under different stress conditions. The upper part of the figure concerns the dilatant failure under stress (brittle field). Insights gained on the development of brittle faulting in porous sandstones from the various observation methods can be summarised as follow: the formation of a macroscopic shear fracture (along which the sample fails; Figure 1.6(b)(c), El Bied et al., 2002; Menéndez et al., 1996) under stress results from the opening and growth of intergranular microcracks mostly directed parallel to σ_1 and their ultimate unstable propagation and linking-up (Figure 1.6(a), Menéndez et al., 1996). Appreciable differences have been observed between weakly cemented sandstones and more compact ones: in the pre-failure stage, Menéndez et al. (1996) reported for the weakly cemented Berea sandstone (with a porosity of 0.21) microcracking was mostly intergranular whereas Wu et al. (2000) showed the significant contribution of intragranular microcracking in the development of dilatancy in the more compact Darley Dale sandstone (with a porosity of 0.13). Observations made on Vosges and Fontainebleau sandstones, with porosities higher than 0.20, agree with what was reported by Menéndez et al. (1996).

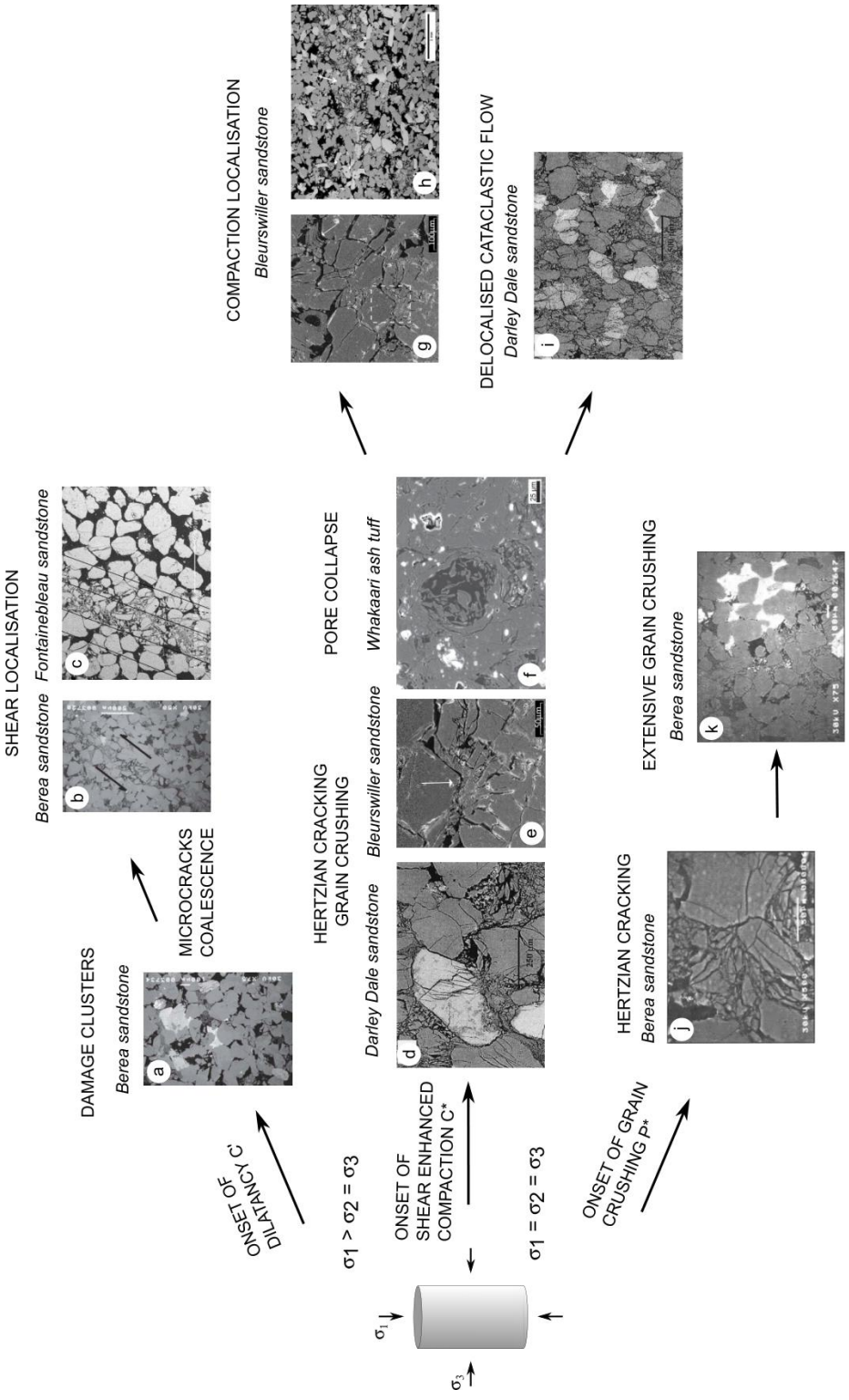

Figure 1.6 Diagram of the microstructure and damage evolution under triaxial compression at low effective pressure (a, b, Paterson & Wong, 2005; c, El Bied et al., 2002) and high effective pressure (d, Wu et al., 2000; e, f, Fortin et al., 2006; g, Heap, Brantut, et al., 2015; h,

Baud et al., 2015; i, Wu et al., 2000) and during hydrostatic compression (j, k, Guéguen & Boutéca, 2004).

Under higher effective pressure, a transition from dilatancy (brittle faulting) to inelastic compaction occurs. The evolution of damage in deformed sandstones is presented in Figure 1.6 (d to h). Microscopic observations of sandstone samples deformed up to the onset of shear-enhanced compaction revealed the presence of isolated clusters of intragranular cracks radiating from grain contacts (Figure 1.6(d), Wu et al., 2000; (e), Fortin et al., 2006), microstructural features referred to as *Hertzian contacts* or *Hertzian fractures*. With the further increase in stress and development of shear-enhanced compaction, the density of intragranular microcracks increases, leading to grain crushing, pore collapse and/or comminution (Guéguen & Boutéca, 2004). The main failure micromechanism can vary depending on the microstructure: whilst sandstones typically suffer grain crushing, pore collapse is also frequent in rocks such as limestones (Baud et al., 2000, 2017; Zhu et al., 2010) porous tuffs (Heap, Kennedy, et al., 2015; Wong & Baud, 2012; Zhu et al., 2011) and volcanic rocks (Heap, Farquharson, et al., 2015; Heap & Violay, 2021; Zhu et al., 2016).

In a dilatant rock, failure is generally associated to strain localisation in the form of macroscopic shear bands and although compactant porous rocks have been observed to fail by distributed cataclastic flow, compaction localisation has also been reported. Under relatively high confinement, grain crushing and pore collapse form clusters of damage that ultimately become delocalised and lead to failure by distributed cataclastic flow, as seen in Darley Dale (Wu et al., 2000) or Boise sandstones (Cheung et al., 2012). However, in an intermediate regime between shear faulting and delocalised cataclastic flow, grain crushing, and pore collapse can evolve into elongate, connected clusters of damage crosscutting through the samples, referred to as *compaction bands* (Figure 1.7). Localised compactant failure in the form of compaction bands (Figure 1.6(f), Fortin et al., 2006; (g), Baud et al., 2015) was observed as a transitional failure mode in many porous sandstones such as Bentheim (Figure 1.7; Baud et al., 2004; Klein et al., 2001), Berea (Menéndez et al., 1996), Bleurswiller (Figure 1.7; Baud et al., 2015; Fortin et al., 2006), Castlegate (Olsson, 1999), Diemelstadt (Tembe et al., 2008), Vosges (Bésuelle et al., 2000). Compaction localisation can dramatically reduce the permeability (Fortin et al., 2005; Olsson et al., 2002; W. L. Taylor & Pollard, 2000; Vajdova et al., 2004). Therefore, compaction localisation is central to a variety of solid earth

processes involving fluid movements and the factors responsible for the different manifestations of compaction localisation have been studied in the past decades (Holcomb et al., 2007). Although compaction localisation was reported in sandstones with porosities higher than 0.13, discrete compaction bands were only observed in sandstone with porosities in the range 0.22 - 0.25 (Baud et al., 2015). Moreover, Cheung et al. (2012) demonstrated that discrete compaction bands preferentially occur in sandstones with uniform grain size distribution. Thus, previous work suggest that compact bands would develop in more homogeneous and more porous rock samples. However, additional experimental work is still required to fully understand the microstructural conditions for the occurrence of compaction localisation.

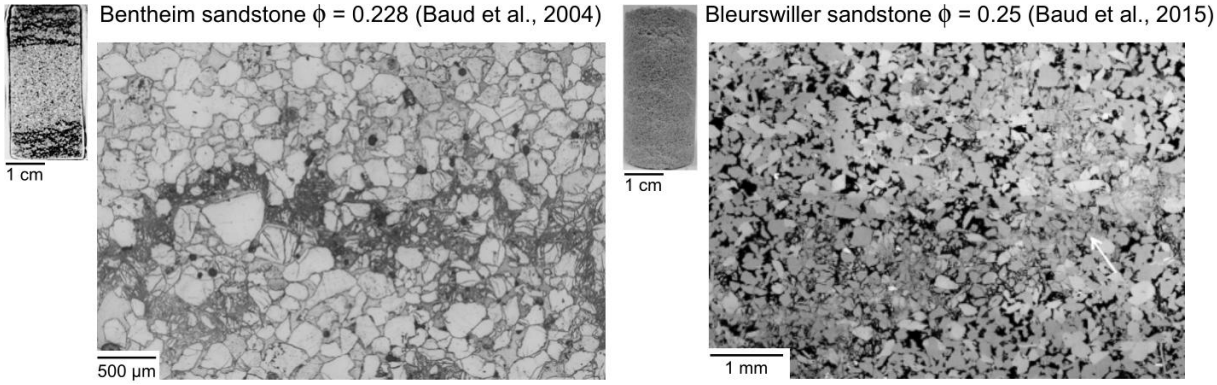

Figure 1.7 Discrete compaction bands in Bentheim and Bleurswiller sandstones, at the sample scale and the grain scale.

Finally, inelastic compaction under hydrostatic conditions results from the development of Hertzian fractures at grain-grain contacts, which extend across the grains and lead to delocalised and extensive grain crushing and pore collapse (Figure 1.6(i)(j), Guéguen & Boutéca, 2004). The characterisation and understanding of damage evolution for the three main modes of deformation, i.e., shear localisation, compaction localisation and cataclastic compaction, was greatly helped by stereological and AE measurements (Fortin et al., 2009; Olsson & Holcomb, 2000). Wong et al. (2001) provided representations of the spatial distribution of damage (in terms of crack density [mm^{-1}]) in Darley Dale sandstone samples and suggested that mosaics of high-angle shear bands and compaction bands developed preferably near the end of the samples in the transitional regime. Fortin et al. (2009) provided

important results regarding the spatial evolution of damage and the source mechanisms using acoustic emissions sources characteristics and evolution of acoustic emissions number. They showed that the acoustic signature for the formation of compaction bands and cataclastic compaction are similar, with a predominance of pore collapse events, while shear localisation is characterised by the predominance of shear events. Moreover, they suggested that pre-existing microcracks and high porosity clusters constitute preferential nucleation sites, i.e., zones of stress concentration which control the local strength of the rock.

1.3.3 Micromechanics of failure under compressive loading

Mechanical and microstructural data provided by experimental studies on porous sandstones showed that, in response to an applied compressive stress, intergranular or intragranular microcracks nucleate and propagate from different locations depending on the undeformed geometric attributes of the pore space. Two endmembers can be identified in terms of pore space topology: low porous compact sandstones and highly porous weakly compacted sandstones. The former can be modelled as an elastic continuous volume within which pores or cracks are embedded (inclusion model) while the latter is well approximated by a pack of spheres in elastic contact (granular model). The previous description gives a simplistic view of the distinction upon which the failure micromechanisms have been addressed. Micromechanical models provide a mathematical framework within which the mechanical properties can be derived, using an idealised microstructure characterised by given parameters, sources of stress concentrations and failure criteria. In the following, we introduce three micromechanical models that were extensively used to describe and interpret laboratory results on sandstones.

Figure 1.8 presents the elementary geometry that acts as a source of stress concentration for each of the three models. In all three cases, the driving force for the growth of microfracture is characterised by the stress intensity factor K_I at the nucleation site (propagation in opening mode or mode I (Irwin, 1968), where nucleation starts when it reaches a critical value, i.e., when $K_I = K_{Ic}$. Two scenarios of inclusion model are often considered: a crack or a spherical pore embedded in an elastic continuum. In the first scenario, the *sliding wing crack model* (Ashby & Sammis, 1990) considers sources of stress concentration at the tips of pre-existing microcracks (Figure 1.8 (top)). Under an applied stress, when the condition for crack

nucleation is met, tensile wing cracks are predicted to propagate from the tips of the pre-existing crack in the direction of the maximum principal stress σ_1. In an elastic volume with pervasive microcracks loaded under axial stress, wing cracks nucleate and, as they propagate to longer distances, start to interact to eventually coalesce into a macroscopic fracture. The other scenario of inclusion model was used by Sammis and Ashby (1986) to formulate the *pore-emanated crack model*, which considers source of tensile stress concentrations at the poles of spherical pores (Figure 1.8 (middle)). Similar to the wing crack model, stress-induced microcracks are predicted to propagate from the surface of the pores when the stress intensity factor at the poles reaches a critical value K_{Ic} in a direction parallel to σ_1, and as stress is increased, to propagate further, interact and link-up into a macroscopic shear fracture. The sliding wing crack model and the pore-emanated crack model were used mainly to describe the brittle behaviour of rocks under uniaxial compression (Wong & Baud, 2012). Due to the location of the source of stress concentration (Figure 1.8), the former often served to predict the strength of more compact rocks, i.e., with a very small porosity and a pore space dominated by microcracks, whereas the latter served to predict the strength of porous rocks, i.e., with a pore space dominated by more or less equant spherical pores (Baud et al., 2014).

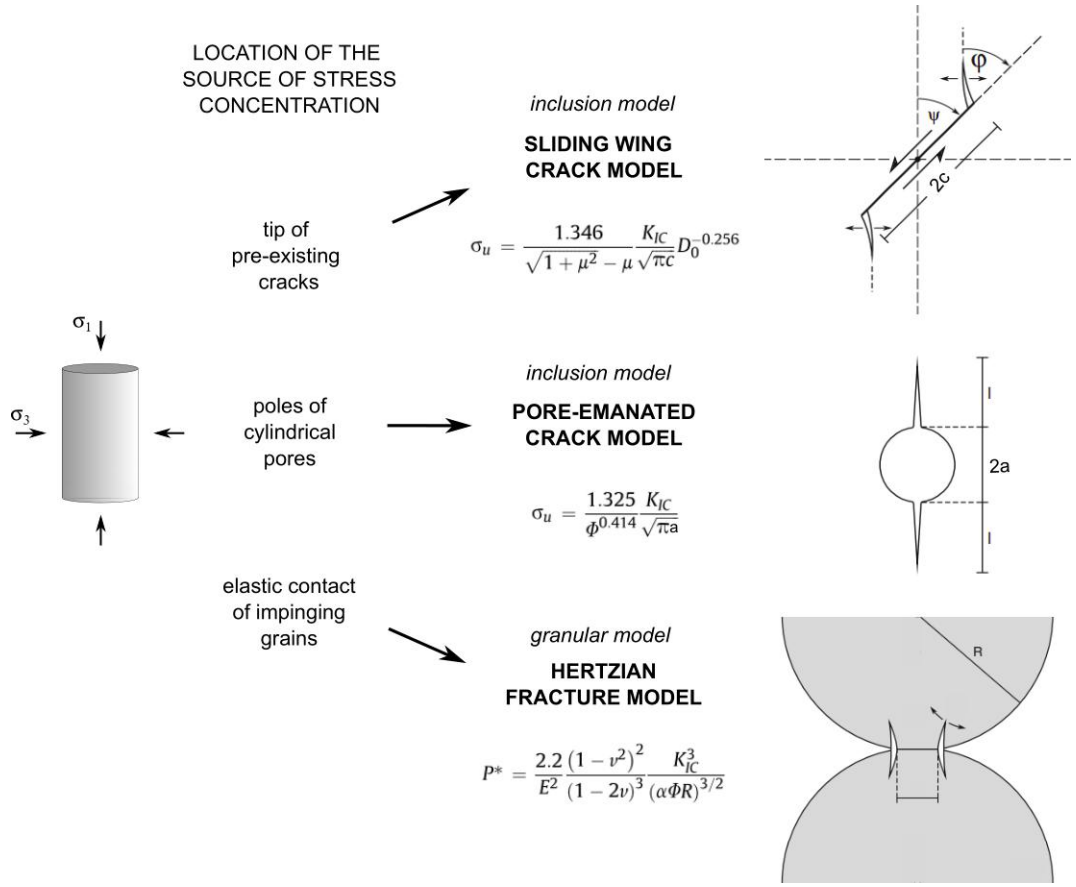

Figure 1.8 Geometrical element considered for the formulation of models for the micromechanics of compaction of porous rocks.

For weakly cemented rocks, which grains are connected through elastic contacts which are readily ruptured under an applied load, granular models that accounts for the relative slipping and rotation of grains have been developed. The *Hertzian fracture model* (Zhang et al., 1990) was developed based on the Hertzian contact theory to analyse the micromechanics of grain crushing and provides a mathematical solution to derive the stress at the onset of grain crushing under hydrostatic conditions. The Hertzian fracture model considers that the maximum tensile stress is located at the circular boundary of the contacting area between adjacent grains (Figure 1.8 (bottom)) and that, under normal loading, tensile microcracks radiate from the grain contact towards the interior of the contacting grains, forming deformation features known as Hertzian fractures or Hertzian contacts.

1.4 Influence of porosity on the hydromechanical behaviour of crustal rocks

1.4.1 The permeability-porosity relationship

Porosity has been identified as a first-order control on hydraulic properties of rocks. In the Earth crust, the pore space evolves according to various geological processes which either produce pores or destroy them, and change the fluid transport properties of rocks, the permeability. Although there is no universal permeability-porosity relationship valid for all rock types, the overall trend is that an increase in rock porosity causes an increase in rock permeability to fluids (Doyen, 1988; Farquharson et al., 2015; Nelson, 1994). Deviation from this broad trend can be interpreted in terms of conduction efficiency of the pore space, i.e., because of geometrical attributes such as pore shape and accessibility, not all pores are equally efficient in conducting fluid flow. Among the numerous flow models that were proposed, the most popular approach, in agreement with the percolation theory, is to describe the dependency of permeability on porosity as a power law $k \approx \varphi^{\alpha}$, where k is the permeability and φ the porosity, with a variable exponent α that is related to the proportion of the pore space of the rock that is effective in conducting fluids (Bernabé et al., 2003; Saar & Manga, 1999; Scheidegger, 1958). For Fontainebleau sandstone, constituted of 100% of quartz and occurring on a broad range of porosity with constant grain size and chemical properties, the permeability-porosity evolution was found to be well described by the power law with $\alpha = 3$ (Bourbie & Zinszner, 1985).

Moreover, due to the importance of fluid flows in a wide variety of environmental and technological processes, predicting fluid permeability using known microstructural attributes of the rock is critical. Consequently, there has been a great deal of effort in providing a universal scaling for fluid permeability of random porous media. Martys et al. (1994) simulated Stokes flows in variably polydisperse porous systems of overlapping or non-overlapping grains and provided a scaling relation to predict permeability which was extended by Wadsworth et al. (2016) to the whole range of porosity achieved during granular densification and integrated a theoretical estimation for the specific surface, otherwise rarely known because rarely measured in the laboratory. Wadsworth et al. (2016) successfully tested this scaling against data from the literature for andesite, obsidian, welded block-and-ash flow, well-sorted sandstones and sintering glass beads.

1.4.2 Evolution of strength with porosity

Geological processes that take place in sedimentary or volcanic settings often involve deformation mechanisms such as mechanical compaction, extension, dilatancy, faulting, etc. In that case, the mechanical properties of the rock in place, e.g., its compressive strength, control the rock response to the applied stress state. Porosity exerts a first-order control on the mechanical behaviour. Figure 1.9 presents a compilation of experimental data from the literature for the evolution of strength as a function of porosity. Broadly speaking, an increase in rock porosity causes a decrease in brittle rock strength (Baud et al., 2014; Chang et al., 2006) (Figure 1.9).

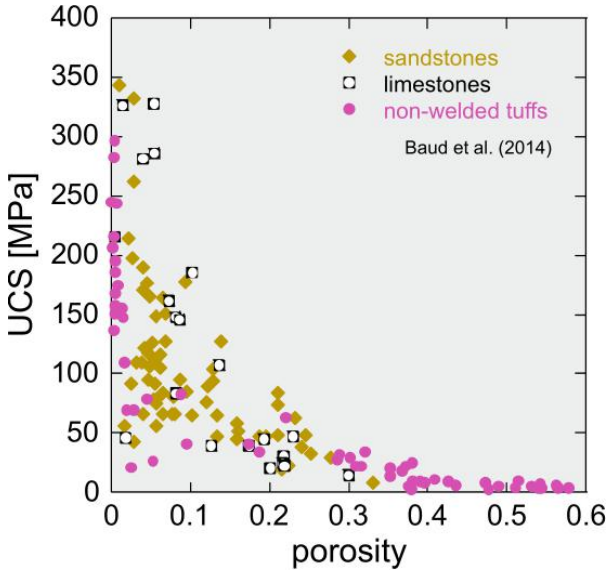

Figure 1.9 Compilations of published data for the evolution of uniaxial compressive strength (UCS) with porosity (after Baud et al., 2014). Data points are results of deformation laboratory experiments on samples of sandstones (yellow), limestones (black) and non-welded tuffs (pink).

Under unconfined compressive loading, sandstones, limestones and tuffs typically fail at stress values that follow a power law of porosity (Jizba, 1991; Kwasniewski, 1989; Zhu et al., 2011). Zhu et al. (2010) derived an analytical solution for the UCS based on Sammis and Ashby's pore-emanated crack model (1985) (Figure 1.8) and predicted that the UCS scales with the fracture toughness and inverse square root of pore radius:

$$\sigma_u = \frac{1.325}{\varphi^{0.414}} \frac{K_{IC}}{\sqrt{\pi a}}. \quad (1.2)$$

Wong and Baud (2012) compiled UCS data for sandstones and show that they are bracketed by two theoretical curves that correspond to values for the average pore size from 11.4 µm to 290 µm in the pore-emanated crack model.

1.4.3 Control of porosity on the brittle-ductile transition

Porosity also exerts an influence on the type of rock failure that can result from the application of crustal stresses, i.e., brittle failure by development of a macroscopic shear fracture or ductile failure by cataclastic flow.

Low-porosity rock will remain brittle even under a wide range of relevant pressure conditions, whereas high-porosity rock will only be brittle at relatively low-pressure and transitions to ductile behaviour at high-pressure (Wong & Baud, 2012). Scott and Nielsen (1991) showed that the brittle-ductile transition was reached at a lower confining pressure in high-porosity sandstones than in low-porosity sandstones, as observed on Figure 1.10. Overall, the brittle failure envelopes all fall on a straight line (known as the Mohr-Coulomb line) while the compactive yield caps appear to expand with decreasing porosity. In detail, samples with close porosity yield at different critical stresses due to differences in microstructural attributes other than porosity, such as cement content, clay content or grain size (Figure 1.10). Variations in the shape of the compactive yield cap have also been reported. In agreement with previous observations from Fortin et al. (2006, 2009), Baud et al. (2015) reported a linear compactive cap for Bleurswiller sandstone and suggested that the deviation from the elliptical shape generally reported for porous sandstones (Wong & Baud, 2012) could be attributed to the presence of porosity patches in Bleurswiller sandstone. The model for granular microstructure proposed by Guéguen and Fortin (2013) also predicts the high-pressure experimental envelope to be a straight line. Further work is necessary to resolve the issue of the shape of the compactive cap, but the observations reported above suggest that the typology of the pore space might control the linear-to-elliptical behaviour of sandstones in the ductile regime.

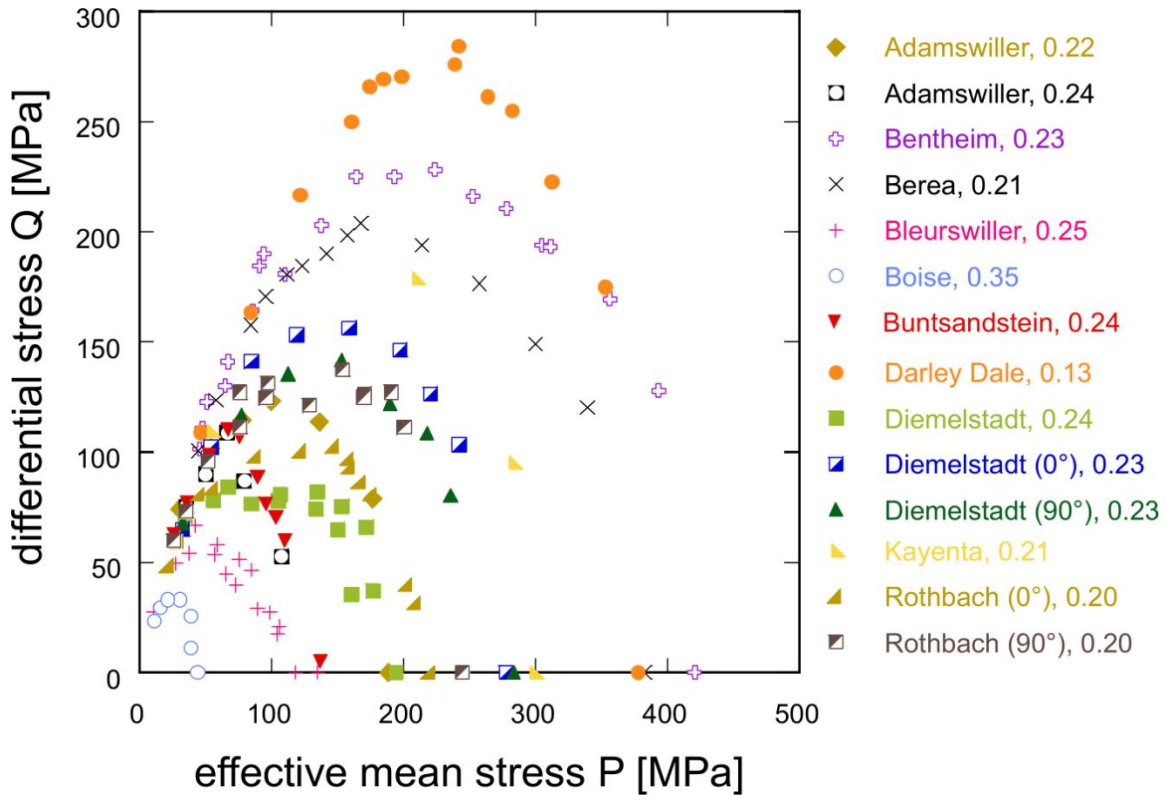

Figure 1.10 Compilation of failure envelopes for porous sandstones with porosity ranging from 0.13 to 0.35 (data for Muschelkalk from a personal communication, Carbillet (2018); other data from Wong & Baud, 2012).

1.4.4 Influence of porosity on the hydrostatic behaviour

Passed the brittle-ductile transition on the failure envelopes, porosity also exerts a first-order control on the critical pressure to reach the onset of grain crushing P* under hydrostatic loading: the higher the porosity, the lower P* (Figure 1.11; Baud et al., 2017; Wong & Baud, 2012; Zhu et al., 2011). This was demonstrated on porous sandstones by Zhang et al. (1990) who adopted a micromechanical approach based on the Hertzian fracture model (section 1.3.3) to describe the hydrostatic behaviour. The model predicts that the critical pressure for the onset of grain crushing P* decreases with porosity and follows a power law of the product of grain radius and porosity: $P^* \propto (\alpha\varphi R)^{-\frac{3}{2}}$ with α the ratio of the initial crack length to radius of grains (Figure 1.11b). While experimental data for coarse sand, sandstones and basalt compiled in Wong et al. (1997) are well predicted by the previous model, the

compilation augmented by data on other sandstones provided by Rutter and Glover (2012) was best described by a slope lower than the model prediction. Guéguen and Fortin (2013) proposed a slightly different model for which the local failure mechanism considered, contrary to the one considered by Zhang et al. (1990), assumes a random packing of identical spheres, which is close to the real situation of well-sorted sandstones. Using their model, they predict a slope of +1 for the evolution of P^* with $(1-\varphi) \times R^{-3/2}$, in good agreement with data from the literature for sandstones (Baud et al., 2006; Rutter & Glover, 2012; Wong et al., 1997; Wong & Baud, 2012).

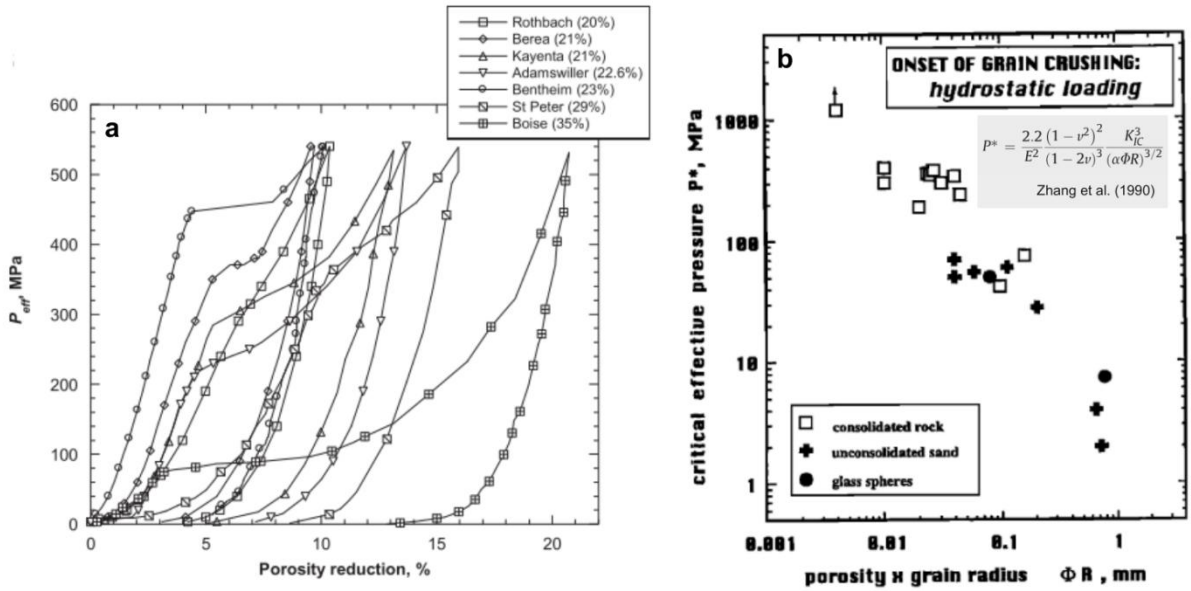

Figure 1.11 Mechanical data for sandstones deformed under hydrostatic compression. (a) Hydrostatic curves as presented in terms of the effective pressure against the (absolute) porosity reduction for sandstones with porosity ranging from 0.21 to 0.35 (Wong & Baud, 2012). (b) The grain crushing model predicts that the critical pressure for the onset of grain crushing P^* is positively correlated to the product of mean grain radius with porosity to the power -3/2 (Wong et al., 1997).

1.5 Influence of grain size on the hydromechanical behaviour of crustal rocks

1.5.1 Microstructural description

Although grain size is often cited as a controlling parameter for the hydromechanical behaviour of rocks, and therefore often used as a model parameter (e.g., Zhang et al., 1990), it remains understudied, especially in laboratory experiments, in comparison with porosity. Due to the variety in the attributes used to study the influence of grain size, partly owed from the variety in petrology and microstructure of crustal porous rocks, results reported in different studies are still insufficient to allow for the elaboration of a comprehensive framework on the control of grain size on the hydromechanical behaviour of porous rocks.

1.5.2 Experimental observations

Conclusions relevant to the study of the macroscopic mechanical behaviour of granular rocks ensue from works on the grain breakage processes, where the primary control of grain size (McDowell & Bolton, 1998) and shape (Sharma & Penumadu, 2020), coordination number (Salami et al., 2015) and the presence of surface flaws (Brzesowsky et al., 2011) on the strength of single grains are demonstrated. However, understanding the macroscopic response of granular materials to an applied load based on the grain level interactions is complicated by a number of parameters such as packing density, bonds strength and particle distribution in the assembly. Indeed, geometrically speaking, natural rocks consist of assembled mineral particles with different sizes and shapes connected through interfaces with different geometrical attributes. For simplicity, most studies on the influence of grain size on the bulk mechanical behaviour of porous rocks choose mean grain size, i.e., the first moment of the grain size distribution, to be the investigated microstructural attribute. Figure 1.12 presents a compilated data from Baud et al. (2014) for the evolution of strength as a function of mean grain size. Atapour and Mortazavi (2018) investigated the influence of mean grain size on the unconfined compactive strength of weekly cemented reservoir sandstones and pointed out that different studies on granular porous rocks reported different results concerning the influence of mean grain size on strength. Yet, several studies demonstrated that porous rocks with a higher mean grain size have lower compactive strength, using either natural rock (Figure 1.12;

Baud et al., 2000; Fredrich et al., 1990; Olsson, 1974; Zhang et al., 1990) or numerical samples (Yu et al., 2018).

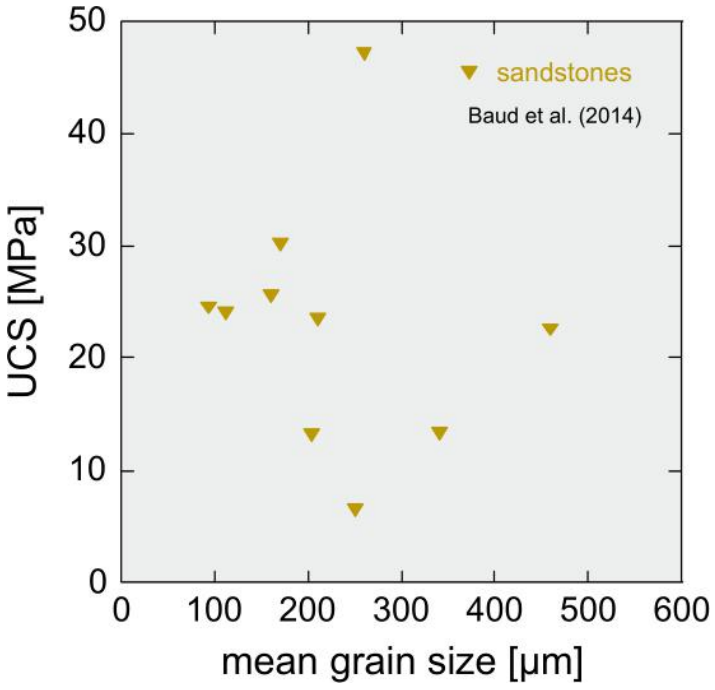

Figure 1.12 Compilation of uniaxial compressive strength (UCS) data for porous sandstones as a function of mean grain size (after Baud et al., 2014).

However, mean grain size does not accurately capture differences in width and shape in the distributions since an infinite number of distributions can have the same first moment. In comparison with mean grain size, experimental data sets on the relationship between grain size distribution and bulk mechanical properties are very scarce but demonstrate that grain size distribution exerts a first order control on various geomechanical processes. Cheung et al. (2012) compared the grain size distributions of Bleurswiller and Boise sandstones and suggested that uniform grain size distributions promote compaction localisation without affecting much the strength. This result highlighted the influence of sorting on the propensity for the development of compaction bands in natural rocks, in agreement with previous field observations (Fossen et al., 2011). In addition, numerical analysis using grain-based models helped improve our understanding of the influence of the grain size distribution. For instance, Peng et al. (2017) proposed to use grain size distribution to derive an heterogeneity index and showed that under mechanical compaction, peak strength and Young modulus increase with

increasing homogeneity, i.e., well-sorted numerical sample with closely clustered grain size distributions (close to monodisperse) are stronger than samples with wider grain size distributions. They also show that the failure micromechanism changes with the heterogeneity index: under compressive stress, the more homogeneous a sample is, the fewer grain boundary tensile cracks develop and the more intragrain microcracks grow. Using a bonded particle model to investigated failure under uniaxial compression, Ergenzinger et al. (2010) demonstrated that the strength of a sample with a parabolic particle size distribution is lower than one with a uniform size distribution, both of which lower than that of a sample with an inverse parabolic distribution. Further, they investigated the influence of bond strength distribution and showed that, for a linear particle distribution, a sample within which all bonds have the same strength is stronger than ones with uniform, parabolic and inverse parabolic bond strength distributions, which all result in comparable strengths. As the particle size distribution exerts a primary control on the manner in which applied external forces are transmitted from one particle to the next via their contacts, the numerous attempts made toward the characterisation of the force network are also of relevance to the study of the influence of grain size on the mechanical behaviour of porous rocks. Overall, these studies showed that, under compressive loading, a strong network develops in granular systems, involving less than half of the particles (Radjai et al., 1998) and that, within this network, less than half of the particle participate to the formation of force chains, i.e. actual strong contact force pathways (Peters et al., 2005).

1.6 Modelling of the behaviour of porous rock using synthetic rock samples

1.6.1 Alternative use of synthetic rocks

Experimental studies using natural rocks have given many insights into the control of porosity and grain size on hydraulic and mechanical bulk properties. However, they also highlighted the dependency of effective properties on nontrivial details of the microstructure that results from the complex interactions between the different phases of natural rocks. The compilations presented in Figures 1.9 and 1.12 highlight the important scatter in experimental data sets, where the overall trend in the porosity or mean grain size dependency of strength is complicated by the unsystematic and sample-specific coupling and complex interplay of all

microstructural attributes. Indeed, although obtained from a single rock formation or field site, multiple samples will very likely exhibit differences not only in porosity and/or grain size but also in other microstructural attributes such as clay content or cementation, which can both strongly influence bulk strength (Baud, Zhu, et al., 2000; Bernabé et al., 1992; Heap et al., 2021; Yin & Dvorkin, 1994). Therefore, the variability from sample-to-sample results in an uncertainty regarding the effect of varying individual microstructural parameters on the bulk hydromechanical properties, hardly solvable using laboratory experiments on natural rocks. Avenues to sharpen our understanding of the relationship between microstructure and effective properties have been found in the use of numerical samples. Unlike laboratory measurements on natural rock samples, numerical modelling allows for the independent control of input parameters and thus for the examination of the deconvolved influence of specific microstructural attributes on macroscopic properties. Although numerical simulations based on, for instance, the discrete element method (DEM), the finite element method (FEM) and/or a bonded-particle model (BPM) provided key results and new insights into the relationship between the microstructure and the bulk behaviour of rock (Oliveira et al., 2020; Sun et al., 2018a, 2018b), experimental validation is still missing for a lot of them. A fruitful way forward would be to find a material for which microstructural attributes can be controlled and deconvolved and that can be studied in the laboratory, thus providing experimental results to test results from numerical simulations against. To achieve this, numerous attempts have been made to prepare precisely controlled synthetic rocks with chemico-physical properties falling in the range of natural crustal rocks. Stimpson (1970) offered a review of the material used to simulate natural rocks and proposed a classification with a first division made between granular and non-granular materials. The former is further subdivided into non-plastics and plastic and the latter into cemented and uncemented. In granular materials, sand is most frequently used as primary component and has been cemented with plaster most commonly to model sedimentary rocks. Glass occurs in both non-granular and granular categories, used either in the form of flat plates or beads. Overall, the review by Stimpson (1970) shed light over the great variety of materials which can be used to model natural rocks. Gell et al. (2019) later reviewed the validity of the use of synthetic specimens as analogues for natural rocks based on their potential to behave similarly to real rocks under the same experimental conditions and argued that synthetic rock materials provide accurate and reliable conclusions which could not be drawn using natural rock samples. Synthetic rocks made of

sand with halite or silica cement (Bernabé et al., 1992; den Brok et al., 1997; David et al., 1998; Haeri et al., 2005; Holt et al., 1993) have been successfully used to reproduce the brittle-ductile transition and failure modes observed in natural sedimentary rocks. Figure 1.13 presents results from the literature illustrating the resemblance between the mechanical behaviour of synthetic samples made of sintered glass or cemented sand and natural sandstones. The addition of cement in different locations in the microstructure of the synthetic samples allowed Bernabé et al. (1992) to demonstrate that if deposited at the grain-grain contacts, very small amount of cement can significantly strengthen the granular material. Moreover, David et al. (1998) showed that the stress required to reach inelastic compaction under hydrostatic and triaxial conditions was significantly higher in a synthetic rock with 5%vol of cement than one with 3%vol of cement (the addition of 2%vol of cement in the sample increases the peak stress from 148 to 173 MPa for a triaxial test at P_e = 30 MPa) and that the addition of cement shifted the brittle-ductile transition to higher stress (Figure 1.13 (b)).

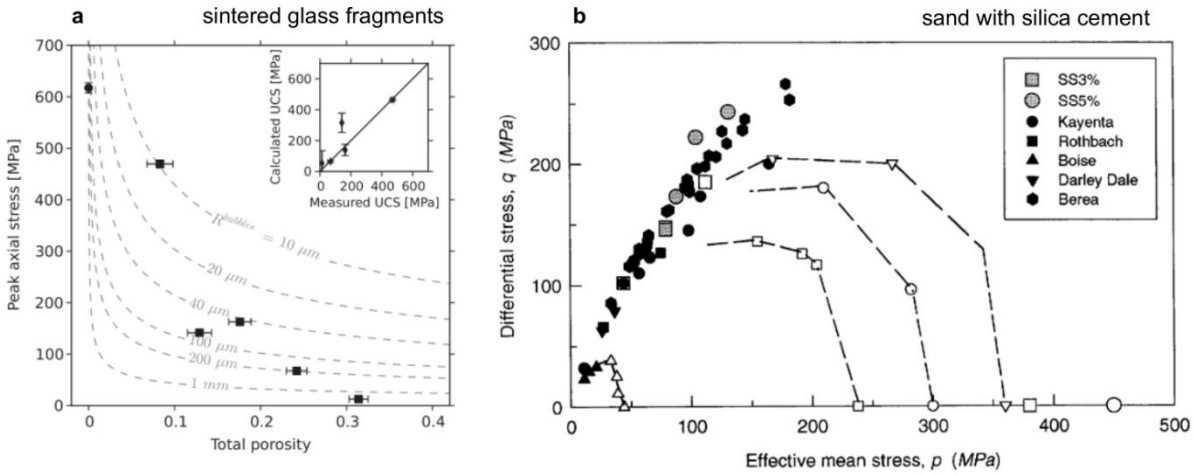

Figure 1.13 Mechanical behaviour of synthetic rocks made of (a) sintered glass fragments (Vasseur et al., 2013) and (b) sand with variable proportion of silica cement (SS3% contains 3%vol of cement and SS5%, 5%vol) (David et al., 1998).

More recently, Vasseur et al. (2013) used sintered fragments of glass without any cement to study strength recovery with densification and demonstrated that, all else being equal, an increase in porosity from 0 to 0.33 decreases the peak axial stress under uniaxial compression by more than a factor of 6, in agreement with predictions from the pore-emanated crack

model (Figure 1.13(a)). Finally, although they did not reproduced all failure modes observed in natural sandstones, Rice-Birchall et al. (2021) proposed that loose sand cemented with amorphous quartz could be used to model the mechanical behaviour of poorly consolidated high-porosity natural sandstones.

1.6.2 Viscous sintering of glass beads

Among the different materials studied, synthetic samples made of loose or fused glass beads provide an ideal two faces medium with uniform spherical grains of known diameter, hence their early use as porous material for investigating relationships between microstructure and physical properties of composites (Leverett et al., 1942; Wyllie et al., 1956, 1958). Unconsolidated porous reservoir sands or oceanic sediments have been studied using loose glass beads (Domenico, 1977; Johnson & Plona, 1982) while experimental simulation of consolidated rocks was achieved by cementing or sintering glass (Wigal, 1963; Berge et al., 1995; Li et al., 2018; Winkler, 1983, 1985). Sintering consists in the combination of individual discrete particles into a unique continuous body under forces acting on the particles either internally or externally. In the case where the particles that amalgamate are in a liquid state, the process is referred to as viscous sintering.

When heated to a temperature higher than the upper temperature of the glass transition, silicate glass beads act as viscous droplets and undergo time-dependent coalescence. The viscous sintering of glass beads, similar to sediments diagenesis, results in a granular densification accompanied by a progressive decrease in porosity (Wadsworth et al., 2017). A more extensive description of viscous sintering and of its use to prepare synthetic rocks is given in the following chapter (Chapter 2).

1.7 Structure of the thesis

Most of our understanding about the relationship between microstructural geometries and bulk properties arises from detailed experimental work using natural materials. However, because it is extremely rare to find natural rock formations that show variability in one microstructural attribute whilst others remain constant (as is the case for Fontainebleau sandstone which occurs over a large range of porosity values) and because the high degree of

variability of rock in both time and space limit consistency and reproducibility in laboratory experiments, the testing of synthetic rock materials has become a major topic of research in the past decades. It is now well established that synthetic rocks offer the opportunity to realistically model real rock behaviour and the evolution of effective properties throughout geological processes such as diagenesis.

This thesis seeks to build upon the work outlined above and explore how the use of synthetic rocks prepared by sintering glass beads may help define a comprehensive framework for the influence of porosity and grain size on the hydraulic and mechanical properties of crustal rocks. Although there exist a great number of other microstructural attributes which require careful deconvolved study, as they contribute to building the complex and highly variable hydromechanical behaviour of rocks that form the Earth's crust, we chose to lay the foundations of using sintered glass beads samples for rock mechanics laboratory experiments and investigate the simplest case of a two-phase (solid and gas) granular medium with no cement. Therefore, the following chapters mainly focus on the control of porosity and grain size distribution, which also stand out as first order controls of the hydromechanical properties.

Ultimately, this research aims to help understanding how effective properties are derived mathematically using the rock microstructure information and constituent properties, as it is of great interest to numerous environmental and industrial applications. Indeed, the data acquired in this research should allow to improve model predictions, routinely used in many aspects of geoscience and engineering while still only relying on simple-to-measure microstructural metrics. For example, understanding how physical properties evolve during the granular densification process will help us to better understand fluid pressurisation that can lead to fracturing, a major issue for exploration drilling and thus for the management and optimisation of hydrocarbons and geothermal reservoirs.

In light of the introduction above, this thesis seeks to address the following questions:

1. Can synthetic rocks made by sintering glass beads satisfactorily simulate the hydromechanical behaviour of porous crustal rocks and therefore be used to unravel the contribution of specific microstructural attributes on bulk hydromechanical properties?
2. All else being equal, what if the effect of total porosity/mean grain size variations on the onset of inelastic compaction?
3. How do the width and shape of the grain size distribution influence the mechanical behaviour and failure mode of porous granular rocks?

In order to answer the previous questions, this thesis was conducted as a systematic study of variations in physical properties, such as permeability, elastic wave velocity and strength, as a result of controlled variations in porosity or in grain size distribution. This manuscript is built upon two milestones: (1) the simplest case of a two-phase granular medium with a very closely clustered grain size distribution and (2) a slightly more complicated case where the granular medium presents a variably polydisperse grain size distribution. Beforehand, Chapter 2 details the technique for the preparation of the synthetic rocks by viscous sintering, using a monodisperse grain size distribution or a polydisperse grain distribution, and Chapter 3 summarises the main experimental methods used in this research. The following chapters introduce the results.

Chapter 4 investigates how the mechanical behaviour and failure mode of monodisperse granular rocks evolve as a result of variations in porosity or in mean grain size, in both cases whilst all other microstructural geometries are kept unchanged. The mechanical data are analysed alongside microstructural data obtained using Scanning Electron Microscopy (SEM). The results and discussion are presented in: Carbillet, L., Heap, M. J., Baud, P., Wadsworth, F. B., & Reuschlé, T. (2021). Mechanical Compaction of Crustal Analogs Made of Sintered Glass Beads: The Influence of Porosity and Grain Size. Journal of Geophysical Research: Solid Earth, 126, e2020JB021321. https://doi. org/10.1029/2020JB021321

Chapter 5 addresses the influence of the degree of polydispersivity and modality of the grain size distribution on the mechanical behaviour and failure mode of porous rocks, by means of

triaxial compression experiments and microstructural observations. The results and discussion have been prepared for a submission as: Carbillet, L., Heap, M.J., Baud, P., Wadsworth, F.B., & Reuschlé, T. The Influence of Grain Size Distribution on Mechanical Compaction and Compaction Localization in Porous Rocks to the Journal of Geophysical Research: Solid Earth.

Finally, Chapter 6 gathers and puts the conclusions of the preceding chapters into perspective.

Chapter 2

Preparation Procedure: The Cooking Recipe for Sintered Glass Bead Samples

2.1 Viscous sintering of glass beads under no external load: theoretical framework

2.1.1 State of forces acting on a liquid droplet

The preparation of the synthetic rocks is based on viscous sintering, a process which takes place in systems of droplets in a liquid state. In such state, the individual shape of a drop in the surrounding fluid might differ from perfect sphericity, depending on the forces acting on it. The importance of gravitational forces compared to surface tension (capillary) forces, which controls the shape of a droplet in a fluid is given by the Eötvös number (Eo) or Bond number (Bo) (Wadsworth et al., 2016):

$$Eo = Bo = \frac{\rho g R^2}{\Gamma} \tag{2.1}$$

where ρ is the density of the droplet in [kg.m^{-3}], g is the gravitational acceleration in [m.s^{-2}], R is the droplet radius in [m] and Γ the surface tension in [N.m^{-1}]. When gravitational forces dominate ($Eo \gg 1$), the shape may deviate from sphericity as the droplet deforms under its own weight. When surface tension forces dominate ($Eo \ll 1$), the droplet remains round.
Secondly, the importance of viscous forces compared to inertial forces, which controls the motion of the droplet, is captured by the Ohnesorge number (Oh) (Wadsworth et al., 2016):

$$Oh = \frac{\mu}{\sqrt{\rho \Gamma R}} \tag{2.2}$$

with μ the droplet viscosity in [Pa.s]. The bonding of two adjacent droplets is in the regime

where inertia is negligible, and viscosity dominates when $\mathrm{Oh} \gg 1$. When the system is such that $\mathrm{Eo} \ll 1$ and $\mathrm{Oh} \gg 1$, the sintering process mechanically consists in a viscous flow driven by interfacial tension.

In the following, attention is given to the case of interest to this work, i.e., the case of molten silicate glass droplets, which viscosity is high (compared to that of water, for instance) and therefore tend to be in the regime where inertia is negligible, and viscosity dominates.

2.1.2 Coalescence and porosity decrease with time

Not one liquid droplet but two liquid droplets in contact, i.e., a system of two spherical viscous particles surrounded by an inviscid fluid (e.g., air), are considered now. The bonding of the two particles by viscous flow driven by interfacial tension, sometimes refer to as coalescence, first occurs through a micromechanism known as the *neck growth* (Figure 2.1(b)). As theorised by Frenkel (1945), the formation of necks between initially adjacent droplets results in a decrease in the porosity of the system. When the initial system is simple, e.g., in coalescing pairs of droplets of similar size and shape, the sintering time scales with the initial droplet radius and the porosity can be derived from:

$$\overline{\varphi} = \frac{1}{\varphi_i}\left(1 - \frac{1}{\varphi_i}\right)\left(1 - \frac{3}{8}\bar{t}\right)^{-3} \tag{2.3}$$

where φ_i is the initial gas volume fraction and where the normalised porosity $\overline{\varphi} = \varphi/\varphi_i$ and time $\bar{t} = \frac{t\Gamma}{R_i\mu}$, with R_i the initial droplet radius, are introduced (Wadsworth et al., 2016). However, Wadsworth et al. (2018) compiled experimental datasets with model predictions for two-droplets coalescence and draw attention to the discrepancy between Frenkel's model and experimental results at long-time scale. They demonstrated that the more general model for the viscous sintering of two droplets proposed by Eggers et al. (1999), where $R_n \propto t \ln t$, provides a more accurate description of the dynamics of neck growth.

Adding one or more droplets to the previously described system renders the dynamics of viscous flow driven by interfacial tension far more difficult to analyse and describe. Mackenzie and Shuttleworth (1949) proposed that the sintering of a many-droplet system is driven by another micromechanism than neck growth, i.e., by the *shrinking* of pores

interstitial to the droplets (Figure 2.1(c)). In the vented bubble model (Mackenzie & Shuttleworth, 1949), they model pores as spherical bubbles embedded in liquid shells of finite size (Figure 2.1(c)) and the sintering dynamics is described in terms of the evolution of the gas volume fraction, which corresponds to the saturated void volume fraction in the system, i.e., the saturated porosity, with time. Wadsworth et al. (2016) re-casted the vented bubble model into the following differential equation:

$$\frac{d\overline{\varphi}}{d\bar{t}_b^*} \approx -\frac{3}{2}\overline{\varphi} \tag{2.4}$$

where $\bar{t}_b^* = \Gamma \int_0^t \frac{1}{\mu a(t)} dt$, with $a(t)$ the pore radius as a function of time. They derived an analytical solution for the differential equation, which gives the evolution of porosity with time as a function of the interstitial pore radius:

$$\overline{\varphi} = e^{-\frac{3}{2}\bar{t}_b^*} \tag{2.5}$$

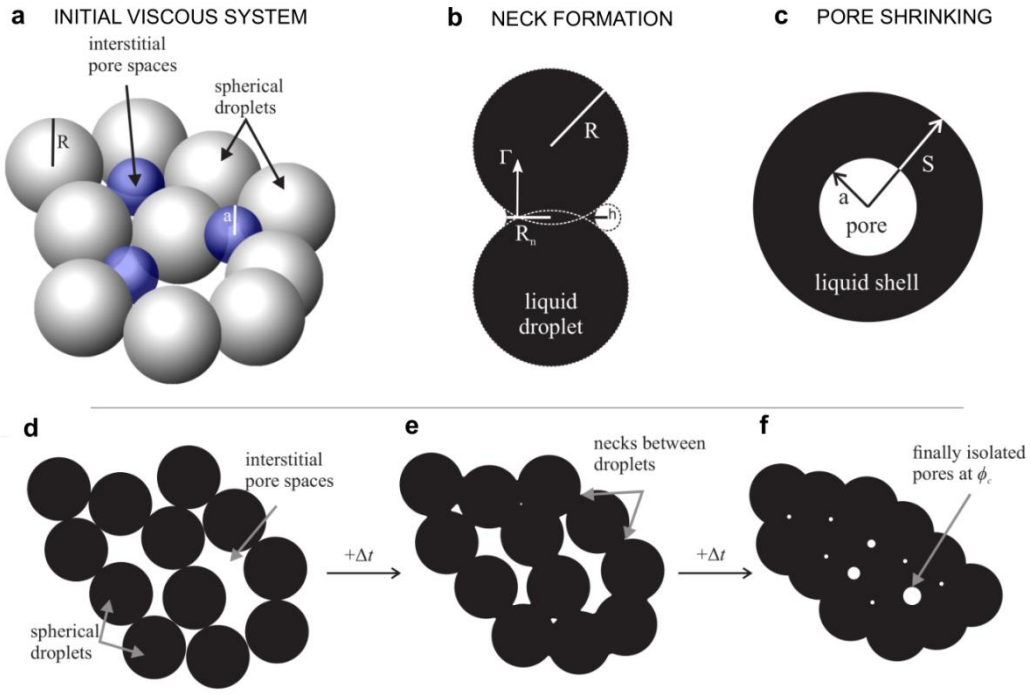

Figure 2.1 Schematic representation of the coalescence of a many-droplet viscous system with time. (a, d) Initially, the system is composed of spherical droplets (grey) with initial radius R and interstitial spherical pores (blue) with initial radius a. The system undergoes

coalescence driven by capillary forces (surface tension is denoted Γ) through two main micromechanisms: (b) the formation of necks with radius R_n and height h between beads that initially shared contact (e), and (c) the progressive shrinking of pores, which ultimately form isolated vented bubbles in a liquid continuum (f) (adapted from Wadsworth et al., 2016).

During sintering of more complex systems than coalescing pairs or small clusters, the microstructure evolves such that the neck formation model is generally considered valid for the early-stages of coalescence while the vented bubble model is considered valid for the intermediate to end-stages of coalescence (Figure 2.1; Prado et al., 2001; Wadsworth et al., 2017; Wadsworth et al., 2016). Therefore, in such systems, the sintering timescale first evolves with the droplet size and further with the interdroplet pore size as the micromechanism at play transitions from neck growth to pore shrinking (Figure 2.1(d to f)).

2.1.3 Pore space and granular densification

Besides a decrease in porosity, viscous sintering is also accompanied by a decrease in the connectivity of the pore space due to progressive pore shrinking, ultimately leading to pore-space isolation at approximately 0.03 (Wadsworth et al., 2017). For modelling purposes, the geometry of the pore space can be approximated with pores modelled either as overlapping or non-overlapping spheres (Torquato, 2002). Figure 2.2 presents the evolution of the mean pore size as a function of porosity, for pores modelled as solid or overlapping spheres. Such distinction yields different results for the evolution of their initial radii with time, which respective accuracy can be tested against modelling results for the evolution of physical properties of sintered media during densification (e.g., fluid permeability; Wadsworth et al., 2016).

Significant attention was given to the constraint of the lengthscales R_i and a_i, the radii of initially spherical glass beads and interstitial pores, respectively (Torquato & Avellaneda, 1991). The mean pore size of an arbitrary packing of beads can be derived using the cumulative probability density of the pore size distribution, which solving is a non-trivial problem addressed by Torquato (2002) and Wadsworth et al. (2016). In summary, an initial system of spherical viscous droplets and interstitial pores evolves during viscous sintering into a continuous liquid melt within which isolated spherical pores are embedded (Figure 2.1),

i.e., it undergoes densification. Throughout such densification, the microstructure evolves not only in connected porosity but also in pore-phase topology (Figure 2.2). Indeed, the evolution from non-closed packed viscous droplets, i.e., a microstructure dominated by individual particles surrounded by gas, to bubbles isolated in a connected viscous phase, i.e., a microstructure dominated by individual pores surrounded by a liquid continuum, can be described as a topological inversion (Wadsworth et al., 2017).

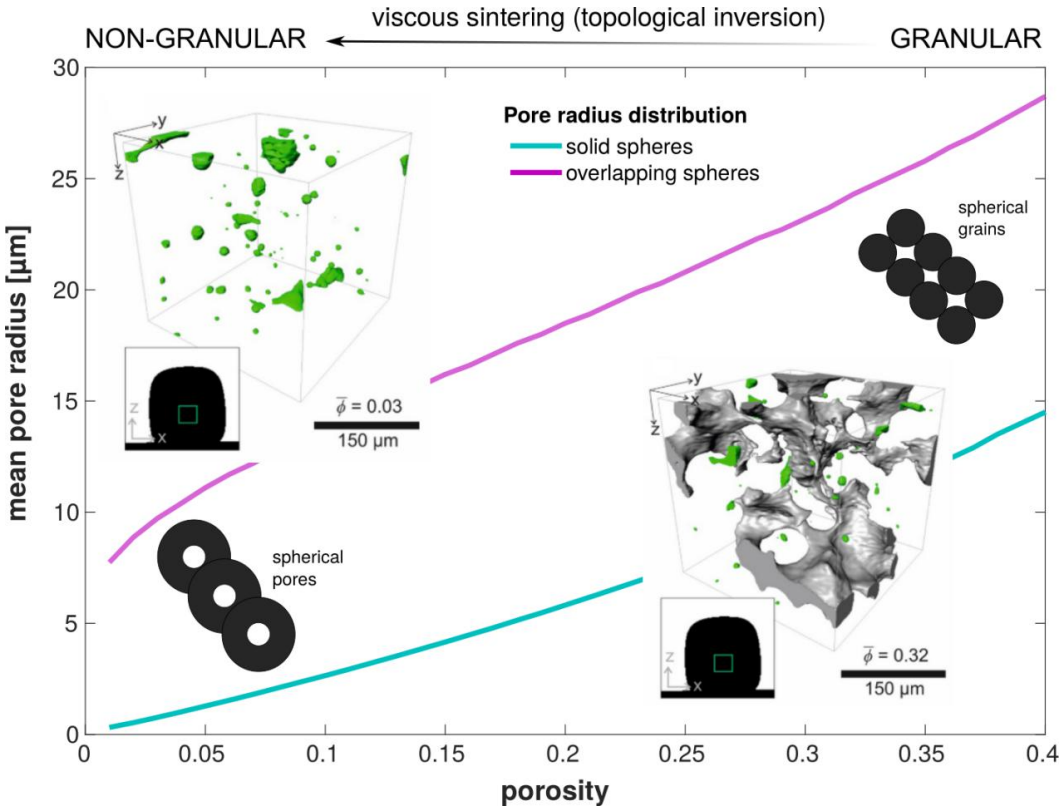

Figure 2.2 Mean pore radius evolution during granular densification by viscous sintering. Mean pore radius data have been derived using Wadsworth et al. (2016), for a mean grain size of 500 µm. From a porosity of 0.4 to 0.02, the mean pore radius is expected to be reduced by more than a factor of three. Results are different for pores modelled as solid spheres (blue) or ones modelled as overlapping spheres (purple). 3D representations of the pore space, where grey is the connected pore space and green the isolated pore space, are extracted from Wadsworth et al. (2017).

Densification therefore results in a transition from a granular microstructure to a non-granular microstructure, similar to that resulting from compaction and cementation in sedimentary

settings (Doyen, 1988; Fredrich et al., 1993). Wadsworth et al. (2017) used X-ray Computed Tomography (CT) to demonstrate such topological inversion in a sintering system and ultimately help unifying the previously presented descriptions (Figure 2.2). They showed that the topological transition from a droplet geometry to a bubble geometry can be associated to the onset of pore-space isolation and therefore predict that, for a given initial particle size, there exists a critical pore fraction above which the neck formation model cast for the porosity evolution accurately describes the experimental data and below which the one from the vented bubble model is more accurate.

2.1.4 Sintering glass beads: temperature-dependent viscosity and model parameters

To assess the viscous sintering of droplets, populations of silicate glass spheres can be used. Indeed, glass viscosity varies inversely with temperature such that glass mechanically behaves as a solid at low temperature and as a liquid at high temperature. The temperature dependency of viscosity is linked directly to the glass chemical composition. The amorphous material transitions from a brittle solid state to a viscous liquid state over a range of temperature, which is usually referred to simply as *glass transition temperature* (Avramov et al., 2005; Stebbins et al., 1995; Webb, 1997). In fact, the value referred to as transition temperature T_g conventionally corresponds to the onset of the glass transition, and this convention is adopted here.

Therefore, when glass spheres are heated to a temperature above the glass transition temperature, they act as viscous droplets and, if they are in the low Eötvös number - high Ohnesorge number regime, undergo time-dependent coalescence driven by capillary forces. The models presented above can be used to pre-determine the mean grain size and final porosity (and estimate the corresponding mean pore size using the method described by Wadsworth et al. (2016)).

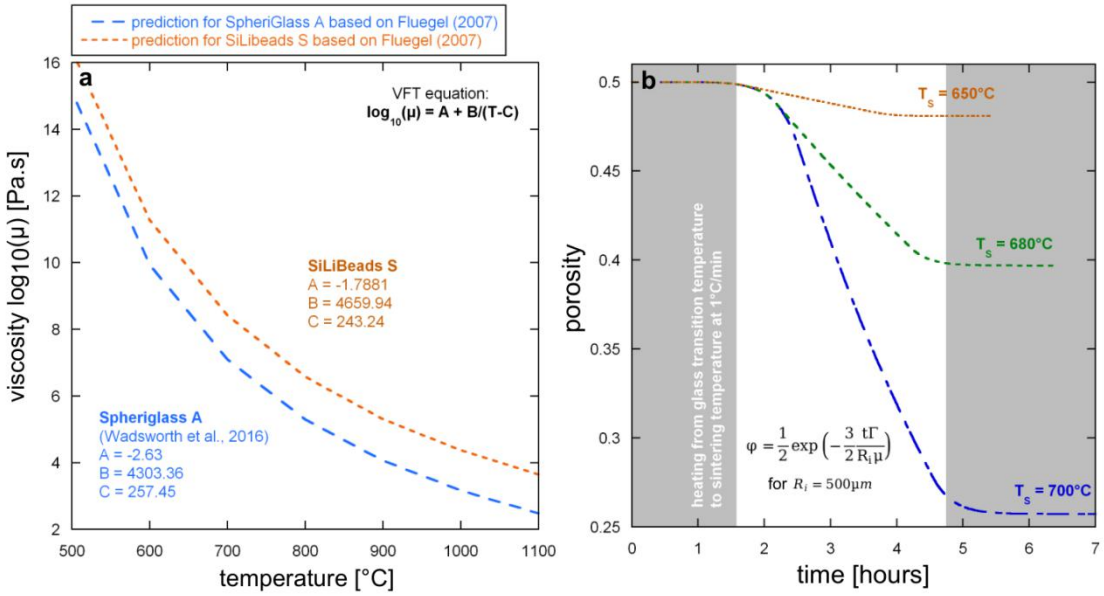

Figure 2.3 (a) Temperature dependency of viscosity, estimated using Fluegel (2007) for the industrial glasses used in this work and (b) resultant porosity reduction in SiLiBeads S glass beads with time for different sintering temperature (written at the end of the corresponding curve), derived using the simplified equation presented, with R_i = 0.5 μm and Γ = 0.3 N.m^{-1}.

To do so, it is first necessary to calibrate for the temperature dependency of viscosity. This is illustrated in Figure 2.3, which shows the temperature-dependent viscosity of two industrial glasses (a) and the evolution of porosity with time for glass beads with diameter of 500 μm for different sintering temperatures (b). Such calibration can be achieved using the glass chemical composition in the multicomponent model of Fluegel (2007), which is based on the Vogel-Fulcher-Tamman (VFT) equation

$$\log \mu = \frac{A + B}{T - C} \tag{2.6}$$

with μ the glass viscosity, T the temperature and (A, B, C) fitting parameters. Knowing the parameters (A, B, C), the glass viscosity at a given temperature can be estimated and used in (2.3) or (2.5) to predict the porosity of the sintering system after some time. Therefore, given the theoretical models presented above, viscous sintering of glass spheres can be parameterised specifically in order to prepare materials with known mean grain and pore sizes and porosity.

2.2 Practical procedure for the preparation of synthetic rocks: ingredients and equipment

The work conducted for this thesis relies on the preparation of synthetic rocks with variable microstructural attributes (e.g., porosity and grain size) by sintering glass beads. The theoretical framework detailed here above was used as a guide to design samples with pre-determined microstructural attributes and to parameterise specifically for the study of chosen parameters in isolation, i.e., to vary one parameter while keeping the others constant. In the following, the recipe developed for that purpose, based on the work of Berge et al. (1995), Guyon et al. (1987) and Wadsworth et al. (2016), among others, is presented. While Berge et al. (1995) sintered monodisperse distributions glass beads in Pyrex beakers, Guyon et al. (1987) used a specifically designed apparatus, consisting of two vibrating electromagnetic distributors filling beads in a rotating graphite mould, to prepare bidisperse distributions of glass beads to sinter. This thesis' originality lays in the preparation of samples that span a wide range of porosity and grain size, which required to perfect the procedures reported in the literature, but also in the development of a new methodology for preparing samples individually.

2.2.1 Ingredients

To prepare the synthetic rocks, only three ingredients are necessary: plaster, water and glass beads. The glass beads are to be chosen carefully as they must fulfil certain conditions. Microspheres of known chemical composition and size which enter the low Eötvös number - high Ohnesorge number regime are to be used. In that regime, the diameter of the beads should also remain ten times inferior to the size of the final samples to ensure that the sample bulk behaviour is not affected by the beads, i.e., that the sample size is larger than that of the representative elementary volume.

In the different studies conducted for the present work, soda-lime-silica glass beads were used. The soda-lime-silica glasses are widely used multicomponent glasses characterised by a high silicon dioxide content usually supplemented by calcium, sodium and aluminium oxides in lower proportions but for which wide variations in compositions are observed. Two commercial soda-lime silica glasses – SpheriGlass A-Glass from Potters Industry (Malvern,

Pennsylvania, United States; https://www.pottersindustries.com/micro-glass-beads/) and SiLiBeads Type S from Sigmund Lindner (Warmensteinach, Germany; https://www.sigmund-lindner.com/en/products/glass-beads/), with very close chemical compositions (Table 2.1) were chosen.

Table 2.1 Chemical composition of the soda-lime-silica glass beads used to prepare the synthetic samples

Composition, weight %	Glass	
	SpheriGlass A-Glass	SiLiBeads S-Type
SiO_2	72.5	72.5
Na_2O	13.7	13.00
CaO	9.8	9.06
MgO	3.3	4.22
Al_2O_3	0.4	0.58
FeO/Fe_2O_3	0.2	-
K_2O	0.1	-
B_2O_3	0.0	-

The reason for ordering microspheres from two different companies - in different glasses - is that they manufacture microspheres in different size distributions, of interest to this work. The results of the chemical and physical analysis of the industrial glasses were provided by the manufacturers (see Annex 1).

The transition temperature for SiLiBeads S-Type solid microspheres was provided by the Sigmund Lindner (Annex 1). Wadsworth et al. (2014) measured the onset of the glass transition interval for SpheriGlass A-Glass solid microspheres using a differential scanning calorimeter and thermogravimetry. The temperature-dependent viscosity of the two glasses was derived using the method presented in section 2.1.4 and results are presented in Table 2.2. A non-exhaustive list of mechanical properties of soda-lime-silica glass is also given in Table 2.3.

Table 2.2 Thermal properties of the soda-lime-silica glasses used to prepare the synthetic samples

Thermal properties		Glass	
		SpheriGlass A-Glass	SiLiBeads S-Type
Glass transition temperature T_g, °C		551	549
VFT fitted parameters (T in °C)	A	- 2.63	- 1.79
	B	4303.36	4659.94
	C	258.45	243.24

Table 2.3 Mechanical properties for the soda-lime-silica glasses used to prepare the synthetic samples

Parameter	Glass	
	SpheriGlass A	SiLiBeads S
Young's modulus E, GPa	69	63
Shear modulus G, GPa	30	-
Coefficient of friction μ	0.9 – 1.0	
Fracture toughness K_{Ic}, MPa.m$^{1/2}$ (Aktas et al., 2017)	0.7 – 0.9	

2.2.2 Equipment

The equipment needed for the preparation of sintered glass bead samples is detailed here below.

(1) Sieves of different mesh sizes are needed to prepare samples with various bead size distributions.

(2) A cup, a teaspoon, a measuring tube with a cap and a flat plastic tray will serve to manipulate, i.e., collect, measure, mix, pour, etc., the glass beads.

(3) A porous ceramic tray should serve as a vessel in which to sinter packs of beads. The shape and dimensions of the tray must be determined in order to allow for the coring of

samples with the shape and dimensions required for subsequent experimental use. Long flat combustion trays from Umicore Friatec (Brussels, Belgium; https://www.umicore-ceramics.com/gb/products/high-temperature-ceramics) in Frialit Degussit alumina AL24 with dimensions 205×125×50 mm were used for this thesis.

(4) An electric box furnace which maximum temperature is higher than the chosen sintering temperature, therefore higher than the transition temperature of the glass beads to be sintered, is required. The model used to conduct this work is Nabertherm (Lilienthal, Germany; https://nabertherm.com/en/products/laboratory/muffle-furnaces) Muffle Furnace L9/11/SKM, which chamber dimensions are 240x230x170 mm (i.e., 9L capacity), with heating from four sides (thus ensuring a more homogeneous heating than box furnaces with two heating sides) up to a maximum temperature of 1100°C.

(5) To ensure safety for the steps of the preparation performed at high temperature, metal crucible tongs, highly heat resistant gloves and furnace goggles should be used.

(6) Finally, the preparation of cylindrical samples with chosen dimensions requires the use of a corer and a grinder.

2.3 Practical procedure for the preparation of synthetic rocks: instructions

Practically speaking, the procedure to prepare sintered glass beads samples is structured by three main stages: the design of the grain size distribution at room temperature, the decrease of porosity up to the desired value by viscous sintering at high temperature, the sample preparation at room temperature. Figure 2.4 gives an overview of the type of distribution which were prepared in the course of this work: (a) monomodal and closely clustered for the distributions referred to as monodisperse, (b) with two principal peaks (i.e., two sizes) for the bidisperse distributions and (c) with multiple peaks (i.e., multiple sizes) for the polydisperse distributions. S quantifies the degree of dispersivity ($0 < S < 1$, with $S = 1$ the monodisperse limit) of a distribution. Depending on the type of grain size distribution, the experimental procedure varies slightly. The methods corresponding to each one of the types of distribution described above are described in the following.

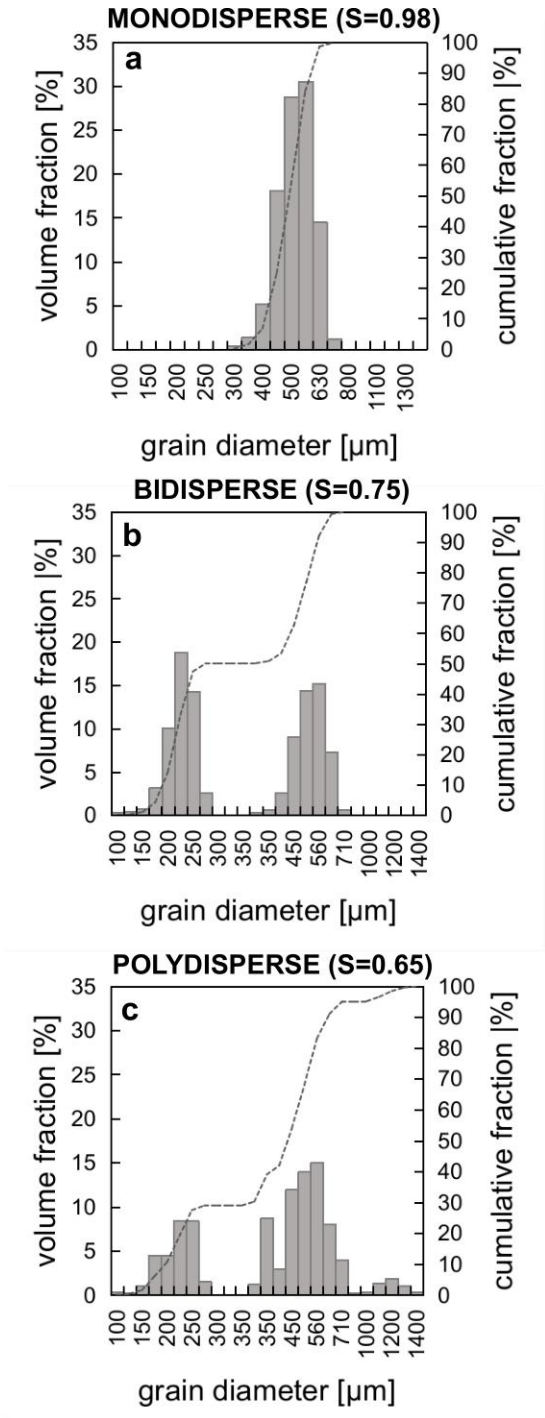

Figure 2.4 Types of grain size distributions used to prepare the synthetic samples used in the present work. The simplest distribution which can be prepared is (a) a monomodal closely clustered distribution of bead sizes, which are referred to as monodisperse for simplicity. (b) Beads of two sizes can be mixed to prepare bidisperse distributions and (c) beads of various sizes can be mixed to prepare polydisperse distributions. S quantifies the degree of dispersivity ($0 < S < 1$, with $S = 1$ the monodisperse limit).

2.3.1 Method 1: block preparation using a monodisperse distribution of beads

For the case of a monodisperse distribution, the synthetic rocks are prepared as blocks from which samples are cored. Figure 2.5 outlines the preparation steps for the block method. First (Figure 2.5(1)), the grain size distribution is prepared at room-temperature. To get a

monomodal closely clustered distribution, beads can be sieved down to a small diameter range, which requires using sieves with very close mesh sizes. However, such distributions can also be purchased. Indeed, as spherical glass beads are used as engineered glass materials serving the highway safety, polymer additive, metal finishing, and conductive particle markets, glass beads with a wide range of chemical composition and sizes are marketed. Beads of two sorts of industrial glasses (SpheriGlass A-Glass from Potters Industry and SiLiBeads Type S from Sigmund Lindner) were purchased in different size distributions, detailed in Table 2.4. Figure 2.6 shows the grain size distributions for the SiLiBeads microspheres. These distributions were used as they are to prepare samples referred to as monodisperse samples.

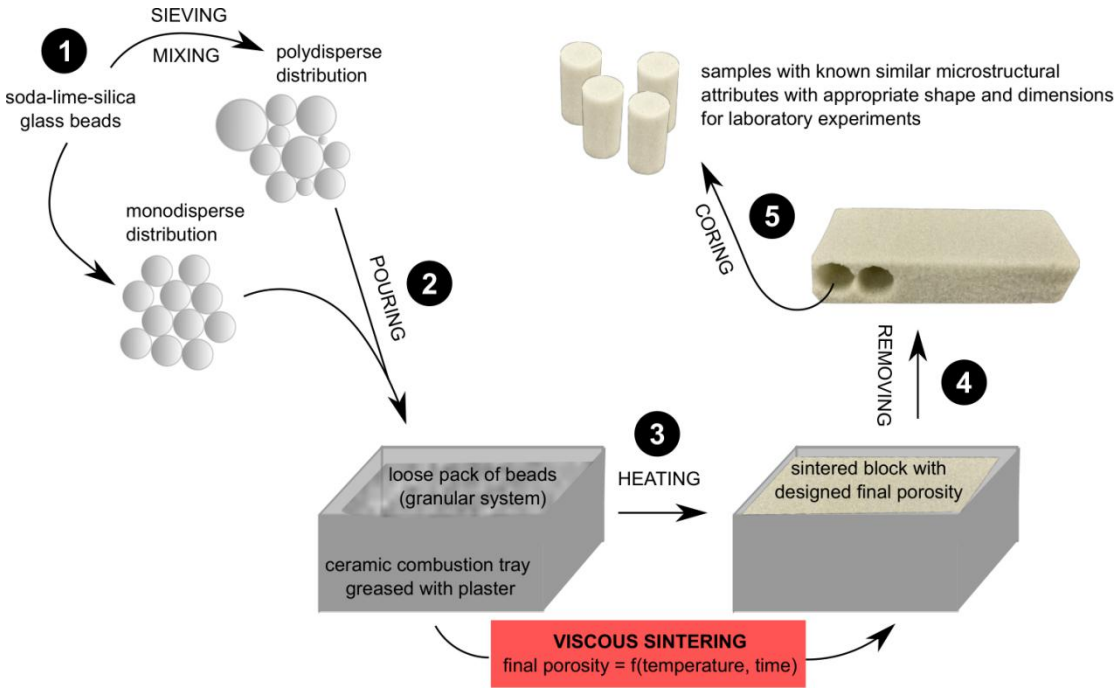

Figure 2.5 Schematic representation of the experimental procedure for the preparation of sintered samples: the case of sintered blocks (not to scale). A detailed description of each step is provided in the main text.

Table 2.4 Grain size distributions and corresponding mean grain and pore radius derived using Wadsworth et al. (2016). The size distributions were provided by the manufacturers (Annex 1).

Glass	Size distribution		Mean grain radius [µm]	Mean pore radius [µm] (at φ = 0.5)		Degree of dispersivity
	diameter [µm]	volume fraction [%]		hard spheres	overlapping spheres	
SiLiBeads type S 4504	<900	0.09	601	110	186	0.99
	1000	3.07				
	1100	27.96				
	1200	38.20				
	1300	21.95				
	1400	7.81				
	>1400	0.92				
SiLiBeads type S 5218	<300	0.19	261	49	82	0.97
	355	1.37				
	400	5.16				
	450	18.12				
	500	28.77				
	560	30.50				
	630	14.52				
	710	1.23				
	>710	0.14				
SiLiBeads type S 5215	<100	0.19	112	21	35	0.97
	125	0.39				
	150	1.57				
	175	6.37				
	200	20.08				
	225	37.68				

	250	28.55				
	275	5.17				
	>275	0				
SpheriGlass A-Glass 1922	150-250	100	-	-	-	-
SpheriGlass A-Glass 2530	45-90	100	24.7	5.9	-	0.98

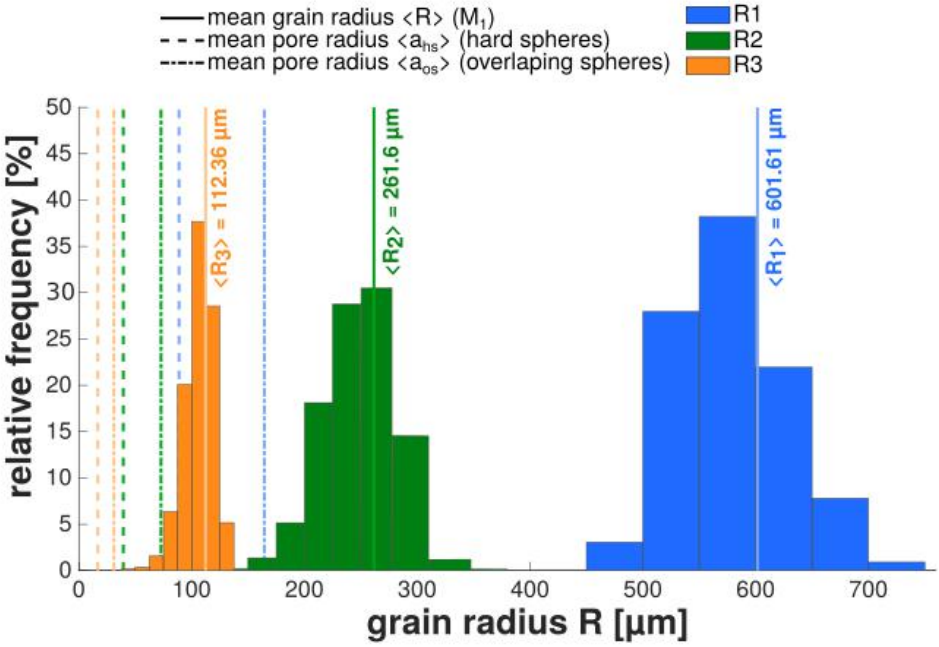

Figure 2.6 Grain radius distributions of the SiLiBeads microspheres used to prepare synthetic samples. The degree of dispersivity S is approximately 0.98 for the three distributions (with S=1 the monodisperse limit).

Second (Figure 2.5(2)), the beads are poured in the combustion tray, which interior was covered beforehand with a 0.5 cm thick layer of plaster, which acts as a non-stick layer and greatly helps in the unmoulding of the sintered block (Figure 2.5(4)). The tray is then manually shaken to flatten out the bead pack surface (at that stage, the porosity of the bead pack is approximately 0.5) and placed inside the furnace.

Third (Figure 2.5(3)), the bead pack is heated at a constant rate of 3°C min^{-1} to a temperature above the glass transition onset temperature (Table 2.2), which will be maintained constant for a certain time depending on the target final porosity. All the samples were prepared at a sintering temperature of 680°C, at which the viscosity of the glass beads is approximately $\mu \approx 10^9$ Pa. s (Figure 2.3a) which gave sintering times of hours to obtain high final porosity values, to days to obtain low final porosity values (Figure 2.3b). Halfway through the dwell, using two metal crucible tongs and wearing the goggles and gloves, the tray is moved in the furnace to 180° of its initial position to reduce the heterogeneity of the block sintered that may arise when the temperature distribution in the chamber is not even. After holding the temperature constant for a fixed time, it is lowered to 500°C at a cooling rate of 1°C min^{-1} and finally decreased to ambient temperature at a cooling rate of 3°C min^{-1}. This cooling workflow is designed to minimise thermal microcracking (Berge et al., 1995).
Finally (Figure 2.5(4)(5)), the sintered block is removed from the combustion tray at room-temperature. Samples of the desired diameter are then cored along the horizontal axis of the resulting block to minimise gravity induced porosity gradients along the axis of the samples and cut and precision-grounded to the desired length. All the samples used in this work were cylindrical samples of 20x40 mm.

2.3.2 Method 2: block preparation using bidisperse or polydisperse distributions of beads

For the case of bidisperse and polydisperse distributions, two methods were explored: a similar procedure than that for monodisperse distributions, in the form of blocks, and a procedure to prepare samples individually. In the following, the first method is described.
While steps (3) to (5) (Figure 2.5) are similar to the method for monodisperse samples, additional steps have to be performed to prepare bidisperse and polydisperse samples using sintered blocks. Prior to the preparation of the distribution at room-temperature, the beads are sieved into very small diameter ranges: 100 µm wide intervals in the range 150 - 1400 µm, within the limits of the sizes available in the distributions presented in Figure 2.6. Mixing various volumes of the resulting bead batches, variably disperse distributions can be prepared. The distribution of beads is poured into a large flat plastic tray and beads are manually jumbled together until no size cluster is visible anymore. To prevent from graded beddings to form while filling the combustion tray with the prepared distribution, small portions of mixed

beads are collected from the large plastic tray using a teaspoon and placed in the ceramic combustion tray, while checking for statistical homogeneity by visual inspection until the tray is full. Further, the procedure is similar to that previously described for monodisperse distributions. After samples are cored and precision-grounded, final visual inspection allows to segregate and reject samples which show graded beddings.

2.3.3 Method 3: single sample preparation

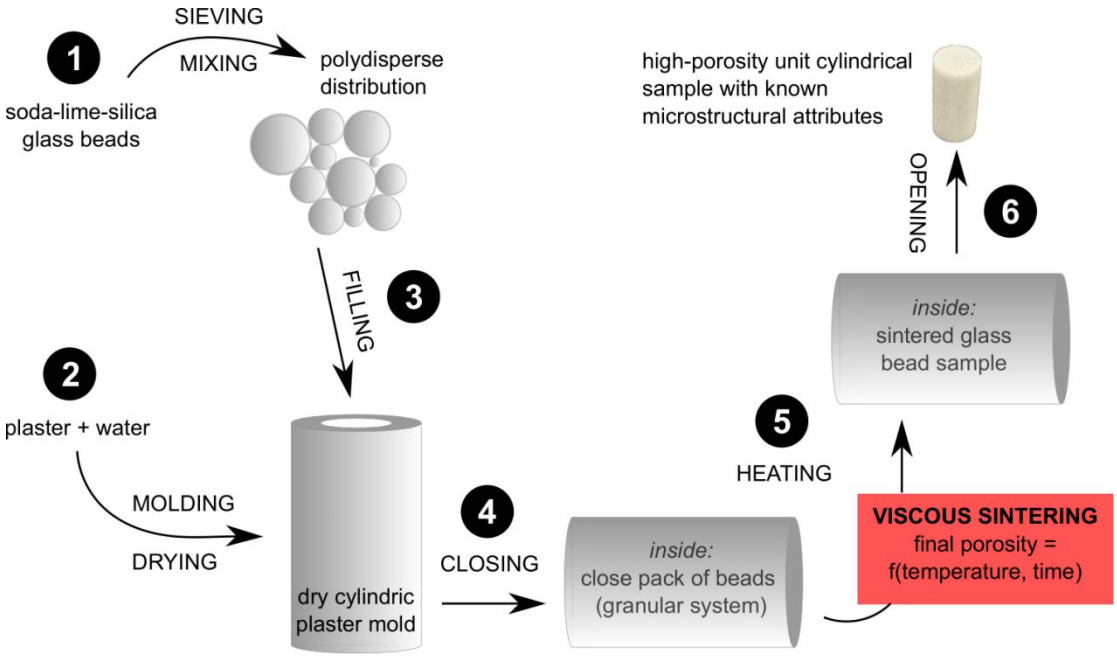

Figure 2.7 Schematic representation of the experimental procedure for the preparation of sintered samples: the case of unit cylindrical samples (not to scale). A detailed description of each step is provided in the main text.

Finally, bidisperse and polydisperse samples were also prepared individually. This method was developed specifically for the purpose of this thesis and ensures that the grain size distribution of every single sample is perfectly known and controlled. Figure 2.7 outlines the preparation steps for the unit sample method. The first step consists in preparing a bidisperse or polydisperse distribution (Figure 2.7(1)) according to the procedure detailed above (see 2.3.2). Second (Figure 2.7(2)), a mixture of plaster and water is moulded into a tube closed on one side, with external dimensions of 70 x 90 mm and 25 mm-thick walls, and dried on the

hot plate at 50°C for 48h. Then (Figure 2.7(3)), the cylindric mould is filled with the glass beads and a plastic cylinder with a diameter of 20 mm is used to compress the bead pack in the tube (close packing) and flatten its surface. Prior to heating, the mould is closed using a piece of andesite of 20x13 mm as an endcap (which thermal properties are constant over the whole sintering temperature range; Heap et al. (2018)) endcap to allow for cooking the mould horizontally (Figure 2.7(4)). This is necessary to prevent gravity forces to generate a porosity gradient in the axial direction of the cylindrical sample. Viscous sintering is then conducted using a similar procedure than the one presented above (see 2.3.1). After sintering, once the temperature in the furnace has been lowered to room-temperature, the plaster mould is taken out of the furnace and the sintered sample is accessed by gently breaking the mould using a hammer (Figure 2.7(6)).

Although allowing for a strong control over the grain size distribution, this method serves only to prepare high-porosity samples. Indeed, as the porosity is reduced throughout viscous sintering, the sample in the mould progressively shrinks. Therefore, this method was used to prepare samples with porosity ranging from 0.3 to 0.38, where the bulk volume change during viscous sintering is negligible and samples with appropriate final shape and dimensions can be prepared.

2.4 Overview of the synthetic samples: from the sample scale to the grain scale

Synthetic samples with grain size distributions of the three different types - monodisperse, bidisperse, polydisperse - are presented in Figure 2.8, alongside samples of Fontainebleau and Bentheim sandstones, two well-sorted monomineralic sandstones. Visually speaking, the monodisperse synthetic samples evolve gradually from samples with coarser grains which are more translucent to samples with very small grains which are more matt. More polydisperse synthetic samples somehow look more alike to the monomineralic well-sorted Fontainebleau and Bentheim sandstones.

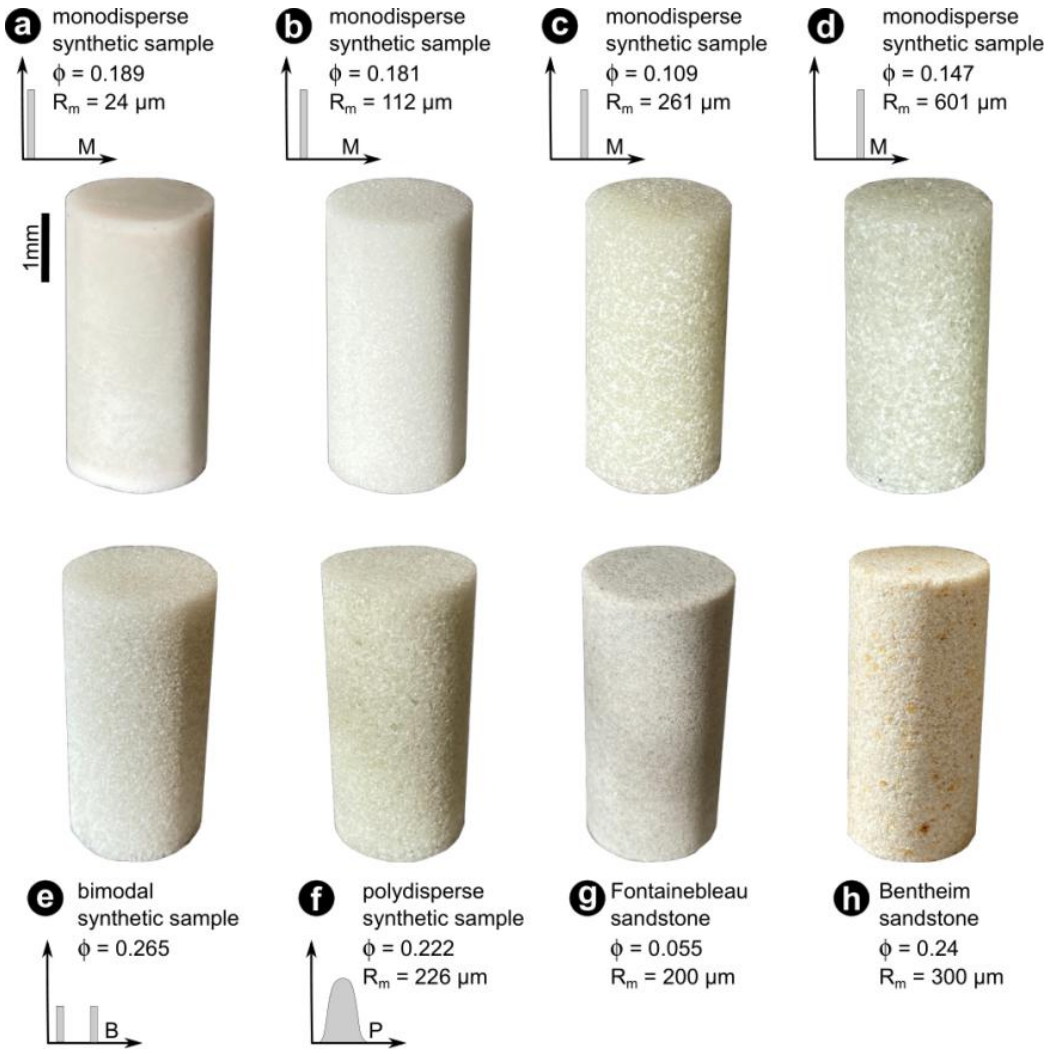

Figure 2.8 Overview of synthetic and natural sandstone samples with various grain size distributions. Four monodisperse distributions of grain size were used to prepare synthetic samples with mean grain radius of (a) 24 µm, (b) 112 µm, (c) 261 µm and (d) 601 µm. Glass beads from different size ranges were mixed in various proportions to prepare samples, with either (e) bidisperse or (f) polydisperse grain size distributions. The synthetic samples are presented next to two well-sorted natural sandstones which have been extensively studied in the laboratory: (g) a Fontainebleau sandstone sample with a porosity of 0.055 and a mean grain radius of 220 µm and (h) a Bentheim sandstone sample with a porosity of 0.24 and a mean grain radius of 300 µm.

Insights into the microstructure of the synthetic samples were gained using polished thin sections observed under a scanning electron microscope (SEM). Figure 2.9 shows the microstructure of synthetic samples with different porosity and grain size distributions. As porosity decreases, the microstructural transition from a granular state to a non-granular state can be observed. At high porosity (Figure 2.9(a)(c)), adjacent beads are connected by a neck and pore space remains between the bonded grains, as predicted by the Frenkel model. While a material is only truly granular when the individual grains can move relative to one another (which is the case for the glass beads prior to sintering), the high-porosity synthetic rocks are close to that granular end member case. At intermediate porosity (Figure 2.9(d)), sintering has progressed and begun to close the pore network. Finally, at low-porosity (Figure 2.9(b)), synthetic rocks exhibit pore structures close to isolated pores in a glass medium (the equilibrium porosity at the end of sintering is 0.03; Wadsworth et al., 2016), as predicted by the vented-bubble model.

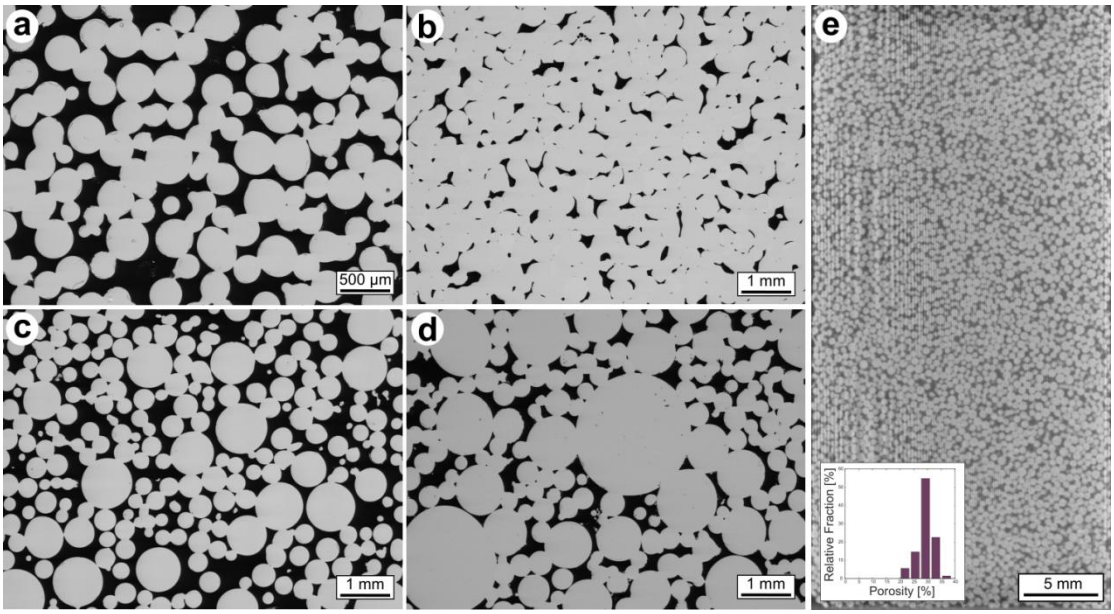

Figure 2.9 Microstructure of sintered glass bead samples. SEM images of monodisperse synthetic samples with a mean grain radius of 112 µm and porosity of (a) 0.32 and (b) 0.07, a (c) bidisperse synthetic sample with a porosity of 0.35 and beads with radii of 261 and 112 µm and (d) polydisperse synthetic sample with a porosity of 0.25 and mean grain radius of 454 µm. (e) 2D slice through a 3D X-ray tomography scan of a monodisperse sample with a porosity of 0.30 and a mean grain diameter of 261 µm, for which 2D porosity measurements

made in a squared window of 2mm of edge length (REV) yielded values clustering around 0.30.

Although statistically homogeneous, the granular materials prepared by sintering glass spheres present heterogeneities on the scale of 2-3 grains. Indeed, SEM images of intact samples reveal small heterogeneities in the pore size distribution (Figure 2.9). As the preparation workflows presented above allows for controlling the diameter of the grains and the degree of dispersivity but not for designing the exact nature and structure of the porous space, some porous patches, whose width can reach 0.4 mm, can be observed in the intact samples (Figure 2.9). Using a square window of 2mm of edge-length, 2D porosity measurements were performed on a 2D slice of a 3D X-ray tomography scan of an intact monodisperse sample (using ImageJ) with a porosity of 0.30 (laboratory measurement) and a mean grain radius of 261 μm. The square window with an edge-length of 2 mm ensures that the measured area contains at least 10 glass beads in any one direction, to ensure a representative element volume (REV). Figure 2.9(e) presents the histogram of the distribution of the 2D porosity measurements, a monomodal distribution closely clustered around 0.30, with local values between 0.21 and 0.38. The areas yielding higher porosity value will be referred to as porosity clusters. Sintered porous materials are random heterogeneous but isotropic porous media in terms of their microstructure, where 'heterogeneous' is used to refer to the lack of structural order. However, the samples are homogeneous in the sense that the random variation in the microstructure occurs on length scales much less than the sample lengths.

2.5 Concluding remarks

Building on the theoretical and experimental work outline in section 2.1, an experimental procedure to prepare synthetic rocks by viscous sintering of glass beads was designed. The existing theoretical models for viscous flow driven by interfacial tension provide a comprehensive framework for the analysis of the evolution of microstructural geometries during sintering. Therefore, the use of viscous sintering allowed for pre-determining and controlling microstructural attributes such as the grain and pore size distributions and the porosity of the rock samples. Two preparation protocols were developed: the sintering of bead

packs in the form of blocks from which samples were cored and the sintering of bead packs directly shaped into cylindrical samples. Ultimately, this approach allowed for the preparation of highly reproducible precisely controlled rock analogues and to parameterise specifically for the importance of porosity and grain or pore size on the mechanical behaviour of porous materials in general, thus to move beyond phenomenological approaches to naturally variable materials. Before serving as materials for deformation experiments, the synthetic samples were characterised in the laboratory and their physical properties (permeability, P- and S-waves velocity, electrical conductivity, thermal conductivity) compared to that of natural sandstones. The results are presented in Chapter 3, which sets out to demonstrate the suitability of sintered glass beads samples as analogues for porous sandstones.

Chapter 3

Methods and Sample Characterisation: Assessing the Suitability of Sintered Glass Beads as Analogues for Sandstones

This chapter sets out to characterise the physical properties of the synthetic samples in order to assess their suitability as analogues for crustal granular rocks and, in particular, sandstones. Therefore, the experimental data were compared to data from the literature on Fontainebleau sandstone, a monomineralic well-sorted natural sandstone from France which has been extensively studied in the laboratory. A reason for that is that Fontainebleau sandstone spans a broad range of porosity (0.03–0.28) while the mean grain diameter (0.250 mm), and other microstructural attributes, remain almost constant (Bourbie & Zinszner, 1985; Louis et al., 2009; Revil et al., 2014). In addition, where simple theoretical models for the evolution of a physical property with porosity or grain size exist, the experimental data are compared to the model predictions for the synthetic samples.

A range of experimental methods were used to characterise the samples, to assess their suitability as crustal rocks analogues and to conduct the specific studies presented in Chapter 4 and Chapter 5. Therefore, to avoid redundancy, we present all experimental methods used throughout the thesis in the present chapter.

3.1 Microstructural observations

Uncovered polished thin sections were prepared using intact and deformed synthetic samples. Prior to cutting, deformed samples were impregnated under vacuum using EpoThin 2 Epoxy Resin and EpoThin 2 Hardener from Buehler. For technical reasons, the subsequent preparation of the thin sections was performed in external thin section laboratories:

- TS Lab & Geoservices (Pisa, Italy) (www.tslab.eu)
- Atelier de lithopréparation, Université de Montpellier (Montpellier, France) (www.lithos.univ-rennes1.fr/)

All the measurements presented in the following were conducted at the Ecole et Observatoire de la Terre, in Strasbourg. Micrographs of the thin sections were obtained using a TESCAN Vega 2 XMU (low vacuum) scanning electron microscope (SEM) in backscatter mode (www.ites.unistra.fr/services-plateformes/microscopie-electronique-a-balayage). The SEM was used with a 15 kV accelerating voltage and a 23 mm working distance.

3.2 Characterisation of the pore space

3.2.1 Porosity

Porosity φ quantifies the proportion of void in a material and is mathematically defined as the ratio between the volume of pores (or the difference between the bulk volume and the solid volume) and the bulk volume of the material. Prior to characterisation, all samples were dried at 40°C under vacuum for at least 48 hours.

To measure porosity, the dimensions (diameter and length) and mass of the sample were measured and the total porosity φ was derived using

$$\varphi = 1 - \frac{m}{\rho_s V_b} \tag{3.1}$$

where the sample bulk volume is $V_b = \pi R^2 L$, with $R = D/2$ and L the sample radius [cm] and length [cm], respectively, and with ρ_s the glass solid density [g.cm^{-3}] and m the sample (solid) mass [g].

The solid density of beads, before and after heating to 680°C, was determined using a helium pycnometer (Micromeritics AccuPyc II 1340). According to the measurements, the glass solid density remained unchanged after sintering/heating (using the procedure detailed in Chapter 2), i.e., 2.49 g.cm^{-3}, in agreement with the value provided by the manufacturers (SpheriGlass and SiLiBeads). The total porosity of the synthetic samples prepared in the course of this work is in the range 0.026 - 0.397.

The uncertainty associated with the porosity measurements can be defined as

$$\delta\varphi \leq \varphi \sqrt{\left(\frac{\delta m}{m}\right)^2 + \left(\frac{V_b \sqrt{\left(\frac{\delta R}{R}\right)^2 + \left(\frac{\delta L}{L}\right)^2}}{V_b}\right)^2}. \qquad (3.2)$$

The mean error associated to the porosity calculation was estimated using the previous equation at $\delta\varphi < 0.005$.

The preparation procedure presented in Chapter 2 was designed for viscous sintering to take place in the regime where coalescence is driven by capillary forces only and where gravity does not affect the sintering on the bead scale. However, to ensure that these expectations are met in practice and that the samples are homogeneous, image analysis was performed on intact sintered samples (Chapter 2). In addition, porosity measurements were also conducted on cylindrical samples cut in half along the axis. The results obtained on a sample which porosity was estimated at 0.352 using the dimensions and mass of the two halves yielded porosity values of φ = 0.349 +/- 0.007 (L = 39.96 mm; l = 10.01 mm; m = 20.404 g) for one half and φ = 0.353 +/- 0.007 (L = 39.97 mm; l = 9.95 mm; m = 20.121 g) for the other half. The difference in porosity between the two halves of the cylindrical sample is $\Delta\varphi$ = 0.004, which is smaller than the mean error associated with the porosity calculation (0.005). Therefore, no variation of porosity over the diameter of the synthetic samples was measured.

3.2.2 Specific surface area

3.2.2.1 Experimental procedure

The specific surface area s, in [m^{-1}], is a microstructural parameter mathematically defined as the surface area of pores divided by the solid volume of the rock.

Specific surface measurements were conducted in a Sorptomatic 1990 from Carlo Erba Instruments, using a Brunauer-Emmet-Teller (BET) technique, which is based on the adsorption of nitrogen on the surface of the solid. This method consists in measuring the

amount of gas adsorbed on the connected internal surface of the measured sample. To achieve this, defined quantities of nitrogen were introduced in several steps in a burette containing the tested sample and, at each step, the pressure at which the system reached equilibrium was measured. Gas was introduced until the equilibrium pressure reached the saturation gas pressure, at which condensation occurs. Measurements were performed on a suite of selected synthetic samples, with porosity in the range 0.06–0.30 and mean grain radius in the range 112–601 µm. The specific surface data obtained are used later to interpret electrical conductivity and permeability data.

3.2.2.2 Results

Results for the evolution of the specific surface with porosity for synthetic samples with mean grain radius of 112, 261 and 601 µm are presented in Figure 3.1. Overall, at constant porosity, increasing the grain radius decreases the specific surface area, in accordance with studies on natural sandstones (Heap et al., 2017). For samples with a mean grain radius of 112 µm, the specific surface area increases with porosity: at a porosity of 0.06, the specific surface is approximately 1 m^{-1} and at a porosity of 0.30, s is 3.9 m^{-1}.

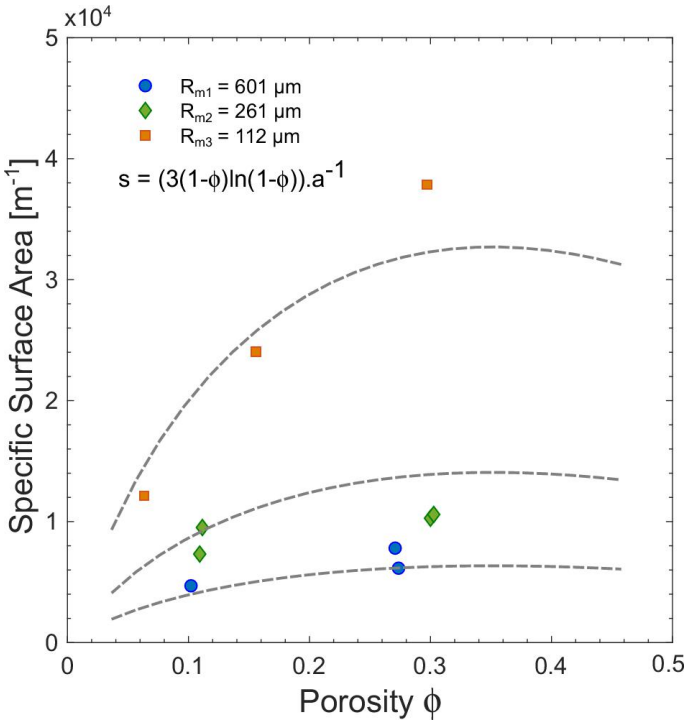

Figure 3.1 Specific surface area of synthetic samples with porosity in the range 0.6–0.30 and mean grain radius of 112 (orange squares), 261 (green diamonds) and 601 (blue circles) µm. The experimental data are compiled with modelled curves computed using the method described by Wadsworth et al. (2016) (equation 3.3) (grey dashed line).

For samples with mean grain radius of 261 and 601 µm, the change in specific surface area associated to an increase in porosity is lower than the measurement incertitude.
For a close packing of spheres with a monodisperse size distribution, the specific surface area s can be computed using

$$s = \frac{3(1-\varphi)\ln(1-\varphi)}{a} \tag{3.3}$$

where φ is the porosity and a the pore radius [m], a function of porosity (Torquato, 2002). Using this equation, the specific surface area was derived for different pore size functions. The evolution of the pore radius with porosity $a(\varphi)$ was computed using the known grain radius distributions of the synthetic samples (Chapter 2) using the method outlined by Wadsworth et al. (2016). The experimental specific surface data follow the general trend in the modelled porosity-specific surface curves. According to the model predictions, the mean pore radius of synthetic samples with a mean grain radius of 601, 261 and 112 µm varies in the ranges 51–137 µm, 23–60 µm and 10–26 µm for a porosity between 0.03 and 0.35.

3.3 Physical properties of sintered glass beads

3.3.2 Elastic wave velocity

3.3.1.1 Experimental procedure

P- and S-waves are compressional and shear waves, respectively, the velocity of which depends on the elastic properties of the rock in which they propagate. The velocity of elastic P- and S- waves in the sintered samples was obtained by measuring the travel time of waves through the samples, which dimensions are known. Measurements were performed using a device, schematised in Figure 3.2 (Heap et al., 2014), that includes a generator to create periodic signals with a certain frequency and an oscilloscope to record the transmitted and received signals, according to the procedure described in the following. Frequencies of 700 kHz and 300 kHz were used to measure P-waves and S-waves velocity, respectively.

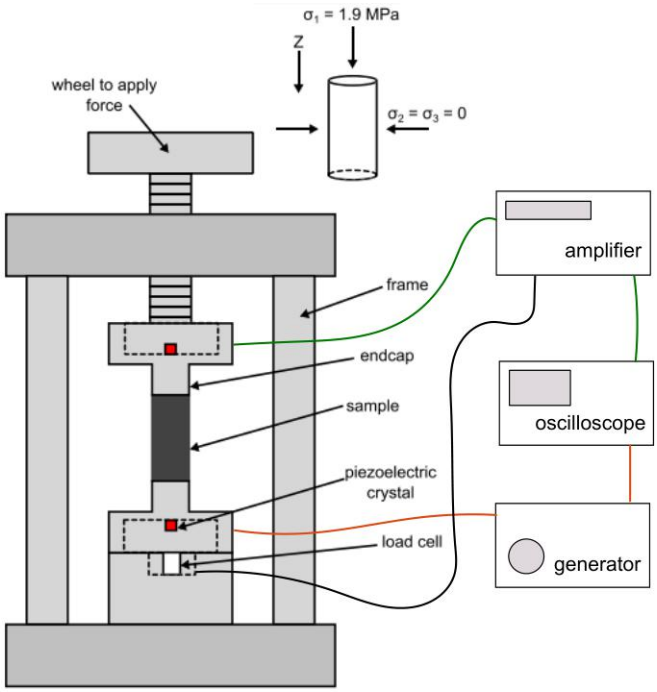

Figure 3.2 Schematics of the experimental device for wave velocity measurements (adapted from Heap et al., 2014). Frequencies of 700 and 300 kHz were used to measure P- and S-waves velocity, respectively.

The sample is placed in a jig between two metal endcaps connected to the transmitting and receiving sensors (piezoelectric ceramic crystals). A load cell is embedded in the bottom endcap of the jig so that a constant contact force of 300N can be applied to the samples for all measurements. The electrical signal is transformed by the transmitter into a sine wave distortion, which propagates through the sample and is conversely transformed by the receiver into a sinusoidal voltage, displayed on the oscilloscope. The travel time between the emission of the signal and its reception can be measured on the oscilloscope and used, with the sample dimensions, to derive the wave velocity. P- and S-wave velocity were measured on dry synthetic samples with porosity in the range 0.026–0.38 and mean grain radius between 24 and 601 μm.

3.3.1.2 Results: comparison to natural sandstones and model predictions

Dry P- and S-wave velocities are presented as a function of porosity in Figure 3.3. Overall, velocity decreases linearly as a function of porosity. Figure 3.3 shows data for monodisperse synthetic samples with mean grain radius between 24 and 601 μm and data for polydisperse synthetic samples, which degree of polydispersivity is $S = 0.89$, with a mean grain radius of 226 μm. The negative linear trend in porosity-velocity is the same for all samples, whatever

the degree of polydispersivity and mean grain radius. Therefore, our data show that P- and S-wave velocity of the synthetic samples does not depend on the grain size distribution but is controlled by porosity. Moreover, the trend in porosity-velocity is in excellent agreement with that predicted by the equation of Raymer et al. (1980)

$$V = (1 - \varphi)^2 . V_{solid} + \varphi . V_{fluid} \quad (3.4)$$

using P- and S-wave velocity in quartz and air for V_{solid} and V_{fluid}. The wave velocity values for the synthetic samples are also compiled with data from the literature for Fontainebleau sandstone (Bourbie & Zinszner, 1985; Zamora & Poirier, 1990). The observed velocities for synthetic samples follow the same trend than that for Fontainebleau, which are slightly lower for a given porosity (Figure 3.3).

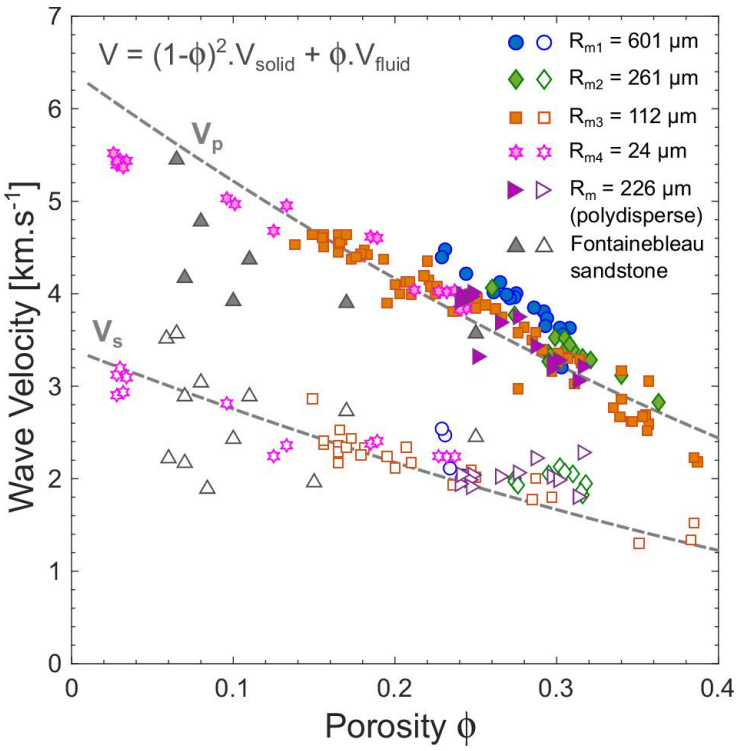

Figure 3.3 Porosity dependency of P- (solid symbols) and S-wave (open symbols) velocity in monodisperse synthetic samples with a mean grain radius of 601 (blue circles), 261 (green diamonds), 112 (orange squares) and 24 (pink stars), polydisperse synthetic samples (degree of polydispersivity S = 0.89) with a mean grain radius of 226 µm (purple right triangles) and

Fontainebleau sandstone samples (grey triangles) (Bourbie & Zinszner, 1985; Zamora & Poirier, 1990). Grey dashed lines are modelled porosity-velocity curves for V_p and V_s derived using the equation of Raymer et al. (1980) (equation 3.4).

3.3.2 Thermal conductivity

3.3.2.1 Experimental procedure

Thermal conductivity κ, in [W.(m.K)$^{-1}$], quantifies the ability of a material to conduct heat (Gustafsson, 1991). Thermal conductivity measurements were performed on a suite of synthetic samples with porosity of 0.17-0.36 and mean grain radius of 112–601 μm, using a Hot Disk TPS 500 Thermal Constants Analyser. The experimental device is presented in Figure 3.4 (Heap et al., 2022). Measurements required the use of pairs of samples with similar attributes (porosity and grain size). Samples were placed on top of one another, with the Hot Disk sensor placed between the plane surfaces of the samples and held using a specifically designed assembly clamping the samples together to ensure the sensor was in close contact with both sample surfaces. The sensor consists in a 10 micron-thick nickel foil insulated on both sides by a 30 micron-thick Kapton, connected to a computer so that measurements can be conducted using the Hot Disk program. Each measurement consists in transmitting a thermal pulse with a chosen power and duration to the system through the sensor (Gustavsson et al., 1994). The parameters depend on the sample and were found using a trail-and-error method.

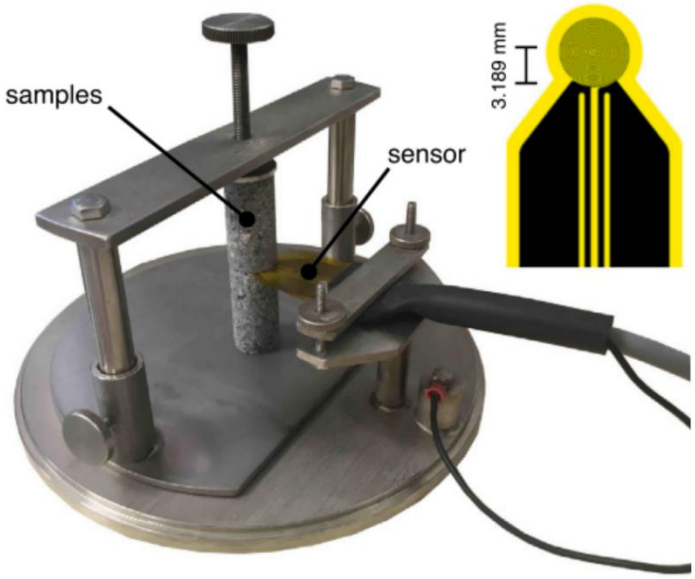

Figure 3.4 Experimental setup for thermal conductivity measurements. The sensor used, made of 10 µm-thick nickel foil spirals encased and insulated with 30 µm-thick kapton, is placed between two samples with similar microstructural attributes. The assembly is tightened using the screw on top on the set-up (Heap et al., 2022).

3.3.2.2 Results: comparison to natural sandstones and model predictions

The thermal conductivity of synthetic samples as a function of porosity is presented in Figure 3.5. Overall, the thermal conductivity values vary in a very small range around 0.5 $W.mK^{-1}$. The experimental data do not allow to observe a porosity-dependency for the thermal conductivity of sintered glass bead samples. Moreover, for a given porosity, changing the grain radius does not significantly change the thermal conductivity. This might be explained by the very low thermal conductivity of the soda-lime silica glass which compose the synthetic samples, for the variations of thermal conductivity with porosity and/or grain radius are smaller than the incertitude on the measurements. For comparison, Figure 3.5 includes thermal conductivity data for Fontainebleau sandstone samples (Zamora et al., 1993).

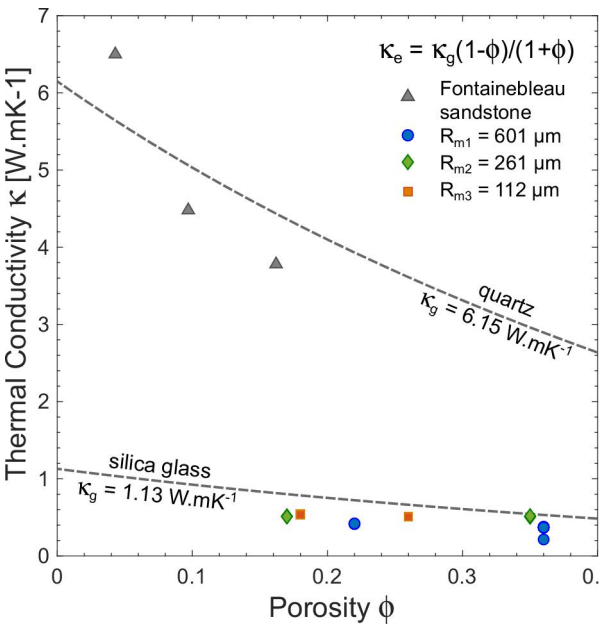

Figure 3.5 Dry thermal conductivity as a function of porosity for the synthetic samples with mean grain radius of 601 (blue circles), 261 (green diamonds) and 112 (orange squares) µm and Fontainebleau sandstone samples (Zamora et al., 1993). Grey dashed lines are model predictions for the porosity-thermal conductivity curves computed using the Rayleigh–Maxwell equation (equation 3.5) for quartz and the soda-lime silica glass of the synthetic samples.

In addition, modelled porosity-thermal conductivity curves were also computed using the Rayleigh-Maxwell equation

$$K_e = K_g \frac{1-\varphi}{1+\varphi} \tag{3.5}$$

where K_e and K_g are the thermal conductivities of the equivalent medium and the solid constituant. Using values of 1.13 and 6.15 W.mK^{-1} for silica glass (SiLiBeads resources, Annex 1) and quartz (Heap et al., 2019), which synthetic samples and Fontainebleau sandstone are respectively composed entirely of the Rayleigh-Maxwell equation provides a good description of the experimental data, for both Fontainebleau and the glass bead data. Such result is in agreement with Heap et al. (2020) who used a similar effective medium approach to describes the thermal conductivity data for a range of andesites with different pores sizes and found that the modelled curve described the experimental data perfectly, also suggesting that porosity is the first-order control.

3.3.3 Electrical conductivity

The electrical conductivity σ , in [S.m^{-1}], quantifies the ability of a material to transport electric charges. For most common crustal rocks, the measured electrical conductivity is the

sum of the contribution of the pore-fluid conductivity σ_w and of the surface conductivity σ_s, which result from the concentration of extra charges in the vicinity of the pore-fluid interface - hence proportional to the specific surface area. The effective conductivity can therefore be written (Waxman & Smits, 2003)

$$\sigma = \frac{1}{F}\sigma_w + \sigma_s \tag{3.6}$$

with F the formation factor, an intrinsic property which depends on the rock microstructure and can be derived using Archie's law:

$$F = \varphi^{-m} \tag{3.7}$$

with m the cementation exponent (Guéguen & Palciauskas, 1994).

3.3.3.1 Experimental procedure

The procedure for measuring the electrical conductivity of the suite of samples for a given solution conductivity is presented in the following. Prior to measurement, samples are covered with isolation tape to prevent electrical conduction along the sample surface and loss of fluid during the measurement. Then, samples are saturated with a solution of water and NaCl (in nine different concentrations depending on the targeted solution conductivity), in which they are left to equilibrate for at least two weeks. Electrical conductivity is measured using a WTW LF2000-type conductivity meter connected to electrodes excited at a constant frequency of 4 kHz, under room pressure-temperature conditions. The solution conductivity is measured first and then, the conductivity of each sample σ is measured using a specifically designed device which consists in a frame with two spring-loaded electrodes to ensure that the force applied to the sample between the electrodes is constant. Once the conductivity of all samples is measured at a given conductivity, samples are dried, washed by saturation with distilled water and dried again.

Electrical conductivity measurements were performed on a suite of monodisperse synthetic samples with porosity in the range 0.026–0.291 and mean grain radius in the range 24–601

µm, saturated with solutions of increasing NaCl concentrations, corresponding to fluid conductivities in the range 100–1740 µS.cm^{-1}.

3.3.3.2 Results: comparison to natural rocks and model predictions

The synthetic samples electrical conductivity is plotted against the solution conductivity in Figure 3.6(a) for samples with a mean grain radius of 24 and 112 µm and porosity values of 0.026–0.29. At a given porosity, the sample conductivity increases positively and linearly with the solution conductivity. According to equation 3.6, the slope of the linear fit to the data gives the inverse of the formation factor F and the intercept with the y-axis gives the surface conductivity σ_s, which is close to zero. Values for F were derived from the experimental data and are plotted as a function of porosity in Figure 3.6(b). For comparison, experimental data from the literature for Fontainebleau sandstone (Gomez et al., 2010; Revil et al., 2014; Saadi et al., 2017) are compiled with data for the synthetic samples. The formation factor values for the synthetic samples follows a power law of porosity, in agreement with what was reported for Fontainebleau sandstone. Using Archie's law (equation 3.7), the cementation exponent m was estimated to fall between 1.3 and 2, with the best-fit achieved for m = 1.7, for synthetic samples and Fontainebleau sandstone samples. More generally, cementation factor values in the range 1.5–2.5 were reported for natural sandstones (Guéguen & Palciauskas, 1994). The excellent agreement between the dataset, with a surface conductivity close to zero, obtained using synthetic samples with what was reported for natural sandstones shows the suitability of sintered glass beads as sandstone analogues in terms of geometry of the porous network. In the following, results from electrical conductivity measurements are used to extend this comparison in terms of another transport property, permeability.

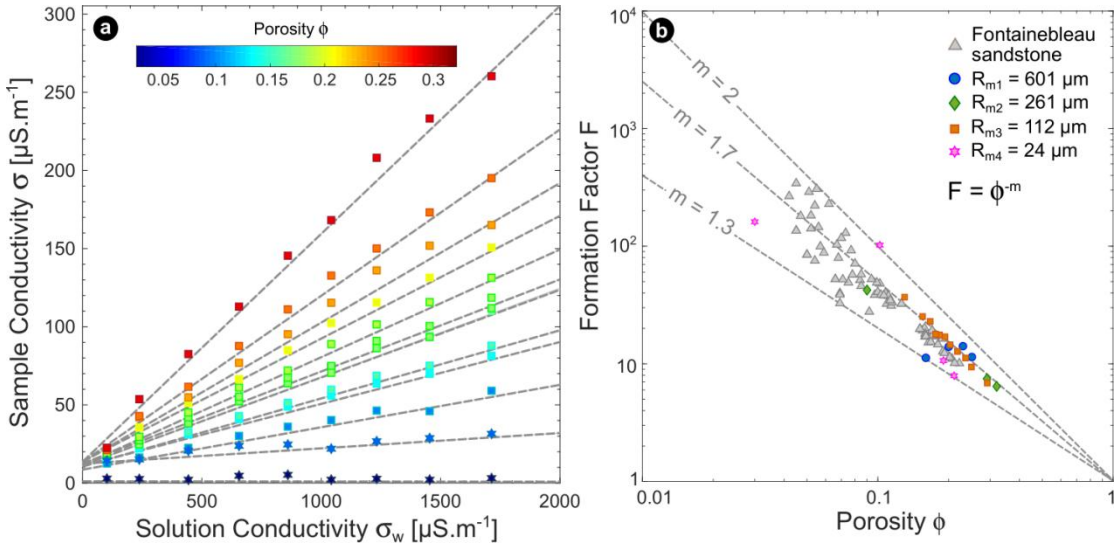

Figure 3.6 Electrical conductivity of the synthetic samples. (a) Synthetic sample conductivity σ as a function of solution conductivity σ_w for samples with porosity of 0.026–0.29 and mean grain radius of 24 (star) and 112 (square) µm, fitted by linear regression (grey dashed line). (b) The slope of the linear fit gives the inverse of the formation factor F, which is related to porosity through Archie's law (equation 3.7). F values determined for the synthetic samples are compiled with data for Fontainebleau sandstone (Gomez et al., 2010; Revil et al., 2014; Saadi et al., 2017). The best-fit to the data using Archie's law yielded a value of 1.7 for the cementation factor m for Fontainebleau sandstone and the synthetic rocks.

3.3.4 Gas-permeability

3.3.4.1 Experimental procedure

Permeability k, in [m^2] but also often in Darcy [D], quantifies how easily fluids flow through a rock. The permeability of synthetic samples was measured using a benchtop gas permeameter, schematised in Figure 3.7 (Farquharson et al., 2016) in a steady state set-up. All measurements were conducted on oven-dry samples, using nitrogen and under a confining pressure P_c of 1 MPa (to prevent leaking of the pore fluid around the sides of the sample). The permeability measurements were performed according to the procedure described in the following, with references to the different elements of the set-up using the indices in Figure 3.7.

Prior to measurement, the sample to be measured was jacketed with insulation tape and inserted in a silicon rubber jacket (with an internal diameter of 20 mm and external diameter of 25 mm), assembly then placed into a tubular Viton jacket (7). After the sample was mounted in the pressure vessel (4), the upstream (2) and downstream platens (9) were screwed until both spreader plates (3)(8) are touching the extremities of the sample.

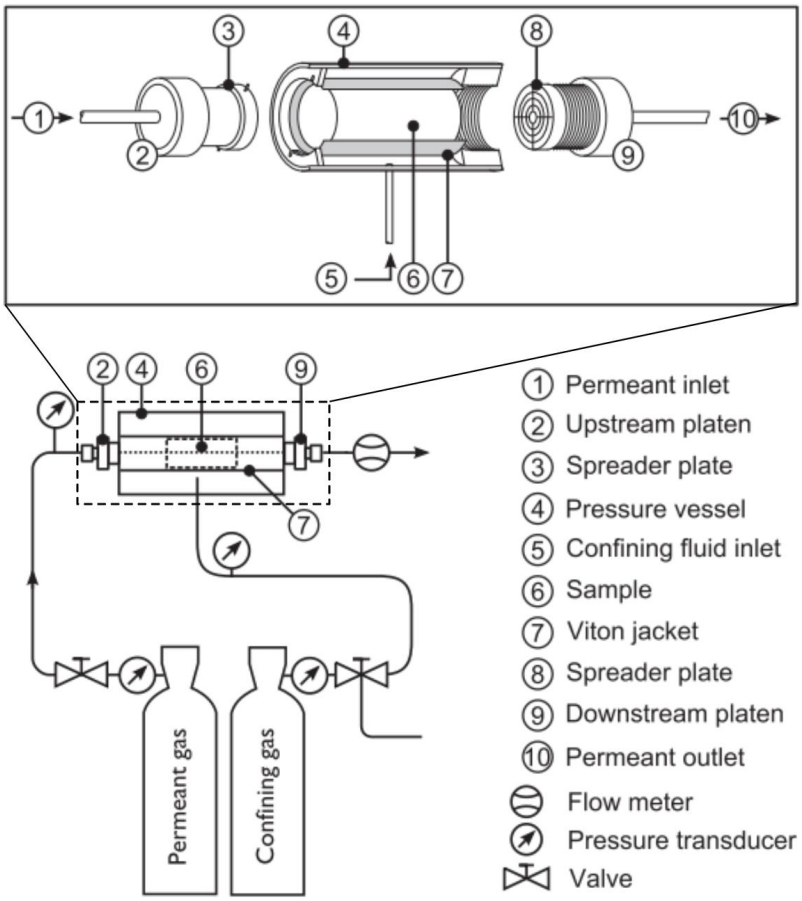

Figure 3.7 Schematics of the benchtop steady state permeameter used in this work (not to scale) (modified from Farquharson et al., 2016). Nitrogen was used as both permeant (pore fluid) and confining gas. Using the indices (1–10) to refer to the different parts of the set-up, a detailed description of the experimental procedure for the permeability measurements is given in the main text.

Then, the confining pressure was increased to the target value and the system was left to equilibrate for at least 1 hour. Then, a flow of permeant gas (nitrogen) in the sample was

created by imposing a pressure gradient to the sample. The pressure gradient ΔP is the difference between the upstream pore fluid pressure P_u and the downstream pore fluid pressure P_d, which, in this set-up, is simply the atmospheric pressure (P_d = 101,325 Pa). The resulting flow was characterised in terms of the volumetric flow rate Q_v, monitored using a gas flowmeter positionned downstream from the sample (Figure 3.7). For the steady state method, the volumetric flow rate was measured for several pressure gradients ΔP and, for each value, Darcian permeability k_D was derived using:

$$k_D = \frac{Q_v}{P_m \Delta P} \frac{\mu L P_d}{A} \tag{3.8}$$

(Heap et al., 2017) with $P_m = \frac{1}{2}(P_u + P_d)$ the mean pore fluid pressure, μ the pore fluid viscosity (1.76×10^{-5} at 20°C for nitrogen), L the sample length and A the sample cross-section area.

This method allowed for correcting the Darcian permeability measurements from artefacts which may have arisen due to turbulent flow, i.e., the Forchheimer effect, and/or gas slippage along flow channel walls, i.e., the Klinkenberg effect. If the Forchheimer correction is required, the trend in $\frac{1}{k_D}$ for each ΔP against the corresponding Q_v is linear positive, i.e.,

$$\frac{1}{k_D} = aQ_v + b \tag{3.9}$$

with a a positive integer. The corrected permeability k_{forch} is equal to the inverse of the y-intercept of the best-fit linear regression of the data, i.e., $k_{forch} = \frac{1}{b}$.

When the Forchheimer correction is required, the need to correct for the Klinkenberg effect is evaluated by deriving k_{forch} for each ΔP and plotting k_{forch} against $\frac{1}{P_m}$. A correction for the Klinkenberg effect must be applied if the trend in the data is linear positive, i.e., if

$$k_{forch} = c\frac{1}{P_m} + d \tag{3.10}$$

with c a positive integer. The corrected permeability k_{klin} is given by the y-intercept of the best-fit linear regression of the data, i.e., $k_{klin} = d$.
When the Forchheimer correction is not required, data are to be corrected from the Klinkenberg effect if the trend in k_D against $\frac{1}{P_m}$ is linear positive, i.e., if

$$k_D = e\frac{1}{P_m} + f \tag{3.11}$$

with e a positive integer. In that case, the corrected permeability k_{klin} is given by the y-intercept of the best-fit linear regression of the data, i.e., $k_{klin} = f$.

Permeability was measured on monodisperse synthetic samples with porosity of 0.06–0.38 and mean grain radius between 24 and 601 µm. Permeability values over 10^{-11} m^2 could not be measured accurately, for they are above the maximum permeability measurable using the set-up previously described.

3.3.4.2 Results: comparison to natural sandstones

The permeability of the synthetic samples, presented in Figure 3.8, increases as porosity is increased, for all mean grain radius. Moreover, at a given porosity, increasing the mean grain radius increases the permeability. For samples with a mean grain radius of 24 µm, the permeability ranges from $4\text{x}10^{-14}$ m^2 for a porosity of 0.06 to $7\text{x}10^{-13}$ m^2 for a porosity of 0.23. For samples with a porosity of 0.18, the permeability increases from $4\text{x}10^{-13}$ m^2 for a mean grain radius of 24 µm to $2\text{x}10^{-12}$ m^2 for a mean grain radius of 261 µm.
Comparing the data for synthetic samples with that reported by Bourbié and Zinszner (1985) for Fontainebleau sandstone samples, an overlap is observed between the permeability values for synthetic samples with a mean grain radius of 261 µm and that for Fontainebleau, which grains have a mean grain radius of approximately 250 µm. Such compilation also emphasises that, for a given grain radius, the slope in the porosity-permeability curve decreases significantly above a porosity of approximately 0.12. The existence of two families with different porosity-permeability laws was also reported by Bourbié and Zinszner (1985) for Fontainebleau sandstone. Such an observation can be explained by an increase in the

percentage of the pore space which is part of the conduction process, due to increasing pore sizes and pore entry radii, with porosity (Fredrich et al., 1995).

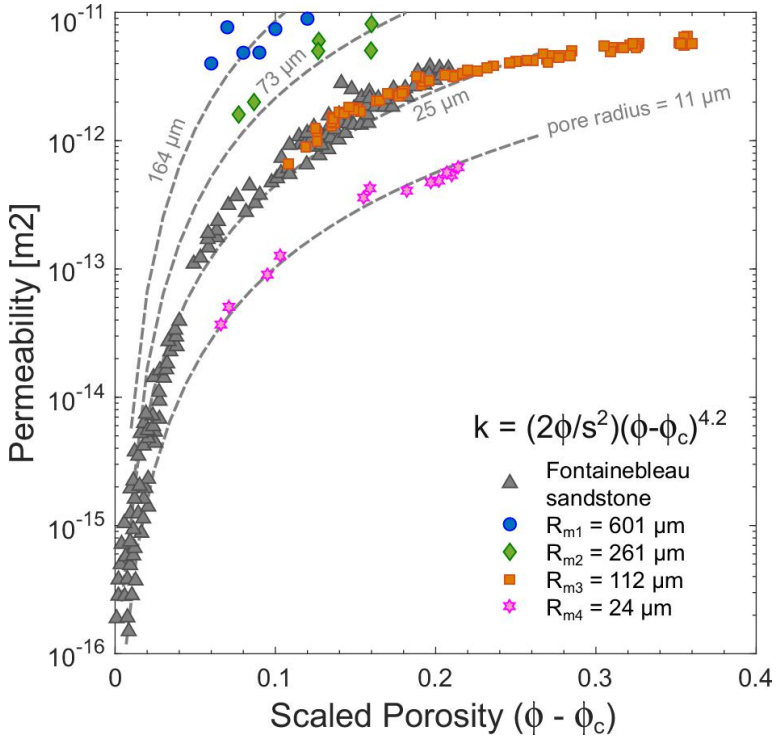

Figure 3.8 Permeability evolution with porosity for monodisperse synthetic samples with mean grain radius of 601 (blue circles), 261 (green diamonds), 112 (orange squares) and 24 (pink stars) µm and Fontainebleau sandstone samples (grey triangles; Bourbié & Zinszner, 1985). Grey dashed lines are model predictions for the porosity-permeability curves computed using equation 3.9 (Wadsworth et al., 2016). The specific surface (parameter s) was derived for different mean pore radius, indicated next to each modelled curve (equation 3.3).

To explore this observation further, the experimental data were compiled with modelled porosity-permeability curves derived from

$$k_D = \frac{2\varphi}{s^2}(\varphi - \varphi_c)^{4.2} \qquad (3.12)$$

(Martys et al., 1994; Wadsworth et al., 2016) where φ_c is the percolation threshold (taken to be 0.03 for sintered glass bead samples, Wadsworth et al., 2016). The specific surface s was

derived for the four grain radii tested and the effective pore radius values that give the best fit between the modelled curves and the experimental data are given in Figure 3.8.
The excellent fit between the permeability dataset for the synthetic samples and that for Fontainebleau sandstone and the general agreement of the data with the model presented shows the suitability of sintered glass beads as analogues for well-sorted sandstones in terms of microstructural geometries.

3.3.4.3 Results: comparison to permeability models

Several approaches have been proposed to model permeability using parameters related to microstructural geometries. Equivalent medium permeability models consider an idealised porous medium in which the microstructural attributes contributing to the permeability process can be described in terms of a characteristic length. The equivalent channel model considers that the porous medium in which the fluid flows is populated by cylindrical tubes or cracks which size control the transport process (Baud et al., 2017; Walsh & Brace, 1984). Further, the model predicts that the mean hydraulic radius r_h is related to the permeability and the formation factor by

$$r_h = \sqrt{bkF} \tag{3.13}$$

where b is a geometrical parameter between 2 and 3 for a tube and a crack geometry, respectively. Permeability as a function of the formation factor was computed for the synthetic samples for which F could be derived using electrical conductivity results (see section 3.3.3). Modelled curves are compiled with experimental data in Figure 3.9. A value of 2 was used for the parameter b, because the void space in the synthetic samples is best described by "tubes" rather than "cracks". For a given mean grain radius, experimental data are well described using a constant value for the hydraulic radius for all porosity values. The hydraulic radius values providing the best fit to the experimental data were estimated at 14.9, 7.8 and 2.7 µm for monodisperse synthetic samples with a mean grain radius of 261, 112 and 24 µm, respectively.

Mathematically, the hydraulic radius r_h is also defined as the ratio of the pore volume and the pore surface (Guéguen & Palciauskas, 1994). Using the specific surface measurements on the synthetic samples and the previous definition, r_h values of 7.11 and 13.33 µm were estimated for synthetic samples with a mean grain radius of 112 and 261 µm. The equivalent channel model predictions and the values derived from specific surface measurements are in good agreement. Therefore, according to these results, grain radius and hydraulic radius are positively and linearly correlated: increasing the grain radius by a factor of two increases the hydraulic radius by a factor of two, approximately.

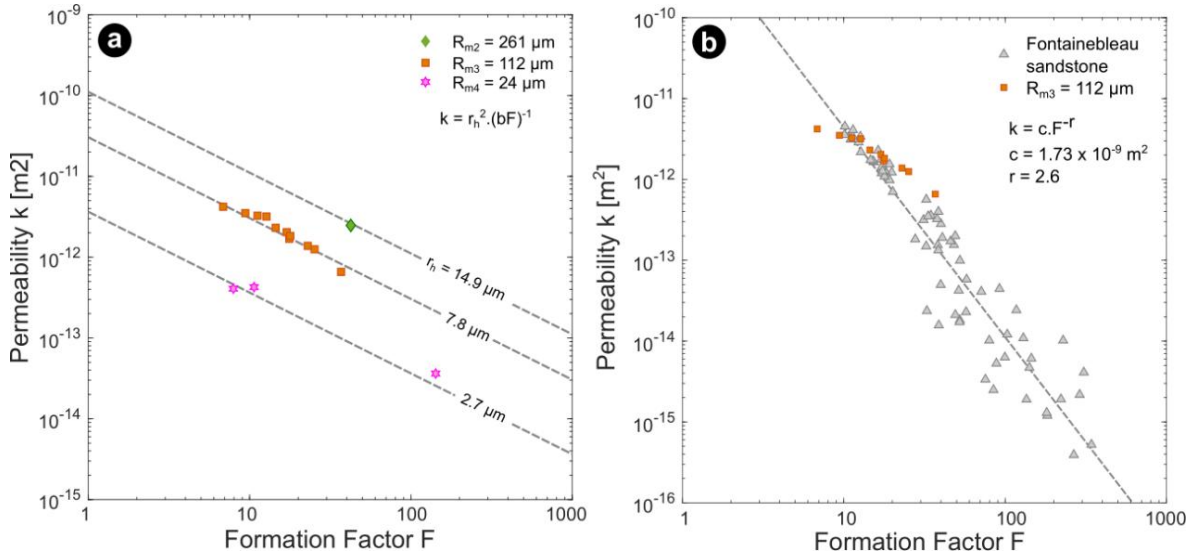

Figure 3.9 Evolution of permeability as a function of the formation factor for synthetic samples with a mean grain radius of 261 (green diamonds), 112 (orange squares) and 24 (pink stars) µm. Experimental data for F were derived using the results of electrical conductivity measurements (Figure 3.6). (a) Modelled formation factor-permeability curves (dashed grey line) were computed using the equivalent channel model (equation 3.13). The value of hydraulic radius r_h providing the best fit between the model and the data are written on each corresponding curve. (b) Experimental data for monodisperse synthetic samples with a mean grain radius of 112 µm are compared to results reported for Fontainebleau by Revil et al. (2014).

A power law dependence on the formation factor for permeability was also reported for Fontainebleau sandstone by Revil et al. (2014). In Figure 3.9(b), the results for monodisperse

synthetic samples with a mean grain radius of 112 µm are compiled with those reported for Fontainebleau. Revil et al. (2014) found that a value of 2.6 for the parameter r provided the best-fit to the experimental data for Fontainebleau, which is close to the theoretical value of 3 (Revil et al., 2014). Although the range of formation factor-permeability values of the synthetic samples is not broad enough to test the model against, the sintered glass bead data appear to fall on a close trend to that for Fontainebleau (Figure 3.9(b)).

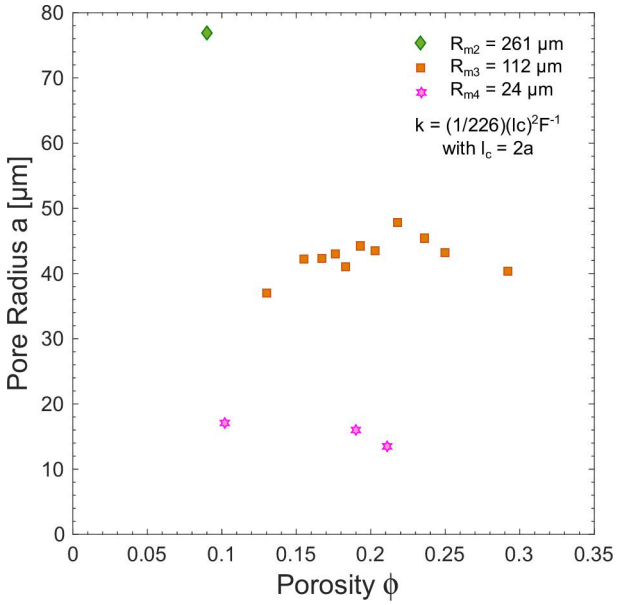

Figure 3.10 Porosity dependency of the pore radius of monodisperse synthetic samples with mean grain radius of 261 (green diamond), 112 (orange squares) and 24 (pink stars) µm. Values were derived using the permeability model of Katz and Thompson (1986) (equation 3.14).

The evolution of permeability as a function of the formation factor can also be studied using the analysis of percolation in a porous medium of Katz and Thompson (1986), which states that

$$k = \frac{1}{226} l_c^{\,2} F^{-1} \qquad (3.14)$$

where another characteristic length parameter is introduced, the critical diameter of the throat allowing percolation, l_c [m]. Using this model, l_c was computed for the synthetic samples. Figure 3.10 shows the model predictions as the pore radius ($a = l_c/2$) evolution with porosity. According to the model of Katz and Thompson (1986), at a fixed grain radius, the pore radius of the synthetic rocks does not vary significantly, even when porosity decreases

from 0.30 to 0.15. However, a significant difference in pore radius is predicted for synthetic samples with the same porosity but a different grain size: at a porosity of approximately 0.1, increasing the grain radius from 24 to 261 μm increases the pore radius by more than a factor of 4. In order to verify these results, mercury injection capillary pressure analysis could be performed on the synthetic samples in the future.

3.4 Procedures for the deformation experiments

Results from several types of deformation experiment are presented throughout this thesis. To avoid redundancy, the procedure used to achieve the state of stress applied for each type of deformation test is detailed in the following. The mechanical data for hydrostatic and triaxial compression tests conducted on monodisperse and polydisperse synthetic samples will be presented later, in Chapter 4 and Chapter 5, respectively, for they constitute the results upon which the studies presented in these chapters are based.

3.4.1 Experimental apparatus and sample preparation

As mentioned in Chapter 1, the convention adopted is that the difference between the confining pressure and the pore pressure gives the effective pressure: $P_e = P_c - P_p$. This simple effective pressure law is operative for the failure of sandstones under static conditions, as shown by Baud et al. (2015) in the brittle and ductile regimes. The effective mean stress is given by the difference between the mean stress and the pore pressure: $P = (\sigma_1 + 2\sigma_3)/3 - P_p$ and the differential stress is given by the difference between the maximum and the minimum principal stresses $Q = \sigma_1 - \sigma_3$. Conventionally, compressive stress and compactive strain, i.e., shortening for axial strain and decreasing volume for volumetric strain, are taken to be positive.

Experiments were performed in the triaxial testing apparatus of the Ecole et Observatoire des Sciences de la Terre, schematised in Figure 3.11 (Farquharson et al., 2017). The main elements of the apparatus are the pressure cell and three independent circuits: (1) the confining pressure circuit, filled with kerosene which can be raised to high pressure to provide the confining pressure (Figure 3.11(c)); (2) the pore pressure circuit, filled with water which pressure can be raised to provide the pore pressure (Figure 3.11(b)) and (3) the axial pressure

circuit which consist in an axial steel piston which can be advanced in the axial direction (downward) to provide the axial pressure (Figure 3.11(a)).

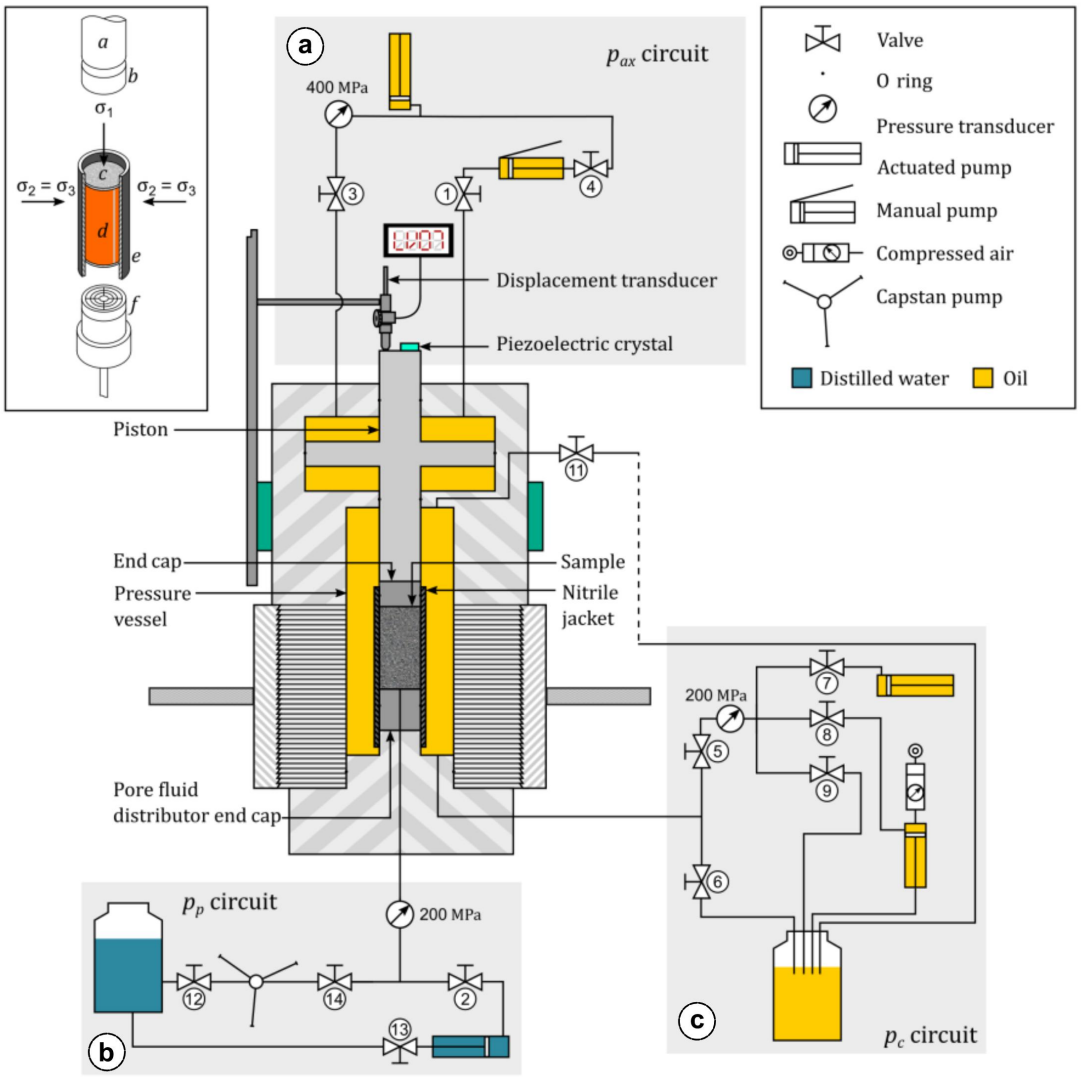

Figure 3.11 Schematics of triaxial press used in this work (not to scale) (Farquharson et al., 2017). The apparatus allows for independently controlling the (a) axial pressure, the (b) pore pressure, i.e., the pressure of the fluid (water) in the pore space of the sample deformed, and the (c) confining pressure, i.e., the pressure in the fluid (kerosene) surrounding the sample.

Computer-controlled stepping motors allow for independently regulating the confining pressure, pore fluid pressure and axial stress. During all tests, a linear variable differential transformer monitored the position of the piston, thus giving access to displacement, and a pressure probe in the axial pressure circuit provided a measurement of the applied axial force.

Using the initial dimensions of the sample, axial stress and strain were obtained. Porosity change was also provided by the conversion of pore volume change given by the displacement of the piston in the pore pressure intensifier. Finally, acoustic emission (AE) activity was recorded using a USB AE Node from Physical Acoustics and a piezoelectric transducer (a micro80 sensor from Physical Acoustics with a bandwidth of 200–900 kHz) attached to the lower piston. AE activity was monitored using the software AEwin with a detection threshold for an AE hit at 28 dB.

Prior to testing, samples were dried under vacuum for at least 48 hours. Then, to preserve bulk sample cohesion following deformation (so that thin sections could be prepared) and to avoid disking, the samples were encased in very thin (<1 mm thick) copper foil jackets. If the tests were to be performed in saturated conditions, samples were then saturated under vacuum using de-aired and deionised water. For all the experiments, samples were positioned between two steel endcaps. For experiments on water-saturated samples, the bottom endcap used has a concentric hole at the centre to allow for fluid access to the pore pressure system. In addition, a thin highly permeable filter, made from coffee filter paper, was placed between the bottom endcap and the sample to prevent broken beads from infiltrating the pore pressure piping during the experiments. The previous assembly was placed into a 0.3 mm-thick Viton jacket, which ensures separation between the sample and the confining pressure fluid and mounted into the cell of the triaxial apparatus.

3.4.2 Hydrostatic compression experiments

During hydrostatic experiments, the principal stresses are equal in all directions, that is, the state of stress is $\sigma_1 = \sigma_2 = \sigma_3$. All hydrostatic tests were performed at room-temperature on water-saturated samples, using a fixed pore pressure P_p of 10 MPa. Data were acquired with a sampling period of 10 s. First, the confining pressure and the pore pressure were increased at a rate of 3×10^{-5} MPa.s^{-1} to 12 and 10 MPa, respectively, corresponding to an effective pressure P_e of 2 MPa. Then, the effective pressure was increased in small steps until reaching a threshold value corresponding to the stress required for the onset of grain crushing P^* (Zhang et al., 1990) or the upper pressure limit of the press at P_c = 200 MPa. At each step, the system was left to equilibrate before increasing the confining pressure further.

Microstructural equilibrium was assumed to be achieved when the rate of the pore volume change was lower than 10^{-2} s^{-1}. The amount by which P_e was increased at each step varied from 1 to 10 MPa depending on the time necessary to reach microstructural equilibrium at the previous step. At the end of the test, P_c and P_p were slowly lowered to zero and the deformed sample was carefully removed from the experimental set-up.

3.4.3 Triaxial compression experiments

During triaxial experiments, an axial stress is superimposed onto a hydrostatic pressure. The principal stress parallel to the axis of the sample is higher than the principal stresses normal to this axis, that is, the state of stress is $\sigma_1 > \sigma_2 = \sigma_3$. All triaxial tests were performed at room-temperature on water-saturated samples, using a fixed pore pressure P_p of 10 MPa. Data were acquired with a sampling period of 1s. First, the sample was placed in an environment of hydrostatic pressure by increasing the confining pressure and pore pressure to their target value using the servo-controlled pumps. The system was left to equilibrate overnight at the resulting effective pressure. Then, at constant effective pressure, the sample was loaded as the upper piston was lowered at a fixed servo-controlled rate corresponding to a nominal strain rate of 10^{-5} s^{-1}. Considering the range of permeabilities of the synthetic samples (from 10^{-13} to 10^{-11} m^2, measured at a P_c of 1 MPa), the strain rate applied during triaxial compression was low enough to ensure drained conditions (i.e., the product of the strain rate and the Darcy timescale $Da = tD\varepsilon = \mu_f L^2/(k\Delta P)$ is much less than unity (Heap & Wadsworth, 2016), i.e., the deformation of the samples proceeded at a rate lower than the response time of the pore pressure intensifier. At the end of each test, samples were unloaded at the same rate than loading, the confining and pore pressures were slowly decreased to zero and samples were carefully removed from the experimental apparatus.

3.5 Uniaxial compressive strength of the synthetic rock

3.5.1 Experimental procedure

A uniaxial compression experiment consists of applying an axial stress onto an unconfined sample. The state of stress is such that the second and third principal stresses, σ_2 and σ_3

respectively, are zero and the maximum principal stress σ_1 is progressively increased. All uniaxial tests were performed at room-temperature and samples were loaded by advancing the piston in the axial direction at a fixed displacement rate corresponding to a strain rate of 10^{-5} s^{-1}. Sample were deformed up to macroscopic failure and the uniaxial compressive strength (UCS) was defined as the peak stress on the stress-strain curve (as shown on Figure 3.12(a)).

3.5.2 Results: mechanical data and microstructure

A representative stress-strain curve for a uniaxial test on a synthetic sample is presented in Figure 3.12(a). When a synthetic sample is deformed under uniaxial compression, the stress-strain curve typically shows three domains (Figure 3.12(a)), similar to what was reported for natural sandstones (Baud et al., 2014): (1) the elastic domain, during which strain increases linearly with stress - sometimes preceded by a non-linear elastic phase attributed to the reorganisation of grains by rotation and sliding - (2) the inelastic domain, during which microcracks initiate and propagate (as indicated by the AE activity) and (3) the failure domain, during which the stress reaches a peak value (σ_p, the UCS of the rock) and microcracks coalesce and form a macroscopic fracture that signals the failure of the sample.

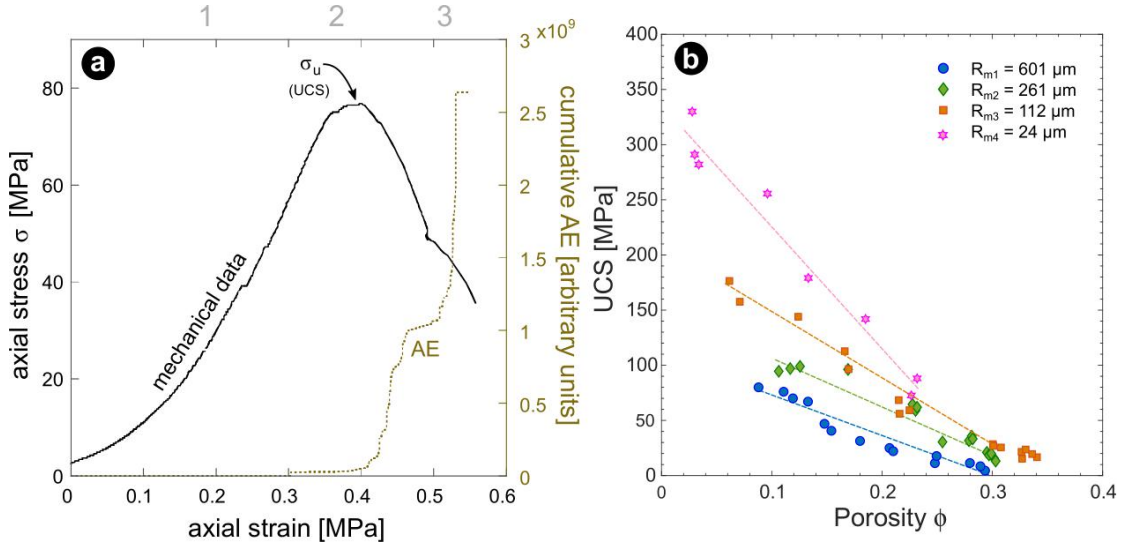

Figure 3.12 (a) Representative mechanical data for the axial stress change with axial strain during uniaxial deformation of a synthetic sample with a porosity of 0.11 and mean grain radius of 601 µm. The peak stress at brittle failure is marked σ_u. The cumulative acoustic

emissions are plotted for the same axial strain. (b) Evolution of the uniaxial compressive strength (UCS) with porosity, for samples of different mean grain radius.

Plots of UCS as a function of porosity of the synthetic samples, with mean grain radius of 24–601 μm, are presented in Figure 3.12(b). Several observations can be made regarding the porosity dependency of UCS of monodisperse sintered glass bead samples. First, broadly speaking, the strength of the synthetic samples is a negative function of porosity, suggesting that the decrease in porosity that accompanies granular densification leads to strength increase. For example, for synthetic samples with a mean grain radius of 24 μm, UCS increases from 88 to 330 MPa as porosity decreases from 0.23 to 0.03. Secondly, the experimental UCS dataset suggests that the decrease in UCS with porosity is linear. This observation will be discussed in below by adopting a micromechanical approach. Finally, all else being equal, grain radius also exerts an influence on the UCS of the synthetic samples. Overall, UCS increases when the mean grain radius decreases. Indeed, for synthetic samples with a porosity of 0.13, increasing the mean grain radius from 24 to 601 μm decreases UCS from 179 to 67 MPa.

All synthetic samples deformed under uniaxial compression failed in a brittle manner. However, different deformation features at the grain-scale were observed depending on the sample porosity. SEM images of synthetic samples deformed up to the peak stress are presented in Figures 3.13 and 3.14. The synthetic samples deformed under uniaxial compression can be discriminated into two families, for which microcracks formed under compression initiate and propagate very differently: those with a microstructure close to granular packing, that typically have a porosity higher than 0.20-0.24 and within which adjacent spherical glass beads are interconnected by necks (Figure 3.13), and those with a non-granular microstructure, that typically have a porosity below 0.14-0.18 and for which pores are isolated (Figure 3.14).

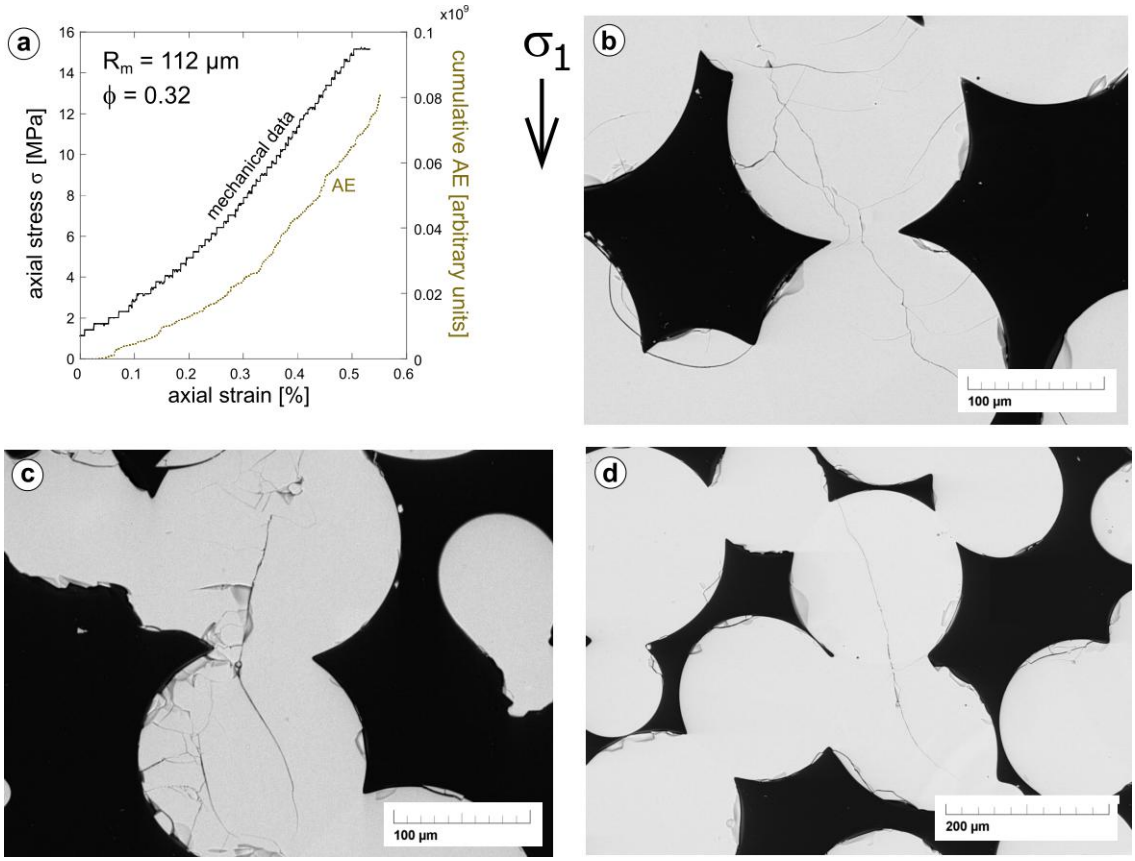

Figure 3.13 (a) Mechanical data and (b)(c)(d) scanning electron micrographs for a synthetic sample with a porosity of 0.32 and mean grain size of 112 µm deformed under uniaxial compression up to an axial strain of approximately 0.5%. The microstructure shows that microcracks initiate at grain-to-grain contacts and form Hertzian fractures.

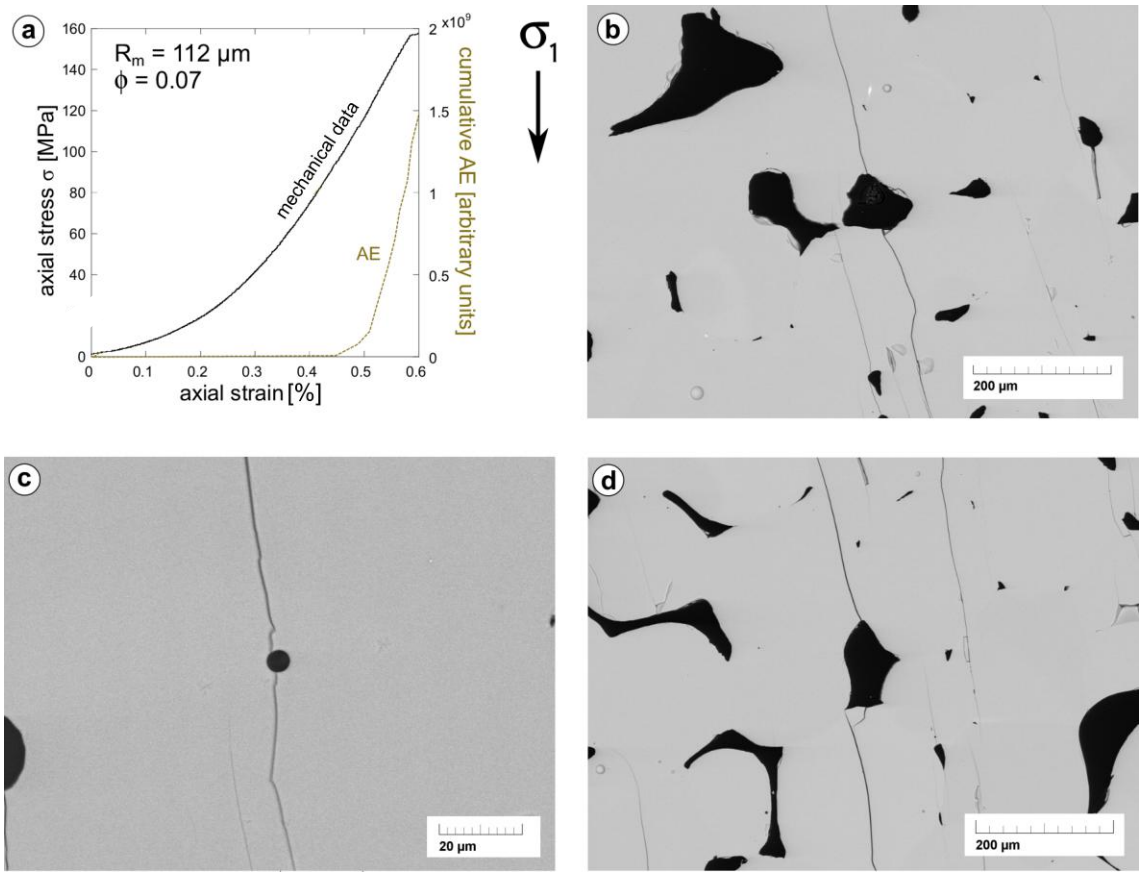

Figure 3.14 (a) Mechanical data and (b)(c)(d) scanning electron micrographs for a synthetic sample with a porosity of 0.07 and mean grain size of 112 µm deformed under uniaxial compression up to an axial strain of approximately 0.6%. The microstructure shows pore-emanated microcracks growing from the poles of pores.

At high porosity, microcracks are found to have developed in the form of radiating fans originating at grain-to-grain contacts (Figure 3.13). Within highly damage areas, the length of microcracks reaches the diameter of the grains which then become comminuted. At low porosity, microcracks have grown from the boundary of pores in a direction parallel to the applied stress (Figure 3.14). In highly damage areas, the microcracks coalesce into larger fractures. Contrary to the wide spatial distribution of damage in high-porosity synthetic samples, damage anisotropy is obvious in the low-porosity samples where pore-emanated cracks develop. Observed microcracks also appear to be shorter in the high-porosity samples than in the low-porosity samples as they are restricted to the diameter of the grains.

3.5.3 Micromechanical interpretation

Under uniaxial compressive stress, natural rocks fail by development of a macroscopic fracture formed by coalesced microcracks. To predict the bulk strength of rocks, it is critical to understand from where in the microstructure and how individual microcracks initiate and propagate. Based on experimental observations, micromechanical models have been developed for the analysis of damage evolution. Sammis and Ashby (1986) derived the pore-emanated crack model which was often used to analyse and interpret UCS datasets (Baud et al., 2014). The PECM is presented in Chapter 1. It belongs to the 'inclusion' model family, which considers a microstructure modelled as discrete void spaces with known dimensions (e.g., spherical pores) embedded in a solid continuum.

Since microstructural observations on some of the deformed synthetic showed pore-emanated cracks (Figure 3.14), the analytical prediction of the pore-emanated crack model (equation 1.2) was compared to the UCS experimental dataset. Using a value of 0.7 MPa.m$^{1/2}$ for the K_{Ic} of soda-lime glass (SiLiBeads resources) in equation (1.2), modelled curves for different values of the pore radius a were computed and tested against the experimental data in Figure 3.15.

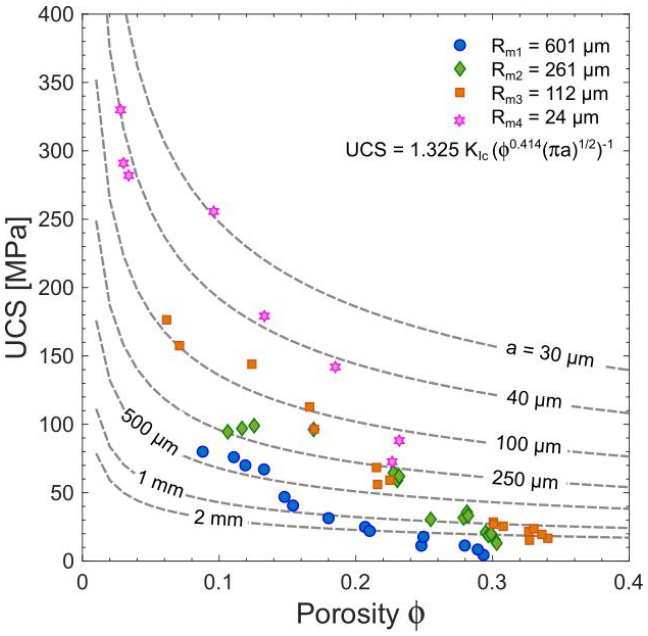

Figure 3.15 Experimental results for UCS for synthetic samples with mean grain radius of 601 (blue circles), 261 (green diamonds), 112 (orange squares) and 24 (pink stars) µm

compared with theoretical predictions of the pore-emanated crack model (Equation 1.2; Sammis & Ashby, 1986).

The data seem to follow the type curve predicted by the model at low porosity. The pore radius values inferred from the model range from 30 to 500 μm, for porosity values between 0.026 and 0.14 and grain radii between 24 and 601 μm. However, above a porosity of approximately 0.14-0.18, the experimental data show a different trend than that predicted by the pore-emanated crack model. Indeed, as stated before, the UCS of the synthetic samples decreases linearly whereas the modelled UCS follows a power law of porosity so that the slope in the modelled curves is much higher at low porosity than at high porosity. The apparent discrepancy at high porosity might be due to a change in the pore radius and/or a change in the micromechanism. In addition, the microstructure of the synthetic samples at high porosity is not consistent with the microstructural foundation of the pore-emanated crack model, i.e., spherical pores embedded in an elastic continuum. Indeed, from high-porosity to low-porosity, the synthetic samples used in this work evolve from a microstructure dominated by spherical grains to one dominated by spherical pores, i.e., from a granular microstructure to a non-granular microstructure (Chapter 2), which corresponds to that considered in inclusion models such as the pore-emanated crack model. Moreover, the microstructural data show differences in the spatial distribution of grain-scale damage in high-porosity and low-porosity samples: whilst a strong stress-induced anisotropy is observed at low porosity, intragranular crack growth in high-porosity appear more isotropic. This is in agreement with the results of Wu et al. (2000) who used stereological techniques to quantify stress-induced damage in several rocks deformed in the brittle regime. For sandstone, they in particular showed significant anisotropy in Darley Dale sandstone of 0.13 porosity and no significant anisotropy in deformed Berea sandstone of 0.21 porosity. Such an observation supports the idea that the pore-emanated crack model, which predicts anisotropic deformation (Paterson & Wong, 2005), is appropriate for the sintered glass bead samples to interpret low-porosity UCS data only. Finally, at high porosity, the microstructural observations made on deformed samples suggest that the failure micromechanism is not pore-emanated cracking. The microcracks grow from the grain-to-grain contacts and are limited in length to the grain diameter (Figure 3.13). Therefore, tensile stress concentrations locate at the grain contacts, which length might thus be the characteristic length controlling the failure process.

Occurrences of isolated clusters of Hertzian fractures and intragranular crack arrays were also reported in natural sandstones deformed in the brittle regime (Menéndez et al., 1996; Wu et al., 2000). Finally, given the granular microstructure of high-porosity synthetic samples, a granular model may be more appropriate to interpret the UCS data of these samples.

3.5.4 Comparison to natural rocks

A comparison of UCS data for synthetic samples with a compilation of UCS data for natural rocks from the literature is presented in Figure 3.16. Overall, the trend in porosity-UCS for synthetic and natural rocks is similar and values found for the strength of synthetic samples span a comparable range than that for natural sandstones. However, at similar porosity and grain size, differences in strength are observed between synthetic and natural rocks. These discrepancies might be explained by differences in the cement content, clay content or pore and grain size distribution, among other microstructural parameters.

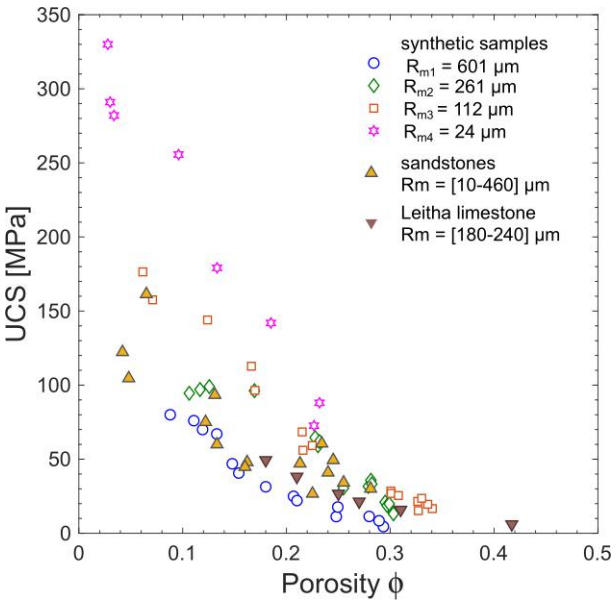

Figure 3.16 Compilation of UCS data for synthetic samples (open symbols) and natural rocks (Baud et al., 2014, 2017) (solid symbols). UCS results are shown as a function of porosity.

For Leitha limestone, a carbonate rock found over a broad range of porosity and grain sizes which pore space is predominantly made of macropores, Baud et al. (2017) also reported a

quasi-linear decrease of strength with porosity up to a porosity of 0.30. The high-porosity Leitha limestone samples have a lower cement content and a more granular microstructure than the low-porosity ones. Such transition to a more granular microstructure at high porosity is somehow similar to that observed in sintered glass bead samples, for which UCS also decreases linearly with porosity. However, due to the paucity of microstructural data for high-porosity rocks deformed under uniaxial compression, the previous results cannot be compared to those for other porous rocks. New microstructural data are therefore needed to test the following hypothesis: the deviation from the pore-emanated model prediction at high porosity may result from a change in the microstructural attribute which controls strength from the pore size to the grain size.

3.6 Concluding remarks

The work conducted in this thesis is based on the use of synthetic samples made by viscous sintering. To assess the suitability of these sintered glass bead samples as analogues for porous rocks, a variety of petrophysical properties were measured: porosity, specific surface, P- and S-wave velocity, thermal conductivity, electrical conductivity, gas-permeability and uniaxial compressive strength.
In the above, the procedures used to conduct these measurements are presented, along with the results for synthetic samples with porosity of 0.026–0.38 and various grain size distributions. A comparison of these results with datasets for natural rocks, in particular with Fontainebleau sandstone, a monomineralic well-sorted natural rock found over a broad range of porosity values, and with theoretical models allowed to establish that:

- overall, physical properties found for the monodisperse synthetic samples span a comparable range than that found for monomineralic well-sorted natural sandstones such as Fontainebleau sandstone;

- the consistency of the results obtained for the transport properties of the synthetic samples with those reported for natural sandstones demonstrate the suitability of sintered glass bead samples as analogues for natural rocks in terms of geometry of the pore space;

- the consistency of the results obtained for the strength of the synthetic samples with that reported for natural sandstones demonstrate the suitability of sintered glass bead samples as analogues for natural rocks in terms of mechanical behaviour.

In the next chapters, the mechanical properties of sintered glass bead samples are studied more extensively, for the cases of monodisperse (Chapter 4) and polydisperse samples (Chapter 5), and the results obtained are used to address issues such as the influence of porosity, mean grain size or dispersivity on the mechanical behaviour and failure modes of natural porous rocks.

Chapter 4

Mechanical Compaction of Monodisperse Porous Synthetic Rocks

The focus of this chapter is the influence of porosity and mean grain size on the mechanical compaction of monodisperse porous synthetic rocks. Further, given the previously established suitability of sintered glass beads as analogues for porous crustal rocks - natural sandstones in particular, the implications for the mechanical behaviour of natural rocks are discussed.

The data and conclusions of this chapter are published as: Carbillet, L., Heap, M. J., Baud, P., Wadsworth, F. B., & Reuschlé, T. (2021). Mechanical compaction of crustal analogs made of sintered glass beads: The influence of porosity and grain size. Journal of Geophysical Research: Solid Earth, 126, e2020JB021321. https://doi. org/10.1029/2020JB021321

4.1 Introduction

The mechanical compaction of porous materials is an important process in the Earth's crust. It is one of the main deformation mechanisms of lithification, diagenesis, fault growth, and/or sealing, and plays a key role in many processes in sedimentary settings such as reservoirs, aquifers, and basins (Bjørlykke, 2006; Guéguen & Boutéca, 2004; S. K. Taylor et al., 2008), and in volcanic settings (Farquharson et al., 2017; Grunder & Russell, 2005; Quane et al., 2009). Understanding the phenomenology and micromechanics of compaction rests upon the ability to characterise the evolution of microstructure through compactant deformation. To predict the occurrence and extent of mechanical compaction, knowledge of the relationship between rock microstructural attributes and bulk mechanical properties is crucial. Indeed, the effective macroscopic properties of heterogeneous materials such as crustal rocks intricately

depend on the phases present, their volume fraction, their spatial distribution, and their properties (e.g., Torquato, 2002). Therefore, relating microstructural attributes of porous rock to bulk properties has been the focus of numerous studies in the past decades, the majority of which relied on direct experimental measurements or numerical simulations (Blair et al., 1993; Doyen, 1988; Eberhart-Phillips et al., 1989; Ghazvinian et al., 2014; Schöpfer et al., 2009; Scott & Nielsen, 1991).

As early as 1990, it had already been suggested the two principle microstructural controls on the mechanical and hydraulic properties of sedimentary rocks were (1) porosity and (2) grain size (Bourbie & Zinszner, 1985; Paterson & Wong, 2005; Rutter & Glover, 2012; Zhang et al., 1990). But the scatter on compiled experimental data remains large (Baud et al., 2014; Chang et al., 2006) as trends in plots of strength as a function of porosity or grain size are complicated by the fact that other microstructural parameters, such as pore size and shape, their distributions, or matrix composition, change together with porosity and grain size. This chapter sets out to investigate the deconvolved influence of porosity and grain size on the mechanical compaction of porous rocks using synthetic samples with monodisperse grain size distributions. In particular, the following questions are addressed: mechanically speaking, how do the sintered glass beads samples compare with natural sandstones? All else being equal, what is the influence of grain size and porosity on mechanical compaction? Considering the importance of compaction bands in the fields of rock mechanics, hydrology, and geology, could this failure mode be reproduced in synthetic samples?

4.2 Preparation and characterisation of the synthetic samples

4.2.1 Viscous sintering of monodisperse populations of glass beads

Chapter 2 provides a detailed description of the viscous sintering process and of its use to prepare variably porous synthetic samples. Three sets of samples with monodisperse populations of glass spheres of diameter between 0.15 and 0.25 mm, 0.4 and 0.6 mm, or 1 and 1.3 mm were prepared following the "block" method described in Chapter 2. The corresponding grain diameter distributions are presented in Figure 4.1(a).

4.2.2 Description of the sintered glass beads samples

A photograph of one of the synthetic samples is provided as Figure 4.1(b). Insights into the microstructure of the synthetic samples were gained using polished thin sections observed under a scanning electron microscope (SEM) (Figure 4.1(c)(d)).

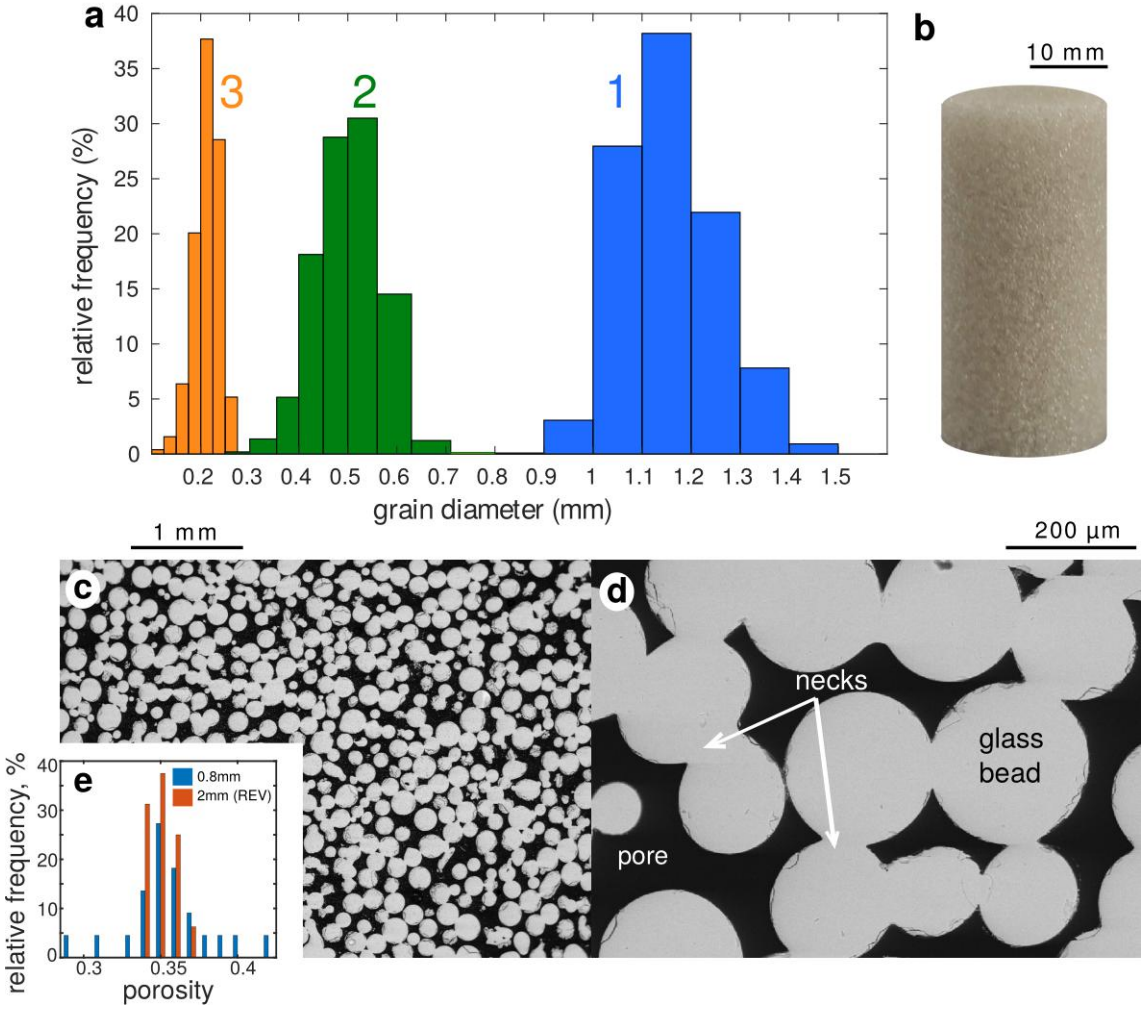

Figure 4.1 Microstructural description of the synthetic samples. (a) Grain diameter distributions corresponding to the different mean grain diameter considered, 3: 0.15-0.25 mm (orange), 2: 0.4-0.6 mm (green), 1: 1.0-1.3 mm (blue). Although these distributions are not technically monodisperse but monomodal, the term monodisperse is used to describe the samples. (b) Photograph of a synthetic sample with a porosity of 0.35 and a mean grain diameter of 0.2 mm and (c) corresponding scanning electron micrograph of its microstructure (black: porosity, grey: glass). (d) Scanning electron micrograph showing the necks that have grown between initially adjacent beads during sintering. (e) 2D porosity distributions

measured for the same sample using a window with a 0.8 mm edge-length (blue) or with a 2 mm edge-length (representative elementary volume, red) using image processing program ImageJ. Frequencies cluster around 0.35, which corresponds to the porosity measured in laboratory.

The SEM images were acquired on a polished slice of a sample with a porosity of 0.35 and a mean grain diameter of 0.2 mm. The lowest porosity obtained in this study is 0.22. Therefore, all the samples are in the range between high porosity – close to the initial packing porosity where incipient sintering has only formed necks – and intermediate porosity – where sintering has progressed and begun to close the pore network. This chapter does not encompass low porosity synthetic rocks which exhibit pore structures close to isolated pores in a glass medium (Chapter 2). Thus, all the samples are in the upper range of porosity encompassed by natural granular rocks.

Similar to what was presented in Chapter 2, the monodisperse synthetic samples used for this study present porosity clusters. Using square windows of 0.8 mm of edge-length and of 2mm of edge-length, 2D porosity measurements were performed on SEM images of intact samples (using ImageJ). The square window with an edge-length of 2 mm ensures a representative element volume (REV), and the square window with an edge-length of 0.8 mm allows for better understanding whether there are variations in porosity on a smaller scale. Figure 4.1(e) presents histograms of the distributions of 2D porosity measurements obtained for the zoomed-out SEM image in Figure 4.1(c). While porosity measurements performed in the larger window provide a monomodal distribution closely clustered around 0.35, porosity measurements performed in the smaller window yield local values up to 0.42 in a sample with an average porosity of 0.35. In addition, the absence of cement is accompanied by heterogeneities in the local grain contacts geometry, as previously reported by den Brok et al. (1997). The previous analysis of the microstructure of an intact monodisperse synthetic samples (as well as that presented in Chapter 2) demonstrated that samples are homogeneous as these random variations in the microstructure occur on length scales much less than the sample lengths.

4.3 Experimental procedures

To study mechanical compaction, a suite of mechanical tests was conducted on sintered glass bead samples. Hydrostatic and triaxial compression experiments were performed. Although the focus here is compaction, a few triaxial tests at relatively low pressure were also conducted to identify the brittle-ductile transition. A summary of all the experiments is provided in Table 4.1. All experiments were conducted at the Ecole et Observatoire des Sciences de la Terre (EOST) in Strasbourg (France) at room temperature on water-saturated synthetic samples following the procedure presented in Chapter 3.

Table 4.1 Experimental conditions and mechanical data of the synthetic samples tested in this study. Triaxial tests were conducted at nominal strain rates of 10^{-5} s^{-1}.

Sample	Porosity	+/- (mean error = 0.005)	Confining pressure P_c (MPa)	Pore pressure P_p (MPa)	Effective pressure $P_{eff} = P_c - P_p$ (MPa)	Peak stress σ_v		Yield stress C*	
						P (MPa)	Q (MPa)	P (MPa)	Q (MPa)
mean grain diameter 1.15 mm									
1814	0.181	0.004	-	-	0	10	30	-	-
1812	0.183	0.003	40	10	30	-	-	92	185
1816	0.189	0.004	60	10	50	-	-	115	194
1412	0.271	0.005	30	10	20	38	55	-	-
1414	0.265	0.005	70	10	60	-	-	80	59
1419	0.262	0.005	100	10	90	-	-	105	45
1413	0.269	0.005	130	10	120	-	-	132	35
1411	0.271	0.005	160	10	150	-	-	159	28
114012	0.294	0.006	-	-	0	1.4	4.3	-	-

114013	0.302	0.006	40	10	30	36	17	-	-
114011	0.308	0.006	70	10	60	74	43	-	-
1314	0.294	0.006	100	10	90	-	-	102	35
1313	0.303	0.006	130	10	120	-	-	128	23
114016	0.294	0.006	-	10	hydrostatic	-	-	*P**	
								156	0
mean grain diameter 0.5 mm									
2317	0.255	0.005	-	-	0	10	31	-	-
23111	0.249	0.005	40	10	30	74	132	-	-
2316	0.256	0.005	70	10	60	-	-	92	97
2318	0.258	0.005	110	10	100	-	-	133	100
2313	0.263	0.005	160	10	150	-	-	177	80
2314	0.256	0.005	190	10	180	-	-	200	60
22114	0.299	0.006	-	-	0	20	7	-	-
2218	0.302	0.006	30	10	20	-	-	40	59
27312	0.304	0.006	50	10	40	-	-	61	63
22111	0.292	0.006	70	10	60	-	-	83	70
27314	0.295	0.006	90	10	80	-	-	99	58
27315	0.294	0.006	110	10	100	-	-	117	52
22213	0.301	0.006	120	10	110	-	-	125	45
27313	0.299	0.006	130	10	120	-	-	133	39
2213	0.299	0.006	150	10	140	-	-	152	36
2217	0.296	0.006	170	10	160	-	-	168	23
27311	0.295	0.006	-	10	hydrostatic	-	-	P*	

								173	0
mean grain diameter 0.2 mm									
31012	0.225	0.005	-	-	0	20	59	-	-
31713	0.220	0.004	40	10	30	-	-	87	172
31013	0.222	0.004	70	10	60	-	-	130	212
37	0.226	0.005	90	10	80	-	-	150	212
31113	0.256	0.005	70	10	60	-	-	109	147
31110	0.266	0.006	130	10	120	-	-	177	170
311	0.262	0.005	160	10	150	-	-	200	150
31114	0.255	0.005	190	10	180	-	-	225	135
3813	0.300	0.005	40	10	30	68	115	-	-
3814	0.307	0.006	70	10	60	-	-	92	95
3413	0.305	0.006	130	10	120	-	-	146	77
3411	0.299	0.006	190	10	180	-	-	200	61
3311	0.346	0,007	30	10	20	-	-	35	46
3612	0.353	0.008	50	10	40	-	-	58	55
339	0.351	0.008	70	10	60	-	-	74	42
3314	0.356	0.007	90	10	80	-	-	91	33
3312	0.357	0.008	-	10	hydrostatic	-	-	*P**	
								118	0
3710	0.385	0.009	40	10	30	-	-	37	22
379	0.387	0.009	50	10	40	-	-	46	19
3711	0.385	0.007	60	10	50	-	-	54	13
3712	0.382	0.007	-	10	hydrostatic	-	-	*P**	

	69	0

4.4 Mechanical data

In the following, compressive stress and compactive strain, i.e., shortening for axial strain and decreasing volume for volumetric strain, will be conventionally taken as positive. The maximum and minimum applied principal compressive stresses are referred to as σ_1 and σ_3, respectively, the differential stress as $Q = \sigma_1 - \sigma_3$ and the effective mean stress as $P = (\sigma_1 + 2\sigma_3)/3 - P_p$.

4.4.1 Results of the hydrostatic and triaxial tests

Representative data for the mechanical response of sintered glass bead samples to hydrostatic loading are presented in Figure 4.2. The hydrostatic experiment was conducted on a synthetic sample with a porosity and mean grain diameter of 0.38 and 0.2 mm (3714 in Table 4.1) and the mechanical data are plotted alongside the corresponding AE activity (dashed purple). The grey dashed curve in Figure 4.2 presents the mechanical data from an experiment performed on a sample with a very similar porosity and the same grain diameter to show the reproducibility (3712 in Table 4.1).

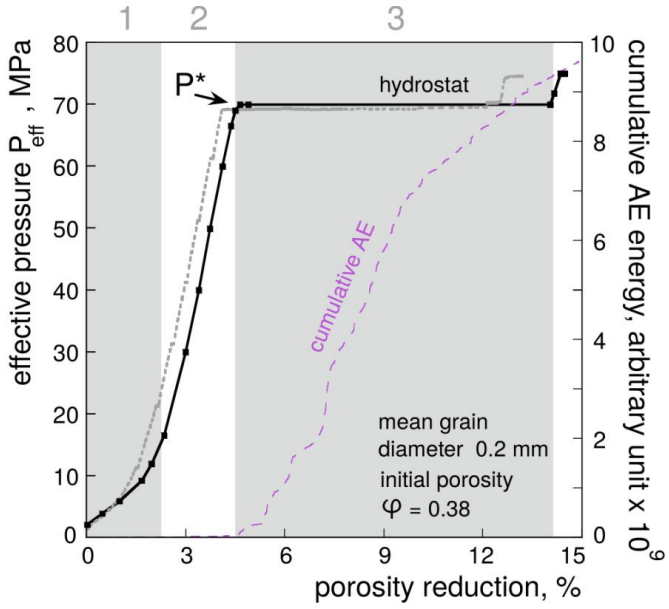

Figure 4.2 Representative mechanical data (black line) and cumulative acoustic emission energy (purple dashed line) for hydrostatic tests performed on the synthetic samples. These data were obtained on synthetic samples of mean grain diameter of 0.2 mm and initial porosity of 0.38. The critical stress for the onset of grain crushing P* is indicated by an arrow. The porosity reduction in percentage corresponds to the absolute loss of porosity, i.e., a porosity reduction of 14% refers to a drop from 0.38 to 0.24. (1) When P_{eff} is first increased, porosity decreases non-linearly as a result of grains rearrangements. (2) As P_{eff} is increased further, the sample undergoes elastic deformation until P_{eff} reaches the critical value P* beyond which (3) the sample porosity decreases suddenly and significantly by grain crushing (inelastic deformation).

The porosity reduction in percentage corresponds to the absolute loss of porosity. In Figure 4.2, the hydrostats present the following characteristic phases. (1) The initial evolution of porosity with increasing effective pressure is non-linear. The duration of this first stage varies from sample to sample, as demonstrated by the difference between the black and the grey curves, and is positively correlated to porosity. (2) The second phase consists of a linear decrease of porosity as a function of increasing effective mean stress, which is characteristic of poroelastic behaviour. Almost no AEs are recorded during the initial non-linear and linear

portions of the hydrostatic experiment (Figure 4.2). However, a sudden increase in cumulative AE, associated with a sharp breaking point in the mechanical data, indicated as P*, marks the transition to (3) a third phase characterised by a large decrease in porosity (of about 0.1) at constant effective pressure. For siliciclastic rock, this inflection on the hydrostat followed by a large porosity reduction is characteristic of inelastic compaction by delocalised grain crushing (Zhang et al., 1990), P* therefore represents the critical stress for the onset of grain crushing. After equilibrium of the system has been reached for the critical state of stress P*, further increase of the effective stress is accompanied by hardening. Samples submitted to hydrostatic loading (up to the maximum capability of the pressure cell, i.e., P_c = 200 MPa) presented effective pressure-porosity reduction curves similar to the hydrostats presented in Figure 4.2.

Triaxial compression experiments were conducted at effective pressures P_{eff} ranging from 20 to 180 MPa and, depending on the effective pressure P_{eff}, led to either brittle or ductile failure. A representative curve for the mechanical data and AE activity corresponding to failure by dilatancy and shear fracture formation (i.e., brittle behaviour) is presented in Figure 4.3. The stress-strain curve can be divided into three parts. (1) First, the axial strain increases linearly with the differential stress and very few AEs are recorded. (2) Second, a sudden increase in the AEs accompanies a small decrease in the slope of the stress-strain curve, which corresponds to the onset of dilatancy (Figure 4.3). (3) Finally, as the AE bursts, the differential stress reaches a peak (marked as σ_v) and then drops to a residual value. Among the synthetic samples deformed under triaxial conditions, samples of porosity below 0.26 demonstrated brittle behaviour up to effective pressures of 30 to 60 MPa, depending on their grain diameter. The peak stresses σ_v for samples deformed in the brittle regime are compiled in Table 4.1.

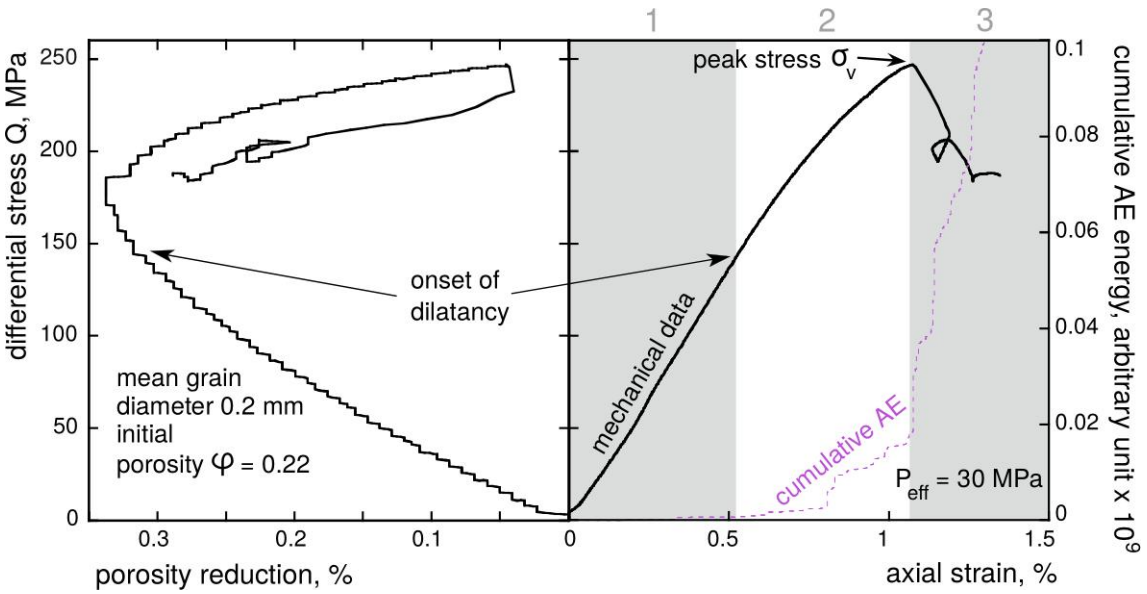

Figure 4.3 Representative mechanical data (black lines) and cumulative acoustic emission energy (purple dashed line) for triaxial tests performed in the brittle regime. The triaxial test presented was performed at P_{eff} = 30 MPa on a synthetic sample of mean grain diameter of 0.2 mm and initial porosity of 0.22. The peak stress σ_v is indicated by an arrow. The porosity reduction in percentage corresponds to the absolute loss of porosity, i.e., a porosity reduction of 0.4% refers to a drop from 0.22 to 0.216. (1) When loading is first applied, the sample undergoes elastic axial strain and porosity decreases linearly. (2) The transition to the inelastic stage of deformation takes place at the onset of dilatancy and, as Q is increased further, it eventually reaches (3) a critical peak stress σ_v at which point brittle failure takes place and the stress drops to a residual value.

Figure 4.4 shows the third type of mechanical data obtained in this study, i.e., mechanical data for triaxial tests conducted on synthetic samples at relatively high confinement and which failed by shear-enhanced compaction. On Figure 4.4, the stress-strain curve can be delimited into two main portions. (1) As the sample is first loaded, axial strain increases linearly with differential stress and no AEs are recorded. (2) Then, a subtle decrease in the slope of the stress-strain curve takes place as the AEs start to increase at the onset of shear-enhanced compaction C* (Wong et al., 1997). Finally, the stress-strain curve reaches a plateau punctuated by stress drops that correlate to spikes in the AEs. These stress drops are

suggestive of the formation of compaction bands (Baud et al., 2004). All samples deformed in the range of effective pressures corresponding to shear-enhanced compaction demonstrated such stress drops, sometimes accompanied by strain hardening. The critical stresses C* for samples deformed in the ductile regime are compiled in Table 4.1.

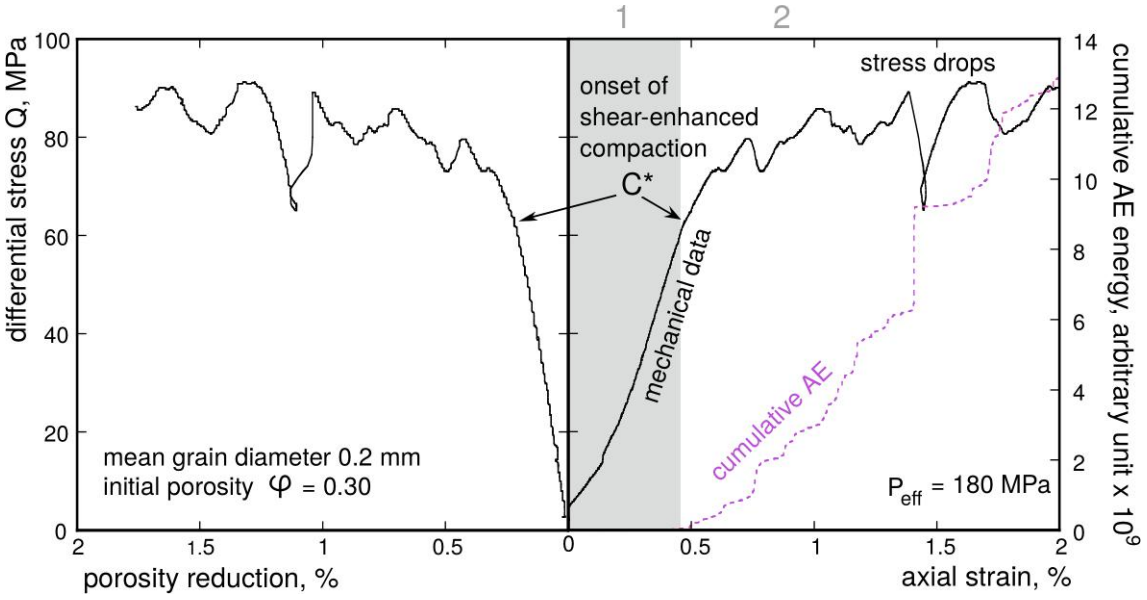

Figure 4.4 Representative mechanical data (black lines) and cumulative acoustic emission energy (purple dashed line) for triaxial tests performed in the regime of shear-enhanced compaction. The triaxial test presented was performed at P_{eff} = 180 MPa on a synthetic sample of mean grain diameter of 0.2 mm and initial porosity of 0.30. The critical stress for the onset of shear-enhanced compaction C* is indicated by an arrow. The porosity reduction in percentage corresponds to the absolute loss of porosity, i.e., a porosity reduction of 2% refers to a drop from 0.30 to 0.28. (1) Axial strain increases and porosity decreases linearly as loading is first applied. (2) The transition to the inelastic stage of deformation takes place as Q reaches the critical value C* for the onset of shear-enhanced compaction.

An overview of the mechanical data collected for this study is presented in Figure 4.5. Mechanical data for triaxial experiments are compiled with the corresponding hydrostatic pressurisation curves, for samples of porosity ranging from 0.18 to 0.38 and for mean grain diameters of 1.15 (blue), 0.5 (green) and 0.2 (orange) mm. At low and high effective pressures, the mechanical data present the phases described for Figure 4.3 and Figure 4.4,

respectively. The mechanical data for triaxial compression follow the hydrostat in the poroelastic domain. The deviation from the hydrostat marks the transition to inelastic deformation, either by dilatancy (increase in porosity) or by shear-enhanced compaction (porosity reduction).

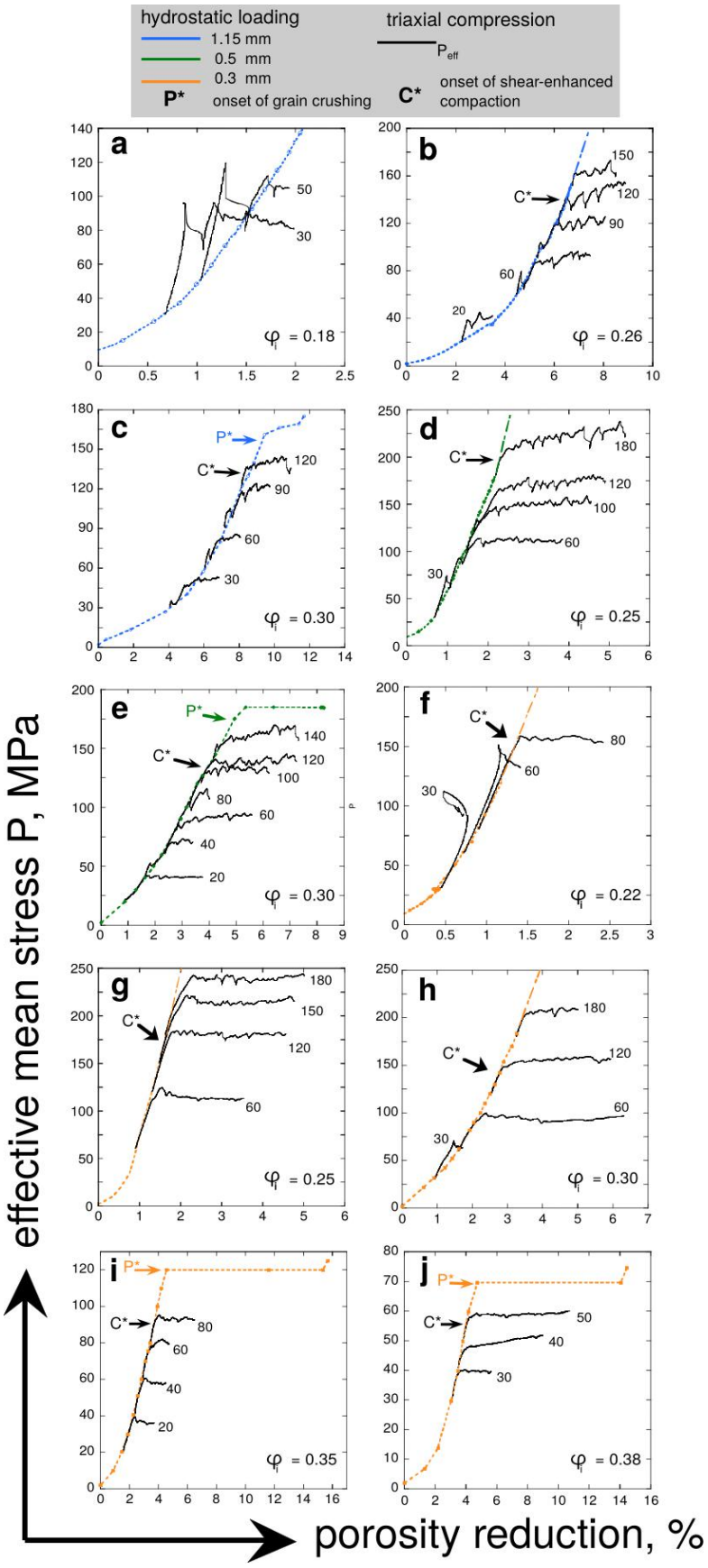

Figure 4.5 Compilations of mechanical data from hydrostatic loading (dashed coloured) and triaxial tests (black) for samples with a mean grain diameter of 1.15 mm (blue) and an initial porosity of (a) 0.18, (b) 0.26 and (c) 0.30; a mean grain diameter of 0.5 mm (green) and an initial porosity of (d) 0.25 and (e) 0.30; and a mean grain diameter of 0.2 mm (orange) and an initial porosity of (f) 0.22, (g) 0.25, (h) 0.30, (i) 0.35 and (j) 0.38. Effective pressures at which triaxial tests were conducted are indicated at the end of the corresponding curves. The onset for inelastic deformation corresponds to the departure of the effective mean stress – porosity reduction curve from the hydrostat. For illustration, the onset of shear-enhanced compaction is indicated as C* by black arrows. The critical stresses P* for the onset of grain crushing are indicated by coloured arrows on the hydrostats.

Some samples deformed in a mode that cannot be easily defined as “brittle” or “ductile”. The mechanical data for the experiments performed at effective pressures of 30, 60, and 90 MPa in Figure 4.5(c) are representative of this hard-to-define failure mode, which will be referred to as transitional. For all the experiments, peak stresses and critical stresses were identified to map out the failure envelopes of the synthetic samples (Table 4.1).

4.4.2 Critical stress states: effect of porosity and grain size

For all experiments, critical stress values were identified in accordance with the failure mode (Figures 4.2, 4.3 and 4.4). Regarding experiments conducted in the brittle and transitional regime, critical stresses P and Q were respectively identified at the peak and at the first stress drop. For experiments conducted in the ductile regime, the stresses P and Q were identified at the deviation from the hydrostat, i.e., at the onset of shear-enhanced compaction C* (Figure 4.5).

Table 4.1 includes all experiments for which the critical stresses could be clearly identified using mechanical data and AE measurements. When plotted in the effective mean stress P - differential stress Q space, peak stresses map out the brittle failure envelope (open symbols) and C* values map out the compactive yield envelope (solid symbols). When it could be measured, P* anchors the yield envelope on the x-axis (P* could not be measured for all combinations of porosity and grain size due to the pressure limitations of the triaxial press). The experiments that exhibited a transitional failure mode exist where the brittle envelope meets the yield cap. Figure 4.6 presents a compilation of failure envelopes for the synthetic samples. Overall, several common features of the envelopes should be noted. First, brittle failure of these porous materials is restricted to a small area of the stress space. Second, regarding compactive yield caps, P and Q are linearly correlated, which is particularly clear for the caps on Figure 4.6(c). Third, shear-enhanced compaction occurs over a wide range of stress states. For a given grain diameter, porosity is seen to influence compactive yield behaviour.

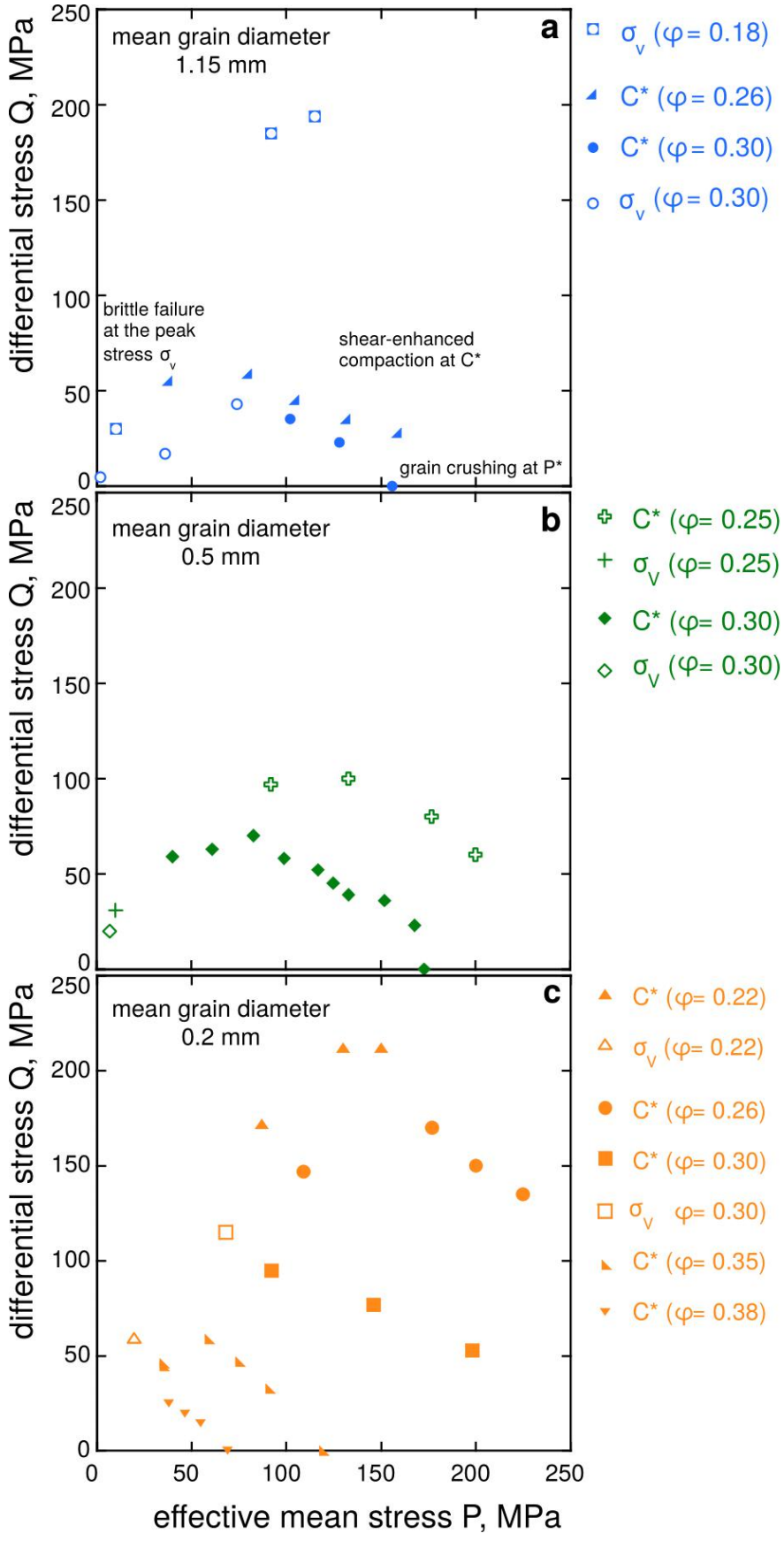

Figure 4.6

Compilations of failure envelopes for synthetic samples of mean grain diameter of (a) 1.15 mm, (b) 0.5 mm and (c) 0.2 mm. Initial porosity of the synthetic samples is indicated in the legend. Failure envelopes are mapped out by critical stresses σ_v (brittle triaxial test), C* (ductile triaxial test) and P* (hydrostatic test). Open symbols correspond to peak stress values and solid symbols to C* values. P* (also a solid symbol) anchors the envelope to the x-axis.

Broadly speaking, the higher porosity, the lower the stress that required for inelastic yield. For example, samples of mean grain diameter of 1.15 mm (Figure 4.6(a)) submitted to triaxial compression under an effective pressure of 120 MPa yielded at 23 and 35 MPa of differential stress for initial porosities of φ = 0.30 and φ = 0.26, respectively.

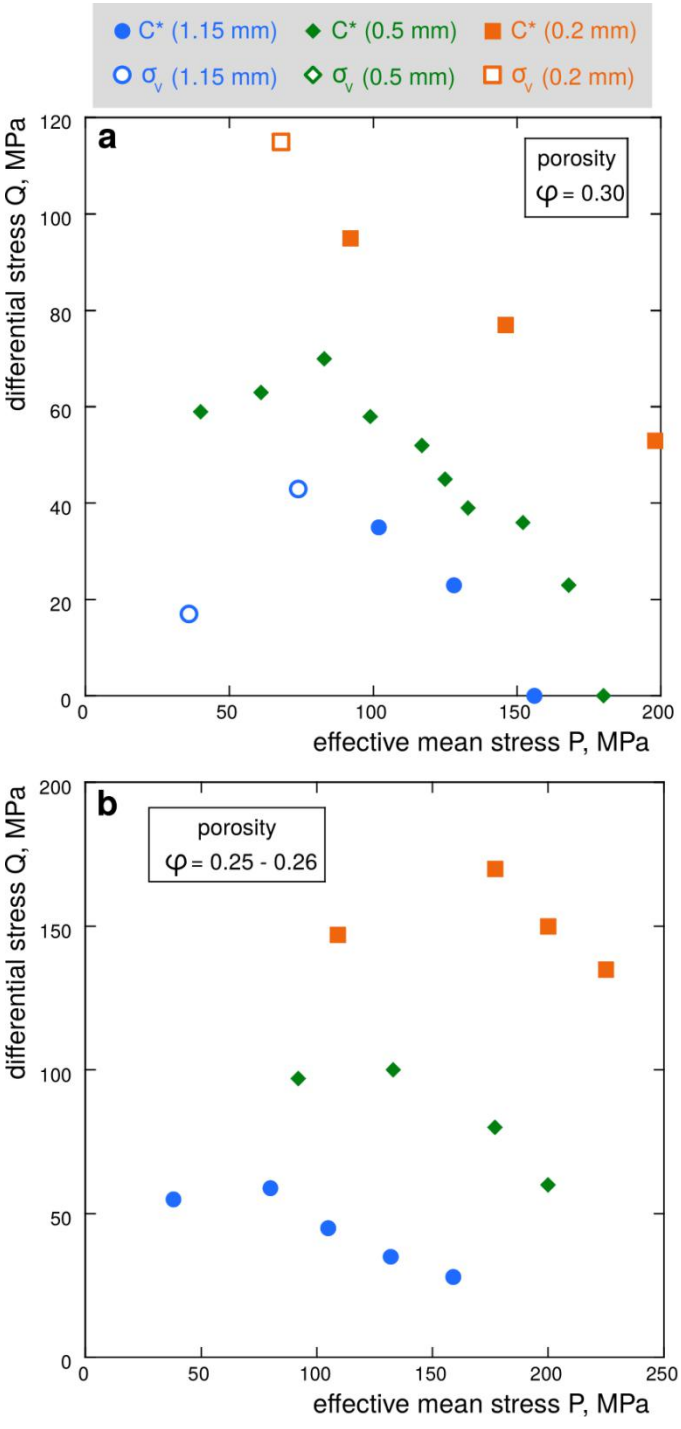

Figure 4.7 Compilations of failure envelopes for synthetic samples with a porosity of (a) 0.30 and (b) 0.25. Mean grain diameter of the synthetic samples is indicated in the legend. Failure envelopes are mapped out by critical stresses σ_v (brittle triaxial test), C* (ductile triaxial test) and P* (hydrostatic test). Open symbols correspond to peak stress values and solid symbols to C* values. P* (also a solid symbol) anchors the envelope to the x-axis.

For samples of mean grain diameter of 0.5 mm (Figure 4.6(b)), triaxial compression under an effective pressure of 100 MPa resulted in critical differential stresses of 100 MPa for φ = 0.26 compared to 52 MPa for φ = 0.30. Finally, for synthetic samples of mean grain diameter of 0.2 mm (Figure 4.6(c)) deformed at P_{eff} = 60 MPa, inelastic yielding took place at 223 MPa when φ = 0.22, 147 MPa when φ = 0.26, 95 MPa when φ = 0.30, and 42 MPa when φ = 0.35. In summary, increasing the porosity from 0.22 to 0.35 decreased the stress required for C* by more than a factor of five (Table 4.1). All else being equal, grain diameter also exerts an important influence on the compactive behaviour. Figure 4.7(a) and Figure 4.7(b) present a compilation of caps for φ = 0.30 and 0.25-0.26, respectively, for three different mean grain diameters (1.15 mm in blue, 0.5 mm in green, and 0.2 mm in orange). For φ = 0.25-0.26 and P_{eff} = 60 MPa, shear-enhanced compaction started at 59, 97 and 147 MPa for monodisperse samples of 1.15, 0.5 and 0.2 mm of mean grain diameter, respectively. For φ = 0.30 and P_{eff} = 120 MPa, C* was reached at 23, 39 and 77 MPa for samples of 1.15, 0.5 and 0.2 mm of mean grain diameter, respectively. In summary, increasing the mean grain diameter from 0.2 to 1.15 mm decreased the stress required for C* by more than a factor of two (Table 4.1).

4.5 Microstructural observations

Representative SEM micrographs for the microstructure of a synthetic sample after hydrostatic compression to beyond P* are presented in Figure 4.8. The images correspond to a sample with an initial porosity and mean grain diameter of 0.357 and 0.2 mm (sample 3312, Table 4.1), respectively, deformed up to a porosity reduction of 0.16. The corresponding mechanical data are presented in Figure 4.5(i). At the lowest magnification, the thin section shows extensive delocalised grain crushing. Zooms into the microstructure confirm that most grains were entirely crushed and that the resulting shards progressively filled the porosity as the sample compacted. Uncrushed glass beads allow for the observation of cross-cutting microfractures propagating from grain to grain. On the basis of 2D image analysis (using ImageJ), the local final porosity was estimated. The least and most damaged areas yielded porosity values around 0.30 and 0.11, respectively.

Representative SEM for the microstructure of a synthetic sample triaxially deformed to beyond C* are presented in Figure 4.9. The images correspond to a sample with an initial

porosity and mean grain diameter of 0.35 and 0.2 mm (sample 3314, Table 4.1), respectively, triaxially deformed at an effective pressure of 80 MPa up to an axial strain of 3.5%. The corresponding mechanical data are presented in Figure 4.5(i). As suggested by the small stress drops punctuating the stress-strain curve beyond C* and the corresponding bursts of AE activity (Figure 4.5(i)), the sample contains evidence of compaction localisation. Several discrete bands were observed in the upper and lower parts of the thin section, i.e., at the extremities of the sample, and one cross-cutting discrete band was observed in the middle (Figure 4.9).

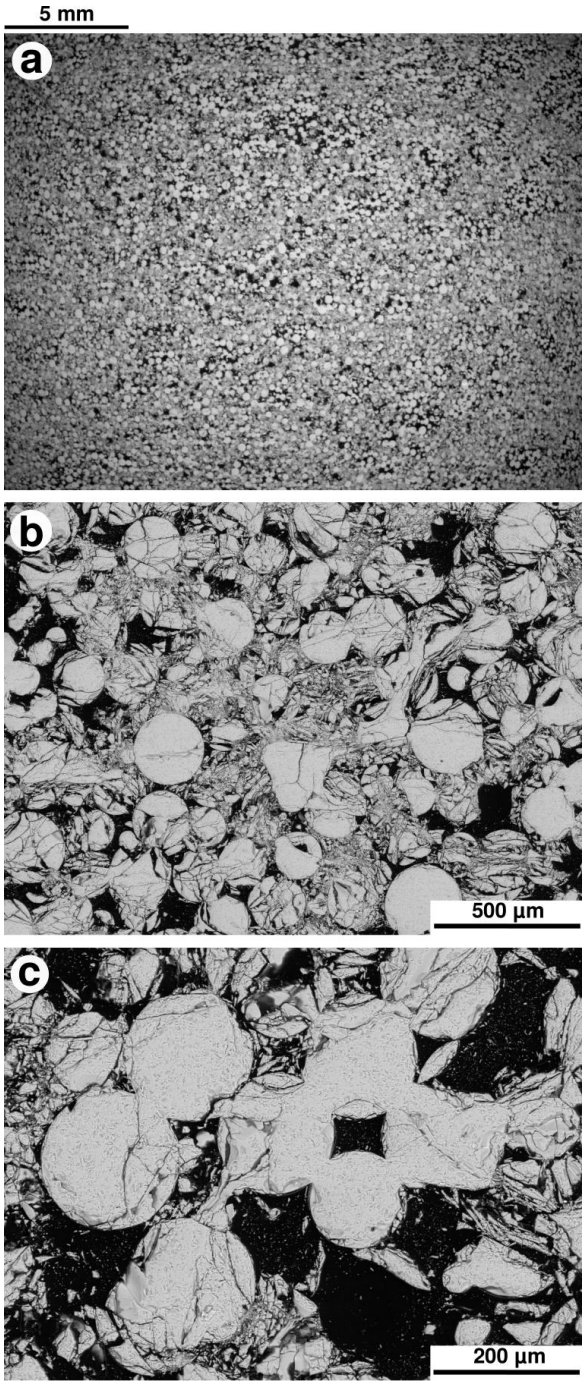

Figure 4.8. Representative scanning electron micrograph of the (**a**) microstructure of a synthetic sample deformed under hydrostatic loading up to an effective stress beyond P*. (**b**)(**c**) Zooms in showing extensive grain crushing. Black: porosity, grey: glass.

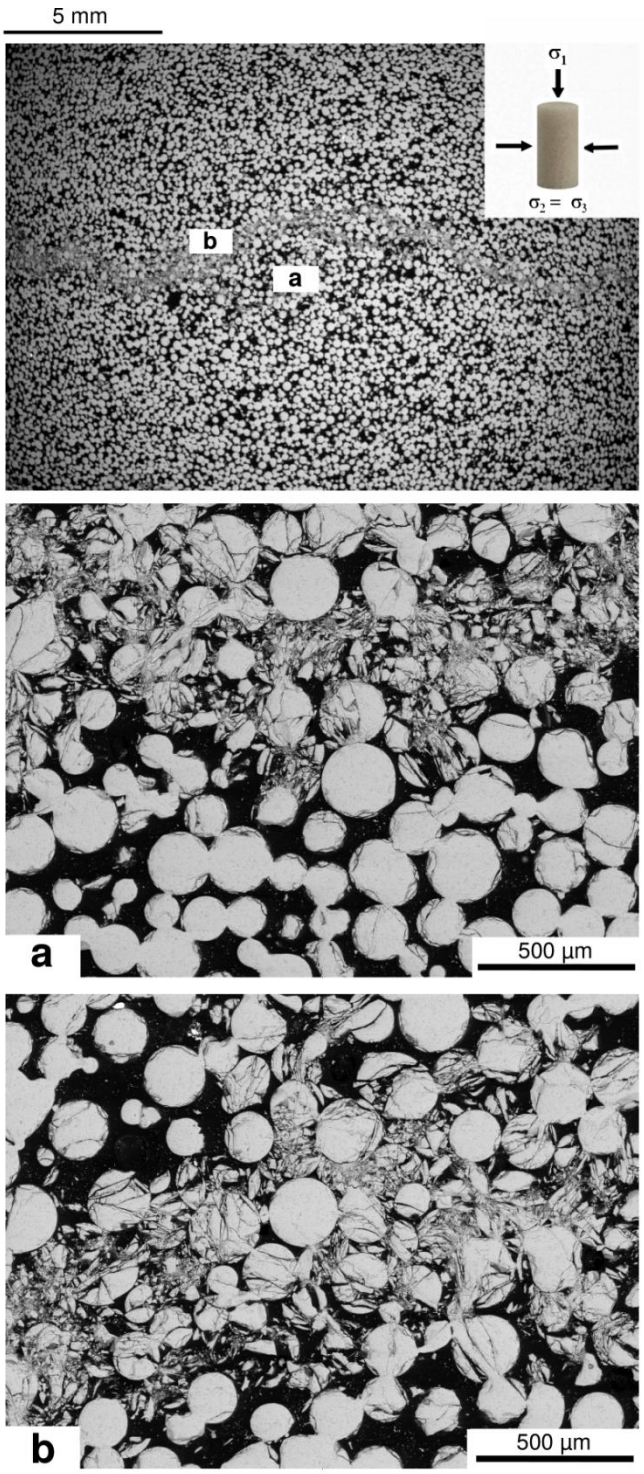

Figure 4.9 Scanning electron micrograph of the microstructure of a synthetic sample that failed by development of discrete compaction bands. Sample 3314, with a porosity of 0.35 and a mean grain diameter of 0.2 mm, was deformed under 80 MPa (Table 4.1). Overview of the thin section allows for the observation of a discrete compaction band in the middle, formed in a direction normal to the maximum principal stress σ1. (a) and (b) show micrographs of a discrete 2-5 grain-thick band within which most grains are crushed. The microstructure outside of the band is almost intact. Black: porosity, grey: glass.

The compaction band in the middle is 2-5 grains wide – i.e., thickness of 0.4 to 1 mm – and is oriented normal to the direction to the maximum principal stress σ_1. Note that the band appears to avoid the porosity patches, and thus slaloms between them. A zoom on the band shows extensively fractured and compacted glass beads (Figure 4.9). Shards resulting from the fracturing and crushing fill the porosity within the band, reducing the porosity from 0.35

to approximately 0.27 (estimation based on 2D measurements on the SEM images using ImageJ). The grains are unaffected outside the compaction band, and the porosity was estimated using ImageJ to be similar to that measured in the laboratory (0.36).

4.6 Discussion

4.6.1 Suitability of sintered glass beads as crustal analogues

Synthetic granular rocks such as the sintered soda-lime silica glass beads provide a well-characterised two-phase medium for investigating mechanical processes in siliciclastic rock. the motivation for using synthetic samples was to quantify the influence of individual microstructural parameters (e.g., porosity and grain diameter) on the mechanical behaviour of granular rock by keeping all other parameters constant. In natural sandstones, for example, samples with different porosities may also be characterised by different grain and pore sizes and distributions. However, understanding the mechanical behaviour of sandstones using fused glass bead synthetics hinges on the comparability of natural and synthetic sandstones. Before discussing the suitability of sintered glass beads as analogues for crustal rocks, the differences between the microstructure of the synthetic samples and natural crustal rocks will be briefly mentioned. First, the grain size distribution of all the synthetic samples is monomodal and closely clustered (Figure 4.1(a)). Natural sandstones, for example, can be characterised by polydisperse grain size distributions. Second, the grains in the synthetic samples are spherical and have identical physical and mechanical properties, while natural sandstones often contain non-spherical grains and diverse types of grains (e.g., quartz and feldspar). Finally, natural sandstones can contain cement (e.g., clay cement between grains). the synthetic samples do not contain cement (Figure 4.1(c)(d)).

To compare the synthetic samples to natural sandstones, sandstones whose porosity and grain diameter lie in the range covered by the synthetic samples (the porosity range is 0.18-0.38 and the grain diameter range is 0.2-1.2 mm) were chosen: Boise sandstone (porosity of 0.35 and average grain radius 0.46 mm; Bedford et al., 2019; Zhang et al., 1990), Idaho Gray sandstone (porosity of 0.36 and average grain radius 0.7 +/- 0.2 mm; Bedford et al., 2019) and Bentheim sandstone (porosity of 0.23 and average grain radius 0.3 mm; Klein et al., 2001). Bentheim sandstone is a monomineralic sandstone with a narrow grain size distribution. Due to its homogeneous mineralogy and well sorted grain size, it has been used in many rock

deformation studies, notably on strain localisation (Baud et al., 2004; Tembe et al., 2006, 2008; Wong et al., 2001). It is therefore an ideal sandstone to compare with the synthetic samples. Mechanical data from hydrostatic and triaxial experiments conducted in conditions similar to those imposed during experiments on the synthetic samples, i.e., at room temperature on water-saturated samples at a fixed pore pressure of 10 MPa, were compiled. Figure 4.10 presents selected mechanical data from this study database alongside mechanical data from hydrostatic experiments (a) and triaxial experiments (b) conducted on Boise, Idaho Gray and Bentheim sandstones.

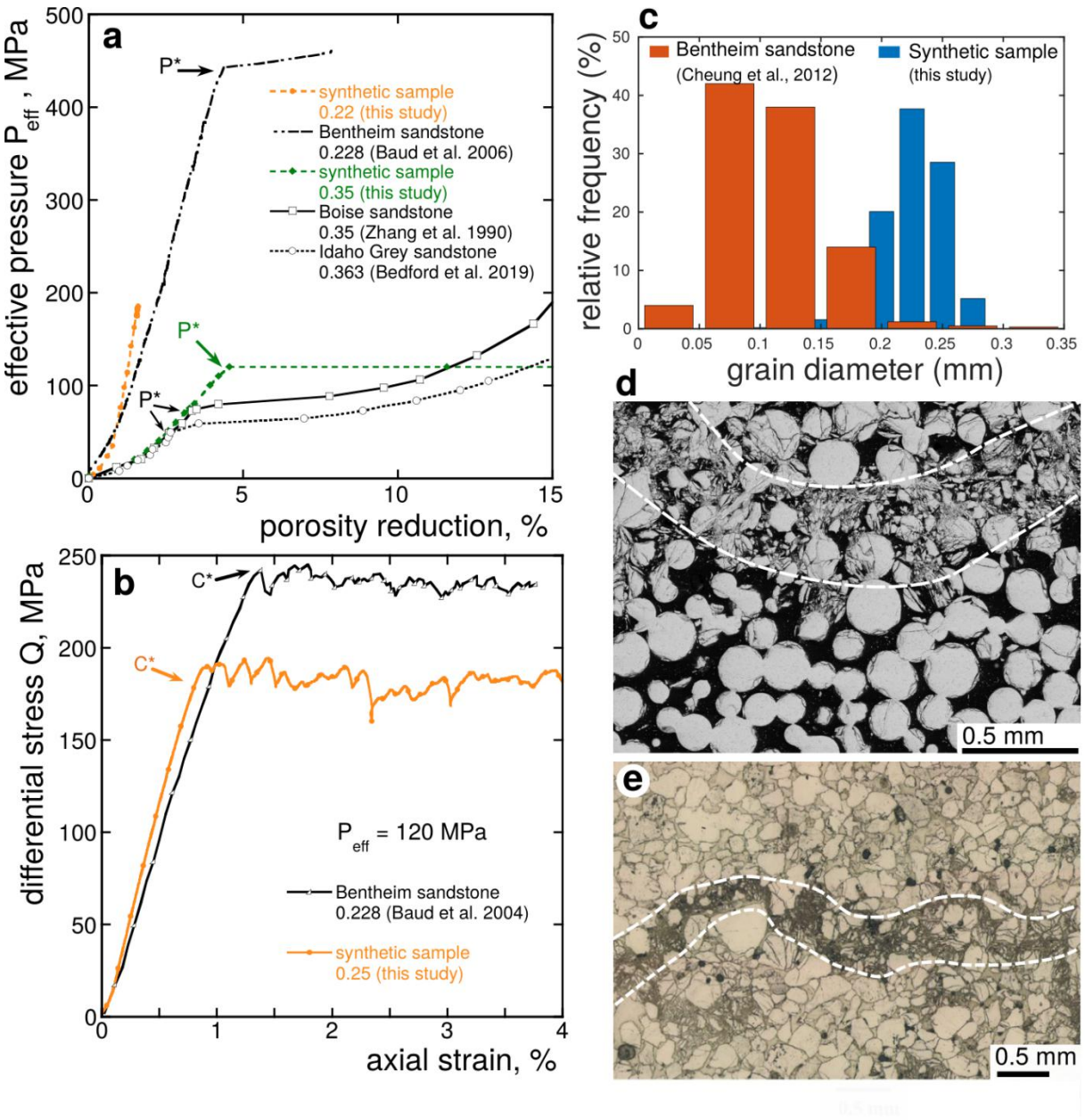

Figure 4.10 Data from tests performed on synthetic samples compared to data for sandstones from the literature. (a) Comparison of the hydrostatic loading curve of a synthetic sample (green dashed) with a porosity of 0.35 and a mean grain diameter of 0.5 mm and of the hydrostatic loading curve of a synthetic sample (orange curve) with a porosity of 0.22 and a mean grain size of 0.2 mm, with the hydrostat of Boise sandstone (black line), with a porosity of 0.35 and a mean grain diameter of 0.92 mm (Zhang et al., 1990), the hydrostat of Idaho Gray sandstone (dashed black) with a porosity of 0.363 and a mean grain diameter of 0.7 mm (Bedford et al. 2019) and the hydrostat of Bentheim sandstone with a porosity of 0.228 and a grain diameter of 0.3 mm (Baud et al., 2006). The onset of grain crushing is indicated as P*.

(b) Comparison of stress-strain curves obtained during a triaxial test at an effective pressure of 120 MPa performed on a synthetic sample (orange line) with a porosity of 0.25 and a mean grain diameter of 0.2 mm and on Bentheim sandstone (black line) (Baud et al., 2004). The onset of shear-enhanced compaction is indicated as C*. (c) For reference, the smallest grain size distribution used in this study is presented along the grain size distribution of Bentheim sandstone (data from Cheung et al. 2012). (d) Comparison of a scanning electron micrograph of a discrete compaction band observed in a synthetic sample ($\varphi = 0.35$) and (e) an optical microscope image of a discrete compaction band in Bentheim sandstone ($\varphi = 0.23$; Baud et al., 2004).

Regarding the hydrostatic behaviour. (Figure 4.10(a)), it can be noted that, during the initial loading and increase of the effective pressure up to P*, Boise, Idaho Gray, and the synthetic sample with a porosity of 0.35 present porosity reduction curves that are almost identical. The characteristic "tail" at the beginning of the hydrostat is typically attributed to the closure of microcracks (Walsh, 1965). Assuming the sintered glass beads do not contain microfractures at the beginning of the hydrostatic pressurisation, as indicated from the microstructural analysis of the intact material, the non-linear initial portion of the hydrostat can be attributed to grain rotations and rearrangements, which is corroborated by the positive correlation between the size of the tail (i.e., the amount of compaction) and the porosity of the sample. Qualitatively speaking, the compaction curves evolve differently beyond P*. While a progressive inflection and strain hardening is observed for both Boise and Idaho Gray sandstones, P* manifests as a sharp breaking point beyond which the synthetic sample undergoes a porosity reduction of about 0.1 without hardening. Zhang et al. (1990) demonstrated that the first inflection in the hydrostat corresponds to the inception of grain crushing and that increasing the effective pressure beyond this point exacerbates the deformation. This gradual behaviour is absent for the synthetic sample, which experiences extensive grain crushing and porosity loss at the state of stress just higher than P*. The observation of extensive grain crushing at a stress just above P* is similar to that reported for Bentheim sandstone, a rock that also contains a closely-clustered monomodal grain size distribution (Baud et al., 2006)(Figure 4.10(a)(c)). Examination of the microstructure showed that very few areas in the sample remained uncrushed (Figure 4.8). Contrary to most natural sandstones (e.g., Caruso et al., 1985), the synthetic rocks are composed of monomodal

distributions of uniform grains of identical elastic properties. Thus, the force chains induced in the granular framework during loading are expected to be more homogeneously distributed in the monodisperse synthetic samples (Guéguen & Boutéca, 2004; Papadopoulos et al., 2018). As a result of this homogeneity, when the externally applied effective pressure reaches the critical value P*, the normal forces induced at the grain contacts must reach the critical value at the same time, and most grains are thus crushed at the same state of stress. Quantitatively, the effective stress at which the onset of grain crushing (P*) occurs is higher in the synthetic rock (120 MPa) than it is in Boise (75 MPa) and Idaho Gray (55 MPa) sandstones. Several differences between the synthetic and natural samples could be considered to explain the higher P* in the synthetic samples. First, Boise and Idaho Gray sandstone have a larger average grain diameter. Second, Boise and Idaho Gray sandstone contain minerals other than quartz that are characterised by lower values of fracture toughness, such as feldspar (Atkinson & Meredith, 1987). However, although the mineral composition of the two sandstones is very close, the P* of Boise sandstone is about 25 MPa higher than that of Idaho Gray sandstone (Figure 4.10(a)). Therefore, the much higher P* for the synthetic samples might arise from the difference in grain diameter (the smaller the grains, the stronger the sample).

In the following, the behaviour of natural sandstones is compared with the one of the synthetic samples when subject to triaxial compression. Figure 4.10(b) presents mechanical data from triaxial tests conducted on a synthetic sample with a porosity of 0.3 (orange line) and on Bentheim sandstone (Baud et al., 2004) (black line) under an effective pressure of 120 MPa. Qualitatively, the stress-strain curves are very similar. Quantitatively, C* is about 50 MPa higher in Bentheim sandstone than in the synthetic sample and is likely the result of the difference in porosity and grain size (both higher for the synthetic sample). Beyond C*, the mechanical data for both samples show small stress drops, suggesting that the samples failed by development of compaction localisation, as shown by Baud et al. (2004).

Although studies on the mechanical behaviour of tuffs under hydrostatic and triaxial compression are comparatively rare (e.g., Heap et al., 2015; Zhu et al., 2011), the new data for sintered synthetic samples are also relevant to welded granular materials. Indeed, in the case of welded tuffs – the product of the deposition of hot volcanic ash and lapilli – the samples are an exact analogue, where volcanic welding and glass sintering are fundamentally the same dynamic process (Wadsworth et al., 2019). It should be noted that in nature, welding of tuff

can be associated with internally porous clasts, vesiculation or resorption, viscosity or temperature gradients, and shear, all of which can conspire to complicate microstructure relative to sintered glass beads, but that nevertheless, the broad theme of mechanical results given here are relevant in volcanic environments as well as other crustal scenarios.

4.6.2 Deconvolution of microstructural parameters

In nature, porosity is often related to grain diameter. However, numerous other parameters such as grain sorting, shape, orientation, location of cements, and the extent of compaction, can influence the porosity of a porous rock (Rogers & Head, 1961; Scherer, 1987). One of the results of this multi-component control on porosity is that crustal rocks that show a low porosity are not necessarily composed of small grains and vice versa. In fact, crustal rocks span a wide range of porosity-grain size combinations and can demonstrate complex porosity-grain size relationships.

For illustration, the porosity and the mean grain diameter of nineteen natural sandstones that have repeatedly been used in laboratory studies are compiled in Figure 4.11. Porosity values are in the range 0.03-0.38 and mean grain diameter values are in the range 0.075-0.92 mm. Considering only this subset of natural sandstones, several observations can be made: (1) for the few sandstones with a porosity higher than 0.25, the mean grain diameter varies over a range twice as large as sandstones of lower porosity (0.2-0.9) and (2) for sandstones of porosity lower or equal to 0.25, mean grain diameter is lower than 0.5 mm and clusters around 0.28 mm; such that the grain size effect on porosity becomes attenuated as diagenesis progresses as pore and pore throats are compacted. By compiling these data, it can be concluded that (3) sandstones that come from a single formation (see for example Buntsandstein, Fontainebleau or Boise sandstones) can cover a broad range in grain diameter and porosity, within which variations in grain diameter appear to occur independently from variations in porosity and vice versa. For example, the porosity of Fontainebleau sandstone can vary greatly (0.03-0.28), while the mean grain diameter (0.250 mm) remains constant (Bourbie & Zinszner, 1985; Lindquist et al., 2000; Louis, Baud, et al., 2007). It is important to note that there is some bias in sample selection for laboratory studies, such that crustal rocks with a low variability within a unit are favoured so that repeat measurements can be made (e.g., Menéndez et al., 1996). Field studies reported a much wider range of average grain size and porosity for sandstones, which can be encountered as very fine-grained (0.0625 mm;

Selley, 2004) and can grade up to very coarse-grained and pebbly (2 mm; Selley, 2004), with well to poorly-sorted distributions and porosity ranging over more than one order of magnitude 0.02-0.30 (e.g., Morrow, Nugget, Bartlesville, and Grimsby sandstone; Nelson & Kibler, 2003). For instance, anomalously high porosities were reported in a significant number of deeply-buried (> 4 km) reservoir sandstones worldwide (e.g., porosity in the range 0.24-0.40 in the Tertiary channel-fill sandstone, offshore west Africa; Bloch et al., 2002).

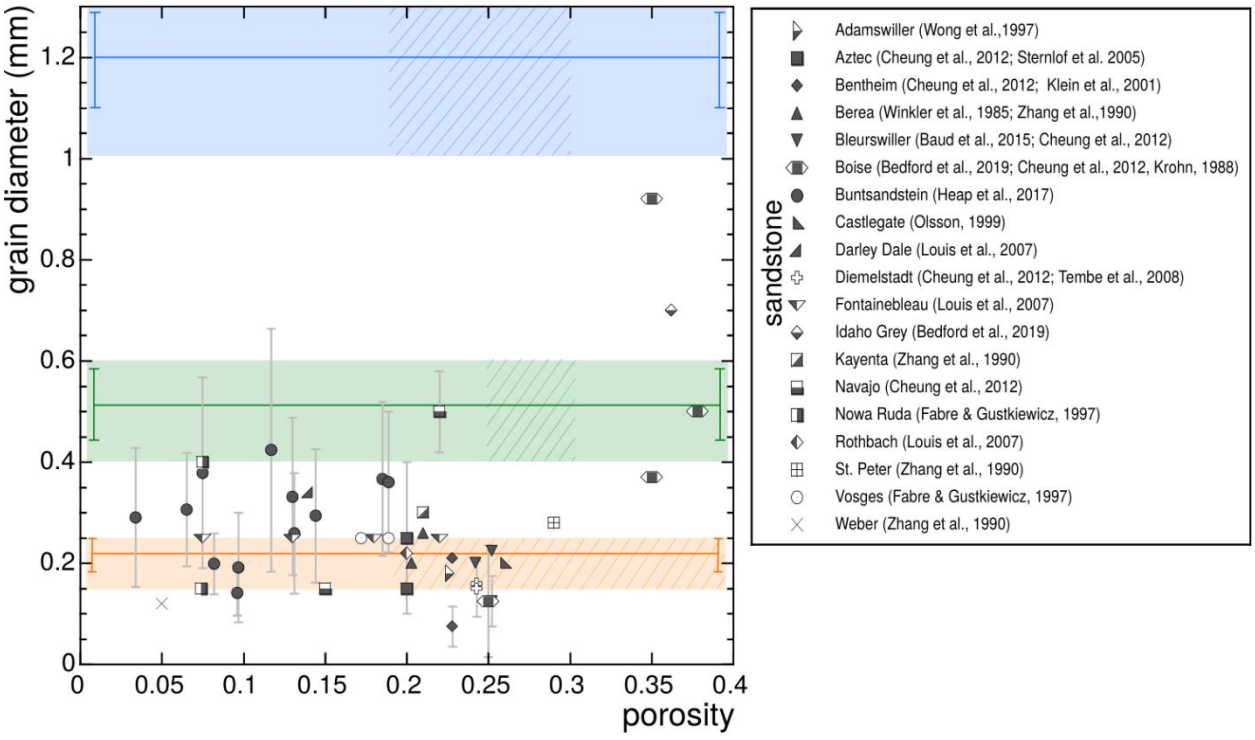

Figure 4.11 Compilation of porosity and grain diameter for laboratory sandstones. All data are from the literature, references are given in the legend. Coloured areas correspond to the range of porosity-grain diameter accessible by sintering glass beads. The dashed areas correspond to the range specifically investigated in this study. The error bars give the standard deviation of the grain diameter distribution, when it has been reported.

Deconvolving structural parameters such as porosity and grain size is necessary to derive definitive constraints on the micromechanics of compaction from experimental studies. Indeed, while the importance of porosity in controlling yield strength is well-established for crustal rocks (e.g., Wong & Baud, 2012), the independent effect of a change of grain or pore

size is only poorly investigated (Atapour & Mortazavi, 2018). As revealed when compiling grain diameter and porosity for laboratory sandstones (Figure 4.11), it is possible that the approximate consistency in the grain diameter has meant that its influence on compactive yield strength has been masked in rock mechanics study thus far. Sintering glass beads has allowed for effectively deconvolving the effect of porosity and grain diameter and other microstructural factors, to parameterise specifically for their importance.

4.6.3 Influence of porosity and grain size on compactive yield

The synthetic samples were designed and prepared to maximise microstructural homogeneity. Yet, they present heterogeneities in the porosity distribution and in the geometry of grain-to-grain contacts (Figure 4.1). Similar porosity clusters have been reported in Bleurswiller sandstone, the mechanical compaction of which has been investigated in several studies (Baud et al., 2015; Fortin et al., 2005, 2006; Tembe et al., 2008). These published works have demonstrated the importance of porosity clusters on the micromechanical processes leading to inelastic compaction. Indeed, while yield envelopes reported for natural sandstones are typically elliptical in shape (Baud et al., 2006; Guéguen & Fortin, 2013; Wong et al., 1997), Bleurswiller sandstone presents an approximately linear yield cap (Baud et al., 2015). The linear yield envelope of Bleurswiller was fitted by Baud et al. (2015) using a dual-porosity micromechanical model for cataclastic pore collapse. The pore collapse model, initially developed for dual-porosity carbonates, treats the pore size distribution as bimodal with the pore space divided into microporosity and macroporosity (i.e., a porosity cluster) (Zhu et al., 2010). Assuming the matrix into which porosity clusters are embedded fails according to the Coulomb criterion, the pore collapse model predicts that a porosity cluster collapses when the stress field in its vicinity attains the critical state according to the Coulomb criterion, which results into a linear dependence of the differential stress at the yield point C* with the mean effective stress (Baud et al., 2015). Although the yield caps that include P* appear linear, further microstructural analysis need to be done to identify the micromechanical process and clarify the role of pore collapse in the failure of the synthetic samples.

The pore space heterogeneities of the synthetic samples appear to influence the micromechanics of failure. Yet, they do not prevent from discussing the relative influence of porosity on the compactive yield behaviour. A compilation of six yield envelopes for synthetic samples of porosity of 0.25 and 0.30 and of mean grain diameter of 0.2, 0.5 and 1.15 mm is presented in Figure 4.12. All of the compactive yield caps are linearly shaped with a negative slope. Overall, for a given grain diameter, increasing porosity decreases the stress at which C* occurs and that a difference in porosity of 0.01 results in a difference in C* of approximately 8% +/- 5%. This appears to apply whatever the grain diameter is in the range 0.15-1.3 mm. Indeed, at an effective pressure of 60 MPa, an increase of porosity from 0.26 to 0.30 (+0.04), decreases the stress at which C* occurs from 59 to 43 MPa (-28%), 97 to 70 MPa (-28%) and from 147 to 95 MPa (-35%) for mean grain diameter of 1.15, 0.5 and 0.2 mm, respectively.

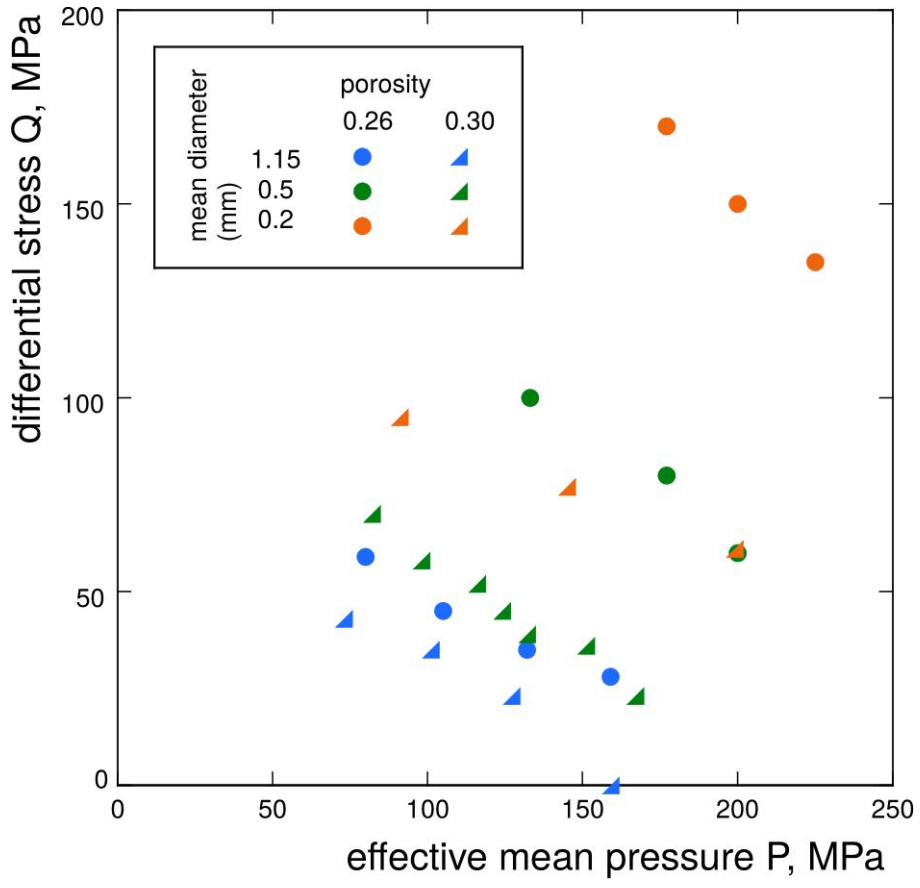

Figure 4.12 Influence of porosity on the compactive yield strength. Compactive yield envelopes for synthetic samples with a porosity of 0.26 (round solid symbol) or 0.30 (triangle

solid symbol) and a mean grain diameter of 1.15 mm (blue), 0.5 mm (green) or 0.2 mm (orange) are compiled.

As for porosity, grain size was experimentally identified to have a first-order control on compactive yield of porous siliciclastic rock (Wong, 1990; Wong et al., 1992, 1997; J. Zhang, Wong, & Davis, 1990) and has been included as a parameter in micromechanical models (e.g., Sammis & Ashby, 1986; Zhang et al., 1990). In the Hertzian fracture model of Zhang et al. (1990), average grain radius acts as a scaling parameter for the critical pressure P* with an equal weight than porosity. This model was successfully applied to a number of natural and synthetic sandstones and unconsolidated materials (David et al., 1998; Wong et al., 1997) with some scatter. However, although a consensus on the key influence of grain size has been reached, compactive yield caps compilations for sandstones often only discuss the influence of porosity. Figure 4.13 shows a compilation of compactant failure caps for Boise and Bleurswiller sandstones (data from Cheung et al., 2012) and sintered samples that only differ from one another in terms of their average grain diameter. Considering only the yield caps of the synthetic samples, it can be observed that, all else being equal, an increase in average grain diameter from 0.2 to 0.5 mm (+130%) or from 0.5 to 1.15 mm (+150%) shifts the stress at which C* occurs to values approximately two times lower (-50%) (Figure 4.13). Moreover, the difference in C* that results from a change in grain diameter remains approximately the same whatever the porosity. Thus, the data show that an increase in average grain diameter by a factor of 2 results in a decrease in the stress to reach C* of approximately 50 +/- 5%. As for Boise and Bleurswiller sandstone, they are similar in mineralogy and porosity but, although both their grain diameter distributions present a peak at 125 µm, the former has a wider sorting that extends up to 725 µm. Despite significantly different grain sorting, their compactive yield caps for the onset of shear-enhanced compaction are very similar, albeit slightly different in shape with a more linear cap for Bleurswiller sandstone. The caps of the synthetics are similar in shape to those of the natural sandstones but are mapped out at very different stress states (Figure 4.11). Tembe et al. (2008) reported that Bentheim sandstone, although similar to Boise and Bleurswiller sandstones in terms of porosity, presents a compactive yield cap characterised by higher stresses. Indeed, the abundance of secondary minerals (feldspar, oxide and mica) in Boise and Bleurswiller compared to Bentheim (>99% quartz) likely causes the decrease in the compactive yield stresses for Boise and Bleurswiller

sandstones. Similarly, since Bleurswiller and Boise sandstones present a grain diameter distribution with a peak at 125 μm, their compactive yield caps would be expected to be mapped out at higher stresses than the caps for the synthetic samples that have grain diameter distributions with peaks at 200, 500 and 1150 μm (Figure 4.13). The discrepancy in compactive yield stresses between Boise and Bleurswiller sandstones and the synthetic samples can be attributed neither to porosity nor to grain size, but possibly to the presence of cement and of secondary minerals other than quartz (feldspar, oxide and mica).

Overall, grain diameter was varied by one order of magnitude (Figure 4.11) and a large effect of that variation on the yield compactive strength of the synthetic samples is observed. Grain diameters of natural sandstones can also vary by more than one order magnitude (Nelson & Kibler, 2003), but the effect of that variation has not hitherto been deconvolved from other microstructural factors. Thus, if grain size were to be accounted for quantitatively, its effect would be similar to that of porosity. However, for the range of porosity and grain diameter used herein, the influence of porosity on compactive yield is higher than the influence of grain diameter. Indeed, to cover a similar range in the stress space, the average grain diameter of the synthetic samples was increased by up to 600 % (relative to the lowest range used, 0.15-0.25 mm) while porosity was only increased by up to 120% (relative to the lowest porosity used, 0.18).

4.6.4 Compaction localisation

For all of the synthetic samples deformed in the regime of shear-enhanced compaction, mechanical data show stress drops of variable amplitude (Figure 4.5), suggesting that compaction localisation took place (Baud et al., 2004; Heap et al., 2015; Louis et al., 2006). This observation concurs with the general consensus that microstructural homogeneity promote strain localisation in granular materials (Katsman et al., 2005; Louis et al., 2009; Wang et al., 2005). Indeed, Cheung et al. (2012) demonstrated that uniform grain size distribution promotes the development of discrete compaction bands. As the synthetic samples are characterised by a monodisperse distribution of grain size, compactant deformation was expected to localise in the form of compaction bands. In Figure 4.10(c) and Figure 4.10(d), SEM micrograph of a discrete compaction band in a synthetic sample and a

micrograph of a discrete compaction band in Bentheim (from Baud et al., 2004) are juxtaposed. The compaction bands present very similar microstructural attributes (Figure 4.10(c)(d)). An important difference is that the micrograph has been obtained on a sample of porosity of 0.35. To the knowledge, the range of porosity over which compaction bands were reported in sandstones is approximately 0.13; 0.29 (Fossen et al., 2011; Schultz et al., 2010; Tembe et al., 2008). The mechanical behaviour of sandstones with a porosity higher than 0.29 at or near the brittle-ductile transition has been studied (e.g., Bedford et al., 2019; Cheung et al., 2012; Wong et al., 1997) but high-porosity sandstones typically used in laboratory often have polydisperse distributions of grain size (see for example, Boise sandstone), which has been recognised to inhibit strain localisation. Therefore, the effect of porosity on the propensity for compaction localisation may have been masked by the influence of other structural parameters. These new data therefore extend the upper limit of porosity for which compaction localisation has been observed to 0.35 and suggest that compaction localisation can occur in samples with a porosity up to 0.38 (the highest porosity of the set of samples).

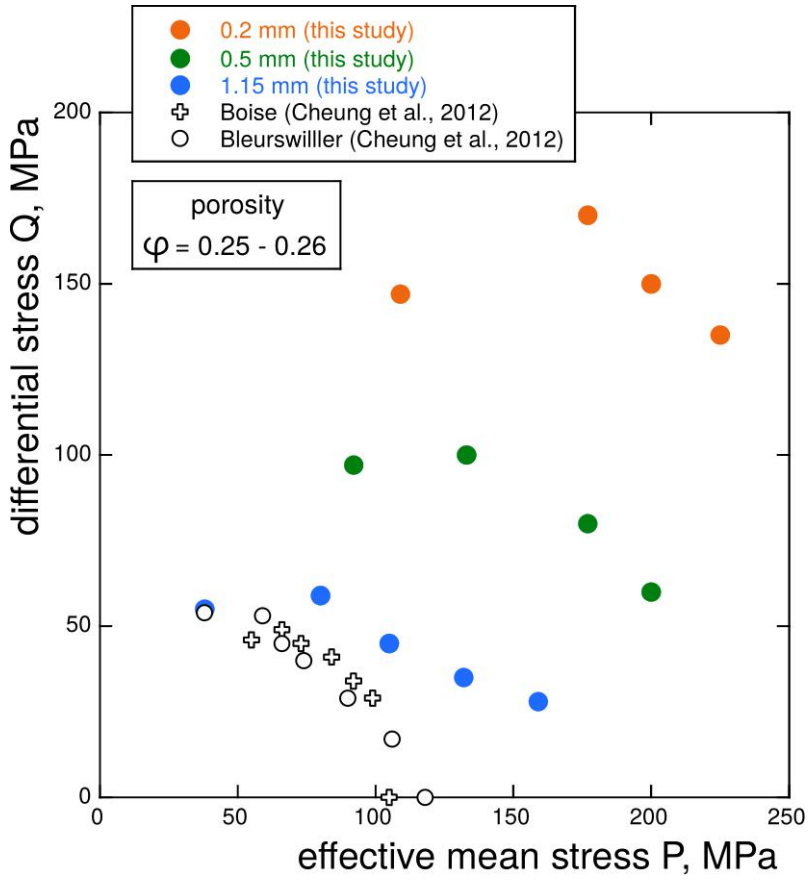

Figure 4.13 Influence of grain diameter on the compactive yield strength. Compactive yield envelopes for synthetic samples with a porosity of 0.25 and a mean grain diameter of 0.2 mm (orange), 0.5 mm (green) and 1.15 mm (blue) are compiled with yield envelopes for Boise (open cross) and Bleurswiller (open circle) sandstones (data from Cheung et al., 2012).

However, although numerical simulations suggested compaction localisation could occur in sand packs (Marketos & Bolton, 2009), experimental validation for the formation of compaction bands in high-porosity granular aggregates such as unconsolidated sands has not been reported. For example, Hangx and Brantut (2019) performed triaxial experiments on Ottawa quartz sand with a porosity of 0.36 and did not observe strain localisation in the compactant regime of deformation. These authors proposed that the possibility for grain rotation and rearrangement – permitted by the lack of cementation – allows grain failure to be accommodated and prevents stress concentration to occur. Although the high-porosity synthetic samples do not have cement, this work shows that they can develop compaction bands in the regime of shear-enhanced compaction. Therefore, it can be speculated that the

necks formed at grain contacts during sintering in the synthetic samples act as the cement in consolidated sandstones and play a key role in controlling compaction localisation. To a first-order, the potential for compaction localisation appears to be controlled not by porosity, but by the granular/non-granular and/or unconsolidated/consolidated nature of rock, which is intimately related to the degree of cementation at grain contacts and by extension, in some cases, to porosity (Lemée & Guéguen, 1996). Additionally, given that the porosity of a loose packing of grains is approximately 0.38 +/- 0.01 (Johnson & Plona, 1982), the observation of discrete compaction bands in a synthetic sample of porosity of 0.35 suggests that even a small proportion of consolidated/cemented grain contacts could be sufficient to trigger stress concentrations within aggregates and the formation of compaction bands.

4.7 Crustal implications and concluding remarks

Crustal rocks such as sandstones and tuffs, the primary microstructural elements of which are comparable with the synthetic samples, occur as geological units in reservoirs, aquifers, fault zones and in volcanic environments; settings where they typically undergo structural changes due to geologic processes. Therefore, implications – and applications – of the results of this study for natural systems are broad. For example, in the context of hydrocarbon and/or geothermal reservoirs, depletion-induced reservoir compaction is an ubiquitous phenomenon that eventually leads to surface subsidence (Gambolati et al., 2006; Nagel, 2001). On assessing which sedimentary layer compacts first and/or to the highest extent, unconsolidated upper formations and clay-rich formations are usually considered as the best candidates. However, reservoir formations are often only vaguely described as coarse- or fine-grained and grain size is rarely considered in numerical terms (Sun et al., 2018b), even in geotechnical models predicting the extent of irreversible compaction for the bulk reservoir (Buscarnera et al., 2020; Hol et al., 2018). The data presented in this chapter suggest that formations with large grain diameters, alongside those with a high porosity, could be prime candidates for mechanical compaction and should therefore be considered when assessing reservoir subsidence.

In volcanic contexts, inelastic compaction of edifice-forming rock (including non-volcanic basement rocks) presumably acts as a driving force in the growth and destruction life-cycle of large volcanoes (Bakker et al., 2015; Concha-Dimas et al., 2005; Heap et al., 2015c; Van Wyk De Vries & Borgia, 1996), which involves episodes of spreading that eventually leads to catastrophic collapses (Van Wyk De Vries & Francis, 1997). Since flank and/or edifice collapse models often invoke a weak/ductile internal or basal unit to explain instability and collapse (Ablay & Hürlimann, 2000; Morgan & McGovern, 2005; Voight, 2000), it is important to understand what controls the mechanical behaviour of porous rocks, especially considering that porous volcanic rocks can also develop compaction bands (Heap et al., 2015, 2020). The synthetic materials could help understand whether simple empirical or theoretical models can effectively describe the relationship between grain size, porosity and compactive yield strength, and thus give accurate predictions for the evolution of inelastic compaction and subsequent subsidence and/or edifice spreading. Moreover, since the synthetic samples consist of a very simplified two-phase medium, such laws can be easily tested against discrete element method simulations of reservoir compaction (Alassi et al., 2006; Sun et al., 2018a) or volcanic collapses (Harnett et al., 2018) for example.

The approach adopted in this study has allowed for the study of the influence of deconvolved microstructural attributes on mechanical compaction. The set of mechanical and microstructural data presented in this chapter show that the failure mode of analogue samples made of sintered glass beads transit from brittle at low confinement to ductile with shear-enhanced compaction at high confinement. Compactive yield caps are mapped out on a range of stress states comparable to those for natural crustal rocks (the porosity and grain diameter of which are similar to those of the synthetic samples, i.e., 0.18-0.38 and 0.2-1.15 mm, respectively) and are linearly shaped when P* is known and are likely linearly shaped for the porosity-grain diameter combinations for which P* could not be measured (due to the pressure limit of the triaxial apparatus). Qualitatively speaking, mechanical and microstructural data are very similar between the natural and synthetic samples. Regarding the influence of porosity and grain size, the following main conclusions can be drawn from the results presented in this chapter. First, increasing only porosity or only grain diameter decreases the stress at which the onset of shear-enhanced compaction C* occurs. Second, to increase the stress at C* by 50%, porosity has to be decreased – in isolation – by 0.06 (30% relative to the range 0.18-0.38) whereas average grain diameter has to be decreased – in

isolation – by 0.50 mm (53% relative to the 0.2-1.15 mm). Although the influence of porosity can be regarded as higher than the influence of grain size, this study demonstrates that, over the investigated range of porosity and grain diameter, they both exert a first-order control on the mechanical compaction of natural crustal rocks, which can span over a much broader range of porosity and grain diameters. Therefore, alongside porosity, grain diameter should become a routinely measured structural parameter when dealing with the mechanical compaction of natural crustal rocks.

Overall, this chapter demonstrates the great suitability of sintered glass beads as crustal rock analogues and the great opportunity they embody for studying microstructural parameters such as porosity and average grain diameter in isolation. Since mixtures of glass beads of different diameters can be prepared, variably disperse sintered samples have also been synthesised and used to explore the influence of grain size distribution and dispersivity on the mechanical behaviour. In the next chapter, the control of grain size distribution is studied specifically using bidisperse and polydisperse samples.

Chapter 5

Mechanical Compaction of Porous Synthetic Rocks: The Influence of Grain Size Distribution

In the preceding chapters, it was demonstrated that monodisperse sintered glass beads can be used to replicate and the hydromechanical behaviour of porous crustal rocks, especially monomineralic well-sorted sandstones such as Fontainebleau and Bentheim sandstones. In this chapter, synthetic samples are parameterised specifically to investigate the influence of the degree of dispersivity of the grain size distribution on the mechanical compaction of porous synthetic rocks.

5.1 Introduction

The varied formation processes and source materials for clastic sedimentary rocks can produce rocks with wildly different microstructures. For example, the grain size for clastic sedimentary rocks can vary from 0.01 μm to up to 10 cm (Guéguen & Palciauskas, 1994). Sandstones are a type of sedimentary rock with a grain size in the range 0.06–2 mm. Although exceptionally well-sorted sandstones exist, such as the widely-studied Fontainebleau sandstone (France; Bourbié & Zinszner, 1985; Revil et al., 2014; Sulem & Ouffroukh, 2006), field studies report a wide range of grain size distributions for natural sandstones (Selley, 2004). Clastic rocks such as sandstones can therefore vary greatly in terms of their grain size and grain size distribution.

The grain size distribution in a granular system can be characterised in terms of its dispersivity, which relates to sorting in detritic sedimentary rocks such as sandstones. The

granular assembly is called monodisperse if all particles have the same size, bidisperse if they have two sizes, and polydisperse if particles have more than two different sizes (Torquato, 2002). The grain size distribution was previously identified as a control on the mechanical behaviour and failure mode of lithified sedimentary rocks (Guéguen & Boutéca, 2004; Guéguen & Fortin, 2013), in particular compaction localisation is known to be promoted by microstructural homogeneity, i.e., by the low dispersivity of the grain size distribution (Baud et al., 2004; Cheung et al., 2012; Holcomb et al., 2007). However, studying the control of dispersivity of the mechanical behavior of porous rocks in the laboratory is extremely challenging as changes in dispersivity are typically accompanied by variations in other microstructural parameters such as the mean pore diameter, which also influences mechanical behavior (Xiong et al., 2021; Zhu et al., 2010). Over the past decades, the development of network science provided powerful tools (Papadopoulos et al., 2018) which have been used to analyse the impact of grain size distribution on the strength of granular materials. Wang et al. (2008) for example reproduced the phenomenology of the brittle-ductile transition in simulations based on a discrete element method and showed that microstructural homogeneity promotes compaction localisation. However, to date, this type of simulations is limited to 2D and direct comparison with experimental data remains therefore difficult. This issue is addressed in the present chapter, using porous synthetic samples for which the grain size distribution is designed and changed specifically, while keeping other microstructural parameters constant.

5.2 Materials and Methods

5.2.1 Experimental procedure for the preparation of the samples

The synthetic samples used to conduct this work were prepared by the viscous sintering of spherical glass beads, following the methods presented in Chapter 2. Samples with a porosity of 0.25–0.35 and with bidisperse or polydisperse distributions. The procedure for sintered glass beads blocks (Chapter 2) was used for samples with a porosity < 0.35 and the procedure for individual samples (Chapter 2) for samples with a porosity > 0.35.

5.2.2 Description of the samples

The microstructural attributes of the synthetic samples are presented in Table 5.1. In total, eight different bead size distributions, presented in Figure 5.1, were used to prepare the samples. For each distribution, the first, second, and third moments were calculated and the degree of dispersivity S was calculated. S is in the range 0–1, where 0 is highly polydisperse and 1 is the monodisperse limit. The degree of dispersivity of the distributions varies between 0.60 and 0.89. In addition, the distributions can be segregated into two categories, depending on type of grain size distribution: bidisperse (BP) distributions correspond to samples with two different sizes of grains and polydisperse (PP) distributions to those with grains with more than two different sizes. Figure 5.1 includes small schematics that represent bidisperse and polydisperse distributions, which will be repeated in the figures presented throughout this chapter to facilitate comprehension.

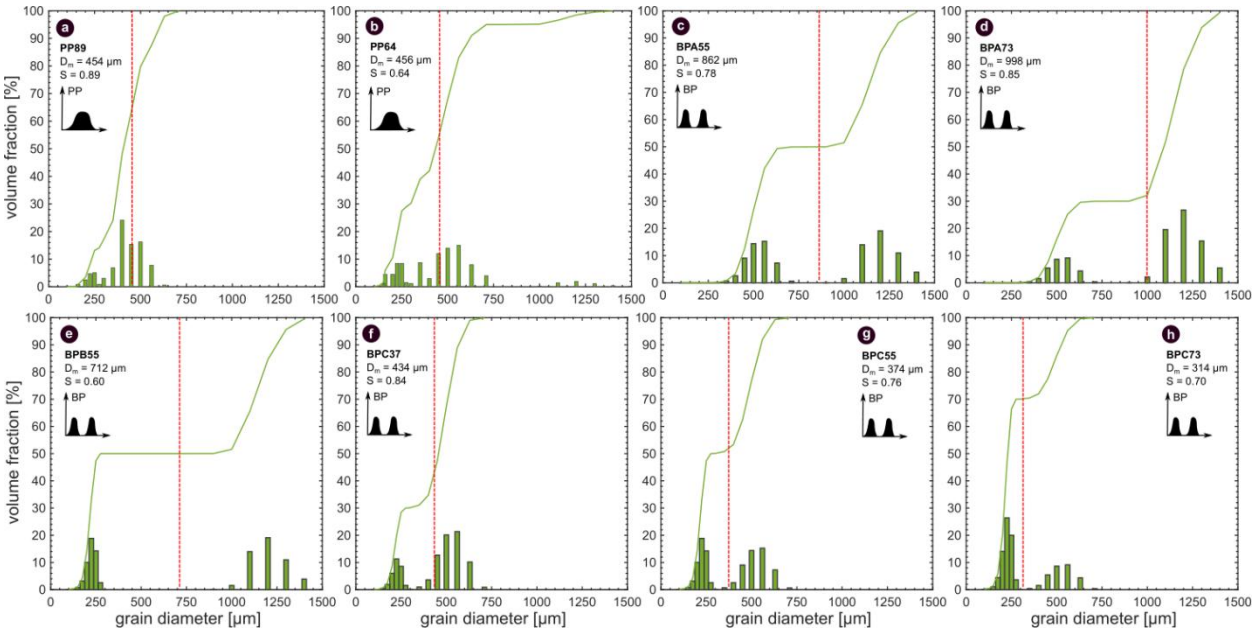

Figure 5.1 Grain size distributions of the synthetic samples. The distributions are presented in terms of volume fraction against grain diameter [µm], with the cumulative volume fraction (green solid lines) and the first moment of the distribution, i.e., the mean grain diameter (dashed red lines). Distributions (a) P89 and (b) P64 are polydisperse distributions, and

distributions (c) BPA55, (d) BPA73, (e) BPB55, (f) BPC37, (g) BPC55 and (h) BPC73 are bidisperse distributions. The mean grain diameter D_m and the degree of dispersivity S of each distribution are given on the corresponding plot, above a schematic which indicates the distribution type (polydisperse, PP, or bidisperse, BP). For clarity, these schematics will be used throughout the chapter. S is in the range 0-1, where 1 is the monodisperse limit.

For the purpose of this work, two polydisperse distributions (Figure 5.1(a-b)) and six bidisperse distributions were prepared (Figure 5.1(c-h)). The polydisperse distributions (a) PP89 and (b) PP64 have a similar mean grain diameter, approximately 455 μm, but the latter is less closely clustered, i.e., more disperse. The bidisperse distributions have different volume fractions of grains with diameters of 224 (referred to as small beads), 523 (medium beads), and 1203 (large beads) μm. Although it does not accurately capture the size of the grains that compose the bidisperse samples, the mean grain diameters of the bidisperse distributions are also indicated in Figure 5.1 (dashed red lines). Overall, the samples composed of the largest grains are those prepared using the BPA distributions, and those with the smallest grains are those prepared using the BPC distributions (Figure 5.1).

Backscattered scanning electron microscope (SEM) images of synthetic samples with polydisperse and bidisperse grain size distributions are presented in Figure 5.2. As predicted by viscous theory (Frenkel, 1945; Mackenzie & Shuttleworth, 1949; Wadsworth, Vasseur, Llewellin, et al., 2016), the width of the necks found at grain-to-grain contacts increases progressively, from a point-contact geometry to a flat line geometry, as porosity is decreased (compare Figure 5.2(a) with Figure 5.2(b)). Similar to the monodisperse synthetic samples prepared in the previous chapter, microscopic heterogeneities can be observed in the samples prepared herein, especially in the samples with the highest porosity values (Figure 5.2). However, 2D porosity measurements performed by image analysis on the micrographs (using a square window of 2 mm of edge-length in ImageJ), yield closely clustered monomodal distributions (Chapter 2). As random variations in the microstructure occur on lengthscales much smaller than the sample lengths, the synthetic samples prepared can be considered homogeneous.

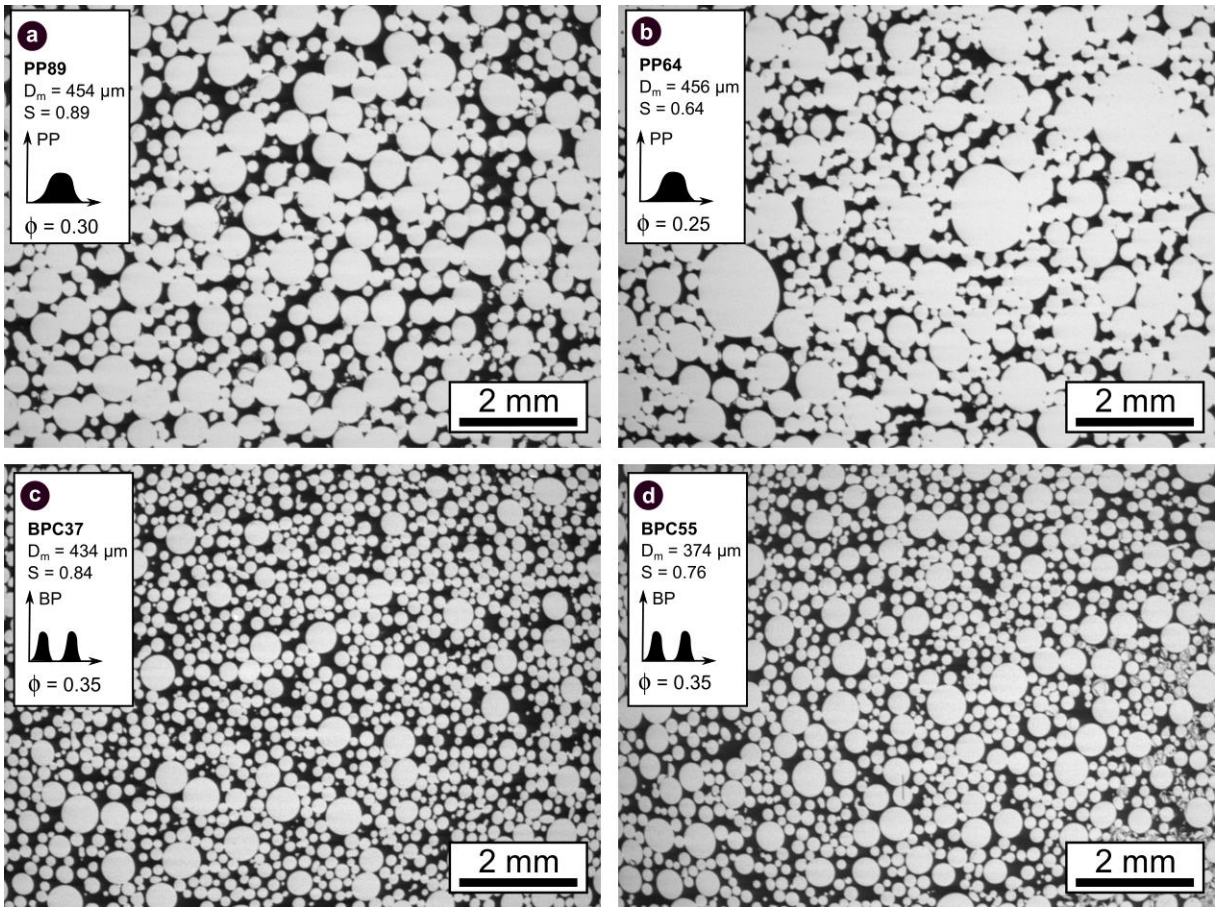

Figure 5.2 Intact microstructure of samples with a polydisperse grain size distribution (a) PP89 and porosity of 0.30 and (b) PP64 and porosity of 0.25 and a bidisperse grain size distribution (c) BPC37 and porosity of 0.35 and (d) BPC55 and porosity of 0.35. The degree of dispersivity S is in the range 0-1, where 1 is the monodisperse limit.

5.2.3 Deformation experiments

For this specific study, two types of deformation experiments were performed: hydrostatic and triaxial compression experiments. All the experiments were conducted at room-temperature under saturated and drained conditions according to the procedure presented in Chapter 3. A summary of all the experiments is provided in Table 5.1.

5.3 Results: hydrostatic compression

5.3.1 Mechanical data and microstructural observations

Examples of the mechanical and AE data for hydrostatic compression experiments performed on the samples with a polydisperse and bidisperse grain size distribution are shown in Figures 4(a) and 4(b), respectively. First, Figure 5.3 shows the good experimental reproducibility between samples with identical microstructural attributes. The results for polydisperse and bidisperse samples are qualitatively similar and show four stages. First, the porosity decreases non-linearly as P_{eff} is increased and no AEs are recorded. Then, the porosity decreases linearly with increasing P_{eff} whilst the AE activity remains low. When P_{eff} reaches a threshold value, the critical pressure for grain crushing P^* (Zhang et al., 1990), AEs activity suddenly increases and the slope in the mechanical data decreases progressively. The values for P^* are compiled in Table 5.1. Beyond P^*, the porosity decreases substantially as P_{eff} is increased (porosity decreases by up to 6% for a 10 MPa increase in P_{eff}) and the samples undergo hardening (Figure 5.3).

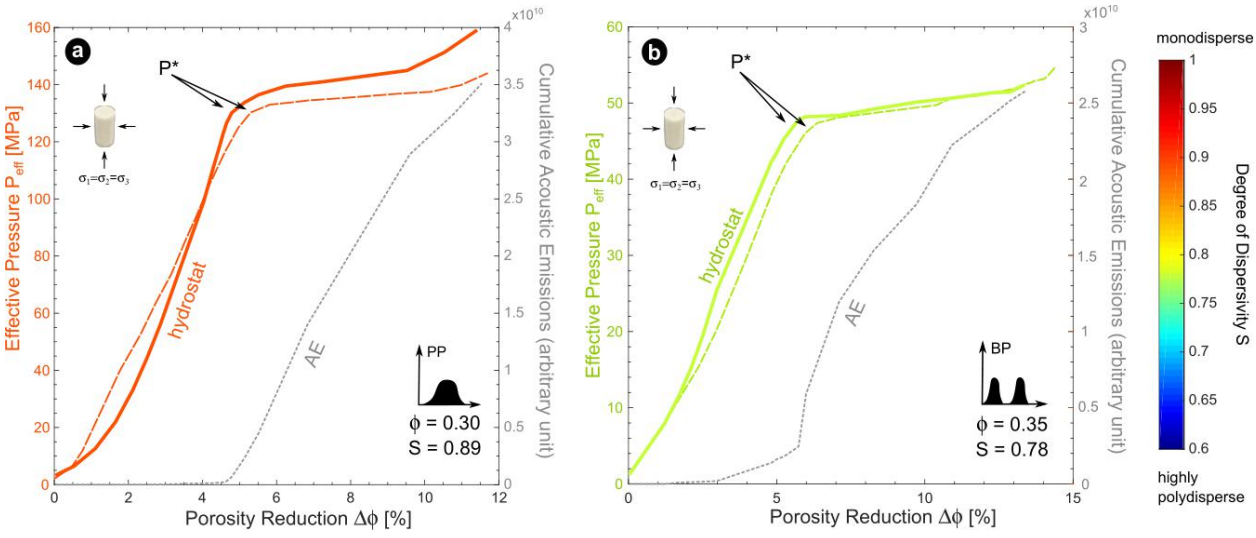

Figure 5.3 Mechanical data (solid lines) and acoustic emission (AE) energy (dashed grey lines) for the hydrostatic compression of (a) polydisperse synthetic samples and (b) bidisperse

synthetic samples. To demonstrate reproducibility, each panel shows the data for two experiments performed on samples with identical microstructural attributes.

The microstructures of a polydisperse sample and a bidisperse sample deformed under hydrostatic compression to beyond P* are presented in Figure 5.4. The SEM images show that the substantial porosity reduction beyond P* is due to extensive delocalised grain crushing, which affects all grains, whatever their size. Further, no differences are observed between the polydisperse and the bidisperse synthetic samples in terms of the microstructural features that developed under hydrostatic compression (Figure 5.4).

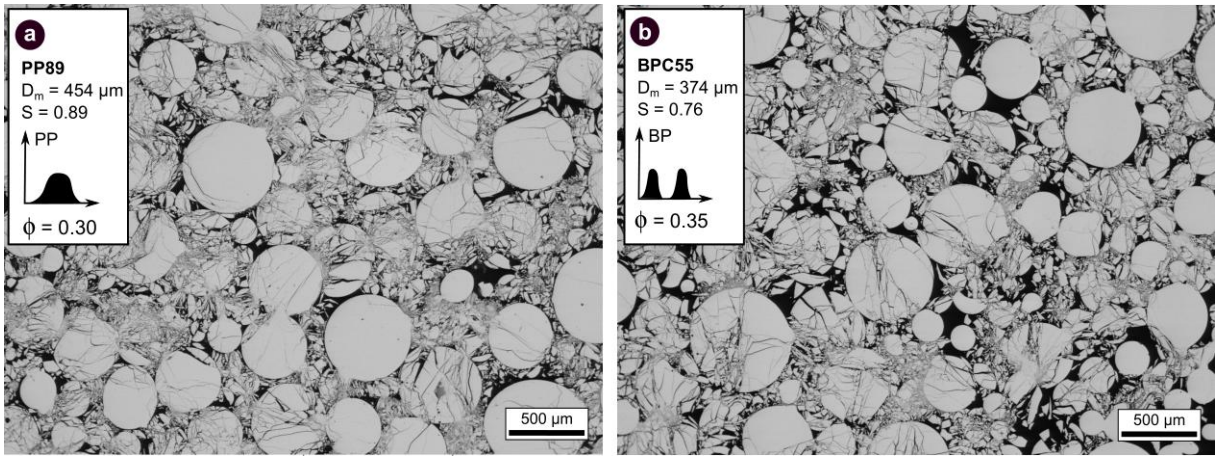

Figure 5.4 Representative backscattered scanning electron microscope images showing the microstructure of synthetic samples deformed under hydrostatic loading up to an effective stress beyond P* for (a) a polydisperse grain size distribution and porosity of 0.30 and (b) a bidisperse distribution and a porosity of 0.35. Extensive grain crushing is observed for both types of distributions. Black: porosity, grey: glass.

Table 5.1 Microstructural attributes of the synthetic samples and critical stress values for the onset of inelastic compaction under triaxial conditions (C*) and hydrostatic conditions (P*).

Sample	Porosity $\boldsymbol{\varphi}$ +/- 0.005	Dispersivity **S** (**0:** polydisperse limit ; 1 : monodisperse limit)	Mean Grain Diameter $\boldsymbol{\emptyset_m}$ [μm]	Confining Pressure $\boldsymbol{P_c}$ [MPa] ($\boldsymbol{P_p}$=10MPa)	Critical Stress C*	
					Differential Stress Q [MPa]	Effective Mean Stress P [MPa]
PP8915	0.297	0.89	454	70	67	72
PP8914	0.301			90	61	90
PP8913	0.290			110	47	106
PP8912	0.297			130	30	120
PP8911	0.291			hydrostatic loading	0	136
PP8916	0.303			hydrostatic loading	0	139
PP6414	0.256	0.64	456	50	76	55
PP649	0.252			80	83	88
PP6410	0.249			110	77	116
PP641	0.251			140	70	133

PP643	0.257			170	46	165
PP642	0.253			hydrostatic loading	0	170
BPA5521	0.361	0.78 (bidisperse)	862	hydrostatic loading	0	47
BPA5531	0.360			hydrostatic loading	0	48
BPA7361	0.357	0.71 (bidisperse)	726	hydrostatic loading	0	27
BPB5541	0.351	0.60 (bidisperse)	712	hydrostatic loading	0	27
BPC3742	0.354	0.83 (bidisperse)	434	35	12	20
BPC3744	0.357			hydrostatic loading	0	53
BPC5543	0.350	0.76 (bidisperse)	374	35	15	30
BPC5546	0.352			hydrostatic loading	0	45
BPC7321	0.360	0.70	314	25	12	17

BPC7322	0.361			hydrostatic loading	0	31

5.3.2 Influence of dispersivity

The bidisperse samples deformed under hydrostatic compression, which have a porosity of approximately 0.35, span a large range of dispersivity (0.60–0.83). Figure 5.5 presents the results of the hydrostatic tests conducted on the bidisperse samples. Overall, the mechanical data show that changing the dispersivity S from 0.60 to 0.83 (i.e., towards a more monodisperse distribution) increases the stress required for the onset of grain crushing P* from 27 to 57 (Figure 5.5). Figure 5.5(b) shows that the evolution of P* with S is well described by a positive linear slope over the range of dispersivity investigated. Therefore, the results suggest that the higher the dispersivity of the grain size distribution (i.e., the lower the value of S), the lower the stress required for the onset of grain crushing.

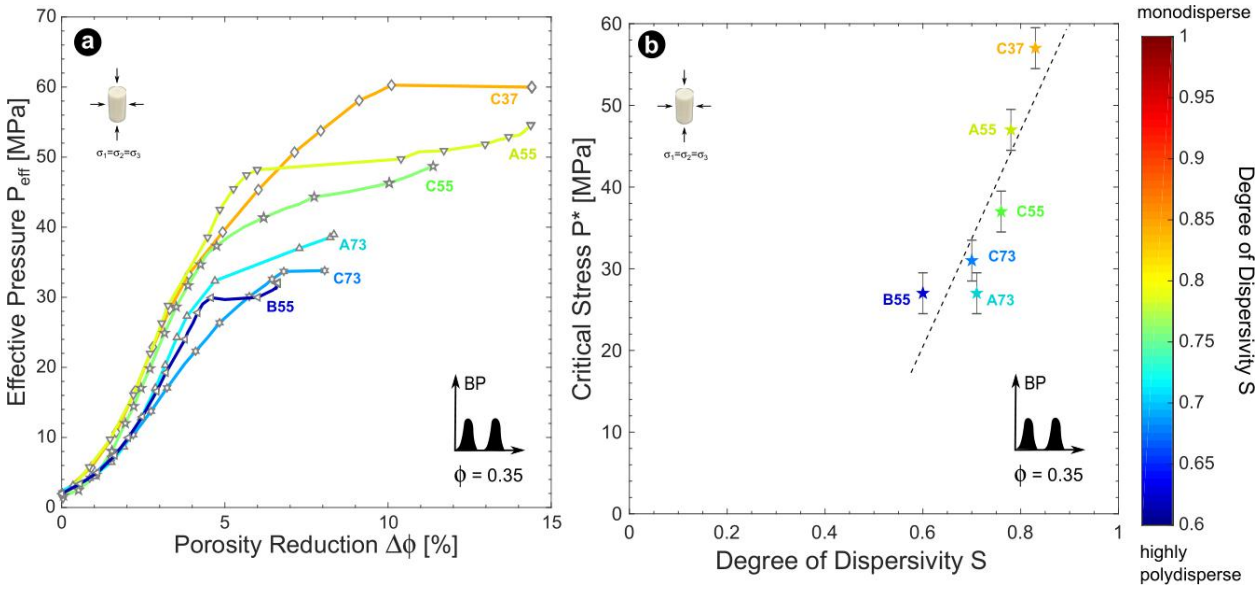

Figure 5.5 Mechanical data for the hydrostatic compression of bidisperse synthetic samples with a porosity of 0.35. (a) The hydrostatic curves are shown as the effective pressure against

the porosity reduction, using a colourmap for the degree of grain size distribution dispersivity. The name of the grain size distribution of each sample is indicated at the end of the corresponding hydrostat. (b) The critical stresses for the onset of grain crushing (P*) are plotted against dispersivity. Over the range investigated, the data are well described by a linear positive slope given by $P^* = 130.S - 59$.

5.4 Results: triaxial compression

5.4.1 Mechanical data

An example of the mechanical (solid-coloured lines) and AE (dashed grey lines) data for triaxial deformation experiments performed on samples with a polydisperse and bidisperse grain size distribution is shown in Figures 5.6(a) and 5.6(b), respectively. Qualitatively speaking, the data show a first stage where the axial strain increases linearly with Q and where the AE activity is low. In a second stage, the slope of the stress-strain curves deviates from linearity and there is an acceleration in AE activity, marking the transition to the inelastic regime of deformation. The critical stress for inelastic deformation, the onset of shear-enhanced compaction, is termed C^* (labeled on Figure 5.6). The values for C^* for all experiments are compiled in Table 5.1. Beyond C^*, the mechanical data for polydisperse and bidisperse samples deformed in the ductile regime are different: the stress-strain curves for polydisperse samples show numerous stress drops, concomitant with small bursts in AE activity, whilst the stress-strain curves for bidisperse samples show much fewer, and much less pronounced, stress drops (Figure 5.6).

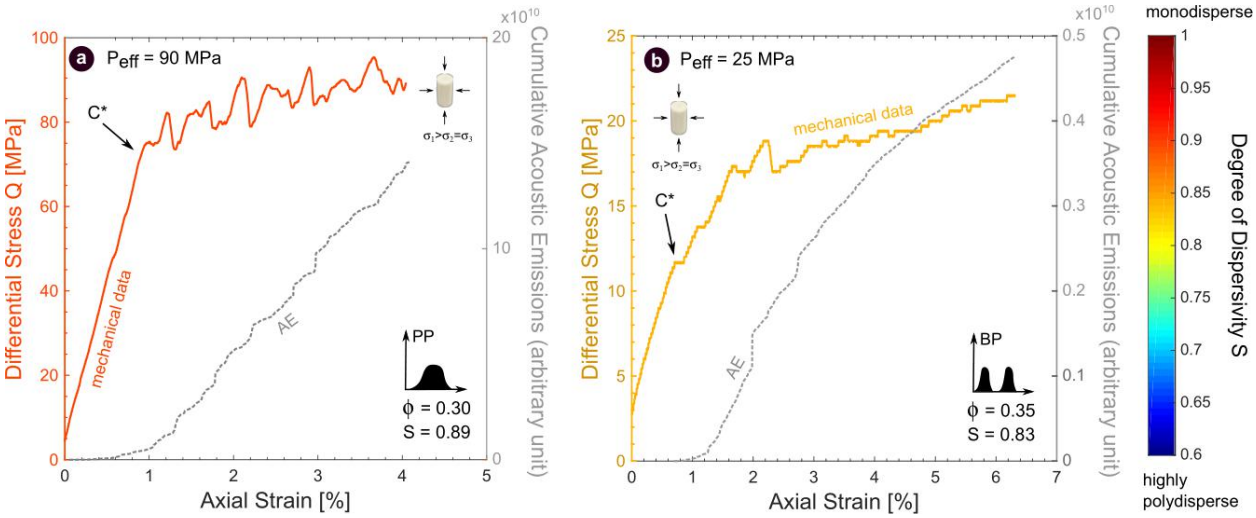

Figure 5.6 Mechanical data (solid lines) and cumulative acoustic emission energy (dashed grey lines) for triaxial tests performed on (a) a polydisperse (PP) synthetic sample and (b) a bidisperse (BP) synthetic sample in the ductile regime.

The complete mechanical dataset for polydisperse samples and bidisperse samples are shown in Figure 5.7 and Figure 5.8, respectively. The effective mean stress-porosity reduction curves for triaxial tests are compiled with the corresponding curve for hydrostatic pressurisation. When plotted in the differential stress-effective mean stress space, the values for the stress required to reach C* and P* map out compactive yield caps for the two polydisperse grain size distributions investigated. The yield caps for the polydisperse samples show an elliptical shape (Figure 5.7). In detail, the polydisperse samples with a porosity of 0.25 have higher the compactive yield stress values than those with a porosity of 0.30 (Figure 5.7(a)(b)). As a result, the compactive yield cap for the polydisperse samples with a porosity of 0.25 is larger than that with a porosity of 0.30 (Figure 5.7(c)(d)).

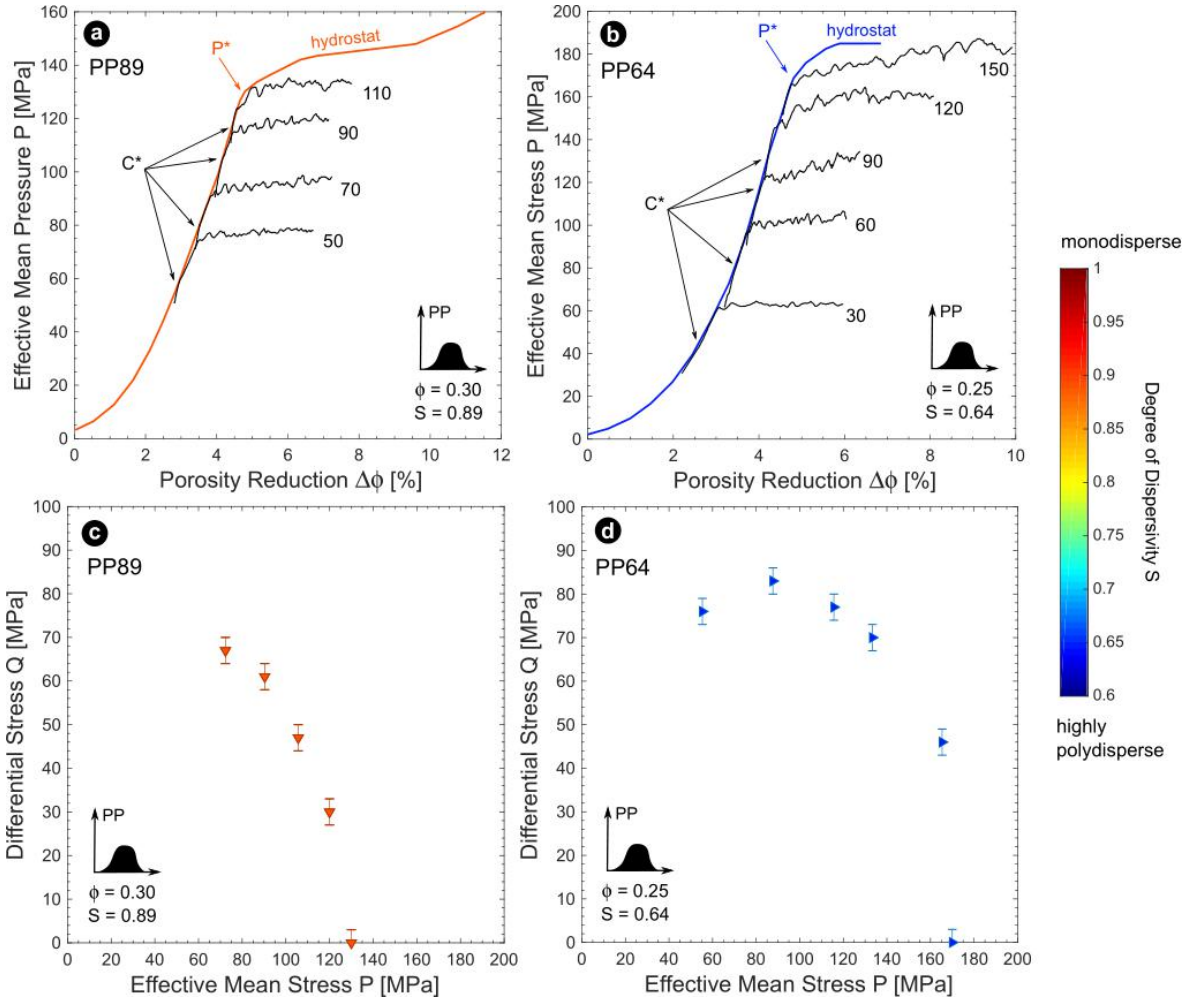

Figure 5.7 Hydrostatic and triaxial mechanical data for polydisperse (PP) synthetic samples. The effective mean stress-porosity reduction curves for triaxial tests (black lines) are compiled with the corresponding hydrostatic curve (coloured lines) for samples with a grain size distribution PP89 (a) and PP64 (b). The critical stress values (C^* and P^* compiled in Table 5.1) are plotted in the P-Q stress space where they map out the compactive yield caps for the distributions (c) PP89 and (d) PP64.

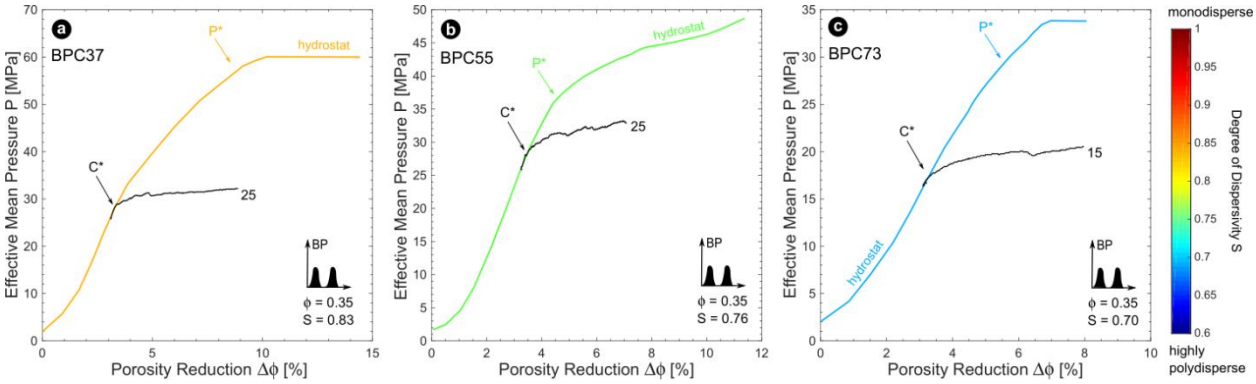

Figure 5.8 Hydrostatic (coloured lines) and triaxial mechanical data (black lines) presented as the effective mean stress against the porosity reduction for bidisperse (BP) synthetic samples with a grain size distribution (a) C37, (b) C55 and (c) C73.

When comparing the mechanical datasets, more numerous and larger stress drops are observed for the polydisperse samples than in those for the bidisperse samples (Figures 5.6, 5.7, 5.8). The stress drops, and concomitant surges in AE activity, are mechanical instabilities that often result from the occurrence of compaction localisation (Baud et al., 2004). In the following, to help interpret the mechanical data, microstructural observations made on the polydisperse and bidisperse samples post-deformation are presented.

5.4.2 Microstructural observations

The deformation features observed in polydisperse and bidisperse samples deformed in the ductile regime are presented in Figures 5.9 and 5.10, respectively. In the polydisperse samples, mechanical compaction was found to form a front growing from both ends of the samples and advancing towards the centre with increasing axial strain (Figure 5.9(a)(c)). For the polydisperse sample with a higher value of S (i.e., closer to monodisperse), 200–500 µm-thick compaction bands were observed in the deformed zones, close to the boundary between the largely intact material and the deformation front (Figure 5.9(b)). This observation suggests that mechanical compaction took place by growth of compaction bands sub-parallel to the maximum principal stress from the extremities of the sample first, and then progressively

towards the centre. For the polydisperse sample with a lower value of S (0.64), i.e., the more disperse sample, the presence of compaction bands in the deformed zones is more ambiguous. However, very tortuous bands of crushed beads which seem to propagate so as to avoid the largest grains are observed (Figure 5.9(d)(e)).

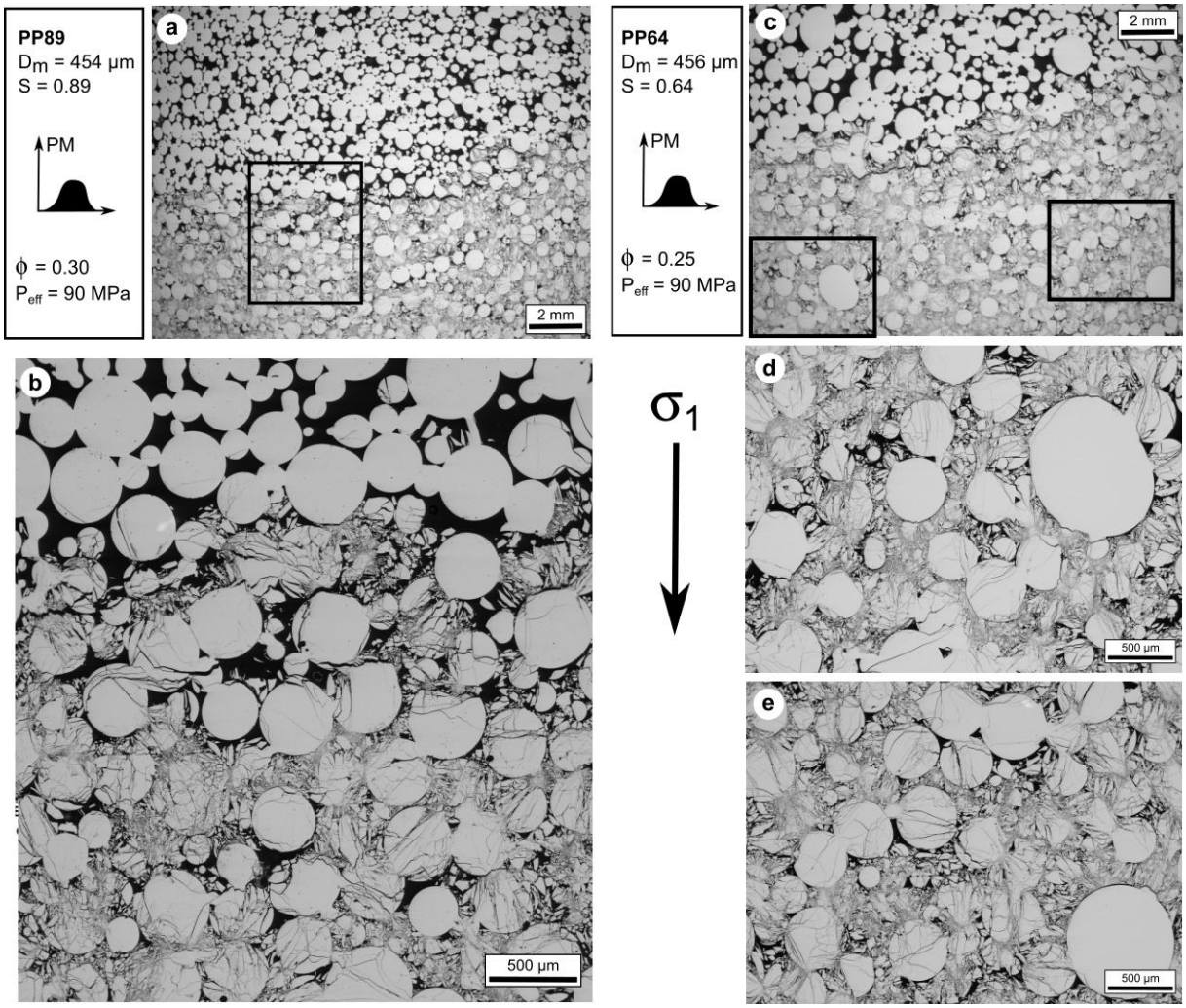

Figure 5.9 Representative backscattered scanning electron microscope images of the microstructure of polydisperse synthetic samples deformed under triaxial compression up to stresses beyond C*. At a degree of dispersivity of 0.89 and porosity of 0.30 (a), mechanical compaction features spread from the extremities towards the centre of the sample and form (b) conjugated compaction bands. At a degree of dispersivity of 0.64 and a porosity of 0.25, (c) mechanical compaction spread from the extremities towards the centre of the sample, (d, e) without affecting the bigger grains. Black: porosity, grey: glass.

In the bidisperse samples, delocalised cataclasis was observed (Figure 5.10). Regardless of the relative percentage of large grains compared to small grains, the microstructural data reveal that the larger grains remained intact but that the smaller grains were extensively crushed. Such observation is in agreement with the mechanical data, where the stress-strain curves for the bidisperse samples show almost no stress drops (Figure 5.6).

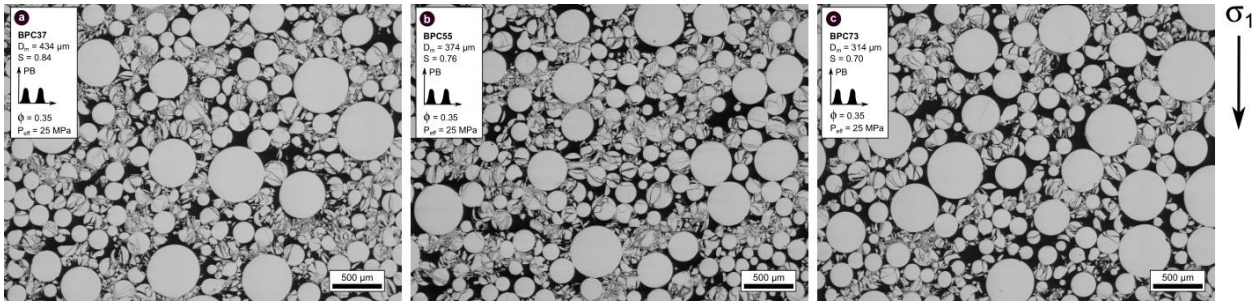

Figure 5.10 Representative backscattered scanning electron microscope images of the microstructure of bidisperse synthetic samples deformed under triaxial compression up to stresses beyond C*. From (a) to (c), the ratio of small grains to big grains decreases. For all distributions, delocalised compaction, where small grains are crushed while bigger grains remain intact, is observed. Black: porosity, grey: glass.

5.5 Discussion

5.5.1 Comparison to monodisperse sintered glass beads samples

The deformation of sintered glass bead samples with monodisperse grain size distributions and different mean grain diameters have been studied in the previous chapter. In the following, results obtained for bidisperse and polydisperse synthetic samples are compared to those presented in Chapter 4. Figure 5.11 shows a comparison of mechanical data obtained on monodisperse, bidisperse and polydisperse samples under hydrostatic and triaxial compression. When submitted to hydrostatic loading, bidisperse and monodisperse synthetic samples behave differently in two main aspects: (1) at constant porosity, the stress required to reach P* is higher for a sample with a monodisperse distribution than for all samples with a

bidisperse distribution, whatever the dispersivity; (2) while the transition to inelastic deformation at P* is very sudden for the monodisperse sample, it is more progressive for the bidisperse samples. The difference in the stress required to reach P* might be partly due to a difference in grain size, which was found to be negatively correlated to the stress required for the onset of inelastic compaction in monodisperse samples (Chapter 4; Carbillet et al., 2021).

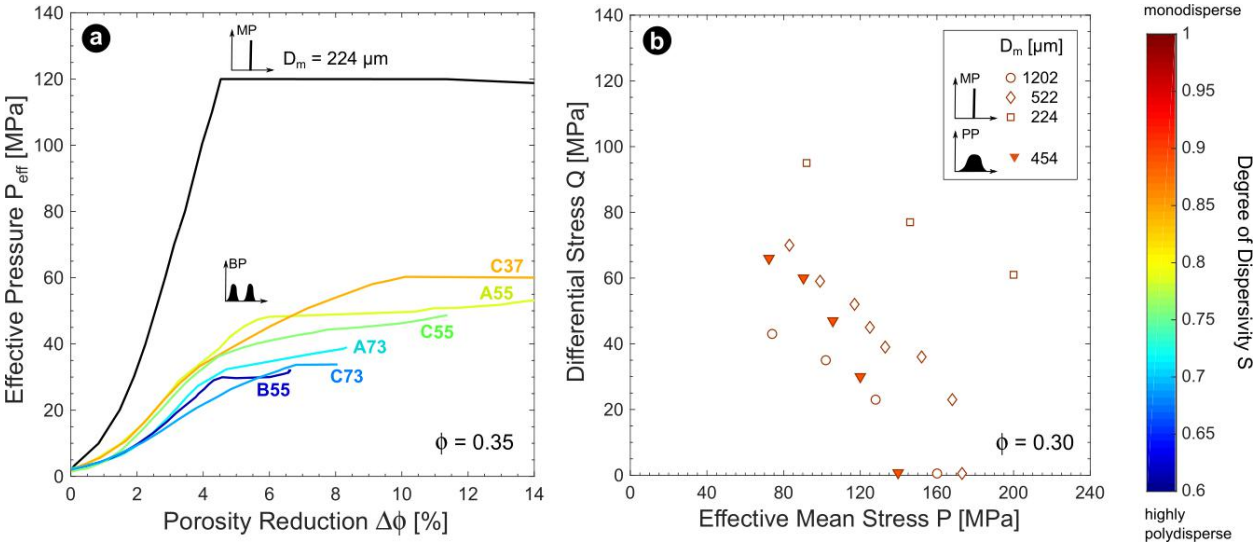

Figure 5.11 (a) Hydrostatic curves for synthetic samples with a porosity of 0.35 and with bidisperse (BP, coloured curves) and monodisperse (MP, black curve) grain size distributions. (b) Compactive yield caps of synthetic samples with a porosity of 0.30 and polydisperse (PP, solid triangles) and monodisperse (open symbols) grain size distributions. The mean of the grain size distributions is given as D_m and the degree of dispersivity S is colour coded using the colour scale on the right.

In Figure 5.11(a), the mean grain diameter of the monodisperse sample is 224 µm whereas the mean grain diameters of the bidisperse samples are in the range 314–998 µm. Moreover, complexities might arise from the fact that the bidisperse synthetic samples are prepared with variable proportions of large, medium, and small beads (Figure 5.1). Therefore, the differences in strength due to changes in the grain size are integrated with those due to changes in the dispersivity of the grain size distribution. For instance, P* is slightly higher for

the distribution BPC73 than for BPA73 although the latter is less disperse and therefore expected to be lower. The difference in P* might be explained by the fact that the distribution BPA73 contains 70 vol% of large beads and 30 vol% of medium beads while the distributions BPC73 contains no large beads but 70 and 30 vol% of medium and small beads, respectively. However, although differences in the relative proportion of large grains to small grains might explain some of the difference in P*, it is not sufficient to explain the very low P* values found for the bidisperse samples compared to monodisperse samples. Furthermore, a comparison of the compactive yield cap for polydisperse samples with those for monodisperse samples shows that for the same porosity and similar mean grain diameter, the stresses required to reach C* are lower for the polydisperse synthetic samples (Figure 5.11(b)). Such an observation concurs with the result that samples with a very disperse grain size distribution undergo inelastic compaction at lower stress states than those with a more closely clustered distribution, closer to the monodisperse limit.

Under an externally applied stress, the bulk mechanical response of granular rocks is controlled by the arrangement of forces at the grain-scale, i.e., by the morphology of the force chain network, defined as the subset of grain-to-grain contacts carrying the largest forces in the system (Guéguen & Boutéca, 2004). Indeed, mechanical deformation is predicted to occur in the strong force network, which carries a force larger than the average force in the system (Zhang et al., 2017). Moreover, discrete element simulations suggest that the strong network only involves a selected number of grains within the microstructure (Peters et al., 2005; Vallejo et al., 2005). To probe the influence of the grain size distribution of granular materials on the geometry and distribution of the force chains, diverse methods of numerical modelling have been developed over the past decades (Papadopoulos et al., 2018). In the present study, the mechanical data obtained using simplified two-phase granular samples suggest that increasing the dispersivity of the grain size distribution decreases the stress require to reach inelastic compaction. This is in agreement with the results from both Lan et al. (2010) and Peng et al. (2017) who reported that numerical samples with a more monodisperse grain size distribution fail at higher stress under uniaxial compression. However, Muthuswamy and Tordesillas (2006) also found that straight force chains with a higher degree of branching, which results in a macroscopically stronger granular material, are more likely to form in more disperse samples, which in their case also have a lower average packing density. In detail, the microstructural data show that deformation affects the small grains more than the large grains,

suggesting that force chains would develop preferentially in smaller particles (Figures 5.9, 5.10). Desu and Annabattula (2019) also reported that smaller grains in a polydisperse assembly have a lower coordination number, the influence of which on the grain strength was measured by Saadi et al. (2017) who showed that grains with a higher coordination number were stronger.

Therefore, the lower critical stress values found for bidisperse and polydisperse synthetic samples (Figure 5.11) are likely due to the homogeneity of the monodisperse sample compared to the bidisperse and polydisperse samples. As the shape and elastic properties of all glass beads are the same, most grains in the monodisperse samples are crushed at the same critical state of stress under hydrostatic compression (Figure 5.11(a)). On the contrary, in the bidisperse and polydisperse samples, normal forces induced at the grain contacts likely reach the critical value at different values of the externally applied effective pressure, resulting in an earlier and more gradual transition to inelastic deformation for the bulk sample. This can explain some of the differences between the shape of the hydrostatic curves in Figure 5.11(a).

5.5.2 Comparison to natural porous rocks

The preceding chapters showed that sintered glass bead samples, which can be prepared to contain predefined porosities and grain size distributions so that these parameters can be studied in isolation, are suitable analogues for natural sandstones. Therefore, the results presented in this study can be compared with those reported for natural sandstones of similar porosity to gain insights into the influence of grain size distribution on the mechanical behaviour of natural porous rocks. In Figure 5.12, mechanical data for monodisperse, bidisperse and polydisperse synthetic samples are compiled with mechanical data for Bleurswiller sandstone (France) and three sandstones from Boise (Idaho, USA), which will be referred to as Boise I, Boise II, and Boise III. Boise I is a coarse-grained and poorly-sorted sandstone with a porosity of 0.35 that is composed of 40% quartz and has a clay content of 6% (Krohn, 1988). Zhang et al. (1990) studied the hydrostatic behaviour of Boise I and reported a value of 75 MPa for P^* (Figure 5.12(a)). Boise II, with a similar porosity of 0.35 and composed of 67% quartz and a clay content of 13%, was studied by Baud et al. (2000) under both triaxial and hydrostatic compression and reported a value of 42 MPa for P^*

(Figure 5.12(a)). Using thin sections of the Boise I and Boise II sandstones studied by Zhang et al. (1990) and Baud et al. (2000), respectively, a grain size analysis was performed following the method of Heap et al. (2017) to determine the grain size distributions and compute the corresponding degrees of dispersivity. Results are summarised in Figure 5.12(d).

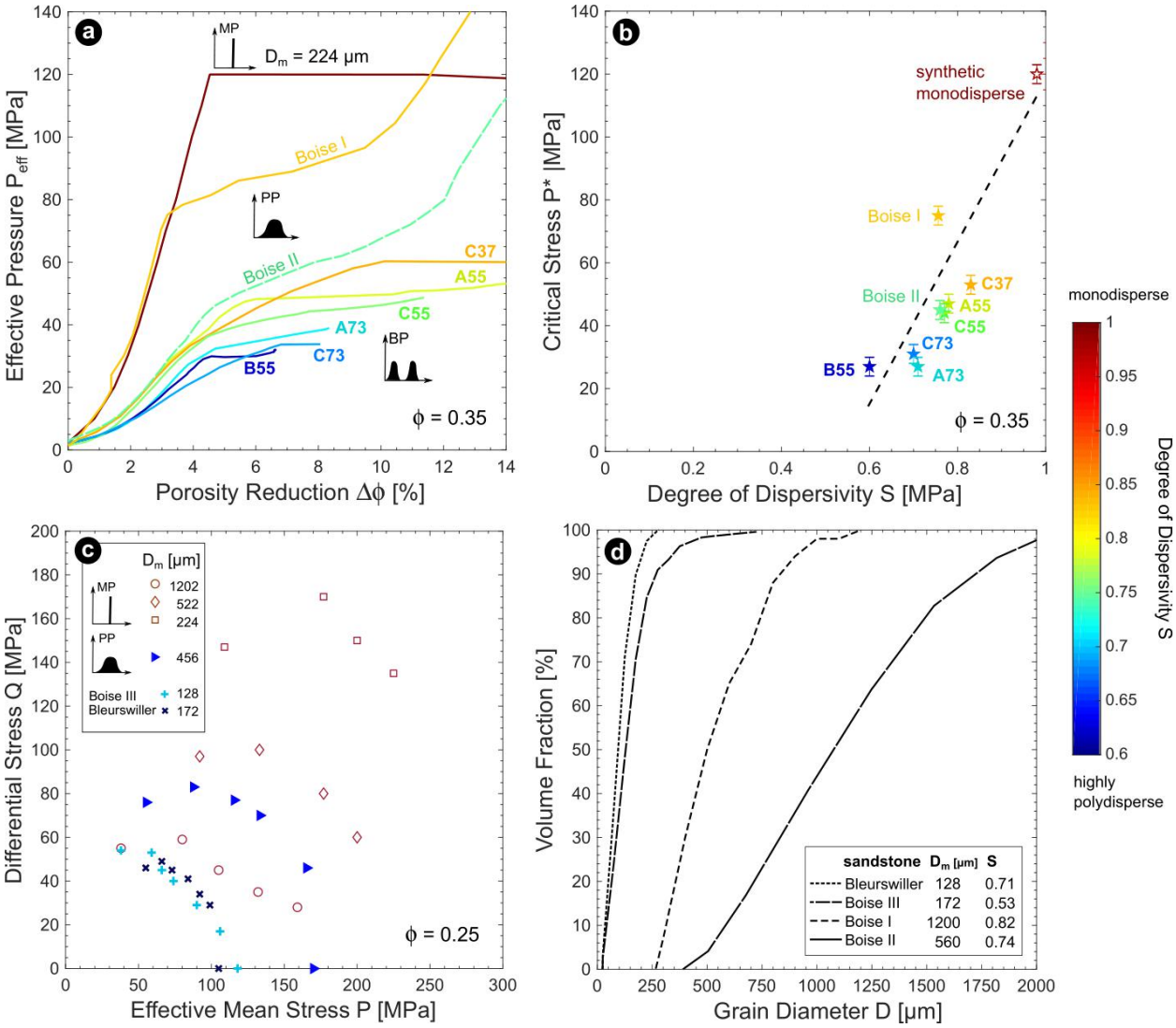

Figure 5.12 Comparison between mechanical data obtained on sintered glass bead samples and mechanical data reported for natural sandstones. (a) The hydrostatic curves of the bidisperse synthetic samples compared to that of a monodisperse synthetic sample (Carbillet et al., 2021) and of Boise I (Zhang et al., 1990) and Boise II (Baud et al., 2000) sandstones. (b) P* values are presented as a function of the degree of dispersivity and fitted using a linear regression. (c) Critical stress values reported for monodisperse synthetic samples (Carbillet et

al., 2021) and for Boise III and Bleurswiller sandstones (Cheung et al., 2012) are compiled with those for polydisperse samples. (d) The grain size distributions of the natural sandstones which the synthetic samples are compared to were used to derive the mean grain diameter D_m and dispersivity S. The latter is colour coded using the colour bar on the right.

The results were also compared to those published in Cheung et al. (2012) for Bleurswiller and Boise III sandstones, both with a porosity of approximately 0.25 and very similar petrological compositions (approximately 60% quartz and a clay content of 11%). The mean grain diameter D_m and dispersivity S were determined using the grain size distributions reported by Cheung et al. (2012) for these two sandstones (Figure 5.12(d)). Comparing the hydrostatic curves of Boise I and II with those for bidisperse and monodisperse synthetic samples, several observations can be made. First, at a fixed porosity of 0.35, the stress required to reach the onset of grain crushing for Boise I is higher than that for Boise II, which are both higher than that for bidisperse synthetic samples and lower than that for a monodisperse synthetic sample. Such an observation cannot be solely explained by differences in the mean grain diameter, which was found to be a first-order control microstructural parameter (Chapter 4; Carbillet et al., 2021). Indeed, the mean grain diameters for Boise I and Boise II were estimated to be 1200 and 560 µm, respectively, while the monodisperse and bidisperse samples have grain diameters of 224 µm and 314–998 µm, respectively. Considering the influence of mean grain diameter only, the stress value P^* would be expected to be higher for Boise II than for Boise I, both being lower than that for the monodisperse synthetic sample and falling in the same range than that for the bidisperse samples. However, the complexities that arise in the compilation in Figure 5.12(b) highlight a possible influence of the degree of dispersivity and the modality of the grain size distribution. Boise I and Boise II both have a monomodal grain size distribution (Figure 5.12(d)) but a degree of dispersivity lower than that of the monodisperse sample ($S = 0.98$) and the hydrostatic curves reported for these two natural sandstones are indeed found to fall between those for the bidisperse and monodisperse synthetic samples. Moreover, the dispersivity found for Boise II is 0.74 whereas it is 0.82 for Boise I, for which P^* is higher. Therefore, the compilation in Figure 5.12 suggests, in agreement with the results for synthetic samples, that the more monodisperse the grain size distribution, the higher the pressure required to reach

P^*. The second observation is that there are important differences in the shape of the hydrostatic curves of Boise sandstones and of the monodisperse synthetic samples, especially in terms of the sharpness of the transition to inelastic compaction (i.e., P^*). The hydrostatic curves reported for Boise sandstones are much more similar to those for the bidisperse samples than the monodisperse sample. As discussed in the previous subsection, this is likely due to the heterogeneity of the microstructure of the natural sandstones in comparison to the highly homogeneous monodisperse synthetic sample.

Figure 5.12 also includes a compilation of the compactive yield caps for polydisperse samples, monodisperse synthetic samples (Chapter 4; Carbillet et al., 2021), and Bleurswiller and Boise III sandstones (Cheung et al., 2012). Such compilation reveals that, at a fixed porosity of 0.25, the stresses required to reach inelastic compaction (C^* and P^* values) are much lower for the two natural sandstones than that for all the synthetic samples, whatever their dispersivity. Such an observation cannot be explained by their mean grain diameters: Bleurswiller and Boise III both have lower mean grain diameters (172 and 128 µm, respectively) than the synthetic samples, which should result, according to the data presented in Chapter 4 (Carbillet et al., 2021), in higher critical stress values than those for the synthetic samples. Moreover, although Bleurswiller and Boise III have very different degrees of dispersivity, their compactive yield caps are almost superposed. Therefore, Figure 5.12(c) also highlights the importance of other microstructural parameters, which may have a stronger control on the compactive strength may be stronger than that of dispersivity. Overall, there is much to learn by comparing data for polydisperse and bidisperse synthetic samples with those for natural rocks, but such comparison also emphasises the complexity of the mechanical behaviour of natural rocks. Therefore, although the observations made using simplified two-phase materials with controllable microstructural attributes cannot simply be transposed to natural rocks, for which multiple microstructural attributes can vary widely and simultaneously, synthetic and numerical samples provide us with means not only to deconvolve and study the isolated influence of microstructural attributes but also to explore the cross-property relationships (Cilli & Chapman, 2021; Torquato, 2002) and ultimately, to find which microstructural attributes are the most important for the mechanical behaviour of porous rocks.

5.5.3 Compaction localisation

Compaction localisation has been extensively studied in the past decades because it can significantly reduce rock permeability and therefore compartmentalise fluid flow (Olsson et al., 2002; W. L. Taylor & Pollard, 2000; Vajdova et al., 2004). Compaction bands have been observed in natural rocks in the field (Aydin & Ahmadov, 2009; Eichhubl et al., 2010; Fossen et al., 2007, 2011; Tudisco et al., 2015) but also in natural rocks deformed in the laboratory (Baud et al., 2004; 2006; Charalampidou et al., 2013; Fortin et al., 2006; Heap & Violay, 2021; Louis et al., 2006; Louis, Wong, et al., 2007; Olsson, 1999) as well as in numerical samples submitted to compressive states of stress (Marketos & Bolton, 2009; Nguyen et al., 2016; B. Wang et al., 2008). Holcomb et al. (2007) reviewed the state of knowledge on localised compaction and highlighted the need for identifying the microstructural parameters that can promote or inhibit compaction localisation. Before and since then, experimental studies on natural and numerical samples showed that compaction bands were more likely to develop in samples with more uniform grain size distributions and, more generally, in more homogeneous samples (Cheung et al., 2012; Das et al., 2011; Katsman et al., 2005; Louis et al., 2009; Louis, Baud, et al., 2007; Wang et al., 2008).

Figure 5.13 shows the microstructure of synthetic samples with different grain size distributions and of Bleurswiller and Boise sandstones deformed to beyond the onset of shear-enhanced compaction C^*. Discrete compaction bands can be seen in a monodisperse synthetic sample with a porosity of 0.35 and a mean grain diameter of 224 µm (Figure 5.13(a)), in a polydisperse synthetic sample with a porosity of 0.30 and a mean grain diameter of 454 µm (Figure 5.13(b)) and in Bleurswiller sandstone with a porosity of 0.25 and a mean grain diameter of 128 µm (Figure 5.13(e)). Although the discrete bands which developed in the monodisperse are 2-3 grains-thick but 1-2 grains-thick in the polydisperse sample, the thickness of the bands is approximately 500 µm in both samples (Figure 5.13(a)(b)). In the polydisperse sample, the discrete bands appear to propagate for the most part in the smaller grains of the assembly, the size of which may therefore control the band thickness. Microstructural observations on the more polydisperse sample (Figure 5.13(c)) with a porosity of 0.25 and grain diameter of 456 µm are somehow ambiguous: compactive deformation is found to progress as a front from both ends of the sample, within which small, conjugated bands are seen between intact larger grains. These microstructural observations

are in agreement with observations previously reported for natural sandstones and results of numerical simulations of granular porous rocks, which show that compaction bands appear to form first from the extremities of the sample and progress towards the centre with increasing axial strain (Baud et al., 2004; Heap, Brantut, et al., 2015; Tembe et al., 2008; Townend et al., 2008; Wong et al., 2001). Using X-ray tomography and computational simulations to study compaction localisation in a high-porosity limestone, Wu et al. (2020) also reported similar compaction band patterns, where compaction fronts initiate from the two ends of samples and progress toward the centre with progressive axial strain increments.

Delocalised cataclastic flow is observed in all the bidisperse samples (Figure 5.13(d)). Similarly, delocalised compaction, where small grains are crushed and large grains are intact, was observed in Boise sandstone (Figure 5.13(f); Cheung et al., 2012). Using a discrete element model for the development of compaction localisation in granular rocks, Wang et al. (2008) also reported very similar results where discrete compaction bands grew in relatively homogeneous granular aggregates, while more diffuse compaction localisation developed in more heterogenous assemblies. These authors also showed that compaction localisation is ultimately inhibited in very heterogeneous aggregated which fail by distributed cataclastic flow. Katsman et al. (2005) observed a similar evolution in the failure micromechanics (i.e., localised to delocalised compaction) in network assemblies with either no, small and large disorder.

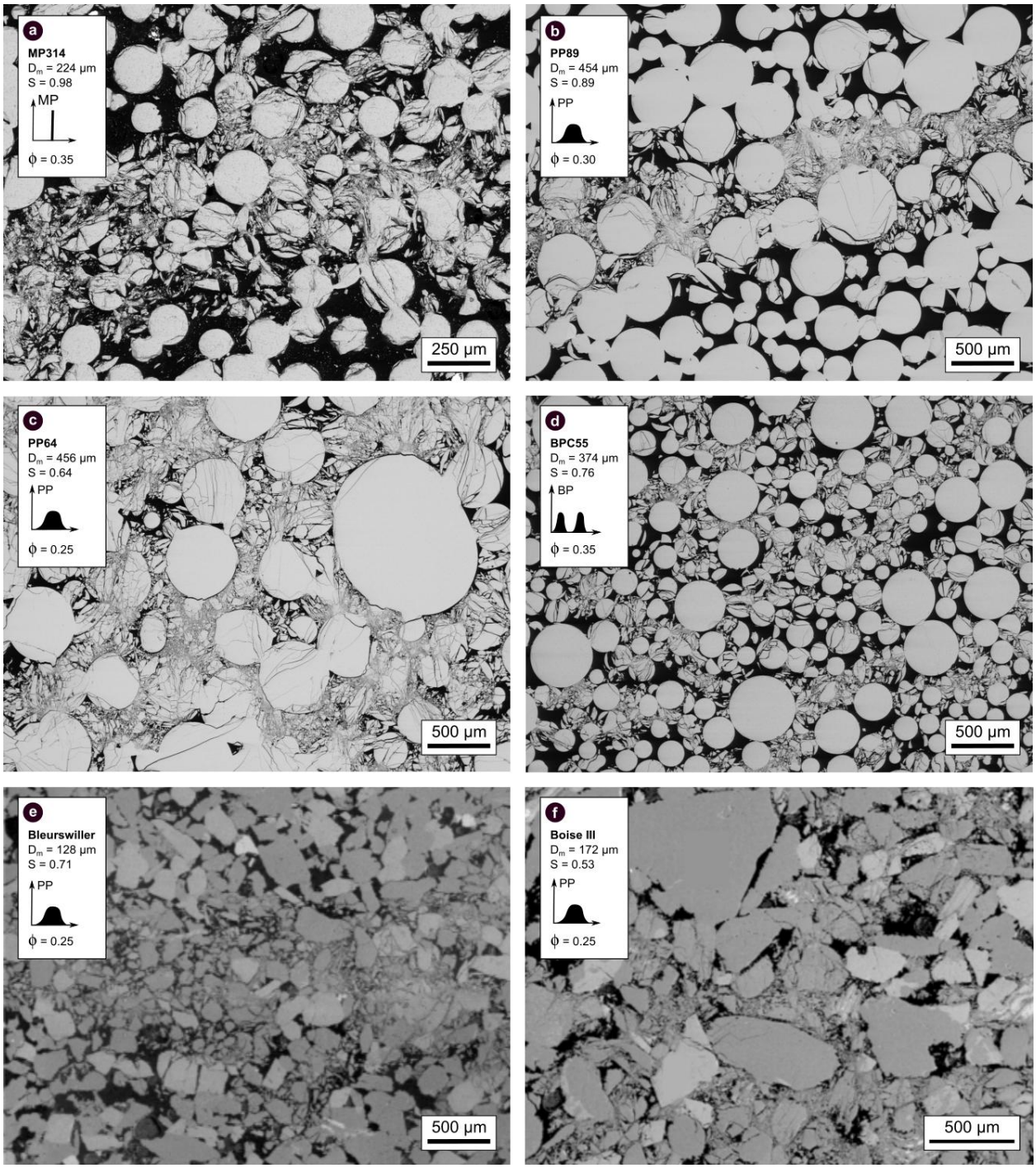

Figure 5.13 Backscattered scanning electron microscope images of the microstructure of sintered glass bead samples with (a) a monodisperse grain size distribution, (b)(c) a polydisperse distribution and (d) a bidisperse distribution compared to that found in Bleurswiller and Boise sandstones (Cheung et al., 2012), after triaxial testing in the regime of

shear-enhanced compaction. The type of distribution, mean grain diameter and degree of dispersivity of each sample are indicated on the corresponding micrograph.

Overall, the data of Chapter 5 suggest that there is a continuous transition from localised to delocalised compaction as the dispersivity of the grain size distribution increases (i.e., when S decreases). Such an observation might be due to changes in the pore space morphology, where local heterogeneities in the pore space, reduced as the width of the grain size distribution increases, act as stress concentrators and promote the growth of compaction bands. Xiong et al. (2021) reported that a high ratio between the number of macropores and micropores promotes compaction localisation. Abdallah et al. (2021) also found, using digital image correlation on deformed Saint Maximin limestone (France) samples, that porosity heterogeneities control the initiation and propagation of compaction bands, which tend to grow in the high-porosity areas of the samples. On the contrary, Baud et al. (2015) reported that the compaction bands formed in Bleurswiller sandstone propagated so as to avoid porosity clusters, which act as barriers to the growth of compaction bands. In this study, where the samples tested are simplified two-phase materials, the grain and pore size distributions are the inverse of one another. The effect of increasing the width of the grain size distribution, and therefore decreasing the width of the pore size distribution, is to progressively inhibit compaction localisation.

Figure 5.14 presents a plot of the degree of dispersivity as a function of porosity for samples that failed by compaction localisation (stars) or by cataclastic flow (squares). Taking into account the results of Cheung et al. (2012) for natural sandstones and Wang et al. (2008) for numerical samples, compaction bands are observed at degrees of dispersivity down to 0.71, a transitional deformation regime between discrete compaction bands and delocalised cataclasis is observed at $S = 0.64$ and delocalised compaction is reported at $S = 0.53$. Although bidisperse synthetic samples have degrees of dispersity in the range where compaction bands would be expected, they do not exhibit any form of compaction localisation. This could likely be explained by the fact that the parameter S does not encompass differences in terms of the modality of the grain size distribution and therefore underestimates the degree of heterogeneity of the microstructure of bidisperse samples.

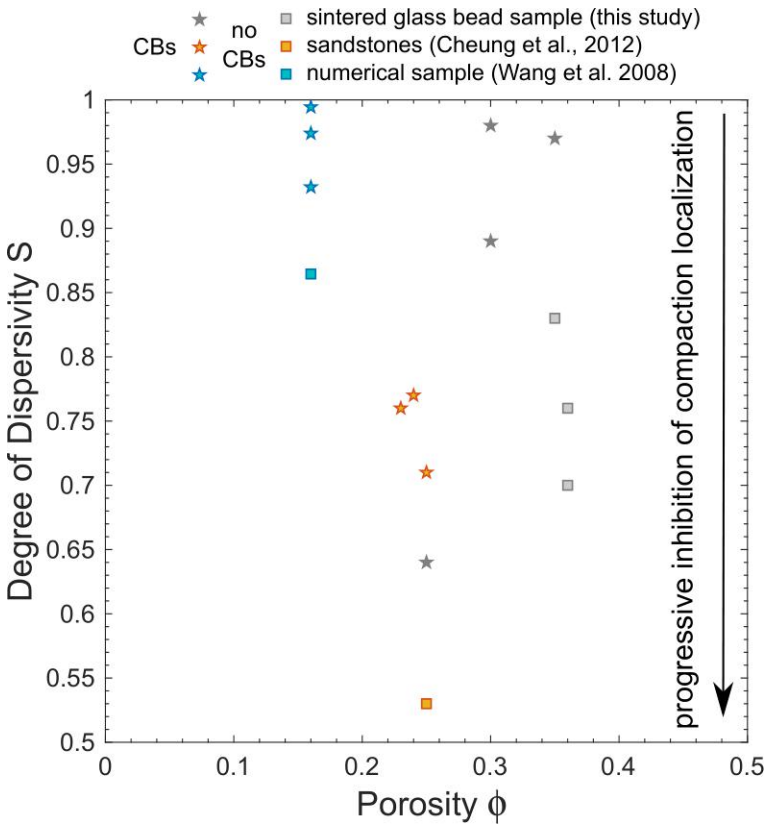

Figure 5.14 The influence of the degree of dispersivity and the porosity on the propensity for compaction localisation. Results for sintered glass bead samples are compiled with that reported by Wang et al. (2008) for numerical samples and that for natural sandstones by Cheung et al. (2012).

Moreover, Desu and Annabattula (2019) reported that the larger the difference in size between the grains, the stronger the effect of the grain size distribution on the contact force distributions. Thus, the effect of mixing grains with very different sizes, as is the case for the bidisperse samples, would likely always lead to the inhibition of compaction localisation. Where delocalised compaction is observed (Figure 5.12(d)(f)), it appears as though the deformation is concentrated on the smaller grains whilst larger grains remain intact. As previously discussed, such an observation might be explained by the high coordination number of larger grains in a polydisperse assembly, rendering these large grains more difficult to break. However, it is plausible that the influence of dispersivity on compaction localisation varies with porosity. Compaction bands have been observed in sandstones with porosities of 0.13-0.28 (Wong & Baud, 2012). For the sintered glass bead samples, although discrete compaction bands have been observed in a monodisperse sample with a porosity of 0.35 (Chapter 4), the absence of compaction bands in bidisperse synthetic samples (grey squares, Figure 5.14) could also be due to their high porosity. Finally, more experiments are now required to populate Figure 5.14 and to better understand the influence of microstructure on compaction localisation in porous granular rocks.

5.6 Conclusions

Clastic sediments found in the Earth's crust are formed by the accumulation of individual minerals and rock fragments rounded by transport and sorted by deposition. However, great structural heterogeneity is still encountered in these sedimentary rocks, which span a wide range of porosity, grain and pore size and shape, and/or petrological composition. Within the crust, the microstructural attributes of a clastic rock determine its mechanical response to the in-situ state of stress. Therefore, understanding the influence of microstructural parameters on the mechanical behaviour and failure mode of porous crustal rocks is critical for industrial applications such as reservoir (water, hydrocarbon and geothermal) monitoring and management but also, for instance, for assessing the risk of natural hazards such as slope collapses and landslides.

In the previous chapter, sintered glass bead samples with monodisperse grain size distributions were used to study the influence of porosity and grain size on the mechanical compaction of porous rocks. This work is extended in the present chapter by using synthetic porous materials to investigate the effect of changing the type (modality) and width of the grain size distribution on mechanical behaviour, while keeping other microstructural attributes constant. In the following, a brief summary of the main results on the influence of the grain size distribution on the mechanical behaviour of porous clastic rocks is given.

Under both hydrostatic and triaxial compression, the stress required to reached inelastic compaction is lower for bidisperse and polydisperse synthetic samples than for monodisperse synthetic samples. This result might be explained by the fact that more uniform grain size distributions promote the formation of a more homogeneous contact force network within the microstructure, resulting in a macroscopically stronger sample. The microstructural data also show that compaction localisation is inhibited in synthetic samples with a bidisperse grain size distribution. Indeed, distributed cataclastic flow is observed in the bidisperse samples deformed under triaxial compression, where the largest grains remained intact while the smaller grains were extensively crushed. In polydisperse samples, the microstructural data suggest that a progressive transition might occur from compaction localisation to delocalised cataclasis as the dispersivity of the grain size distribution increases. Indeed, discrete compaction bands are observed in the less polydisperse sample, in agreement with the

mechanical data, while the deformation features observed in the more polydisperse sample are found in compaction fronts at both ends of the sample but within which deformation features are more diffuse. As for the bidisperse samples, the largest grains are found to remain intact in the most deformed zones in the polydisperse samples with a high dispersivity. This result suggest that well-sorted sandstones could develop discrete compaction bands, acting as barriers for fluid movements and therefore leading to a compartmentalisation of fluid flows. On the contrary, more heterogeneous and poorly-sorted sandstones would limit the development of compaction localisation and thus occurrences of fluid pressurisation in, for instance, hydrocarbons or geothermal reservoirs.

Chapter 6

Conclusions and Perspectives

6.1 Conclusions

As stated in the introduction chapter, this thesis set up to investigate the following issues:

1. Can synthetic rocks made by sintering glass beads satisfactorily simulate the hydromechanical behaviour of porous crustal rocks and therefore be used to unravel the contribution of specific microstructural attributes on bulk hydromechanical properties?

2. All else being equal, what if the effect of total porosity/mean grain size variations on the onset of inelastic compaction?

3. How do the width and shape of the grain size distribution influence the mechanical behaviour and failure mode of porous granular rocks?

In the following, these questions are addressed in the light of the results presented in the preceding chapters.

6.1.1 Suitability of sintered glass beads as analogues for porous crustal rocks

Chapter 3 provided a large dataset of petrophysical properties for the sintered glass beads samples: porosity, specific surface, P- and S-wave velocities, thermal conductivity, electrical conductivity, gas-permeability and uniaxial compressive strength. Comparing these data to those reported for the monomineralic very-well sorted Fontainebleau sandstone (which was extensively studied due to its occurrence over a large range of porosity while other

microstructural attributes remain almost constant). Chapter 3 highlighted first of all the excellent agreement between the trends in elastic wave velocities, formation factor and permeability as a function of porosity for Fontainebleau sandstone, which has a mean grain radius of approximately 125 μm, and those for monodisperse synthetic samples with a mean grain size of 112 μm. Further, using the P- and S-wave velocity in quartz and air in the Raymer-Hunt-Gardner equation, the thermal conductivity of silica glass in the Rayleigh-Maxwell equation and the equivalent channel model to relate the permeability to the formation factor, the experimental datasets for sintered glass beads could be very well modelled. Such consistency in the transport properties of the synthetic samples with that of natural sandstones and with petrological laws validated against natural rocks, demonstrate that sintered glass bead samples can be used to accurately replicate the microstructural geometries of porous natural rocks.

6.1.2 Porosity and grain size control on the mechanical behaviour of crustal rocks

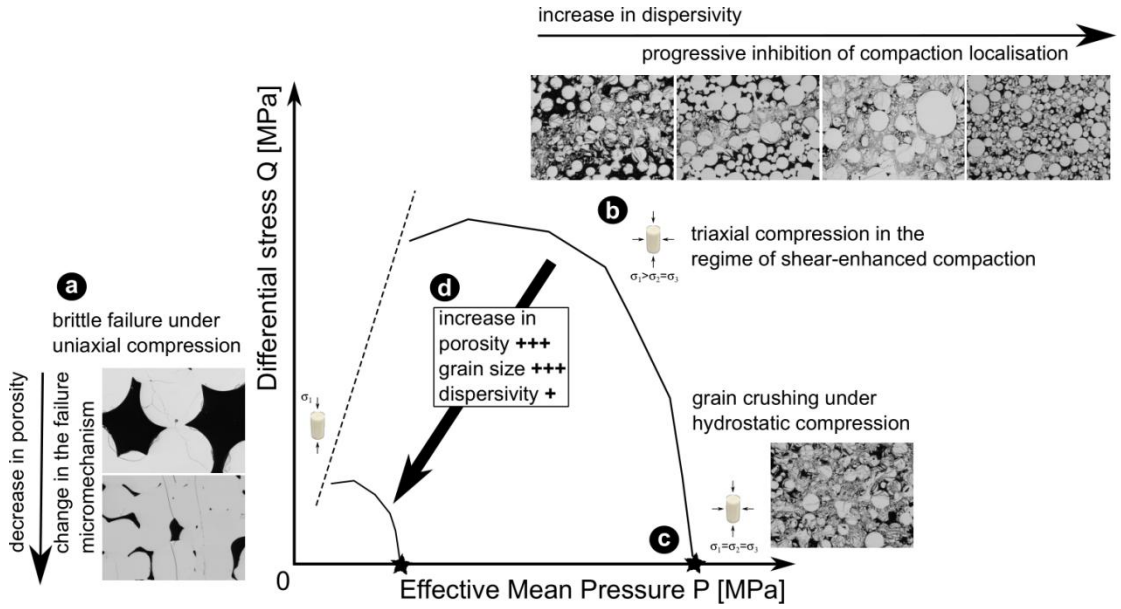

Figure 6.1 The mechanical behaviour and failure mode of sintered glass bead samples: influence of porosity, grain size and dispersivity.

The primary findings of Chapter 3 to 5 are summarised in Figure 6.1. Chapter 3 comprises a UCS dataset for monodisperse synthetic samples with four different grain sizes and porosity

between 0.06 and 0.33. In this porosity range, UCS values span a similar range to that reported for fine grained and coarse-grained sandstones. At a given porosity, the higher the mean grain size, the lower the strength. At a given grain size, the strength of synthetic samples decreases almost linearly with porosity. The microstructural data (Figure 6.1(a)) suggest that the mechanism for failure at the grain-scale evolves from pore-emanated cracking in low-porosity samples, which have a non-granular microstructure, to Hertzian cracking in high-porosity samples, which have a granular microstructure. Such transition might explain the linearly in the porosity-UCS trend in synthetic samples, which has not been reported for natural sandstones but for Leitha limestone, the microstructure of which also transitions from granular to non-granular as porosity decreases by progressive cementation. The threshold porosity for this microstructural transition is positively related to the grain size.
Because crustal rocks span the whole range of microstructures between the granular and non-granular endmembers, Chapter 3 demonstrates that sintered glass bead samples can provide hydromechanical results that have applications not only for natural sandstones but also for other granular rocks such as tuffs and some limestones.

Suites of deformation experiments were carried out on sintered glass bead samples with porosity of 0.18 - 0.38 and mean grain radius of 112 - 601 μm in order to study the influence of porosity and grain size on the mechanical behaviour and failure mode of porous rocks (Chapter 4). The porosity control was investigated while keeping all other microstructural parameters constant. Similarly, the influence of the mean grain size of samples with a grain size distribution close to the monodisperse limit was studied while keeping all other microstructural parameters constant. Overall, results showed that, under hydrostatic compression, the onset of grain crushing was reached at a pressure (star symbol on the x-axis in Figure 6.1(c)) which decreases with increasing porosity or increasing mean grain radius. Under triaxial compression, the brittle-ductile transition occurred at a stress state which decreases with increasing porosity or mean grain radius (Figure 6.1(c)). The stress for the onset of shear-enhanced compaction is multiplied by two for a decrease in porosity of 0.06 and for a decrease in average grain diameter of 0.50 mm. Such behaviour results in a decrease in the size of the failure envelope with increasing porosity or mean grain radius (Figure 6.1(d)).

Importantly, results presented in Chapter 4 highlighted that mean grain size has an influence on the mechanical behaviour as significant as porosity. Therefore, given the broad range of mean grain size that natural porous rocks span, grain radius should systematically be taken into account when studying and modelling the mechanical properties of porous rocks. For example, in the context of depletion-induced reservoir subsidence, measuring the grain size of each reservoir formation will help assess which sedimentary layer will compact first and/or to the highest extent. Indeed, as a decrease of 250 μm in grain radius yields an increase of 50% in the stress to reach inelastic compaction under triaxial compression, coarse-grained reservoir formations can likely undergo compaction earlier and more intensely than fine-grained formations, even if they have very similar porosities.

6.1.3 The influence of grain size distribution on the mechanical behaviour of crustal rocks

In the study of the hydromechanical properties of porous rocks, previous authors pointed out the need for considering the influence of the whole grain size distribution rather than mean grain size, which can only partially describe microstructural geometries (Atapour et al., 2018). This issue was specifically addressed by performing a suite of deformation tests on sintered glass beads prepared with bidisperse and polydisperse grain size distributions (Chapter 5). The main findings of Chapter 5 are summarised in Figure 6.1.

Overall, Chapter 5 showed that an increase in dispersivity decreases the stress and pressure required for the onset of inelastic compaction under triaxial and hydrostatic compression, respectively (Figure 6.1(b)(c)(d)). However, the dispersivity of the grain size distribution exerts a second-order control on the mechanical behaviour of porous rocks in comparison to porosity and mean grain size (Chapter 4).

Chapter 5 also demonstrated that the grain size distribution strongly influences the microstructural deformation features which develop under triaxial compression in the ductile regime. Whilst discrete compaction formed in very well-sorted samples, an increase in dispersivity appears to be accompanied by a progressive transition from localised to delocalised deformation features. Compaction bands were observed down to a degree of dispersivity of 0.65 (where 1 is the monodisperse limit) in synthetic samples, which corresponds to a grain diameter distribution with a minimum of 150 μm and a maximum of 1300 μm, and of 0.70 in natural sandstones. At a degree of dispersivity of 0.53 (Boise

sandstone), compaction localisation was inhibited and deformed samples showed delocalised cataclastic flow. Moreover, a change in the modality of the grain size distribution from monomodal to bimodal inhibits compaction localisation, even at a degree of dispersivity of 0.83. Such an observation reveals the importance of the difference between the sizes of the grains, where samples that contain grains with multiple sizes are more likely to undergo compaction localisation than samples that contain grains with only two different sizes. This also emphasises the fact that the degree of dispersivity might not be the most adequate parameter to assess the microstructural heterogeneity of a porous rock. Indeed, although Chapter 5 provides results that help sharpen the understanding of the control of grain size distribution, dispersivity remains a difficult property to work with as it exists in and amongst other complex parameters. For example, changing the dispersivity also changes the mean pore diameter, which also influences mechanical behaviour. Furthermore, under an externally applied load, the place and manner in which microcracks initiate and propagate vary not only with grain size distribution but also with many other parameters such as the grain sphericity, grain stiffness and packing density, which Chapter 5 does not take into account. Futures studies on synthetic materials should therefore look at the influence of other microstructural attributes such as the grain shape distribution, the cement content, the presence of weaker grains or beddings on the mechanical behaviour and failure mode of porous rocks.

6.2 Perspectives

The use of synthetic materials to model the response of natural rocks to loading dates back to the earliest works of rock mechanics. One notable example is the photoelasticity phenomenon which was first reported in silicate glass (Brewster, 1815) and allowed to visualise how stress is distributed in a loaded material (Frocht, 1944). The great variety of materials employed to model real rocks was classified by Stimpson (1970) and includes cemented and uncemented granular materials and non-granular plastics and metals. More recently, three-dimensional printing technology was developed and begot a new family of synthetic rocks prepared using polymers. The motivation for using synthetic materials is to be able to independently study the control of specific microstructural attributes. In addition, synthetic rocks should help unravel issues of reproducibility or lack of samples which arise when performing destructive deformation experiments on rare and complex natural rocks. In the following, the advantages

and limitations of using sintered glass beads as natural rock analogues is discussed, focusing in particular on the ability to provide meaningful predictive conclusions for porous crustal rocks.

The use of the viscous sintering of glass beads to prepare synthetic rocks arose largely from the simplicity of the process, the very small number of constituents (which chemicophysical properties are very well constrained), and the broad textural similarities in relation to porous crustal rocks (Chapter 2). Furthermore, this method offers the possibility to deconvolve the porosity and the grain size distribution over a broad range of values: the porosities that can be achieved for a given grain size distribution are comprised between the initial packing porosity (approximately 0.4; Beard & Weyl, 1973) and 0.06-0.10 and the grain size distribution can be designed in the limit of the sizes of glass beads which can be purchased or sieved in the laboratory (while adapting the bulk dimensions of the samples to allow for viscous sintering, Chapter 2). Overall, the use of viscous sintering has allowed for the preparation of identical samples, so that tests could be repeated, but also of suites of samples for which only one microstructural attribute was varied while others were kept constant, so that its isolated influence could be explored. Further, over the range of porosity and grain size investigated, it was demonstrated that the sintered glass bead samples have the potential to accurately simulate the evolution of the hydraulic and mechanical properties of natural rocks.
However, technical difficulties arise progressively when trying to model more complex microstructures than that of monomineralic well-sorted sandstones, even when the synthetic samples only contain one component and no cement (Chapter 2). In the course of this work, more than 400 samples were prepared and more than 200 deformation experiments were performed, the results of which helped to draw predictive conclusions for porous crustal rocks. However, one might wonder whether a thorough study of the same properties using natural rocks could have provided more extensive insights on their hydromechanical behaviour because it would not have been slowed down by any technical difficulty associated to the manufacturing of synthetic rocks. More simply, one might ask whether using synthetic samples is worth it. Such questioning is resolved by considering that the conclusions that can be drawn using synthetic rocks or using natural rocks can never be the same. As an illustration of this, extrapolating the conclusions drawn using synthetic rocks to natural rocks can be difficult as the behaviour of natural rocks results from the complex coupling between various

parameters. Further, while working on natural rocks will allow us to progressively establish an extensive catalogue of the different types of behaviour and tend toward more universal descriptions of the control of specific attributes, synthetic rocks have the potential to provide more definitive and therefore predictive conclusions valid for most porous rocks. As an illustration of this, the work conducted for this thesis provided information about the influence of grain size and grain size distribution that were not known before.

Finally, because studies on synthetic or natural rocks can help understanding different aspects of the mechanical behaviour, works on synthetic and natural rocks should be extended collaboratively as far as possible. Indeed, the cohesive integration of laboratory experiments using synthetic and natural rocks, numerical simulations and field observations can serve to further the understanding of the link between the grain scale, the sample scale and the field scale. A particularly interesting way forward would be to develop the comparison between DEM simulations and sintered glass bead samples, where these synthetic rocks should help to set the model parameters and therefore help to move towards more realistic 3D simulations.

References

Ablay, G., & Hürlimann, M. (2000). Evolution of the north flank of Tenerife by recurrent giant landslides. *Journal of Volcanology and Geothermal Research*, *103*(1–4), 135–159. https://doi.org/10.1016/S0377-0273(00)00220-1

Alassi, H. T. I., Li, L., & Holt, R. M. (2006). Discrete Element Modeling of Stress and Strain Evolution Within and Outside a Depleting Reservoir. *Pure and Applied Geophysics*, *163*, 1131–1151. https://doi.org/10.1007/3-7643-7712-7_13

Ashby, M. F., & Sammis, C. G. (1990). The damage mechanics of brittle solids in compression. *Pure and Applied Geophysics PAGEOPH*, *133*(3), 489–521. https://doi.org/10.1007/BF00878002

Atapour, H., & Mortazavi, A. (2018). The influence of mean grain size on unconfined compressive strength of weakly consolidated reservoir sandstones. *Journal of Petroleum Science and Engineering*, *171*, 63–70. https://doi.org/10.1016/j.petrol.2018.07.029

Atkinson, B. K., & Meredith, P. G. (1987). Experimental fracture mechanics data for rocks and minerals. In *Fracture mechanics of rock* (pp. 477–519). Academic Press Inc.(London) Ltd.

Avramov, I., Vassilev, T., & Penkov, I. (2005). The glass transition temperature of silicate and borate glasses. *Journal of Non-Crystalline Solids*, *351*(6–7), 472–476. https://doi.org/10.1016/J.JNONCRYSOL.2005.01.044

Aydin, A., & Ahmadov, R. (2009). Bed-parallel compaction bands in aeolian sandstone: Their identification, characterization and implications. *Tectonophysics*, *479*(3–4), 277–284. https://doi.org/10.1016/j.tecto.2009.08.033

Bakker, R. R., Violay, M. E. S., Benson, P. M., & Vinciguerra, S. C. (2015). Ductile flow in sub-volcanic carbonate basement as the main control for edifice stability: new experimental insights. *Earth and Planetary Science Letters*, *430*, 533–541.

Baud, P., Schubnel, A., & Wong, T. (2000). Dilatancy, compaction, and failure mode in Solnhofen limestone. *Journal of Geophysical Research*, *105*, 289–303. https://doi.org/10.1029/2000JB900133

Baud, P., Zhu, W., & Wong, T. (2000). Failure mode and weakening effect of water on sandstone. *Journal of Geophysical Research*, *105*, 371–389. https://doi.org/10.1029/2000JB900087

Baud, P., Klein, E., & Wong, T. (2004). Compaction localization in porous sandstones: spatial evolution of damage and acoustic emission activity. *Journal of Structural Geology*, *26*(4), 603–624. https://doi.org/10.1016/j.jsg.2003.09.002

Baud, P., Vajdova, V., & Wong, T. (2006). Shear-enhanced compaction and strain localization: Inelastic

deformation and constitutive modeling of four porous sandstones. *Journal of Geophysical Research: Solid Earth*, *111*(B12), n/a-n/a. https://doi.org/10.1029/2005JB004101

Baud, P., Wong, T., & Zhu, W. (2014). Effects of porosity and crack density on the compressive strength of rocks. *International Journal of Rock Mechanics and Mining Sciences*, *67*, 202–211. https://doi.org/10.1016/j.ijrmms.2013.08.031

Baud, P., Reuschlé, T., Ji, Y., Cheung, C. S. N., & Wong, T. (2015). Mechanical compaction and strain localization in Bleurswiller sandstone. *Journal of Geophysical Research: Solid Earth*, *120*(9), 6501–6522. https://doi.org/10.1002/2015JB012192

Baud, P., Exner, U., Lommatzsch, M., Reuschlé, T., & Wong, T. (2017). Mechanical behavior, failure mode, and transport properties in a porous carbonate. *Journal of Geophysical Research: Solid Earth*, *122*(9), 7363–7387. https://doi.org/10.1002/2017JB014060

Beard, D. C., & Weyl, P. K. (1973). Influence of Texture on Porosity and Permeability in Unconsolidated Sand. *American Association of Petroleum Geologists Bulletin*, *57*(2), 349–369. https://doi.org/10.1306/819a4272-16c5-11d7-8645000102c1865d

Bedford, J. D., Faulkner, D. R., Wheeler, J., & Leclère, H. (2019). High-Resolution Mapping of Yield Curve Shape and Evolution for High-Porosity Sandstone. *Journal of Geophysical Research: Solid Earth*, *124*(6), 5450–5468. https://doi.org/10.1029/2018JB016719

Berge, P. A., Bonner, B. P., & Berryman, J. G. (1995). Ultrasonic velocity-porosity relationships for sandstone analogs made from fused glass beads. *GEOPHYSICS*, *60*(1), 108–119. https://doi.org/10.1190/1.1443738

Bernabé, Y., Fryer, D. T., & Hayes, J. A. (1992). The effect of cement on the strength of granular rocks. *Geophysical Research Letters*. https://doi.org/10.1029/92GL01288

Bernabé, Y., Fryer, D. T., & Shively, R. M. (1994). Experimental Observations of the Elastic and Inelastic Behaviour of Porous Sandstones. *Geophysical Journal International*, *117*(2), 403–418. https://doi.org/10.1111/j.1365-246X.1994.tb03940.x

Bernabé, Y., Mok, U., & Evans, B. (2003). Permeability-porosity Relationships in Rocks Subjected to Various Evolution Processes. *Thermo-Hydro-Mechanical Coupling in Fractured Rock*, *160*, 937–960. https://doi.org/10.1007/978-3-0348-8083-1_9

Bésuelle, P., Desrues, J., & Raynaud, S. (2000). Experimental characterisation of the localisation phenomenon inside a Vosges sandstone in a triaxial cell. *International Journal of Rock Mechanics and Mining Sciences*, *37*(8), 1223–1237. https://doi.org/10.1016/S1365-1609(00)00057-5

Bésuelle, P., Baud, P., & Wong, T. (2003). Failure mode and spatial distribution of damage in Rothbach sandstone in the brittle-ductile transition. *Pure and Applied Geophysics*, *160*(5–6), 851–868. https://doi.org/10.1007/PL00012569

Bied, A. El, Sulem, J., & Martineau, F. (2002). Microstructure of shear zones in Fontainebleau sandstone.

International Journal of Rock Mechanics and Mining Sciences, *39*(7), 917–932. Retrieved from https://hal.archives-ouvertes.fr/hal-00311338/

Bjørlykke, K. (2006). Effects of compaction processes on stresses, faults, and fluid flow in sedimentary basins: Examples from the Norwegian margin. *Geological Society Special Publication*, *253*(1), 359–379. https://doi.org/10.1144/GSL.SP.2006.253.01.19

Blair, S. C., Berge, P. A., & Berryman, J. G. (1993). *Two-point correlation functions to characterize microgeometry and estimate permeabilities of synthetic and natural sandstones*. Livermore, CA. https://doi.org/10.2172/10182383

Bloch, S., Lander, R. H., & Bonnell, L. (2002). Anomalously High Porosity and Permeability in Deeply Buried Sandstone Reservoirs: Origin and Predictability. *The American Association of Petroleum Geologists*, *86*(2), 301–328. https://doi.org/10.1306/61EEDABC-173E-11D7-8645000102C1865D

Bourbie, T., & Zinszner, B. (1985). Hydraulic and Acoustic Properties as a Function of Porosity in Fontainebleau Sandstone. *Journal of Geophysical Research*, *90*(4), 524–532.

Brewster, D., Edin, L. D. F. R. S., & Edin, F. S. A. (1815). Experiments on the depolarisation of light as exhibited by various mineral, animal, and vegetable bodies, with a reference of the phenomena to the general principles of polarisation. By David Brewster, LL. D. F. R. S. Edin and F. S. A. Edin. *Philosophical Transactions of the Royal Society of London*, *105*, 29–53. https://doi.org/10.1098/rstl.1815.0004

den Brok, S. W. J., David, C., & Bernabé, Y. (1997). Preparation of synthetic sandstones with variable cementation for studying the physical properties of granular rocks. *Comptes Rendus de l'Académie Des Sciences - Series IIA - Earth and Planetary Science*, *325*(7), 487–492. https://doi.org/10.1016/S1251-8050(97)89866-7

Brzesowsky, R. H., Spiers, C. J., Peach, C. J., & Hangx, S. J. T. (2011). Failure behavior of single sand grains: Theory versus experiment. *Journal of Geophysical Research: Solid Earth*, *116*(6). https://doi.org/10.1029/2010JB008120

Buscarnera, G., Chen, Y., Lizárraga, J., & Zhang, R. (2020). Multi-scale simulation of rock compaction through breakage models with microstructure evolution. *Proceedings of the International Association of Hydrological Sciences*, *382*, 421–425. https://doi.org/10.5194/piahs-382-421-2020

Carbillet, L., Heap, M. J., Baud, P., Wadsworth, F. B., & Reuschlé, T. (2021). Mechanical Compaction of Crustal Analogs Made of Sintered Glass Beads: The Influence of Porosity and Grain Size. *Journal of Geophysical Research: Solid Earth*, *126*(4). https://doi.org/10.1029/2020jb021321

Caruso, L., Simmons, G., & Wilkens, R. (1985). The physical properties of a set of sandstones-Part I. The samples. *International Journal of Rock Mechanics and Mining Sciences And*, *22*(6), 381–392. https://doi.org/10.1016/0148-9062(85)90003-8

Chang, C., Zoback, M. D., & Khaksar, A. (2006). Empirical relations between rock strength and physical

properties in sedimentary rocks. *Journal of Petroleum Science and Engineering*, *51*(3–4), 223–237. https://doi.org/10.1016/j.petrol.2006.01.003

Charalampidou, E. M., Hall, S. A., Stanchits, S., Viggiani, G., & Lewis, H. (2013). Characterization of Shear and Compaction Bands in Sandstone Using X-Ray Tomography and 3D Digital Image Correlation. In *Advances in Computed Tomography for Geomaterials: GeoX 2010* (pp. 59–66). John Wiley & Sons, Ltd. https://doi.org/10.1002/9781118557723.ch7

Cheung, C. S. N., Baud, P., & Wong, T. (2012). Effect of grain size distribution on the development of compaction localization in porous sandstone. *Geophysical Research Letters*, *39*(21), n/a-n/a. https://doi.org/10.1029/2012GL053739

Concha-Dimas, A., Cerca, M., Rodríguez, S. R., & Watters, R. J. (2005). Geomorphological evidence of the influence of pre-volcanic basement structure on emplacement and deformation of volcanic edifices at the Cofre de Perote-Pico de Orizaba chain and implications for avalanche generation. *Geomorphology*, *72*(1–4), 19–39. https://doi.org/10.1016/j.geomorph.2005.05.004

Das, A., Nguyen, G. D., & Einav, I. (2011). Compaction bands due to grain crushing in porous rocks: A theoretical approach based on breakage mechanics. *Journal of Geophysical Research: Solid Earth*, *116*(8). https://doi.org/10.1029/2011JB008265

David, C., Menéndez, B., & Bernabé, Y. (1998). The mechanical behaviour of synthetic sandstone with varying brittle cement content. *International Journal of Rock Mechanics and Mining Sciences*, *35*(6), 759–770. https://doi.org/10.1016/S0148-9062(98)00003-5

Desu, R. K., & Annabattula, R. K. (2019). Particle size effects on the contact force distribution in compacted polydisperse granular assemblies. *Granular Matter*, *21*(2), 1–12. https://doi.org/10.1007/s10035-019-0883-9

Domenico, S. N. (1977). Elastic Properties of Unconsolidated Porous Sand Reservoirs. *Geophysics*, *42*(7), 1339–1368. https://doi.org/10.1190/1.1440797

Doyen, P. M. (1988). Permeability, conductivity, and pore geometry of sandstone. *Journal of Geophysical Research*, *93*(B7), 7729–7740. https://doi.org/10.1029/JB093iB07p07729

Eberhart-Phillips, D., Han, D., & Zoback, M. D. (1989). Empirical relationships among seismic velocity, effective pressure, porosity, and clay content in sandstone. *Geophysics*, *54*(1), 82–89.

Eggers, J., Lister, J. R., & Stone, H. A. (1999). Coalescence of liquid drops. *Journal of Fluid Mechanics*, *401*, 293–310. https://doi.org/10.1017/S002211209900662X

Eichhubl, P., Hooker, J. N., & Laubach, S. E. (2010). Pure and shear-enhanced compaction bands in Aztec Sandstone. *Journal of Structural Geology*, *32*(12), 1873–1886. https://doi.org/10.1016/j.jsg.2010.02.004

Ergenzinger, C., Seifried, R., & Eberhard, P. (2010). A discrete element model to describe failure of strong rock in uniaxial compression. *Granular Matter 2010 13:4*, *13*(4), 341–364. https://doi.org/10.1007/S10035-010-0230-7

Farquharson, J. I., Heap, M. J., Varley, N. R., Baud, P., & Reuschlé, T. (2015). Permeability and porosity relationships of edifice-forming andesites: A combined field and laboratory study. *Journal of Volcanology and Geothermal Research*, *297*, 52–68. https://doi.org/10.1016/j.jvolgeores.2015.03.016

Farquharson, J. I., Heap, M. J., Lavallée, Y., Varley, N. R., & Baud, P. (2016). Evidence for the development of permeability anisotropy in lava domes and volcanic conduits. *Journal of Volcanology and Geothermal Research*, *323*, 163–185. https://doi.org/10.1016/J.JVOLGEORES.2016.05.007

Farquharson, J. I., Baud, P., & Heap, M. J. (2017). Inelastic compaction and permeability evolution in volcanic rock. *Solid Earth*, *8*(2), 561–581. https://doi.org/10.5194/se-8-561-2017

Fluegel, A. (2007). Glass viscosity calculation based on a global statistical modelling approach. *GLASS TECHNOLOGY-EUROPEAN JOURNAL OF GLASS SCIENCE AND TECHNOLOGY PART A*, *48*(1), 13–30. https://doi.org/10.1016/0003-9861(77)90309-5

Fortin, J., Schubnel, A., & Guéguen, Y. (2005). Elastic wave velocities and permeability evolution during compaction of Bleurswiller sandstone. *International Journal of Rock Mechanics and Mining Sciences*, *42*(7-8 SPEC. ISS.), 873–889. https://doi.org/10.1016/j.ijrmms.2005.05.002

Fortin, J., Stanchits, S., Dresen, G., & Guéguen, Y. (2006). Acoustic emission and velocities associated with the formation of compaction bands in sandstone. *Journal of Geophysical Research: Solid Earth*, *111*(10), 1–16. https://doi.org/10.1029/2005JB003854

Fortin, J., Stanchits, S., Dresen, G., & Guéguen, Y. (2009). Acoustic emissions monitoring during inelastic deformation of porous sandstone: Comparison of three modes of deformation. *Pure and Applied Geophysics*, *166*(5–7), 823–841. https://doi.org/10.1007/s00024-009-0479-0

Fossen, H., Schultz, R. A., Shipton, Z. K., & Mair, K. (2007, July 1). Deformation bands in sandstone: A review. *Journal of the Geological Society*. GeoScienceWorld. https://doi.org/10.1144/0016-76492006-036

Fossen, H., Schultz, R. A., & Torabi, A. (2011). Conditions and implications for compaction band formation in the Navajo Sandstone, Utah. *Journal of Structural Geology*, *33*(10), 1477–1490. https://doi.org/10.1016/j.jsg.2011.08.001

Fredrich, J. T., Evans, B., & Teng-Fong Wong. (1990). Effect of grain size on brittle and semibrittle strength: Implications for micromechanical modelling of failure in compression. *Journal of Geophysical Research: Solid Earth*, *95*(B7), 10907–10920. https://doi.org/10.1029/JB095IB07P10907

Fredrich, J. T., Greaves, K. H., & Martin, J. W. (1993). Pore geometry and transport properties of Fontainebleau sandstone. *International Journal of Rock Mechanics and Mining Sciences And*, *30*(7), 691–697. https://doi.org/10.1016/0148-9062(93)90007-Z

Fredrich, J. T., Menéndez, B., & Wong, T. F. (1995). Imaging the pore structure of geomaterials. *Science*, *268*(5208), 276–279. https://doi.org/10.1126/science.268.5208.276

Frenkel, J. (1945). Viscous flow of crystalline bodies under the action of surface tension. *Journal of Physics*, *9*, 385. Retrieved from https://ci.nii.ac.jp/naid/10012829642

Frocht, M. M. (1944). Studies in three-dimensional photoelasticity stress concentrations in shafts with transverse circular holes in tension relation between two- and three-dimensional factors. *Journal of Applied Physics*, *15*(1), 72–88. https://doi.org/10.1063/1.1707370

Gambolati, G., Ferronato, M., & Teatini, P. (2006). Reservoir compaction and land subsidence. *Revue Européenne de Génie Civil*, *10*(6–7), 731–762. https://doi.org/10.1080/17747120.2006.9692854

Gell, E. M., Walley, S. M., & Braithwaite, C. H. (2019). Review of the Validity of the Use of Artificial Specimens for Characterizing the Mechanical Properties of Rocks. *Rock Mechanics and Rock Engineering*, *52*(9), 2949–2961. https://doi.org/10.1007/s00603-019-01787-8

Ghazvinian, E., Diederichs, M. S., & Quey, R. (2014). 3D random Voronoi grain-based models for simulation of brittle rock damage and fabric-guided micro-fracturing. *Journal of Rock Mechanics and Geotechnical Engineering*, *6*(6), 506–521. https://doi.org/10.1016/j.jrmge.2014.09.001

Gomez, C. T., Dvorkin, J., & Vanorio, T. (2010). Laboratory measurements of porosity, permeability, resistivity, and velocity on Fontainebleau sandstones. *Geophysics*, *75*(6). https://doi.org/10.1190/1.3493633

Grunder, A., & Russell, J. K. (2005). Welding processes in volcanology: Insights from field, experimental, and modeling studies. *Journal of Volcanology and Geothermal Research*, *142*(1-2 SPEC. ISS.), 1–9. https://doi.org/10.1016/j.jvolgeores.2004.10.010

Guéguen, Y., & Boutéca, M. (2004). *Mechanics of fluid saturated rocks*. Elsevier Academic Press.

Guéguen, Y., & Fortin, J. (2013). Elastic envelopes of porous sandstones. *Geophysical Research Letters*, *40*(14), 3550–3555. https://doi.org/10.1002/grl.50676

Guéguen, Y., & Palciauskas, V. (1994). *Introduction to the physics of rocks*. *Princeton University Press*.

Gustavsson, M., Karawacki, E., & Gustafsson, S. E. (1994). Thermal conductivity, thermal diffusivity, and specific heat of thin samples from transient measurements with hot disk sensors. *Review of Scientific Instruments*, *65*(12), 3856–3859. https://doi.org/10.1063/1.1145178

Guyon, E., Oger, L., & Plona, T. J. (1987). Transport properties in sintered porous media composed of two particle sizes. *Journal of Physics D: Applied Physics*, *20*(12), 1637–1644. https://doi.org/10.1088/0022-3727/20/12/015

Haeri, S. M., Hosseini, S. M., Toll, D. G., & Yasrebi, S. S. (2005). The behaviour of an artificially cemented sandy gravel. *Geotechnical and Geological Engineering*, *23*(5), 537–560. https://doi.org/10.1007/s10706-004-5110-7

Hangx, S. J. T., & Brantut, N. (2019). Micromechanics of High-Pressure Compaction in Granular Quartz Aggregates. *Journal of Geophysical Research: Solid Earth*, *124*(7), 6560–6580. https://doi.org/10.1029/2018JB016494

Harnett, C. E., Thomas, M. E., Purvance, M. D., & Neuberg, J. (2018). Using a discrete element approach to model lava dome emplacement and collapse. *Journal of Volcanology and Geothermal Research*, *359*, 68–

77. https://doi.org/10.1016/j.jvolgeores.2018.06.017

Heap, M. J., Lavallée, Y., Petrakova, L., Baud, P., Reuschlé, T., Varley, N. R., & Dingwell, D. B. (2014). Microstructural controls on the physical and mechanical properties of edifice-forming andesites at Volcán de Colima, Mexico. *Journal of Geophysical Research: Solid Earth*, *119*(4), 2925–2963. https://doi.org/10.1002/2013JB010521

Heap, Michael J., & Violay, M. E. S. (2021, May 1). The mechanical behaviour and failure modes of volcanic rocks: a review. *Bulletin of Volcanology*. Springer Science and Business Media Deutschland GmbH. https://doi.org/10.1007/s00445-021-01447-2

Heap, Michael J., & Wadsworth, F. B. (2016). Closing an open system: Pore pressure changes in permeable edifice rock at high strain rates. *Journal of Volcanology and Geothermal Research*, *315*, 40–50. https://doi.org/10.1016/J.JVOLGEORES.2016.02.011

Heap, Michael J., Farquharson, J. I., Baud, P., Lavallée, Y., & Reuschlé, T. (2015). Fracture and compaction of andesite in a volcanic edifice. *Bulletin of Volcanology*, *77*(6). https://doi.org/10.1007/s00445-015-0938-7

Heap, Michael J., Kennedy, B. M., Pernin, N., Jacquemard, L., Baud, P., Farquharson, J. I., et al. (2015). Mechanical behaviour and failure modes in the Whakaari (White Island volcano) hydrothermal system, New Zealand. *Journal of Volcanology and Geothermal Research*, *295*, 26–42. https://doi.org/10.1016/j.jvolgeores.2015.02.012

Heap, Michael J., Brantut, N., Baud, P., & Meredith, P. G. (2015). Time-dependent compaction band formation in sandstone. *Journal of Geophysical Research: Solid Earth*, *120*(7), 4808–4830. https://doi.org/10.1002/2015JB012022

Heap, Michael J., Kushnir, A. R. L., Gilg, H. A., Wadsworth, F. B., Reuschlé, T., & Baud, P. (2017). Microstructural and petrophysical properties of the Permo-Triassic sandstones (Buntsandstein) from the Soultz-sous-Forêts geothermal site (France). *Geothermal Energy*, *5*(1), 26. https://doi.org/10.1186/s40517-017-0085-9

Heap, Michael J., Coats, R., Chen, C. feng, Varley, N., Lavallée, Y., Kendrick, J., et al. (2018). Thermal resilience of microcracked andesitic dome rocks. *Journal of Volcanology and Geothermal Research*, *367*, 20–30. https://doi.org/10.1016/j.jvolgeores.2018.10.021

Heap, Michael J., Kushnir, A. R. L., Gilg, H. A., Violay, M. E. S., Harlé, P., & Baud, P. (2019). Petrophysical properties of the Muschelkalk from the Soultz-sous-Forêts geothermal site (France), an important lithostratigraphic unit for geothermal exploitation in the Upper Rhine Graben. *Geothermal Energy*, *7*(1), 1–29. https://doi.org/10.1186/s40517-019-0145-4

Heap, Michael J., Baud, P., McBeck, J. A., Renard, F., Carbillet, L., & Hall, S. A. (2020). Imaging strain localisation in porous andesite using digital volume correlation. *Journal of Volcanology and Geothermal Research*, *404*, 107038. https://doi.org/10.1016/j.jvolgeores.2020.107038

Heap, Michael J., Kushnir, A. R. L., Vasseur, J., Wadsworth, F. B., Harlé, P., Baud, P., et al. (2020). The thermal

properties of porous andesite. *Journal of Volcanology and Geothermal Research*, *398*, 106901. https://doi.org/10.1016/j.jvolgeores.2020.106901

Heap, Michael J., Baumann, T. S., Rosas-Carbajal, M., Komorowski, J. C., Gilg, H. A., Villeneuve, M., et al. (2021). Alteration-Induced Volcano Instability at La Soufrière de Guadeloupe (Eastern Caribbean). *Journal of Geophysical Research: Solid Earth*, *126*(8), e2021JB022514. https://doi.org/10.1029/2021JB022514

Heap, Michael J., Jessop, D. E., Wadsworth, F. B., Rosas-Carbajal, M., Komorowski, J. C., Gilg, H. A., et al. (2022). The thermal properties of hydrothermally altered andesites from La Soufrière de Guadeloupe (Eastern Caribbean). *Journal of Volcanology and Geothermal Research*, *421*, 107444. https://doi.org/10.1016/j.jvolgeores.2021.107444

Hol, S., Van Der Linden, A., Bierman, S., Marcelis, F., & Makurat, A. (2018). Rock Physical Controls on Production-induced Compaction in the Groningen Field. *Scientific Reports*, *8*(1), 7156. https://doi.org/10.1038/s41598-018-25455-z

Holcomb, D., Rudnicki, J. W., Issen, K. A., & Sternlof, K. R. (2007). Compaction localization in the Earth and the laboratory: State of the research and research directions. *Acta Geotechnica*, *2*(1), 1–15. https://doi.org/10.1007/s11440-007-0027-y

Holt, R. M., Unander, T. E., & Kenter, C. J. (1993). Constitutive mechanical behaviour of synthetic sandstone formed under stress. *International Journal of Rock Mechanics and Mining Sciences And*, *30*(7), 719–722. https://doi.org/10.1016/0148-9062(93)90013-4

Irwin, G. R. (1968). Linear fracture mechanics, fracture transition, and fracture control. *Engineering Fracture Mechanics*, *1*(2), 241–257. https://doi.org/10.1016/0013-7944(68)90001-5

Jackson, J. A., & Bates, R. L. (1997). Glossary of Geology - Fourth Edition, 769.

Jaeger, J. C., Cook, N. G., & Zimmerman, R. (2009). *Fundamentals of Rock Mechanics*. *Geofluids* (John Wiley, Vol. 9). https://doi.org/10.1111/j.1468-8123.2009.00251.x

Jizba, D. L. (1991). *Mechanical and acoustic properties of sandstones and shales*. Stanford University.

Johnson, D. L., & Plona, T. J. (1982). Acoustic slow waves and the consolidation transition. *The Journal of the Acoustical Society of America*, *72*(2), 556–565. https://doi.org/10.1121/1.388036

Katsman, R., Aharonov, E., & Scher, H. (2005). Numerical simulation of compaction bands in high-porosity sedimentary rock. *Mechanics of Materials*, *37*(1), 143–162. https://doi.org/10.1016/j.mechmat.2004.01.004

Katz, A. J., & Thompson, A. H. (1986). Quantitative prediction of permeability in porous rock. *Physical Review B*, *34*(11), 8179–8181. https://doi.org/10.1103/PhysRevB.34.8179

Klein, E., Baud, P., Reuschlé, T., & Wong, T. (2001). Mechanical behaviour and failure mode of Bentheim sandstone under triaxial compression. *Physics and Chemistry of the Earth, Part A: Solid Earth and*

Geodesy, *26*(1–2), 21–25. https://doi.org/10.1016/S1464-1895(01)00017-5

Krohn, C. E. (1988). Sandstone fractal and Euclidean pore volume distributions. *Journal of Geophysical Research*, *93*(B4), 3286. https://doi.org/10.1029/JB093iB04p03286

Kwasniewski, M. (1989, August 30). Laws of Brittle Failure And of B-D Transition In Sandstones. OnePetro.

Lan, H., Martin, C. D., & Hu, B. (2010). Effect of heterogeneity of brittle rock on micromechanical extensile behavior during compression loading. *Journal of Geophysical Research*, *115*(B1), 1202. https://doi.org/10.1029/2009jb006496

Lemée, C., & Guéguen, Y. (1996). Modeling of porosity loss during compaction and cementation of sandstones. *Geology*, *24*(10), 875. https://doi.org/10.1130/0091-7613(1996)024<0875:MOPLDC>2.3.CO;2

Li, Y., David, E. C., Nakagawa, S., Kneafsey, T. J., Schmitt, D. R., & Jackson, I. (2018). A Broadband Laboratory Study of the Seismic Properties of Cracked and Fluid-Saturated Synthetic Glass Media. *Journal of Geophysical Research: Solid Earth*, *123*(5), 3501–3538. https://doi.org/10.1029/2017JB014671

Lindquist, W. B., Venkatarangan, A., Dunsmuir, J. R., & Wong, T. (2000). Pore and throath size distributions measured from synchrotron X-ray tomographic images of Fontainebleau sandstones. *Journal of Geophysical Research*, *105*(B9), 509–521.

Lockner, D. (1993). The role of acoustic emission in the study of rock fracture. *International Journal of Rock Mechanics and Mining Sciences And*, *30*(7), 883–899. https://doi.org/10.1016/0148-9062(93)90041-B

Louis, L., Wong, T., & Baud, P. (2006). X-ray Imaging of Compactant Strain Localization in Sandstone. *Advances in X-Ray Tomography for Geomaterials*, 194–198.

Louis, L., Baud, P., & Wong, T. (2007). Characterization of pore-space heterogeneity in sandstone by X-ray computed tomography. *Geological Society Special Publication*, *284*, 127–146. https://doi.org/10.1144/SP284.9

Louis, L., Wong, T., & Baud, P. (2007). Imaging strain localization by X-ray radiography and digital image correlation: Deformation bands in Rothbach sandstone. *Journal of Structural Geology*, *29*(1), 129–140. https://doi.org/10.1016/j.jsg.2006.07.015

Louis, L., Baud, P., & Rolland, A. (2009). Compaction localization in high porosity sandstones with various degrees of heterogeneity : insight from X-ray computed tomography. In *ROCKENG09: Proceedings of the 3rd CANUS Rock Mechanics Symposium* (Vol. 2009, pp. 1–2).

Mackenzie, J. K., & Shuttleworth, R. (1949). A Phenomenological Theory of Sintering. *Proceedings of the Physical Society. Section B*, *62*(12), 833. https://doi.org/10.1088/0370-1301/62/12/310

Marketos, G., & Bolton, M. D. (2009). Compaction bands simulated in Discrete Element Models. *Journal of Structural Geology*, *31*(5), 479–490. https://doi.org/10.1016/j.jsg.2009.03.002

Martys, N. S., Torquato, S., & Bentz, D. P. (1994). Universal scaling of fluid permeability for sphere packings. *Physical Review E*, *50*(1).

McDowell, G. R., & Bolton, M. D. (1998). On the micromechanics of crushable aggregates. *Geotechnique*, *48*(5), 667–679. https://doi.org/10.1680/geot.1998.48.5.667

Menéndez, B., Zhu, W., & Wong, T. (1996). Micromechanics of brittle faulting and cataclastic flow in Berea sandstone. *Journal of Structural Geology*, *18*(1), 1–16. https://doi.org/10.1016/0191-8141(95)00076-P

Morgan, J. K., & McGovern, P. J. (2005). Discrete element simulations of gravitational volcanic deformation: 1. Deformation structures and geometries. *Journal of Geophysical Research: Solid Earth*, *110*(5), 1–22. https://doi.org/10.1029/2004JB003252

Muthuswamy, M., & Tordesillas, A. (2006). How do interparticle contact friction, packing density and degree of polydispersity affect force propagation in particulate assemblies? *Journal of Statistical Mechanics: Theory and Experiment*, *2006*(9), 9003. https://doi.org/10.1088/1742-5468/2006/09/P09003

Nagel, N. B. (2001). Compaction and subsidence issues within the petroleum industry: From Wilmington to Ekofisk and beyond. *Physics and Chemistry of the Earth, Part A: Solid Earth and Geodesy*, *26*(1–2), 3–14. https://doi.org/10.1016/S1464-1895(01)00015-1

Nelson, P. H. (1994). Permeability-porosity relationships in sedimentary rocks. *Log Analyst*, *35*(3), 38–62. Retrieved from https://onepetro.org/petrophysics/article-abstract/170877/Permeability-porosity-Relationships-In-Sedimentary

Nelson, P. H., & Kibler, J. E. (2003). *A Catalog of Porosity and Permeability from Core Plugs in Siliciclastic Rocks*. Retrieved from https://pubs.usgs.gov/of/2003/ofr-03-420/ofr-03-420.html#References

Nguyen, G. D., Nguyen, C. T., Bui, H. H., & Nguyen, V. P. (2016). Constitutive modelling of compaction localisation in porous sandstones. *International Journal of Rock Mechanics and Mining Sciences*, *83*, 57–72. https://doi.org/10.1016/j.ijrmms.2015.12.018

Oliveira, M. M., Pinto, C. L. L., & Mazzinghy, D. B. (2020). FEM-DEM simulation of Uniaxial Compressive Strength (UCS) laboratory tests. *REM - International Engineering Journal*, *73*(4), 561–569. https://doi.org/10.1590/0370-44672019730078

Olsson, W. A. (1974). Grain size dependence of yield stress in marble. *Journal of Geophysical Research*, *79*(32), 4859–4862. https://doi.org/10.1029/JB079I032P04859

Olsson, W. A. (1999). Theoretical and experimental investigation of compaction bands in porous rock. *Journal of Geophysical Research: Solid Earth*, *104*(B4), 7219–7228. https://doi.org/10.1029/1998jb900120

Olsson, W. A., & Holcomb, D. J. (2000). Compaction localization in porous rock. *Geophysical Research Letters*, *27*(21), 3537–3540. https://doi.org/10.1029/2000GL011723

Olsson, W. A., Holcomb, D. J., & Rudnicki, J. W. (2002). Compaction localization in porous sandstone: Implications for reservoir mechanics. *Oil and Gas Science and Technology*, *57*(5), 591–599. https://doi.org/10.2516/ogst:2002040

Papadopoulos, L., Porter, M. A., Daniels, K. E., Bassett, D. S., & Estrada, E. (2018). Network analysis of

particles and grains. *Journal of Complex Networks*, *6*(4), 485–565. https://doi.org/10.1093/comnet/cny005

Paterson, M. S., & Wong, T. (2005). *Experimental Rock Deformation: The Brittle Field, 2nd Edition*. Springer Verlag.

Peng, J., Wong, L. N. Y., & Teh, C. I. (2017). Influence of grain size heterogeneity on strength and microcracking behavior of crystalline rocks. *Journal of Geophysical Research: Solid Earth*, *122*(2), 1054–1073. https://doi.org/10.1002/2016JB013469

Peters, J. F., Muthuswamy, M., Wibowo, J., & Tordesillas, A. (2005). Characterization of force chains in granular material. *Physical Review E - Statistical, Nonlinear, and Soft Matter Physics*, *72*(4), 041307. https://doi.org/10.1103/PhysRevE.72.041307

Prado, M. O., Zanotto, E. D., & Müller, R. (2001). Model for sintering polydispersed glass particles. *Journal of Non-Crystalline Solids*, *279*(2–3), 169–178. https://doi.org/10.1016/S0022-3093(00)00399-9

Quane, S. L., Russell, J. K., & Friedlander, E. A. (2009). Time scales of compaction in volcanic systems. *Geology*, *37*(5), 471–474. https://doi.org/10.1130/G25625A.1

Radjai, F., Wolf, D. E., Jean, M., & Moreau, J. J. (1998). Bimodal Character of Stress Transmission in Granular Packings. *Physical Review Letters*, *80*(1), 61. https://doi.org/10.1103/PhysRevLett.80.61

Raymer, L. L., Hunt, E. R., & Gardner, J. S. (1980). An Improved Sonic Transit Time-To-Porosity Transform. Retrieved from https://www.onepetro.org/conference-paper/SPWLA-1980-P

Revil, A., Kessouri, P., & Torres-Verdín, C. (2014). Electrical conductivity, induced polarization, and permeability of the Fontainebleau sandstone. *Geophysics*, *79*(5), D301–D318. https://doi.org/10.1190/GEO2014-0036.1

Rice-Birchall, E., Bedford, J., Rice-Birchall, E., Faulkner, D. R., & Bedford, J. D. (2021). The manufacture, mechanical properties, and microstructural analysis of synthetic quartz-cemented sandstones Geomechanical and geochemical analysis of the Captain X Sandstone Member in relation to CO2 sequestration View project The geological record of su. *Article in International Journal of Rock Mechanics and Mining Sciences*, 104869. https://doi.org/10.1016/j.ijrmms.2021.104869

Rogers, J. J. W., & Head, W. B. (1961). Relationships Between Porosity, Median Size, and Sorting Coefficients of Synthetic Sands. *Journal of Sedimentary Research*, *Vol. 31*(3), 467–470. https://doi.org/10.1306/74d70ba5-2b21-11d7-8648000102c1865d

Rutter, E. H. (1986). On the nomenclature of mode of failure transitions in rocks. *Tectonophysics*, *122*(3–4), 381–387. https://doi.org/10.1016/0040-1951(86)90153-8

Rutter, E. H., & Glover, C. T. (2012). The deformation of porous sandstones; are Byerlee friction and the critical state line equivalent? *Journal of Structural Geology*, *44*, 129–140. https://doi.org/10.1016/j.jsg.2012.08.014

Saadi, F. Al, Wolf, K.-H., & Kruijsdijk, C. van. (2017). Characterization of Fontainebleau Sandstone: Quartz

Overgrowth and its Impact on Pore-Throat Framework. *Journal of Petroleum & Environmental Biotechnology*, *08*(03). https://doi.org/10.4172/2157-7463.1000328

Saar, M. O., & Manga, M. (1999). Permeability-porosity relationship in vesicular basalts. *Geophysical Research Letters*, *26*(1), 111–114. https://doi.org/10.1029/1998GL900256

Salami, Y., Dano, C., Hicher, P. Y., Colombo, G., & Denain, P. (2015). The effects of the coordination on the fragmentation of a single grain. *IOP Conference Series: Earth and Environmental Science*, *26*(1), 012015. https://doi.org/10.1088/1755-1315/26/1/012015

Sammis, C. G., & Ashby, M. F. (1986). The failure of brittle porous solids under compressive stress states. *Acta Metallurgica*, *34*(3), 511–526. https://doi.org/10.1016/0001-6160(86)90087-8

Scheidegger, A. E. (1958). The Physics of Flow Through Porous Media. *Soil Science*, *86*(6), 355. https://doi.org/10.1097/00010694-195812000-00015

Scherer, M. (1987). Parameters influencing porosity in sandstones: a model for sandstone porosity prediction. *American Association of Petroleum Geologists Bulletin*, *71*(5), 485–491. https://doi.org/10.1306/94886ed9-1704-11d7-8645000102c1865d

Scholz, C. H. (1968). Microfracturing and the inelastic deformation of rock in compression. *Journal of Geophysical Research*, *73*(4), 1417–1432. https://doi.org/10.1029/jb073i004p01417

Schöpfer, M. P. J., Abe, S., Childs, C., & Walsh, J. J. (2009). The impact of porosity and crack density on the elasticity, strength and friction of cohesive granular materials: Insights from DEM modelling. *International Journal of Rock Mechanics and Mining Sciences*, *46*(2), 250–261. https://doi.org/10.1016/j.ijrmms.2008.03.009

Schultz, R. A., Okubo, C. H., & Fossen, H. (2010). Porosity and grain size controls on compaction band formation in Jurassic Navajo Sandstone. *Geophysical Research Letters*, *37*(22), n/a-n/a. https://doi.org/10.1029/2010GL044909

Scott, T. E., & Nielsen, K. C. (1991). The effects of porosity on the brittle-ductile transition in sandstones. *Journal of Geophysical Research*, *96*(90), 405–414.

Selley, R. C. (2004). Sedimentary Rocks: Mineralogy and classification. In *Encyclopedia of Geology* (pp. 25–37). Elsevier Inc. https://doi.org/10.1016/B0-12-369396-9/00304-X

Sharma, A., & Penumadu, D. (2020). Role of particle shape in determining tensile strength and energy release in diametrical compression of natural silica grains. *Soils and Foundations*, *60*(5), 1299–1311. https://doi.org/10.1016/J.SANDF.2020.08.004

Stebbins, J. F., McMillan, P. F., & Dingwell, D. B. (1995). *Structure, dynamics, and properties of silicate melts*. *Structure, Dynamics, and Properties of Silicate Melts* (Vol. 32). Walter de Gruyter GmbH. https://doi.org/10.1515/9781501509384/PDF

Stimpson, B. (1970). Modelling materials for engineering rock mechanics. *International Journal of Rock*

Mechanics and Mining Sciences And, *7*(1), 77–121. https://doi.org/10.1016/0148-9062(70)90029-X

Sulem, J., & Ouffroukh, H. (2006). Hydromechanical behaviour of Fontainebleau sandstone. *Rock Mechanics and Rock Engineering*, *39*(3), 185–213. https://doi.org/10.1007/s00603-005-0065-4

Sun, Z., Tang, H., Espinoza, D. N., Balhoff, M. T., & Killough, J. E. (2018a). Discrete element modeling of grain crushing and implications on reservoir compaction. *Journal of Petroleum Science and Engineering*, *171*, 431–439. https://doi.org/10.1016/j.petrol.2018.07.046

Sun, Z., Tang, H., Espinoza, D. N., Balhoff, M. T., & Killough, J. E. (2018b). Pore-to reservoir-scale modeling of depletion-induced compaction and implications on production rate. *Proceedings - SPE Annual Technical Conference and Exhibition*, *2018-Septe*(Ostermeier 1995). https://doi.org/10.2118/191390-ms

Taylor, S. K., Nicol, A., & Walsh, J. J. (2008). Displacement loss on growth faults due to sediment compaction. *Journal of Structural Geology*, *30*(3), 394–405. https://doi.org/10.1016/j.jsg.2007.11.006

Taylor, W. L., & Pollard, D. D. (2000). Estimation of in situ permeability of deformation bands in porous sandstone, Valley of Fire, Nevada. *Water Resources Research*, *36*(9), 2595–2606. https://doi.org/10.1029/2000WR900120

Tembe, S., Vajdova, V., Wong, T., & Zhu, W. (2006). Initiation and propagation of strain localization in circumferentially notched samples of two porous sandstones. *Journal of Geophysical Research: Solid Earth*, *111*(2). https://doi.org/10.1029/2005JB003611

Tembe, S., Baud, P., & Wong, T. (2008). Stress conditions for the propagation of discrete compaction bands in porous sandstone. *Journal of Geophysical Research: Solid Earth*, *113*(9), 1–16. https://doi.org/10.1029/2007JB005439

Terzaghi, K. (1936). A fundamental fallacy in earth pressure computations. *Boston Society Civil Engineers Journal*, *23*, 71–88.

Torquato, S. (2002). *Random Heterogeneous Materials: Microstructure and Macroscopic Properties* (Springer).

Torquato, S., & Avellaneda, M. (1991). Diffusion and reaction in heterogeneous media: Pore size distribution, relaxation times, and mean survival time. *The Journal of Chemical Physics*, *95*(9), 6477–6489. https://doi.org/10.1063/1.461519

Townend, E., Thompson, B. D., Benson, P. M., Meredith, P. G., Baud, P., & Young, R. P. (2008). Imaging compaction band propagation in Diemelstadt sandstone using acoustic emission locations. *Geophysical Research Letters*, *35*(15). https://doi.org/10.1029/2008GL034723

Tudisco, E., Hall, S. A., Charalampidou, E. M., Kardjilov, N., Hilger, A., & Sone, H. (2015). Full-field Measurements of Strain Localisation in Sandstone by Neutron Tomography and 3D-Volumetric Digital Image Correlation. In *Physics Procedia*. https://doi.org/10.1016/j.phpro.2015.07.072

Vajdova, V., Baud, P., & Wong, T. F. (2004). Permeability evolution during localized deformation in Bentheim sandstone. *Journal of Geophysical Research: Solid Earth*, *109*(B10), 10406.

https://doi.org/10.1029/2003JB002942

Vallejo, L. E., Lobo-Guerrero, S., & Chik, Z. (2005). A Network of Fractal Force Chains and Their Effect in Granular Materials under Compression. *Fractals in Engineering: New Trends in Theory and Applications*, 67–80. https://doi.org/10.1007/1-84628-048-6_5

Vasseur, J., Wadsworth, F. B., Lavallée, Y., Hess, K.-U., & Dingwell, D. B. (2013). Volcanic sintering: Timescales of viscous densification and strength recovery. *Geophysical Research Letters*, *40*(21), 5658–5664. https://doi.org/10.1002/2013GL058105

Voight, B. (2000). Structural stability of andesite volcanoes and lava domes. *Philosophical Transactions of the Royal Society A: Mathematical, Physical and Engineering Sciences*, *358*(1770), 1663–1703. https://doi.org/10.1098/rsta.2000.0609

Wadsworth, F. B., Vasseur, J., von Aulock, F. W., Hess, K.-U., Scheu, B., Lavallée, Y., & Dingwell, D. B. (2014). Nonisothermal viscous sintering of volcanic ash. *Journal of Geophysical Research: Solid Earth*, *119*(12), 8792–8804. https://doi.org/10.1002/2014JB011453

Wadsworth, F. B., Vasseur, J., Llewellin, E. W., Schauroth, J., Dobson, K. J., Scheu, B., & Dingwell, D. B. (2016). Sintering of viscous droplets under surface tension. *Proceedings of the Royal Society A: Mathematical, Physical and Engineering Science*, *472*(2188), 20150780. https://doi.org/10.1098/rspa.2015.0780

Wadsworth, F. B., Vasseur, J., Scheu, B., Kendrick, J. E., Lavallée, Y., & Dingwell, D. B. (2016). Universal scaling of fluid permeability during volcanic welding and sediment diagenesis. *Geology*, *44*(3), 219–222. https://doi.org/10.1130/G37559.1

Wadsworth, F. B., Vasseur, J., Llewellin, E. W., & Dingwell, D. B. (2017). Sintering of polydisperse viscous droplets. *Physical Review E*, *95*(3), 033114. https://doi.org/10.1103/PhysRevE.95.033114

Wadsworth, F. B., Vasseur, J., Llewellin, E. W., Dobson, K. J., Colombier, M., Von Aulock, F. W., et al. (2017). Topological inversions in coalescing granular media control fluid-flow regimes. *Physical Review E*, *96*(3), 33113. https://doi.org/10.1103/PhysRevE.96.033113

Wadsworth, F. B., Vasseur, J., Schauroth, J., Llewellin, E. W., Dobson, K. J., Havard, T., et al. (2019). A general model for welding of ash particles in volcanic systems validated using in situ X-ray tomography. *Earth and Planetary Science Letters*, *525*, 115726. https://doi.org/10.1016/j.epsl.2019.115726

Walsh, J. B., & Brace, W. F. (1984). The effect of pressure on porosity and the transport properties of rock. *Journal of Geophysical Research: Solid Earth*, *89*(B11), 9425–9431. https://doi.org/10.1029/JB089IB11P09425

Walsh, John B. (1965). Effect of Cracks on the Compressibility of Rocks. *Journal of Geophysical Research*, *70*(2), 381–389. https://doi.org/10.1029/JB083iB09p04459

Wang, B., Chen, Y., & Wong, T. F. (2008). A discrete element model for the development of compaction localization in granular rock. *Journal of Geophysical Research: Solid Earth*, *113*(3), 1–17.

https://doi.org/10.1029/2006JB004501

Wang, B. S., Chen, Y., & Wong, T. (2005). Compaction localization in porous sandstone: Acoustic emission activity, microstructural development and discrete element simulation. In *11th International Conference on Fracture 2005, ICF11* (Vol. 4, pp. 2421–2424).

Waxman, M. H., & Smits, L. J. M. (2003). Electrical Conductivities in Oil-Bearing Shaly Sands. *SPE Reprint Series*, *8*(55), 107–122. https://doi.org/10.2118/1863-a

Webb, S. (1997). Silicate melts: Relaxation, rheology, and the glass transition. *Reviews of Geophysics*, *35*(2), 191–218. https://doi.org/10.1029/96RG03263

Winkler, K. W. (1983). Frequency dependent ultrasonic properties of high- porosity sandstones. *Journal of Geophysical Research*, *88*(B11), 9493–9499. https://doi.org/10.1029/JB088iB11p09493

Winkler, K. W. (1985). Dispersion analysis of velocity and attenuation in Berea sandstone. *Journal of Geophysical Research*, *90*(B8), 6793. https://doi.org/10.1029/jb090ib08p06793

Wong, T. (1990). Mechanical compaction and the brittle-ductile transition in porous sandstones. *Geological Society Special Publication*, *54*, 111–122. https://doi.org/10.1144/GSL.SP.1990.054.01.12

Wong, T., & Baud, P. (1999). Mechanical compaction of porous sandstone. *Oil and Gas Science and Technology*, *54*(6), 715–727. https://doi.org/10.2516/ogst:1999061

Wong, T., & Baud, P. (2012). The brittle-ductile transition in porous rock: A review. *Journal of Structural Geology*, *44*, 25–53. https://doi.org/10.1016/j.jsg.2012.07.010

Wong, T., Szeto, H., & Zhang, J. (1992). Effect of loading path and porosity on the failure mode of porous rocks. *Applied Mechanics Reviews*, *45*(8), 281–293. https://doi.org/10.1115/1.3119759

Wong, T., David, C., & Zhu, W. (1997). The transition from brittle faulting to cataclastic flow in porous sandstones: Mechanical deformation. *Journal of Geophysical Research: Solid Earth*, *102*(B2), 3009–3025. https://doi.org/10.1029/96JB03281

Wong, T., Baud, P., & Klein, E. (2001). Localized failure modes in a compactant porous rock. *Geophysical Research Letters*, *28*(13), 2521–2524. https://doi.org/10.1029/2001GL012960

Wu, H., Papazoglou, A., Viggiani, G., Dano, C., & Zhao, J. (2020). Compaction bands in Tuffeau de Maastricht: insights from X-ray tomography and multiscale modeling. *Acta Geotechnica*, *15*(1), 39–55. https://doi.org/10.1007/s11440-019-00904-9

Wu, X. Y., Baud, P., & Wong, T. F. (2000). Micromechanics of compressive failure and spatial evolution of anisotropic damage in Darley Dale sandstone. *International Journal of Rock Mechanics and Mining Sciences*, *37*(1–2), 143–160. https://doi.org/10.1016/S1365-1609(99)00093-3

Van Wyk De Vries, B., & Borgia, A. (1996). The role of basement in volcano deformation. *Geological Society Special Publication*, *110*(1), 95–110. https://doi.org/10.1144/GSL.SP.1996.110.01.07

Van Wyk De Vries, B., & Francis, P. W. (1997). Catastrophic collapse at stratovolcanoes induced by gradual volcano spreading. *Nature*, *387*(6631), 387–390. https://doi.org/10.1038/387387a0

Wyllie, M. R. ., Gregory, A. R., & Gardner, L. W. (1956). Elastic wave velocities in heterogeneous and porous media. *Geophysics*, *21*(1), 1–209. https://doi.org/10.1190/1.1438217

Wyllie, M. R. ., Gregory, A. R., & Gardner, G. H. . (1958). An experimental investigation of factors affecting elastic wave velocities in porous media. *Geophysics*, *23*(3), 421–623.

Xiong, L., Wu, S., & Wu, T. (2021). Effect of grain sorting, mineralogy and cementation attributes on the localized deformation in porous rocks: A numerical study. *Tectonophysics*, *817*, 229041. https://doi.org/10.1016/j.tecto.2021.229041

Xiong, L., Wu, S., Ma, J., & Peng, Y. (2021). Role of pore attribute in the localized deformation of granular rocks: A numerical study. *Tectonophysics*, *821*, 229147. https://doi.org/10.1016/j.tecto.2021.229147

Yin, H., & Dvorkin, J. (1994). Strength of cemented grains. *Geophysical Research Letters*, *21*(10), 903–906. https://doi.org/10.1029/93GL03535

Yu, Q., Zhu, W., Ranjith, P. G., & Shao, S. (2018). Numerical simulation and interpretation of the grain size effect on rock strength. *Geomechanics and Geophysics for Geo-Energy and Geo-Resources*, *4*(2), 157–173. https://doi.org/10.1007/s40948-018-0080-z

Zamora, M., & Poirier, J. P. (1990). Experimental study of acoustic anisotropy and birefringence in dry and saturated Fontainebleau sandstone. *Geophysics*, *55*(11), 1455–1465. https://doi.org/10.1190/1.1442793

Zamora, M., Vo-Thanh, D., Bienfait, G., & Poirier, J. P. (1993). An Empirical Relationship Between Thermal Conductivity and Elastic Wave Velocities In Sandstone. *Geophysical Research Letters*, *20*(16), 1679–1682.

Zhang, J., Wong, T.-F., & Davis, D. M. (1990). Micromechanics of pressure-induced grain crushing in porous rocks. *Journal of Geophysical Research*, *95*(B1), 341. https://doi.org/10.1029/JB095iB01p00341

Zhang, J., Wong, T.-F., Yanagidani, T., & Davis, D. M. (1990). Pressure-induced microcracking and grain crushing in berea and boise sandstones: acoustic emission and quantitative microscopy measurements. *Mechanics of Materials*, *9*(1), 1–15. https://doi.org/10.1016/0167-6636(90)90026-C

Zhang, L., Nguyen, N. G. H., Lambert, S., Nicot, F., Prunier, F., & Djeran-Maigre, I. (2017). The role of force chains in granular materials: from statics to dynamics. *European Journal of Environmental and Civil Engineering*, *21*(7–8), 874–895. https://doi.org/10.1080/19648189.2016.1194332

Zhu, W., Baud, P., & Wong, T. (2010). Micromechanics of cataclastic pore collapse in limestone. *Journal of Geophysical Research: Solid Earth*, *115*(4). https://doi.org/10.1029/2009JB006610

Zhu, W., Baud, P., Vinciguerra, S., & Wong, T. (2011). Micromechanics of brittle faulting and cataclastic flow in Alban Hills tuff. *Journal of Geophysical Research: Solid Earth*, *116*(6), 1–23. https://doi.org/10.1029/2010JB008046

Zhu, W., Baud, P., Vinciguerra, S., & Wong, T. F. (2016). Micromechanics of brittle faulting and cataclastic

flow in Mount Etna basalt. *Journal of Geophysical Research: Solid Earth*, *121*(6), 4268–4289. https://doi.org/10.1002/2016JB012826

Annex 1 Properties of SiLiBeads Type S and SpheriGlass A

CAMSIZER®

SIGMUND LINDNER®

4504 1.00-1.30 mm

Firma:	Sigmund Lindner GmbH
Benutzer:	Quality Control
Ergebnisdatei:	\... Prüfergebnisse inklusive Fotos\Glaskugeln Typ S\Glaskugeln Typ S\4504_Lot_1920033_001.rdf
Messaufgabe:	C:\Camsizer\CAMSYS\4504 1.00-1.30-- 07-05-15.afg
Zeit:	14.08.2019, 10:53, Dauer 6 min 34 s bei 0.3 % Flächendichte , Bildrate 1:1und 60 mm Rinne
Größendefinition:	xc_min
Partikelanzahl:	CCD-B = 68814 , CCD-Z = 4991
Anpassung:	nein
Material:	Glass Beads Typ S
Kommentar:	p3 (1.000mm, 1.300mm) = mind. 85% b/l3 (= Rundheit) mind. 0.95

Kornklasse [mm]	[mm]	p3 [%]	Q3 [%]	b/l3
	< 0.900	0.09	0.09	0.934
0.900	1.000	3.07	3.16	0.950
1.000	1.100	27.96	31.12	0.960
1.100	1.200	38.20	69.32	0.963
1.200	1.300	21.95	91.27	0.966
1.300	1.400	7.81	99.08	0.970
> 1.400		0.92	100.00	0.965

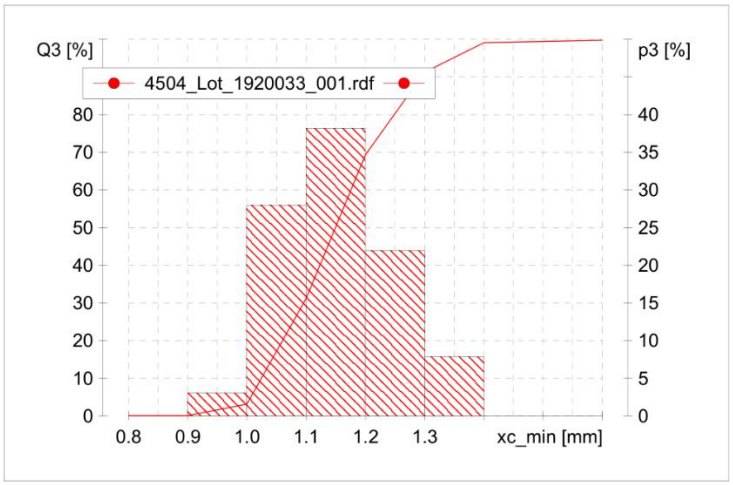

Kenngrößen

Q3 [%]	x [mm]
10.0	1.041
50.0	1.145
90.0	1.292

Sm = 20.715 cm²/g

p3(1.000 mm,1.300 mm) = 88,10 %

Mittelwert b/l3 = 0,963

Benutzer

CAMSIZER: 0245

1 / 1

CAMSIZER®

SIGMUND LINDNER

Art. 5218 / 400-600 µm

Firma:	Sigmund Lindner GmbH
Benutzer:	Quality Control
Ergebnisdatei:	\...sive Fotos\Glaskugeln Typ S Microglas\Glaskugeln Typ S Microglas\5218-7_Lot_1910079_001.rdf
Messaufgabe:	C:\Camsizer\CAMSYS\5218 400-600 - 07-02-26.afg
Zeit:	22.08.2019, 10:32, Dauer 5 min 24 s bei 0.5 % Flächendichte , Bildrate 1:1und 60 mm Rinne mit Leitblech
Größendefinition:	xc_min
Partikelanzahl:	CCD-B = 475848 , CCD-Z = 27677
Anpassung:	nein
Material:	Glass Beads Typ S
Kommentar:	p3 (0.4mm, 0.600mm) = mind. 70% b/l3 (= Rundheit) mind. 0.85

Kornklasse [mm]	[mm]	p3 [%]	Q3 [%]	b/l3
	< 0.300	0.19	0.19	0.612
0.300	0.355	1.37	1.56	0.743
0.355	0.400	5.16	6.72	0.873
0.400	0.450	18.12	24.84	0.938
0.450	0.500	28.77	53.61	0.940
0.500	0.560	30.50	84.11	0.922
0.560	0.630	14.52	98.63	0.897
0.630	0.710	1.23	99.86	0.772
> 0.710		0.14	100.00	0.763

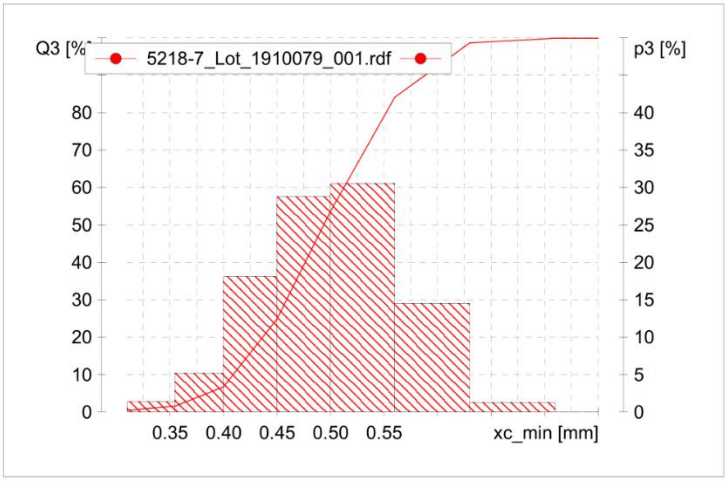

Kenngrößen

Q3 [%]	x [mm]
10.0	0.414
50.0	0.494
90.0	0.578

Sv =	12.095 / mm
Sm =	48.379 cm²/g

p3(0.400 mm,0.600 mm) = 88,50 %
p3(0.425 mm,0.600 mm) = 81,82 %

Mittelwert b/l3 = 0,919

Benutzer

CAMSIZER: 0245

1 / 1

CAMSIZER®

SiLi SIGMUND LINDNER

Art. 5215 / 150-250 µm

Firma:	Sigmund Lindner GmbH
Benutzer:	Quality Control
Ergebnisdatei:	\...ve Fotos\Glaskugeln Typ S Microglas\Glaskugeln Typ S Microglas\5215-7_Lot_1850352_001.rdf
Messaufgabe:	C:\Camsizer\CAMSYS\5215 150-250 - 07-02-26.afg
Zeit:	23.01.2019, 11:13, Dauer 4 min 26 s bei 0.5 % Flächendichte , Bildrate 1:1und 60 mm Rinne mit Leitblech
Größendefinition:	xc_min
Partikelanzahl:	CCD-B = 2571730 , CCD-Z = 152556
Anpassung:	nein
Material:	Weissker 28W1/ITB 150- 250 µm
Kommentar:	Sollwert: p3 (0.150mm; 0.250mm) = 80 % b/l3 (= Rundheit) mind. 0.85

Kornklasse [mm]	[mm]	p3 [%]	Q3 [%]	b/l3
	< 0.100	0.19	0.19	0.857
0.100	0.125	0.39	0.58	0.794
0.125	0.150	1.57	2.15	0.810
0.150	0.175	6.37	8.52	0.865
0.175	0.200	20.08	28.60	0.898
0.200	0.225	37.68	66.28	0.930
0.225	0.250	28.55	94.83	0.940
0.250	0.275	5.17	100.00	0.927
0.275	0.300	0.00	100.00	
0.300	0.325	0.00	100.00	
0.325	0.350	0.00	100.00	
> 0.350		0.00	100.00	

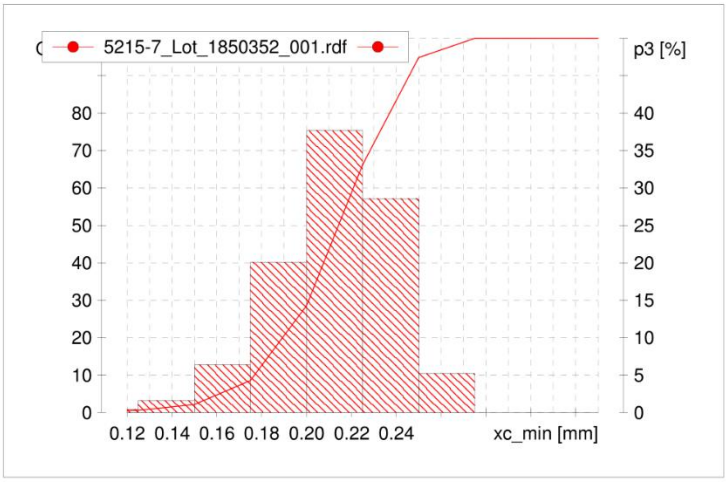

Kenngrößen

Q3 [%]	x [mm]
10.0	0.178
50.0	0.215
90.0	0.243

Sm = 113.044 cm²/g

p3(0.150 mm,0.250 mm) = 92,68 %

Mittelwert b/l3 = 0,920

Benutzer

CAMSIZER: 0245

Glass Properties

www.glasexperte.de

Composition

Oxides	Weight [%]	Mole [%]
Si_O2	74,0000	73,1790
Al2_O3	0,5300	0,3089
Fe2_O3	0,1700	0,0633
B2_O3	0,0800	0,0683
Ca_O	8,4900	8,9960
Mg_O	3,3500	4,9384
Ba_O	0,0800	0,0310
Zn_O	0,2600	0,1899
K2_O	0,5300	0,3343
Na2_O	12,2000	11,6965
Sb2_O3	0,0200	0,0041
S_O3	0,2200	0,1633
Ti_O2	0,0300	0,0223
Summe	99,9600	99,9952

Properties

		[dPas]
1473	°C Melting Temperature	10^2
1058	°C Liquidus Temperature	
1216	°C Gob Temperature	10^3
1048	°C Working Temperature	10^4
1019	°C Sinking Temperature	10^4,22
930	°C Flow Temperature	10^5
740	°C Softening Temperature	10^7,6
599	°C Deformation Temperature	10^11,3
558	°C Annealing Temperature	10^13
552	°C Transformation Temperature	10^13,3
521	°C Strain Temperature	10^15
308,7	K Working Range	
8,57	/10^6·K C.Thermal Expansion 20/400	
2493	kg/m³ Density	
1,5179	Refractive Index	
59,206	Abbé Number	
1322	J / kg·K Spec. Heat >600 °C	
1,133	W / Km Heat Conductivity	
343,8	/10^9 m²/s Thermal Conductivity	
1909,7	W√s / Km² E-Value	
110,9	% RMS	
113,2	Working Number VK	

Date/Time
14.04.2010 15:18:59

Glass Name
Art. 52xx
Glass No.
5
Glass Family
Kalknatron Glas
Base
Analyse
Version
3.16
Created
14.04.2010
Patent No.

Furnace

Company
Sigmund Lindner GmbH
Plant
Warmensteinach
Country
Deutschland

Viskositätskurve

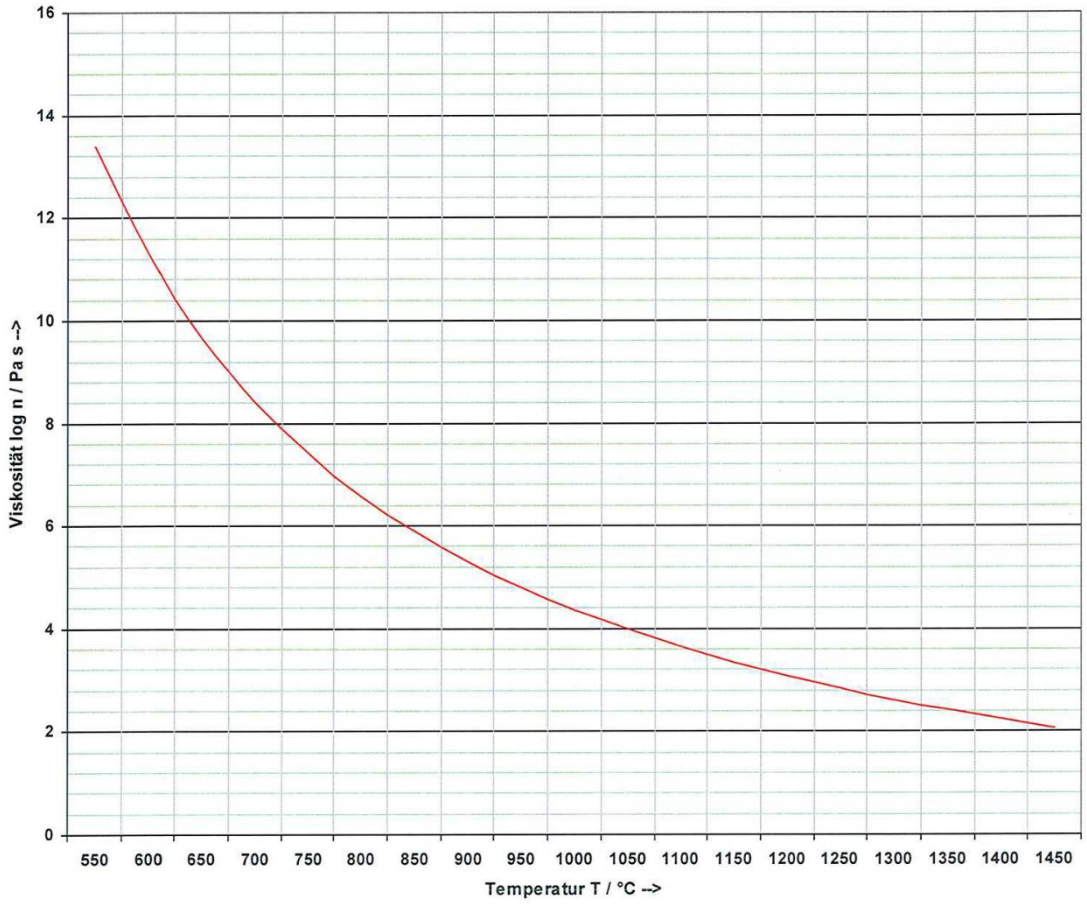

Erstellt am
14.04.2010 15:19:06

Glasbezeichnung
Art. 52xx
Glasnr.
5
Gattung
Kalknatron Glas
Basis
Analyse
Version
3.16
Seit
14.04.2010
Patentnr.

Ofen

Firma
Sigmund Lindner GmbH
Werk
Warmensteinach
Land
Deutschland

Lakatos A	1,7881
Lakatos B	4659,9400
Lakatos To	243,2400

PROPERTIES OF A AND E GLASS

TYPICAL VALUES	A-GLASS Soda-Lime	E-GLASS Boro-Silicate
Physical:		
Specific Gravity	2.5	2.54
Refractive Index	1.51	1.55
Free Iron Content, % max	0.1	0.1
Mechanical:		
Young's Modulus, 10^6 psi	10.0	10.5
Rigidity Modulus, 10^6 psi	4.3	
Hardness (Moh)	6.0	6.5
Coefficient of Friction	0.9-1.0	1.0
Electrical:		
Dielectric Constant, 22°C, 10^6 Hz	6.9	5.8
Loss Tangent, 22°C 10^6 Hz	0.0085	0.0010
Vol. Resistivity, 25°C, ohm-cm	6.5×10^{12}	10^{13}-10^{16}
Thermal:		
Softening Point, °C	704	846
Expansion Coefficient, in/in/°CX10^{-7}	90	28
Thermal Conductivity (cal/(sec)(cm^2)(°C/cm)at 500°C)	0.0036	
Composition %:	A-Glass	E-Glass
SiO_2*	72.5	52.5
Na_2O	13.7	0.3
CaO	9.8	22.5
MgO	3.3	1.2
Al_2O_3	0.4	14.5
FeO/Fe_2O_3	0.2	0.2
K_2O	0.1	0.2
B_2O_3	0.0	8.6

*** No measurable free crystalline silica content as tested by ASTM C-169**

Hydrolytic Leach Resistance:**		
Leachate pH	9.4	8.5
Leach Conductivity, (mmho/cm)	101.0	45.0
Leach Concentrations, (mg/cc)		
Total Alkali	25.7	3.6
Calcium	18.1	20.4
Boron	Trace	18.7
Silica	5.4	1.1

**** One hour boil under reflux with deionized water**

Packaging

Spheriglass® Solid Glass Microspheres are available in paper bags with plastic liners, bulk bags and various bulk shipping modes. Details of packaging options are available as a separate document. Samples in sufficient quantity for testing are available on request.

Other Product Range:

Sphericel® Light Weight Hollow Glass Microspheres
Q-CEL® Ultra-Light Weight Hollow Microspheres
Conduct-O-Fil® Conductive Particles

Safety Information

Material Safety Data Sheets (MSDS) can be supplied on request.

For further information about our range of Solid and Hollow Microspheres, please contact us:

Potters Industries LLC
Engineered Glass Materials Division
PO Box 841
Valley Forge, PA 19482
USA
Tel: 800-552-3237
Fax: 610-408-9724
Website: www.pottersbeads.com

Annex 2: Résumé de la thèse de doctorat (Français)

La majeure partie de nos connaissances sur la relation entre la microstructure des roches et leurs propriétés macroscopiques résulte de travaux expérimentaux menés sur des échantillons de roches naturelles. Or, bien qu'il en existe des exemples bien connus tel que le grès de Fontainebleau, il est rare de trouver des formations rocheuses naturelles pour lesquelles un unique paramètre microstructural (porosité, taille des grains, taille des pores, etc.) varie largement alors que les autres attributs microstructuraux restent constants. Au contraire, sur le terrain au sein d'une même formation ou sur des sites voisins, les échantillons de roches prélevés présentent bien souvent une forte variabilité à la fois en termes de pétrologie que de microstructure. Ce haut degré de variabilité dans le temps et dans l'espace limite la reproductibilité des expériences menées en laboratoire sur des roches naturelles et donc, les conclusions qui peuvent en être tirées. Par exemple, si deux roches naturelles ont la même taille moyenne de grains mais des porosités différentes, très souvent elles présentent également des proportions différentes en ciment ou en argile qui, comme la taille des grains, exercent une influence importante sur les propriétés mécaniques. Aussi, pour dépasser les limites posées par l'hétérogénéité et la variabilité des roches naturelles, de plus en plus d'études ont recourt à des simulations numériques d'expériences de déformation sur des échantillons numériques dont la microstructure est parfaitement connue et contrôlée. Cependant, une autre stratégie peut être adoptée pour déconvoluer les paramètres microstructuraux et étudier leur influence sur les propriétés macroscopiques de façon isolée : la préparation de roches de synthèse. En effet, il est maintenant bien établi que les roches synthétiques offrent la possibilité de modéliser de manière réaliste le comportement mécanique des roches et l'évolution des propriétés effectives au cours de processus géologiques tels que la diagenèse.

Les travaux de cette thèse s'appuient sur l'utilisation de roches synthétiques préparées à partir de billes de verre sodo-calcique par frittage visqueux. (Figure 1) La technique de frittage visqueux permet de contrôler la porosité et la taille des grains de façon indépendante. La méthode consiste à préparer une certaine distribution de billes de verre à température ambiante, ensuite placée à une température supérieure à la température de transition du verre, au-delà de laquelle les billes se comportent de façon visqueuse et s'agglomèrent

progressivement. En pratique, la porosité finale des échantillons de billes de verre est contrôlée en changeant la température et le temps de frittage.

Bien qu'il existe un grand nombre d'autres attributs microstructuraux dont l'influence sur les propriétés effectives nécessite une étude approfondie, car ils contribuent au comportement hydromécanique complexe et variable des roches de la croûte terrestre, cette thèse vise à poser les bases de l'utilisation d'échantillons de billes de verre frittées pour des expériences de déformation mécanique et s'intéresse pour cela au cas le plus simple : un milieu granulaire biphasique sans ciment. Ainsi, les différents chapitres de la thèse s'organisent autour de la question du contrôle de la porosité et de la distribution de taille de grains, identifiés comme deux des paramètres les plus importants pour le comportement mécanique des roches.

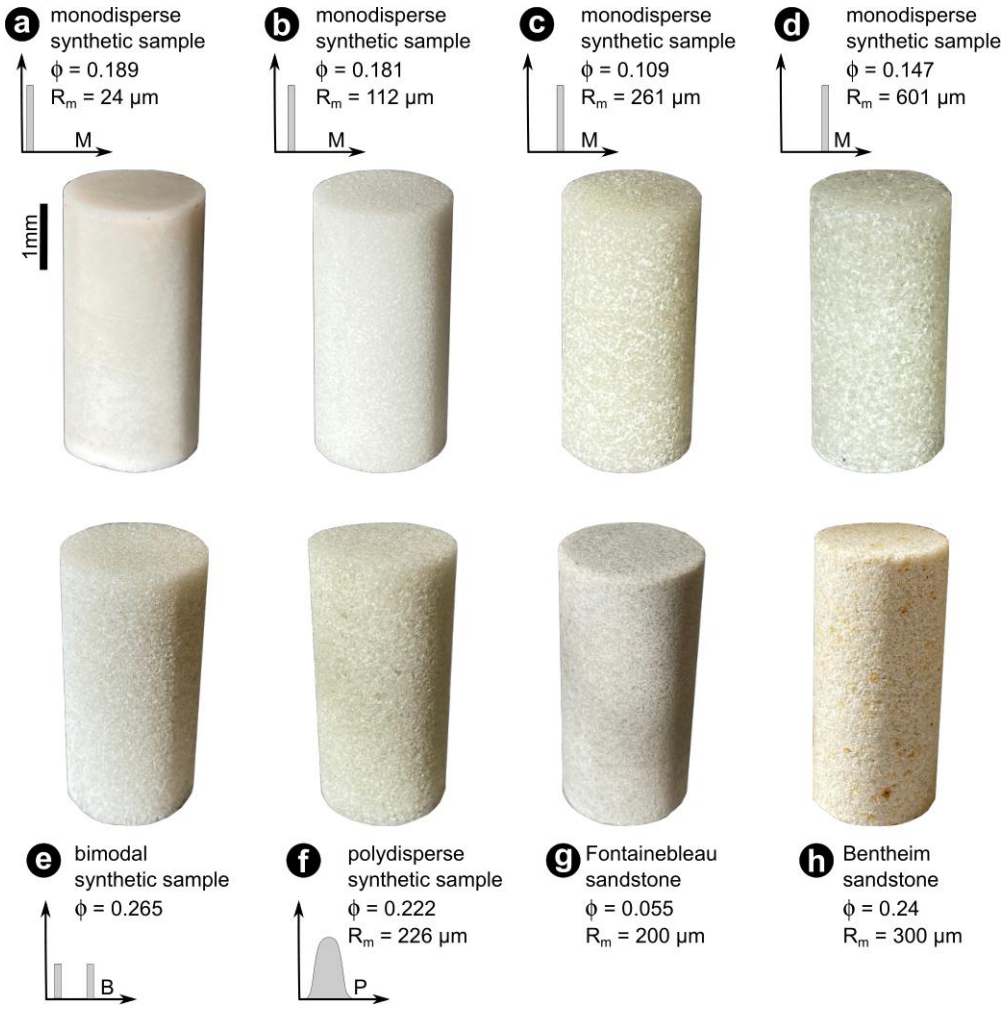

Figure 1 Aperçu d'échantillons synthétiques (a-f) et de grès naturels (g-h) avec différentes

porosités et distributions de tailles de grains (monodisperse (a-d), polydisperse bimodale (e) ou monomodale (f)).

Plus généralement, les travaux menés dans le cadre de cette thèse visent à permettre d'affiner les descriptions théoriques et analytiques existantes du lien entre propriétés effectives et microstructure et propriétés des constituants, sur lesquelles reposent de nombreux modèles d'évaluation de risques environnement ou encore de gestion de site industriels. En effet, les données acquises dans le cadre de cette recherche pourraient permettre d'améliorer les prédictions des modèles couramment utilisés dans de nombreux aspects des géosciences et de l'ingénierie, en ne s'appuyant que sur des paramètres microstructuraux facilement mesurables en laboratoire. Par exemple, comprendre comment les propriétés physiques évoluent au cours du processus de densification granulaire pourra aider à mieux appréhender la pressurisation des fluides pouvant conduire à de la fracturation, enjeu majeur pour les forages d'exploration et donc pour la gestion et l'optimisation des réservoirs d'hydrocarbures et de géothermie.

Ainsi, cette thèse cherche à répondre aux questions suivantes :

1) Les roches synthétiques fabriquées par frittage de billes de verre peuvent-elles simuler de manière satisfaisante le comportement hydromécanique des roches crustales poreuses et donc être utilisées pour étudier l'influence d'attributs microstructuraux spécifiques sur les propriétés hydromécaniques globales ?

2) Toutes choses égales par ailleurs, quel est l'effet des variations de la porosité totale et de la taille moyenne des grains sur la résistance globale ?

3) Comment la distribution de taille de grains influence-elle le comportement mécanique et les modes de rupture des roches granulaires poreuses ? En particulier, existe-t-il un degré d'hétérogénéité structurelle minimal au-delà duquel la localisation de la déformation compactante est inhibée ?

Afin de répondre aux questions précédentes, les variations de propriétés effectives telles que la perméabilité, la vitesse des ondes élastiques ou la résistance mécanique associées à des variations de porosité ou de taille moyenne de grains ont été mesurées de façon systématique. Par ailleurs, la thèse est construite autour de deux jalons :

1) Le cas le plus simple, un milieu granulaire biphasique dont les grains ont des tailles très proches, soit une distribution dite monodisperse ;

2) Un cas plus compliqué où le milieu granulaire présente une granulométrie variablement polydisperse, c'est-à-dire avec des proportions variables de grains ayant des tailles différentes.

Dans un premier temps, les termes et enjeux du sujet sont posés sous forme d'une introduction qui rappelle les résultats importants obtenus par les études antérieures, indispensables à la réalisation de ce travail de thèse.

Puis dans le second chapitre, la technique de préparation des roches synthétiques par frittage visqueux est présentée en détails pour le cas d'une distribution de taille de grains monodisperse et pour le cas polydisperse.

Ensuite, le troisième chapitre permet d'établir la pertinence de l'utilisation d'échantillons de billes de verre frittées en temps qu'analogues de roches clastiques naturelles. Pour cela, les propriétés petrophysiques des échantillons synthétiques sont comparées à des données de la littérature pour des grès naturels et à des modèles analytiques simples. Les tendances pour l'évolution des propriétés de transport telles que la perméabilité (Figure 2), la vitesse des ondes P et S (Figure 3) ou encore la conductivité thermique, avec la porosité et la taille de grains sont très similaires pour les échantillons synthétiques et les grès monominéraux naturels, en particulier le grès de Fontainebleau, et en accord avec les prédictions données par les modèles analytiques.

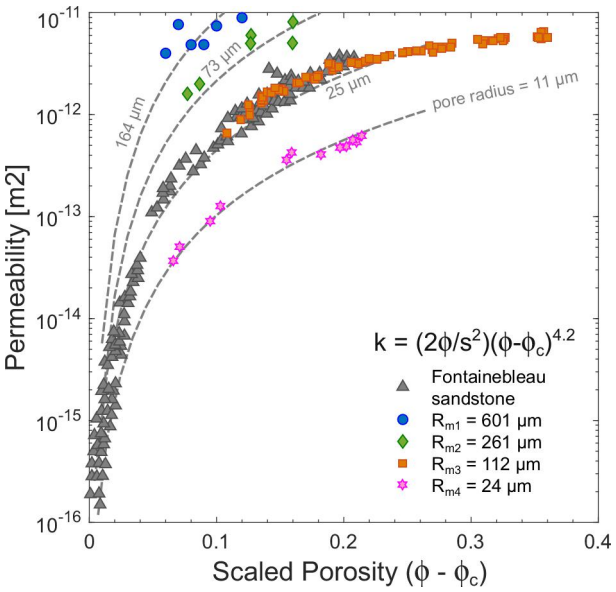

Figure 2 Evolution de la perméabilité en fonction de la porosité pour des échantillons synthétiques monodisperses avec un rayon de grains de 601 µm (rond bleu), 261 µm (losange

vert), 112 µm (carré orange) ou 24 µm (étoile rose) et pour le grès de Fontainebleau (triangle gris; Bourbié & Zinszner, 1985). Les courbes en pointillé gris donnent l'évolution prédite par le modèle de percolation proposé par Martys et al. (1994) et Wadsworth et al. (2016) pour différentes tailles de pores (renseignées au bout des courbes correspondantes).

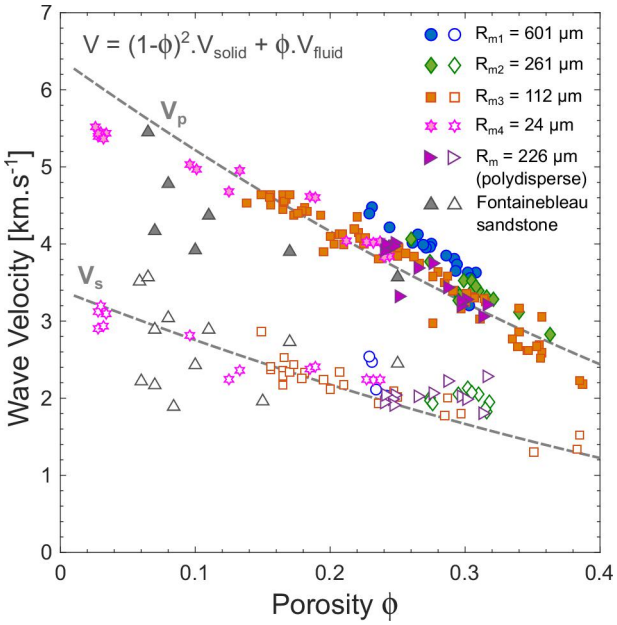

Figure 3 Evolution de la vitesse des ondes P et S en fonction de la porosité pour des échantillons synthétiques monodisperses avec un rayon de grains de 601 µm (rond bleu), 261 µm (losange vert), 112 µm (carré orange) ou 24 µm (étoile rose), des échantillons polydisperses avec un rayon moyen de grains de 226 µm (triangle violet) et pour le grès de Fontainebleau (triangle gris; Bourbié & Zinszner, 1985; Zamora & Poirier, 1990). Les courbes en pointillé gris donnent l'évolution prédite par le modèle de Raymer et al. (1980) (équation en haut du graphique).

Basé sur les résultats d'expériences de compression triaxiale et de compression hydrostatique sur des échantillons synthétiques monodisperses, le quatrième chapitre est consacré à l'étude de l'influence de la porosité et de la taille des grains sur le comportement mécanique et le mode de rupture des roches granulaires poreuses. Les données mécaniques sont analysées en parallèle avec les données microstructurales obtenues par microscopie électronique à balayage (MEB). Les résultats et la discussion sont présentés dans : Carbillet, L., Heap, M. J., Baud, P., Wadsworth, F. B., & Reuschlé, T. (2021). Mechanical Compaction

of Crustal Analogs Made of Sintered Glass Beads: The Influence of Porosity and Grain Size, Journal of Geophysical Research: Solid Earth, 126, e2020JB021321. https://doi.org/10.1029/2020JB021321. Les résultats révèlent notamment que le comportement mécanique des échantillons synthétiques est comparable à celui des grès monominéraux naturels tels que Bentheim et Fontainebleau, en particulier que des bandes de compaction se développent dans les grès synthétiques déformés dans le régime ductile (Figure 4).

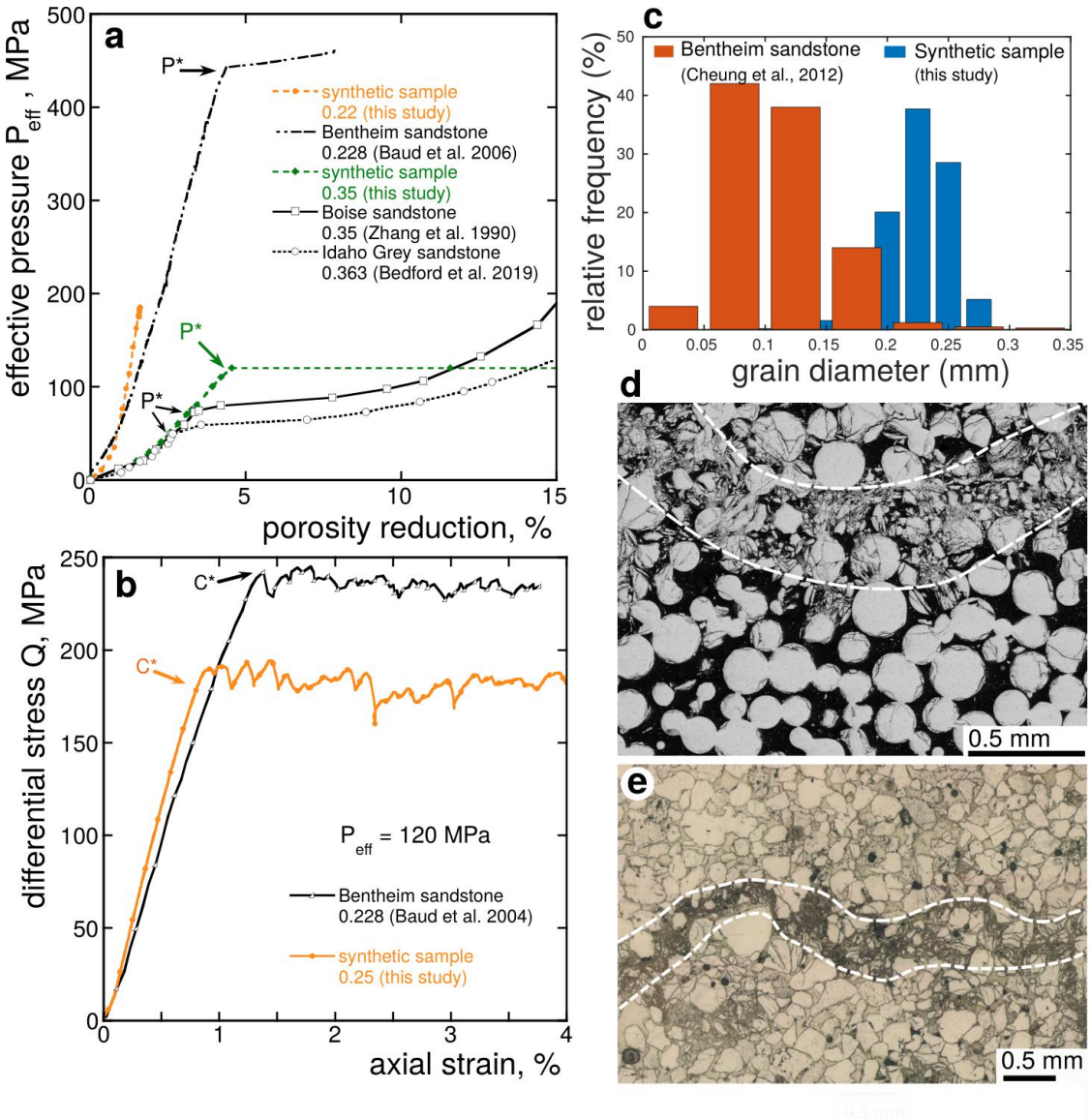

Figure 4 Résultats d'expériences de déformation sur des échantillons de synthèse comparés à des résultats d'expériences de déformation sur un grès naturel, le grès de Bentheim. (a) Comparaison des résultats de la compression hydrostatique d'un échantillon synthétique monodisperse (vert pointillé) avec une porosité de 0.35 et un diamètre de grains de 0.5 mm et

d'un (orange pointillé) avec une porosité de 0.22 et un diamètre de grains de 0.2 mm avec les résultats de la compression hydrostatique de trois grès naturels: Bentheim avec une porosité de 0.23 et un diamètre moyen de grains de 0.3 mm (Baud et al., 2006), Boise de porosité 0.35 et diamètre moyen de grains 0.92 mm (Zhang et al., 1990), et Idaho Grey de porosité 0.36 et de diamètre moyen de grain 0.7 mm (Bedford et al., 2019). Le régime de déformation inelastique débute au niveau du point P*, la contrainte critique pour l'initiation de l'écrasement des grains. (b) Comparaison des courbes contrainte-déformation obtenues par compression triaxiale à une pression de confinement P_{eff} de 120 MPa d'un échantillon synthétique de porosité 0.25 et de diamètre moyen de grains de 0.2 mm (orange) et du grès de Bentheim (Baud et al., 2004). Le point C* indique l'initiation de la compaction inélastique. (c) Comparaison des distributions de tailles de grains d'un échantillon synthétique et du grès de Bentheim (Cheung et al., 2012). (d) Comparaison des figures de déformation, ici, des bandes de compaction, formées au cours d'une expérience en compression triaxiale dans un échantillon synthétique avec celles formées dans (e) le grès de Bentheim.

Enfin, les résultats présentés dans le chapitre 4 mettent en évidence l'importance du contrôle de la taille des grains sur la résistance des roches poreuses à la compression mécanique. En effet, toutes choses égales par ailleurs, une augmentation de la taille des grains de 0,2 à 1,15 mm augmente la contrainte critique à laquelle la déformation devient plastique, donc irréversible, par plus d'un facteur 2 (Figure 5).

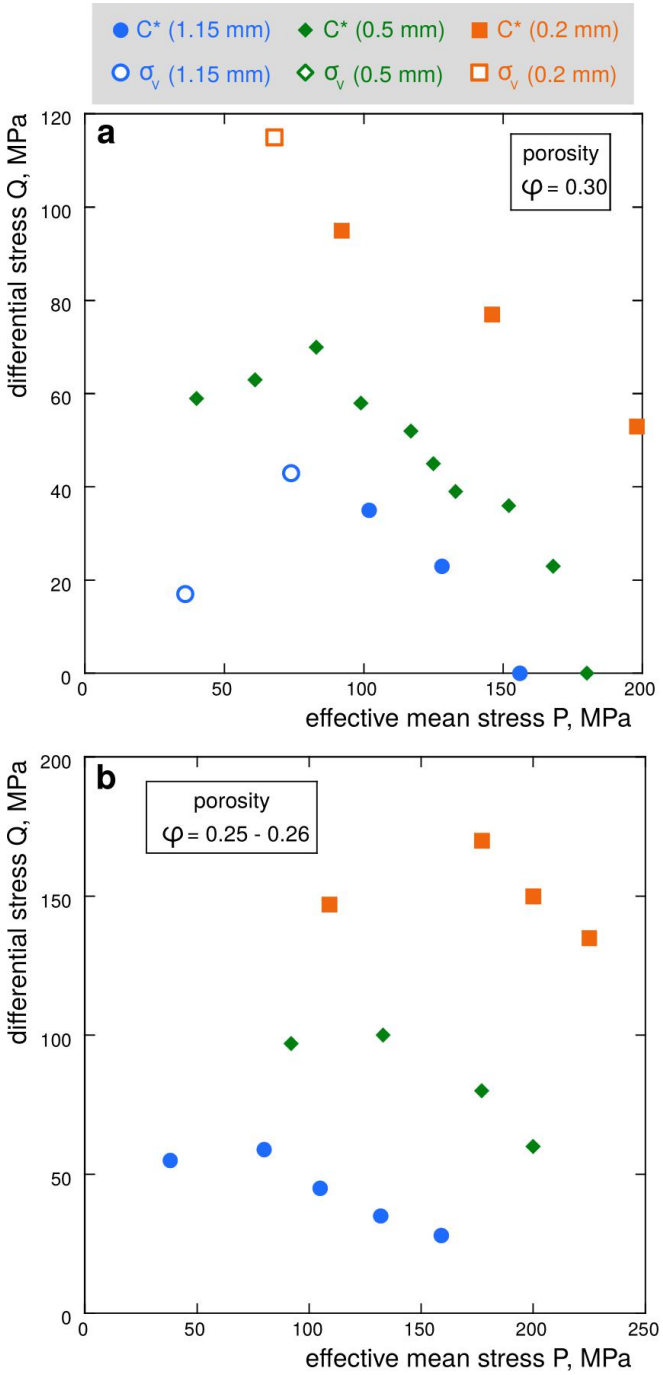

Figure 5 Compilation d'enveloppes de rupture de roches synthétiques avec une porosité de (a) 0.30 et de (b) 0.25. Les diamètres moyens des grains des échantillons sont renseignés dans la légende.

Le cinquième chapitre traite de l'influence du degré de polydispersivité et de la modalité de la distribution de taille de grains sur le comportement mécanique et le mode de rupture des roches poreuses, au moyen d'expériences de compression triaxiale et

hydrostatique et d'observations microstructurales sur des échantillons synthétiques variablement polydisperses. Les résultats montrent que plus les échantillons sont polydisperses, c'est-à-dire plus les échantillons sont hétérogènes en termes de tailles de grains, moins la contrainte critique à laquelle la déformation devient plastique est élevée (Figure 6).

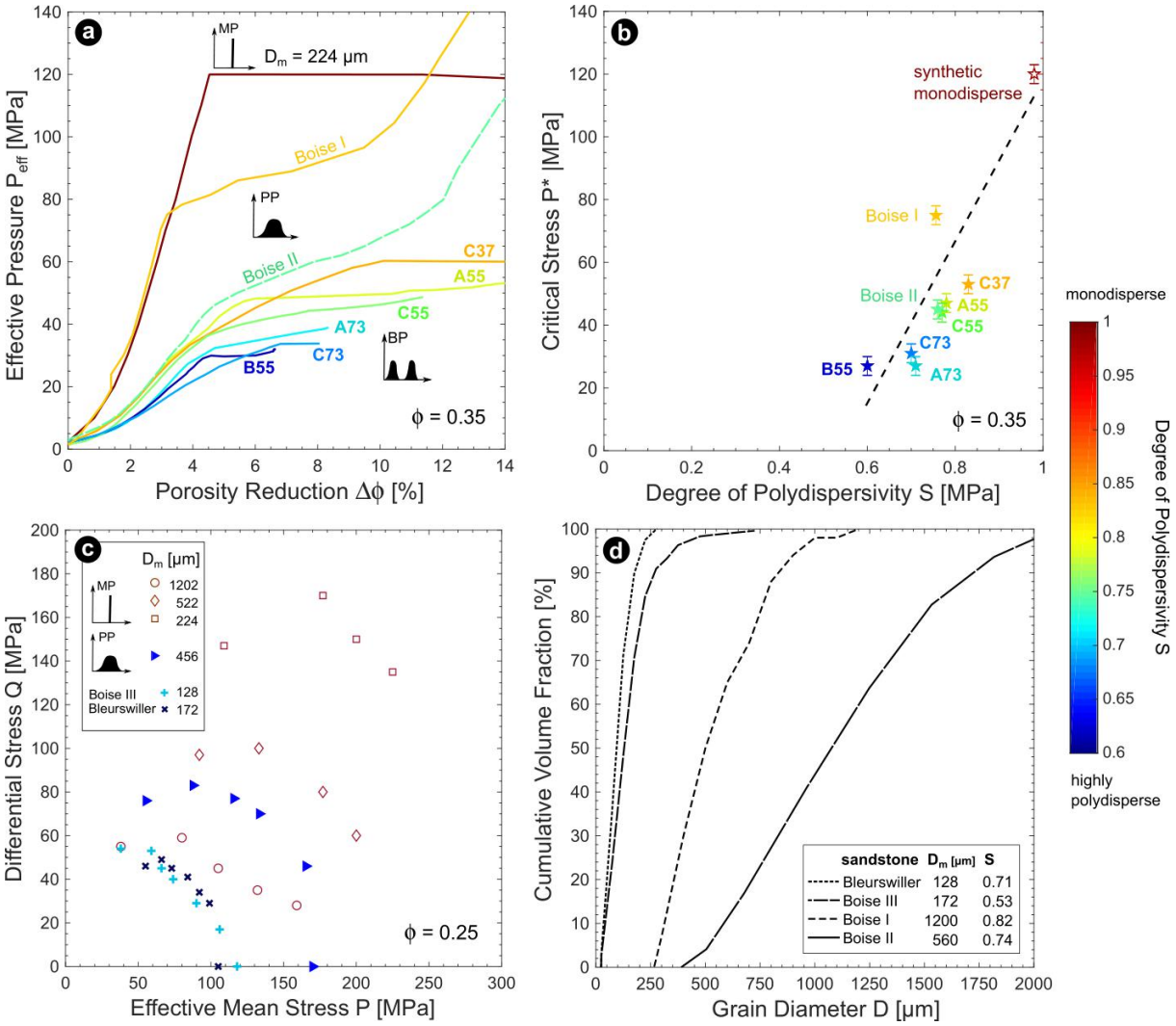

Figure 6 Comparaison des données mécaniques obtenues lors d'expériences de déformation sur des échantillons synthétiques plus ou moins polydisperses avec celles sur des échantillons de grès naturels. (a) Les courbes hydrostatiques d'échantillons polydisperses bimodaux sont compilées avec celles pour les grès Boise I (Zhang et al., 1990) et Boise II (Baud et al., 2000). (b) Les valeurs de P* obtenues d'après les courbes hydrostatiques précédentes sont présentées en fonction du degré de polydispersivité. P* évolue de façon linéaire croissante avec le degré de polydispersivité. (c) Les enveloppes de rupture d'échantillons synthétiques plus ou moins

polydisperses sont comparées à celles des grès de Boise III et Bleurswiller (Cheung et al., 2012), dont les distributions de tailles de grains sont présentées en (d).

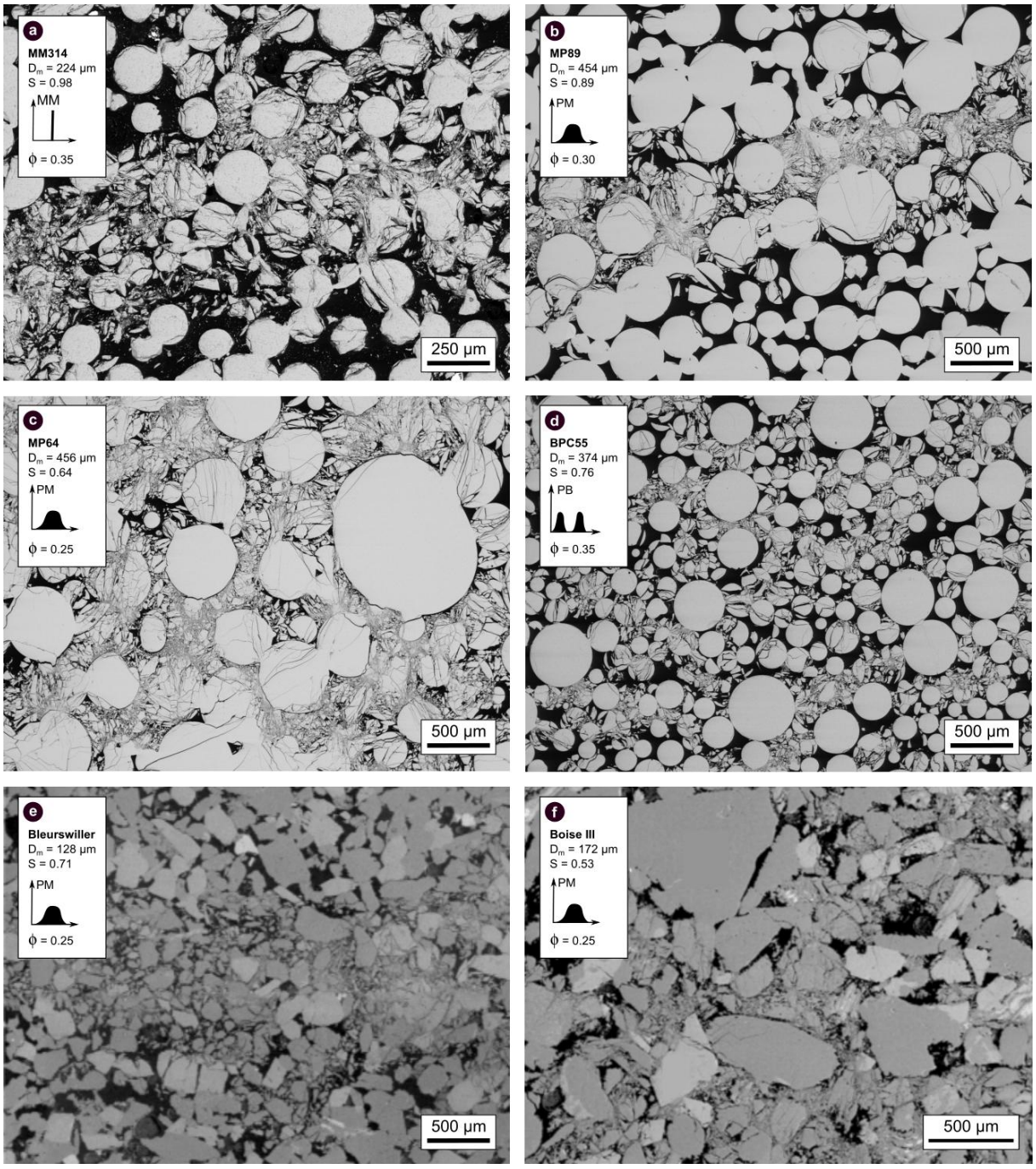

Figure 7 Images de microscopie électronique à balayage de figures de déformation formées lors de la compression triaxiale d'échantillons synthétiques plus ou moins polydisperses (a-d) et des grès naturels (e) Bleurswiller et (f) Boise III (Cheung et al., 2012). Des bandes de compaction sont visibles dans les échantillons synthétiques et naturels les plus homogènes

(avec un degré de polydispersivité S proche de 1) et semblent disparaitre progressivement alors que l'hétérogénéité de la distribution de taille de grains augmente (S diminue).

Par ailleurs, les résultats mettent en évidence l'importance de la distribution de taille de grains pour le développement de figures de déformation localisées (Figure 7). En effet, tandis que des bandes de compaction se forment dans les échantillons monodisperses et faiblement polydisperses déformés dans le régime ductile, la compaction mécanique se développe de façon homogène dans les échantillons les plus polydisperses. Toutes choses égales par ailleurs, plus la microstructure est homogène, plus la probabilité que des bandes de compaction se développent sous l'effet d'un chargement triaxial dans le régime ductile est élevée.

Enfin, le dernier chapitre met en perspective les conclusions des chapitres précédents (Figure 8) et discute de l'intérêt et des limites des roches synthétiques, en particulier des échantillons de billes de verre frittées.

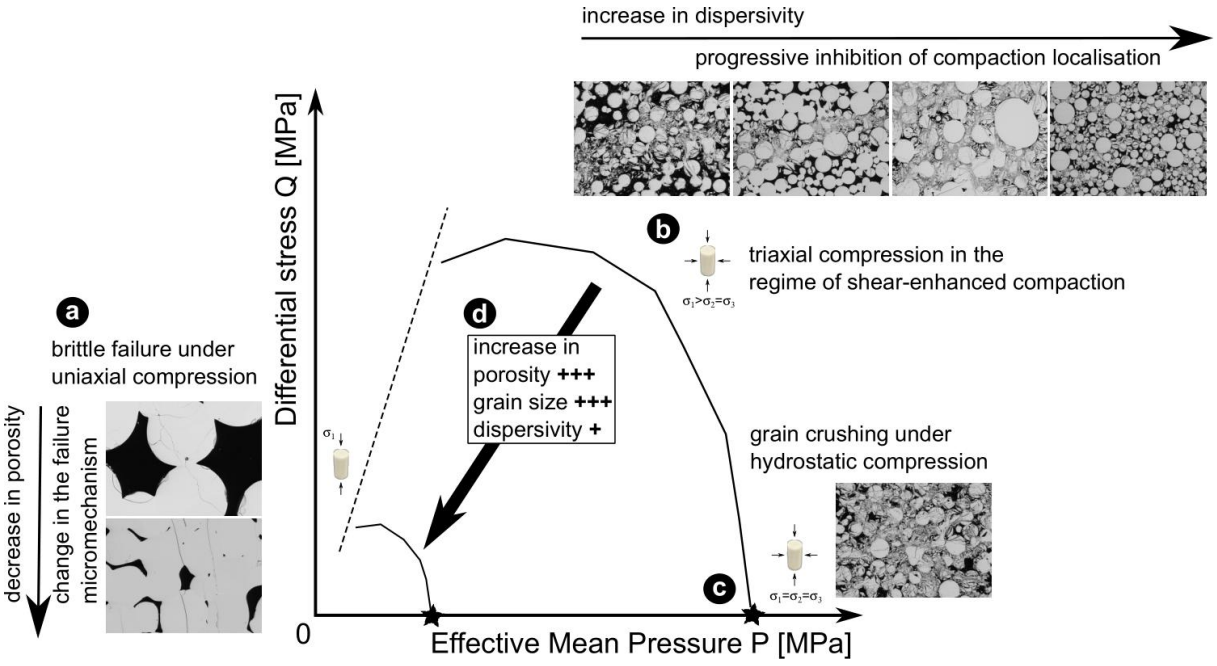

Figure 8 Influence de la porosité, de la taille des grains et du degré de polydispersivité sur le comportement mécanique et les modes de rupture des roches. Plus une roche est poreuse, formée par de gros grains et polydisperse (ou hétérogène en termes de distribution de tailles

de grains), moins la contrainte critique à laquelle elle se déforme de façon irréversible est élevée.

Références

Baud, P., Zhu, W., & Wong, T. (2000). Failure mode and weakening effect of water on sandstone. *Journal of Geophysical Research*, *105*, 371–389. https://doi.org/10.1029/2000JB900087

Baud, P., Klein, E., & Wong, T. (2004). Compaction localization in porous sandstones: spatial evolution of damage and acoustic emission activity. *Journal of Structural Geology*, *26*(4), 603–624. https://doi.org/10.1016/j.jsg.2003.09.002

Baud, P., Vajdova, V., & Wong, T. (2006). Shear-enhanced compaction and strain localization: Inelastic deformation and constitutive modeling of four porous sandstones. *Journal of Geophysical Research: Solid Earth*, *111*(B12), n/a-n/a. https://doi.org/10.1029/2005JB004101

Bedford, J. D., Faulkner, D. R., Wheeler, J., & Leclère, H. (2019). High-Resolution Mapping of Yield Curve Shape and Evolution for High-Porosity Sandstone. *Journal of Geophysical Research: Solid Earth*, *124*(6), 5450–5468. https://doi.org/10.1029/2018JB016719

Bourbie, T., & Zinszner, B. (1985). Hydraulic and Acoustic Properties as a Function of Porosity in Fontainebleau Sandstone. *Journal of Geophysical Research*, *90*(4), 524–532.

Cheung, C. S. N., Baud, P., & Wong, T. (2012). Effect of grain size distribution on the development of compaction localization in porous sandstone. *Geophysical Research Letters*, *39*(21), n/a-n/a. https://doi.org/10.1029/2012GL053739

Carbillet, L., Heap, M. J., Baud, P., Wadsworth, F. B., & Reuschlé, T. (2021). Mechanical Compaction of Crustal Analogs Made of Sintered Glass Beads: The Influence of Porosity and Grain Size. *Journal of Geophysical Research: Solid Earth*, *126*(4). https://doi.org/10.1029/2020jb021321

Martys, N. S., Torquato, S., & Bentz, D. P. (1994). Universal scaling of fluid permeability for sphere packings. *Physical Review E*, *50*(1).

Raymer, L. L., Hunt, E. R., & Gardner, J. S. (1980). An Improved Sonic Transit Time-To-Porosity Transform. Retrieved from https://www.onepetro.org/conference-paper/SPWLA-1980-P

Wadsworth, F. B., Vasseur, J., Scheu, B., Kendrick, J. E., Lavallée, Y., & Dingwell, D. B. (2016). Universal scaling of fluid permeability during volcanic welding and sediment diagenesis. *Geology*, *44*(3), 219–222. https://doi.org/10.1130/G37559.1

Zamora, M., & Poirier, J. P. (1990). Experimental study of acoustic anisotropy and birefringence in dry and saturated Fontainebleau sandstone. *Geophysics*, *55*(11), 1455–1465. https://doi.org/10.1190/1.1442793

Zhang, J., Wong, T.-F., & Davis, D. M. (1990). Micromechanics of pressure-induced grain crushing in porous rocks. *Journal of Geophysical Research*, *95*(B1), 341. https://doi.org/10.1029/JB095iB01p00341

Institut Terre & Environnement de Strasbourg | ITES | UMR 7063 de l'Université de Strasbourg & CNRS & ENGEES

Lucille Carbillet

Ecole et Observatoire des Sciences de la Terre

ED 413 Sciences de la Terre et de l'Environnement

From Grains to Rocks: The Evolution of Hydraulic and Mechanical Properties during Diagenesis

Résumé

Notre compréhension de la relation entre les attributs microstructuraux et les propriétés mécaniques des matériaux naturels découle des travaux expérimentaux en mécanique des roches. Des progrès considérables ont été réalisés mais l'hétérogénéité des roches naturelles, à la fois en termes de pétrologie que de microstructure, limite l'étude de la contribution de chaque paramètre microstructural de façon indépendante. Dans cette thèse, des roches synthétiques pour lesquelles ces paramètres peuvent être contrôlés sont utilisées pour déconvoluer et étudier la contribution d'attributs microstructuraux spécifiques sur les propriétés hydrauliques et mécaniques des roches. En combinant une caractérisation pétrophysique systématique et des expériences de déformation avec une étude de la microstructure, le contrôle de premier ordre de la porosité et de la taille des grains sur l'initialisation de la compaction inélastique est mis en évidence. Par ailleurs, il est montré que, en compression triaxiale, la distribution de la taille des grains exerce une influence significative sur la propension à la localisation de la compaction.

Porosité, taille des grains, distribution de la taille des grains, compaction inélastique, localisation de la compaction

Abstract

Experimental rock mechanics studies underpin our understanding of the relationship between microstructural attributes and bulk mechanical properties of natural materials. Considerable progress has been made but intrinsic variability from sample to sample and structural heterogeneity remain limitations to the study of the contribution of each microstructural parameter independently. In this work, synthetic rocks for which these parameters can be predetermined and designed are used to unravel the contribution of microstructural attributes on the hydraulic and mechanical properties of rocks. Combining systematic petrophysical characterisation and experimental rock deformation methods with analyses of the microstructure, the first-order control of porosity and grain size on the onset of inelastic compaction are exposed and grain size distribution is shown to have a significant influence on the propensity for compaction localisation under triaxial loading.

Porosity, grain size, grain size distribution, inelastic compaction, compaction localisation